

# **A novel technique to analyse trabecular bone mechanics during screw insertion**

Melissa Ryan BSc BEng (Biomed) Hons

A thesis submitted to the School of Computer Science, Engineering and Mathematics  
in the Faculty of Science and Engineering in total fulfilment of the requirements of  
the degree of Doctor of Philosophy

Flinders University of South Australia, Australia

Submitted November 2014

# TABLE OF CONTENTS

<b>Table of Contents</b> .....	<b>I</b>
<b>Publicly Disseminated Work</b> .....	<b>IV</b>
<b>List of Figures</b> .....	<b>V</b>
<b>List of Tables</b> .....	<b>VIII</b>
<b>List of Equations</b> .....	<b>IX</b>
<b>Abbreviations</b> .....	<b>X</b>
<b>Abstract</b> .....	<b>XI</b>
<b>Declaration</b> .....	<b>XIII</b>
<b>Acknowledgements</b> .....	<b>XIV</b>
<b>1 Introduction</b> .....	<b>1</b>
<b>2 Background</b> .....	<b>5</b>
2.1 Structure and function of bone .....	6
2.1.1 Whole bone level .....	7
2.1.2 Macrostructural level (cancellous vs cortical).....	9
2.1.3 Microstructural level (osteonal vs trabecular bone) .....	10
2.1.4 Sub-Microstructural level (lamellar) .....	12
2.1.5 Nanoscale level.....	13
2.2 Bone remodelling.....	14
2.3 Mechanotransduction in bone .....	15
2.4 Morphologic and mechanical properties of cancellous bone .....	16
2.4.1 Morphologic parameters.....	16
2.4.2 Mechanical properties .....	17
2.4.3 Apparent level properties .....	18
2.4.4 Tissue properties.....	21
2.4.4.1 Uniaxial Tensile Testing .....	23
2.4.4.2 Ultrasonic measurements .....	24
2.4.4.3 Bending Tests.....	24
2.4.4.4 Nanoindentation .....	24
2.4.4.5 Back-calculation using finite element models .....	25
2.5 Density .....	25
2.6 Osteoporosis .....	26
2.7 Bone Fractures .....	28
2.8 Implant stability .....	29
<b>3 The finite element method</b> .....	<b>32</b>
3.1 Principles of FEA .....	33
3.2 FE modelling of bone .....	35
3.2.1 Continuum Vs micro models.....	35
3.3 Finite element modelling of cancellous bone .....	36
3.3.1 Geometry .....	36
3.3.2 Discretisation.....	37
3.3.3 Material models .....	39
3.3.4 Loading and boundary conditions .....	40

3.4	Current micro-FE models of cancellous bone: A review of the literature...	41
3.4.1	FE models of bone-implant constructs .....	47
<b>4</b>	<b>Validation of Image based micro-FEA .....</b>	<b>54</b>
4.1	Introduction.....	55
4.2	Aims.....	57
4.3	Methods .....	57
4.3.1	Image Processing.....	58
4.3.2	Experimental Analysis .....	59
4.3.3	FE models.....	60
4.3.4	Statistical Analysis .....	62
4.4	Results.....	62
4.4.1	Convergence .....	62
4.4.2	Thresholding.....	63
4.4.3	Comparison of full-models and mechanical tests.....	63
4.4.4	Comparison of full- and sub-volume models .....	65
4.5	Discussion.....	68
<b>5</b>	<b>Testing the assumption of isotropy for cancellous bone tissue elastic modulus .....</b>	<b>78</b>
5.1	Introduction.....	79
5.2	Aims.....	81
5.3	Methods .....	81
5.3.1	FE Analysis .....	84
5.3.2	Statistical Analysis .....	85
5.3.3	Results .....	86
5.3.4	FEA .....	87
5.3.5	Micromechanical Behaviour .....	89
5.4	Discussion.....	91
<b>6</b>	<b>Nonlinear micro-FE modelling of human vertebral bone under uniaxial compression.....</b>	<b>100</b>
6.1	Introduction.....	101
6.2	Aims.....	102
6.3	Methods .....	103
6.3.1	Statistical Analysis .....	105
6.4	Results.....	105
6.5	Discussion.....	111
<b>7</b>	<b>Determining the relationship between insertion and stripping torques....</b>	<b>119</b>
7.1	Introduction.....	120
7.2	Screw Material.....	124
7.2.1	Identification of Optimal Screw Material for micro-CT Imaging.....	125
7.3	Aims.....	130
7.4	Methods .....	130
7.4.1	Tissue Collection.....	130
7.4.2	Ethical Approval.....	130
7.4.3	Specimen Preparation.....	131
7.4.4	Micro-CT Imaging of Bone Specimens .....	132
7.4.5	Test-Rig .....	132
7.4.6	Screw Insertion.....	134
7.4.7	Signal analysis .....	136

7.4.8	Statistical Analysis .....	138
7.5	Results.....	139
7.6	Discussion.....	145
7.6.1	Screw material .....	145
7.6.2	Establishing a relationship between $T_{\text{plateau}}$ and $T_{\text{stripping}}$ .....	147
7.6.3	Morphological influences on screw insertion .....	150
<b>8</b>	<b>Micro-FE of the bone-implant interface .....</b>	<b>153</b>
8.1	Introduction.....	154
8.2	Aims.....	156
8.3	Methods .....	157
8.3.1	Specimens.....	157
8.3.2	Screw Insertion.....	157
8.3.3	Post-Analysis.....	158
8.3.4	Image Processing.....	158
8.3.5	Image guided failure assessment .....	159
8.3.6	FEA .....	162
8.4	Results.....	165
8.4.1	Experimental analysis.....	165
8.4.2	Morphological assessment .....	169
8.4.3	Image guided failure assessment .....	169
8.4.4	Validation of the micro-FE model.....	175
8.4.5	Biomechanics of the peri-implant bone.....	178
8.5	Discussion.....	180
<b>9</b>	<b>Summary and future recommendations.....</b>	<b>190</b>
9.1	Summary.....	191
9.1.1	Micro-FEA vertebral bone .....	191
9.1.2	Understanding screw insertion .....	192
9.1.3	Micro-FE model of the bone-implant interface.....	192
9.2	Considerations for future work.....	193
9.2.1	Micro-FE model .....	193
9.2.2	Validation of the model.....	194
9.3	Applications .....	194
9.4	Final Remarks .....	195
	<b>Appendices .....</b>	<b>196</b>
	<b>References .....</b>	<b>214</b>

## **PUBLICLY DISSEMINATED WORK**

### **Peer Reviewed Publications:**

Ab-Lazid R, Perilli E, Ryan M, Costi J, and Reynolds K, (2014). “Does cancellous screw insertion torque depend on bone mineral density and/or micro-architecture?” *J. Biomech* 47(2), pp 347-353.

### **Conference Proceedings:**

Ryan MK, Costi JJ, Badiei A, Fazzalari NL, Reynolds KJ. The role of effective tissue modulus in predicting apparent modulus and strength in osteoporotic bone. 56th Annual Meeting of the Orthopaedic Research Society, New Orleans, Louisiana USA, 2010.

Ryan MK, Costi JJ, Badiei A, Fazzalari NL, Reynolds KJ. The role of effective tissue modulus in predicting apparent modulus and strength in osteoporotic bone. ANZORS 12th annual scientific meeting, Adelaide, Australia, 2009.

Ryan MK, Costi JJ, Fazzalari NL, Reynolds KL. Validity of using a linear micro-finite element model to predict trabecular bone apparent mechanical properties: comparison with a non-linear model and experimental data. ANZ/IBMS, Sydney, Australia, 2009. (Poster Presentation)

Ryan MK, Hearn TC, Costi JJ, Fazzalari NL, Reynolds KJ. Assessing failure mechanisms of trabeculae by micro-computed tomography based finite element modelling. 5th Annual Clare Valley bone meeting, Clare, Australia, 2008.

# LIST OF FIGURES

FIGURE 2-1: PARTIALLY SECTIONED HUMERUS, AN EXAMPLE OF A LONG BONE .....	8
FIGURE 2-2: CORTICAL AND CANCELLOUS BONE STRUCTURES OF THE HUMAN VERTEBRA.....	10
FIGURE 2-3: MICROSTRUCTURE OF CORTICAL BONE .....	11
FIGURE 2-4: MICROSTRUCTURE OF CANCELLOUS BONE .....	12
FIGURE 2-5: ATOMIC FORCE MICROSCOPY IMAGE OF (A) COLLAGEN TYPE I FIBRILS, AND (B) HYDROXYAPATITE MINERAL CRYSTALS EXTRACTED FROM BONE .....	13
FIGURE 2-6: TYPICAL LOAD-DEFORMATION CURVES FOR CANCELLOUS AND CORTICAL BONE LOADED IN COMPRESSION .....	19
FIGURE 2-7: COMPARISON OF NORMAL (TOP) AND OSTEOPOROTIC (BOTTOM) BONE ARCHITECTURE IN THE THIRD LUMBAR VERTEBRAE .....	27
FIGURE 2-8: BOX PLOT INDICATING THE MEDIAN AND QUARTILE PULL-OUT STRENGTHS. ....	31
FIGURE 3-1: FE MESH OF TRABECULAR BONE.....	38
FIGURE 3-2: CORRELATION BETWEEN PREDICTED AND EXPERIMENTAL UNIAXIAL APPARENT MODULUS .....	43
FIGURE 3-3: SCHEMATIC OF THE BILINEAR TISSUE MATERIAL MODEL (NOT TO SCALE) .....	44
FIGURE 3-4: EXAMPLE OF HISTOLOGY SECTION (LEFT) AND FE SECTION (RIGHT) .....	46
FIGURE 3-5: FE MODEL OF VERTEBRAL BONE WITH SCREW REMOVED .....	48
FIGURE 3-6: MICRO-CT IMAGE OF HUMERAL HEAD .....	50
FIGURE 3-7: PERI-IMPLANT STRAIN IN BONE FOR THE FREELY CONSTRAINED CONTINUUM MODEL (LEFT) AND DISCRETE MODEL (RIGHT).....	53
FIGURE 4-1: RECONSTRUCTED MIRO-CT SLICE BEFORE IMAGE PROCESSING (LEFT), AND AFTER IMAGE PROCESSING (RIGHT).....	59
FIGURE 4-2: TYPICAL STRESS-STRAIN CURVE FOR THE EXPERIMENTAL UNIAXIAL COMPRESSION TESTS	60
FIGURE 4-3: DIAGRAM SHOWING THE COMPRESSIVE DISPLACEMENT BOUNDARY CONDITIONS FOR THE FE MODEL.....	61
FIGURE 4-4: APPARENT MODULUS DETERMINED EXPERIMENTALLY ( $E_{APP}^{EXP}$ ) VS APPARENT MODULUS PREDICTED BY THE FULL FE MODEL ( $E_{APP}^{FE}$ ).....	64
FIGURE 4-5: APPARENT ULTIMATE STRENGTH DETERMINED EXPERIMENTALLY VS THE FE PREDICTED APPARENT MODULUS ( $E_{APP}^{FE}$ ) FOR THE FULL-VOLUME MODELS .....	64
FIGURE 4-6: FE CALCULATED APPARENT MODULUS FOR THE FULL- AND SUB-VOLUME MODELS .....	67
FIGURE 4-7: APPARENT MODULUS DETERMINED EXPERIMENTALLY ( $E_{APP}^{EXP}$ ) VS APPARENT MODULUS PREDICTED BY THE SUB-VOLUME FE MODEL ( $E_{APP}^{FE}$ ) .....	67
FIGURE 4-8: APPARENT ULTIMATE STRENGTH DETERMINED EXPERIMENTALLY VS THE FE PREDICTED APPARENT MODULUS ( $E_{APP}^{FE}$ ) FOR THE SUB-VOLUME MODELS .....	68
FIGURE 5-1: SCHEMATIC ILLUSTRATING LOADING CONDITIONS FOR THE VERTEBRAL SPECIMENS IN EITHER THE SUPERO-INNERIOR (SI) OR ANTEROPOSTERIOR (AP) GROUP.....	82
FIGURE 5-2: DETERMINATION OF PERCENTAGE OF TOTAL TISSUE YIELDED FOR ONE OF THE SI SPECIMENS.....	85

FIGURE 5-3: PERCENTAGE OF TISSUE YIELDED IN COMPRESSION AND TENSION AT APPARENT STRAIN INCREMENTS FROM 0.5 TO 2.0 % .....	90
FIGURE 5-4: MAXIMUM COMPRESSIVE AND TENSILE TISSUE STRAINS AT EACH STRAIN INCREMENT UP TO 2.0% APPARENT STRAIN FOR VERTEBRAL SPECIMENS LOADED IN EITHER THE SI OR AP DIRECTIONS.....	90
FIGURE 5-5: 3D RENDERINGS OF BONE SLICES TAKEN FROM A 60 YEAR OLD FEMALE SPECIMEN.....	95
FIGURE 6-1: SCHEMATIC OF THE IDEALISED MATERIAL MODEL FOR CAST-IRON PLASTICITY (A) AND THE BILINEAR MATERIAL MODEL IMPLEMENTED FOR THE NONLINEAR FE ANALYSES (B) .....	104
FIGURE 6-2: EXPERIMENTALLY DETERMINED VS FE MODEL APPARENT MODULUS FOR MATERIAL MODELS 2 AND 3 .....	107
FIGURE 6-3: EXPERIMENTALLY DETERMINED VS FE APPARENT YIELD STRESS FOR THE THREE MATERIAL MODELS ANALYSED .....	108
FIGURE 6-4: EXPERIMENTALLY DETERMINED VS FE APPARENT ULTIMATE STRENGTH .....	108
FIGURE 6-5: PERCENTAGE OF COMPRESSIVE TISSUE FAILURE AT APPARENT YIELD STRAIN VERSUS BV/TV .....	110
FIGURE 6-6: PERCENTAGE OF TENSILE TISSUE FAILURE AT APPARENT YIELD STRAIN VERSUS BV/TV .....	111
FIGURE 7-1: THE THREE PHASES OF SCREW PLACEMENT .....	121
FIGURE 7-2: TORQUE VERSUS ROTATION CURVE FOR AN ALUMINIUM SCREW INSERTED INTO CELLULAR POLYURETHANE FOAM (SAWBONES, SEATTLE, WA) .....	123
FIGURE 7-3: THREE SCREW TYPES WERE INVESTIGATED. ....	124
FIGURE 7-4: ALUMINIUM SCREW USED FOR TESTING IN CANCELLOUS FEMORAL HEAD BONE.....	127
FIGURE 7-5: CROSS-SECTIONAL MICRO CT SCANS OF A 7.0MM CANCELLOUS BONE SCREW .....	128
FIGURE 7-6: PEEK SCREWS.....	129
FIGURE 7-7: SPECIMEN PREPARATION .....	131
FIGURE 7-8: CUSTOM DESIGNED TEST RIG, BLOCK DIAGRAM (TOP) AND ACTUAL TEST RIG SET UP IN MICROCT SCANNER (BOTTOM) .....	133
FIGURE 7-9: FEMORAL HEAD INDICATING THE LOCATION OF THE HOLES FOR SCREW INSERTION .....	134
FIGURE 7-10: SCREW PLACEMENT IN THE FEMORAL HEAD .....	135
FIGURE 7-11: TORQUE VERSUS ROTATION TRACE INDICATING THE THREE DIFFERENT REGIONS PLATEAU TORQUE WAS CALCULATED OVER. ....	136
FIGURE 7-12: OUTPUT TRACES OF TORQUE VERSUS ROTATION .....	138
FIGURE 7-13: TORQUE AND COMPRESSION VERSUS SCREW ROTATION .....	140
FIGURE 7-14: PLATEAU VERSUS STRIPPING TORQUE.....	141
FIGURE 7-15: PLATEAU TORQUE VS MAXIMUM COMPRESSION .....	142
FIGURE 7-16: BOX PLOT INDICATING THE DIFFERENCE IN PLATEAU TORQUE IN THE THREE HOLE LOCATIONS .....	143
FIGURE 7-17: COMPARISON OF PREVIOUS AND CURRENT DATA FOR PLATEAU TORQUE VS STRIPPING TORQUE.....	148

FIGURE 8-1: SCHEMATIC OF REGION OF INTEREST SELECTED TO CREATE THE VOLUME OF INTEREST (VOI). THE OUTER DIAMETER OF THE VOI EXTENDED 2.0 MM OUTSIDE THE OUTER EDGE OF THE SCREW. ....	159
FIGURE 8-2: CROSS SECTIONAL TWO-DIMENSIONAL SLICES OF THE BONE AND SCREW.....	161
FIGURE 8-3: THE NODES REPRESENTING THE OUTER SURFACE OF BONE. SPRINGS WERE APPLIED TO THESE NODES TO SIMULATE AN ELASTIC BOUNDARY CONDITION.....	164
FIGURE 8-4 : COMPARISON OF THE HEAD CONTACT DETECTION METHODS IMPLEMENTED. ....	165
FIGURE 8-5: OUTPUT TRACES FROM SOFTWARE. ....	167
FIGURE 8-6: TORQUE VERSUS ROTATION.....	168
FIGURE 8-7: COMPRESSION VERSUS ROTATION. ....	168
FIGURE 8-8: 3D RENDERING OF THE SCREW IN THE FEMORAL HEAD.....	169
FIGURE 8-9: 2D TIME-ELAPSED IMAGES OF THE SCREW IN THE FEMORAL HEAD. ....	171
FIGURE 8-10: 3D TIME ELAPSED SLICES OF BONE DURING SCREW TIGHTENING. ....	172
FIGURE 8-11: TYPICAL DEFORMATION OBSERVED IN A TRABECULAR SPICULE SURROUNDING THE SCREW THREAD.....	173
FIGURE 8-12: STEP-WISE ACQUIRED MASKS FROM MICRO-CT DATA SETS ARE OVER LAID TO VISUALISE THE TRABECULAR DEFORMATIONS.....	174
FIGURE 8-13: CONTACT STATUS OF CONTACT ELEMENTS REPRESENTING THE SURFACE OF BONE IN CONTACT WITH THE SCREW.....	175
FIGURE 8-14: EXPERIMENTAL AND FE TORQUE VERSUS ROTATIONS CURVES. ....	177
FIGURE 8-15: EXPERIMENTAL AND FE COMPRESSION VERSUS ROTATIONS CURVES.....	177
FIGURE 8-16: VOLUMES OF YIELDED TISSUE OVER 20 DEGREES OF ROTATION FROM HEAD CONTACT. ....	178
FIGURE 8-17: TIME-ELAPSED VON MISES STRAIN FIELD OF THE PERI-IMPLANT BONE. ....	179
FIGURE 8-18: AXIAL DISPLACEMENT FIELD AFTER 20 DEGREES OF ROTATION. ....	180
FIGURE 8-19: BINARISED IMAGE OF THE BONE-SCREW INTERFACE.....	188

# LIST OF TABLES

TABLE 2-1: HIERARCHICAL STRUCTURE OF BONE .....	6
TABLE 2-2: MEAN (STANDARD DEVIATION) STRENGTH AND MODULUS VALUES FOR CANCELLOUS BONE SPECIMENS .....	20
TABLE 2-3: AVERAGE REPORTED TISSUE PROPERTIES ( $\pm$ STANDARD DEVIATION) OF CANCELLOUS BONE DETERMINED EXPERIMENTALLY OR BY FINITE ELEMENT ANALYSIS .....	22
TABLE 4-1: OUTPUT RESULTS OF PCG ITERATIVE SOLVER.....	63
TABLE 4-2: STRUCTURAL PARAMETERS FOR THE FULL- AND SUB-VOLUME MODELS ( $N=11$ ).....	66
TABLE 4-3: LINEAR REGRESSIONS ( $\Sigma_y = mE_{APP} + C$ ) OF THE YIELD STRENGTH OF CANCELLOUS TRABECULAR BONE UNDER UNIAXIAL COMPRESSION AGAINST YOUNG'S MODULUS ( $E$ ).....	72
TABLE 4-4: MEAN (SD) TISSUE ELASTIC MODULUS VALUES FOR HUMAN VERTEBRAL TRABECULAR TISSUE.....	73
TABLE 5-1: SPECIMEN PAIRS INDICATING VERTEBRAL LEVEL EACH SPECIMEN WAS TAKEN FROM AND BV/TV .....	83
TABLE 5-2: AVERAGE MORPHOLOGICAL PARAMETERS FOR SI AND AP GROUPS .....	86
TABLE 5-3: LINEAR REGRESSION RESULTS .....	88
TABLE 6-1: FEA RESULTS FOR THE THREE DIFFERENT MODELS TESTED.....	106
TABLE 6-2: LINEAR REGRESSION RELATIONSHIPS BETWEEN THE FE MODELS AND THE EXPERIMENTAL DATA FOR YIELD STRESS AND UFS .....	109
TABLE 6-3: AVERAGE (SD) MECHANICAL PROPERTIES OF HUMAN VERTEBRAL CANCELLOUS BONE SPECIMENS UNDER UNIAXIAL COMPRESSIVE LOADING. ....	114
TABLE 7-1: MATERIAL PROPERTIES MATERIALS INVESTIGATED.....	125
TABLE 7-2: SCANNING ACQUISITION PARAMETERS .....	127
TABLE 7-3: BIVARIATE CORRELATION OF MORPHOLOGICAL AND INSERTION VARIABLES .....	144
TABLE 8-1: AVERAGE REPORTED TISSUE PROPERTIES ( $\pm$ SD) OF CANCELLOUS BONE.....	163
TABLE 8-2: COMPARISON OF THE ALGORITHM PREDICTED AND ACTUAL TORQUE LEVELS FOR STEPWISE SCREW INSERTION. ....	166
TABLE 8-3: BONE AND SCREW VOLUMES FOR STEP-WISE ACQUIRED IMAGE DATA SETS .....	170

# LIST OF EQUATIONS

EQUATION 2-1 ..... 24  
EQUATION 2-2 ..... 24  
EQUATION 2-3 ..... 25  
EQUATION 2-4 ..... 25  
EQUATION 3-1 ..... 34  
EQUATION 3-2 ..... 36  
EQUATION 4-1 ..... 56  
EQUATION 5-1 ..... 96  
EQUATION 8-1 ..... 158

## ABBREVIATIONS

AP	antero-posterior
BV/TV	bone volume fraction
BS/TV	total surface
DA	degree of anisotropy
$E_{\text{Tiss}}$	bone tissue elastic modulus
$E_{\text{FEA}}$	finite element analysis determined elastic modulus
$E_{\text{Exp}}$	experimentally determined elastic modulus
$\varepsilon_y^c$	compressive yield strain
$\varepsilon_y^t$	tensile yield strain
micro-CT	micro-computed tomography
micro-FEA	micro-finite element analysis
SI	supero-inferior
SMI	structure model index
TbN	trabecular number
TbTh	trabecular thickness
TbPf	trabecular pattern factor
TbSp	trabecular separation
$T_{\text{plateau}}$	plateau torque
$T_{\text{Stripping}}$	stripping / maximum torque

## **ABSTRACT**

During screw insertion, surgeons manually tighten until they subjectively feel that adequate torque has been obtained. This “tightening torque” has been shown to equate to approximately 86% of maximum (stripping) torque. The level of torque to which orthopaedic screws are tightened, however, is highly subjective and can lead to over-tightening or even stripping in cases of poor bone quality. Whilst torque limiting devices exist that are able to terminate tightening at specified torque levels, these are of little value if the optimum torque is not known. Furthermore, the ideal level of tightening torque may vary according to anatomic location, bone quality and screw material and design. Bone quality is determined by the geometry of the bone and its underlying micro-architecture, as well as accumulated microscopic damage, the quality of collagen, mineral density and crystallinity, and bone turnover. Therefore to fully understand these interactions at the macroscopic level, and understanding of the bone-screw interactions at the micro-structural level is necessary. The aim of this dissertation was, therefore, to develop a novel technique to analyse the mechanical interactions between cancellous bone and a lag screw during tightening. The ultimate goal was to develop a micro-finite element model that incorporated the screw and its mechanical interactions with the micro-structure of cancellous bone.

The first part of this dissertation explored the application of micro-finite element modelling for analysing vertebral trabecular mechanics at the micro-structural level under a uniaxial load in either the supero-inferior (SI) or antero-posterior (AP) direction. Results demonstrated distinctly different micro-mechanical behaviour between the two loading directions, with a greater volume of tissue reaching yield at the onset of apparent-level yielding, in the SI direction compared to AP. The incorporation of both material and geometric nonlinearity yielded strong agreement between model predictions of apparent yield and experimentally determined values; however the influence of experimental protocol was emphasized if tissue modulus values were derived from experimental data. It was demonstrated that the tissue modulus largely governs the apparent stiffness, whilst tissue yield criterion regulated apparent yield behaviour.

The second part of this dissertation focussed on the main objective, which was to understand the interactions between bone and screw at the micro-structural level. A novel micro-test device was developed that allowed the step-wise insertion of a screw into bone specimens within a micro-computed tomographic (microCT) scanner. Results showed a strong linear relationship between plateau torque and stripping torque, with the screw under investigation. Furthermore, it was demonstrated that the deformation of the trabeculae during screw insertion is restricted to primarily the bone tissue within the screw threads, and that the critical deformation occurs during the load step between 80 % ( $T_{\text{stripping}} - T_{\text{HC}}$ ) and  $T_{\text{stripping}}$ .

## **DECLARATION**

I certify that this thesis does not incorporate without acknowledgement any material previously submitted for a degree or diploma in any university; and that to the best of my knowledge and belief it does not contain any material previously published or written by another person except where due reference is made in the text.

## **ACKNOWLEDGEMENTS**

Firstly I would like to thank my supervisors Professor Karen Reynolds, Dr John Costi & Dr Andrei Kotousov for taking me on as a PhD student. Karen you are an amazing and inspirational person; I have learnt so much from you not only with regard to engineering and orthopaedics, but about being able to juggle work and study with a family, thank you. Thankyou also to John; you provided an immense amount of insight and support for the entirety of this dissertation and without yourself and Karen this work would not have been possible. Thankyou both for your enduring guidance and support.

There is a vast number of others I would like to thank for their assistance and advice in many areas of my research. Richard Stanley assisted immensely in the design of the test apparatus' and protocols as well as pretty much any help I needed in the lab, be it testing, preparing specimens or finding a wayward screw, thank you! Mark Taylor provided an unbelievable amount of assistance in getting my final FE model working and what he has taught me with regard to understanding my models and debugging models is immeasurable! I would also like to thank the numerous friends that have had to share an office with me over the duration of this work, all of whom provided valuable insight and feedback on my thesis as well as life; thanks to Rohan Edmonds-Wilson, Diana Pham, Tae Hwan Joung, Tony Carlisle, Aaron Mohtar, Darius Chapman, Rosidah Lazid, Egon Perilli, Emily O'Brien, Bryant Roberts and Laura Diment. I would especially like to thank Rosidah for all her help with the mechanical testing and Aaron, who was always there to help with testing, writing programs or writing my thesis!

I would like to thank the Musculoskeletal Health ASRI for the scholarship that enabled me to undertake my doctorate, and to acknowledge that none of this work would have been possible without the funding provided by the National Health and Medical Research Grant ID 595933.

Finally I would like to thank my family, Luke, Audrey and Maeve. Deciding to start a family, as well as renovating and building houses, whilst undertaking a PhD has been a huge task and has certainly been a challenge at times. However, we have all learnt a lot of patience and time management skills over the duration. The birth of

my girls provided me the inspiration to continue when times were tough and I thought I would never get there. I would also not have been able to spend the necessary time on this work without the support of my sister Hayley and my parent's in-law, Alan and Jenny. There were many times they cared for our girls so that mummy could spend time writing, as well as the emotional support and continuing encouragement. For this I am forever grateful.

# 1 INTRODUCTION

Osteoporosis is a growing global problem affecting more than 200 million people worldwide [1] and 2.2 million Australians [2, 3]. According to the World Health Organisation (WHO) osteoporosis is defined as a bone mineral density (BMD) 2.5 standard deviations or more below the average value for young health women [4]. Osteoporotic bone is characterised by low bone density and deterioration of the cancellous micro-architecture. The clinical consequence of osteoporosis is fracture, which is associated with an 80% increase in risk of a second fracture [5]. It is estimated that during their lifetime, 1 in 2 Australian women and 1 in 3 men aged over 60 years will develop an osteoporotic fracture [3]. With an ageing population, it is therefore necessary to investigate not only preventative measures for osteoporosis, but also effective measures of osteo-fixation for effective repair of associated fractures.

Irrespective of anatomic location, surgical treatment of a bone fracture will almost always involve internal fixation via the use of screws, either alone or in conjunction with plates. Screws are used for the attachment of implants to bone, for bone to bone fixation, or for soft tissue fixation or anchorage. The reduction in strength, as well as the architectural deterioration associated with osteoporosis, however, clearly impacts the fixation and durability of orthopaedic implants in osteoporotic bone [6-8].

The most common osteoporotic fractures occur at the proximal femur, lumbar vertebra and distal radius, where cancellous bone is present. The treatment for such fractures is challenging, due to the bone quality and often secondary health related issues [6-8]. In the case of proximal femur fractures, for example, the indication may be for total hip arthroplasty however the optimal choice for stabilisation remains controversial. Arthroplasty options include hemiarthroplasty (HA), bipolar arthroplasty (BA) and total hip arthroplasty (THA). Proponents of arthroplasty argue that prosthetic replacement eliminates the need for revision surgery due to avascular necrosis and non-union, both of which are serious problems following internal fixation [9]. The advantages of internal fixation, however, are decreased operative time, blood loss and risk of mortality because the procedure is quicker and often simpler [10]. Therefore adequate methods of internal fixation, that reduce the need for revision surgery, would potentially make it a more favourable option over arthroplasty.

During screw insertion, surgeons manually tighten the screws until they subjectively feel that adequate tightening torque has been obtained. This “tightening torque” has been shown to equate to approximately 86% of maximum torque [11, 12]. The level of torque to which orthopaedic screws are tightened, however, is highly subjective and can lead to over-tightening or even stripping in cases of poor bone quality [11, 13]. In a recent study, the incidence of screw stripping was reported to be as high as 46 % [14]. Whilst torque limiting devices exist that are able to terminate tightening at specified torques, these are of little value if the optimum torque is not known. Furthermore, the ideal level of tightening torque may vary according to anatomic location, bone quality and screw material and design. Wirth *et al.* (2011) demonstrated a moderate relationship between micro-architecture and bone-construct stiffness, however the testing of the bone-screw construct was only performed virtually by finite element analysis with no experimental validation [15]. There is a need to better understand the micro-structural factors that may influence tightening torque and indicate when adequate tightening has been achieved. The purpose of this research, therefore, was to develop a method to allow evaluation of trabecular mechanics during screw insertion, based on experimental data.

The use of micro-finite element (micro-FE) modelling has evolved as a compelling tool for analysing bone biomechanics. A micro-FE model that could simulate the tightening of screws into bone would provide profound insight into the mechanisms that influence screw tightening. Wirth *et al.* (2012) highlighted the importance of incorporating the trabecular micro-architecture to accurately assess the strain distribution within the tissue and load transfer at the bone-implant interface over models that considered the trabecular network as a continuum [16]. Therefore the overall goal of this thesis was to develop a micro-FE model that could be used to assess tissue strain distribution and load transfer at the bone-implant interface during screw tightening.

Such a model that could analyse bone-implant interactions at the micro-structural level is highly complex. In order to establish material properties for the trabecular bone tissue, indirect linear modelling can be implemented. The initial focus of this dissertation, therefore concentrated on developing a micro-FE model in low-density bone. The purpose of this was to understand the methodology for generation of

micro-FE models from micro-computed tomography (micro-CT) data and to analyse the micro-mechanical behaviour of cancellous bone under a specific loading regime. The remainder of the dissertation evaluates the experimental and computer modelling involved in the development of the FE model. More specifically, this dissertation is outlined as follows:

Chapter 2 provides a background on the physiology of bone, osteoporosis and bone fractures, as well as identifying current issues associated with bone screws. Background knowledge of the FE method as well as a review of previous work pertaining to micro-FE modelling of cancellous bone, and more specifically micro-FE models of cancellous bone and implants is provided in chapter 3.

Chapter 4 outlines the methodology used for generating micro-FE models from micro-CT image data and evaluates the use of a sub-volume for analysis in low density bone.

Chapters 5 addresses the current assumption of isotropy applied to the tissue modulus used in micro-FE models of cancellous bone. Chapter 6 extends on this data set, by considering the incorporation of nonlinear material properties to the specimens analysed under on-axis loading in chapter 5.

The focus of Chapter 7 is the development of an algorithm to relate the peak torque during screw insertion to the plateau torque which occurs directly prior to head contact. This was accomplished by a series of insertion tests to failure in femoral head samples using a custom manufactured aluminium bone screw.

Chapter 8 implements the derived algorithm from chapter 7 to perform stepwise screw insertion with micro-computed tomographic imaging. This is a completely novel method, which allows visualisation of trabecular deformation and computational model derived mechanics during screw tightening. The image data along with the FE model are used to assess the trabecular bone mechanics during insertion.

## **2 BACKGROUND**

## 2.1 Structure and function of bone

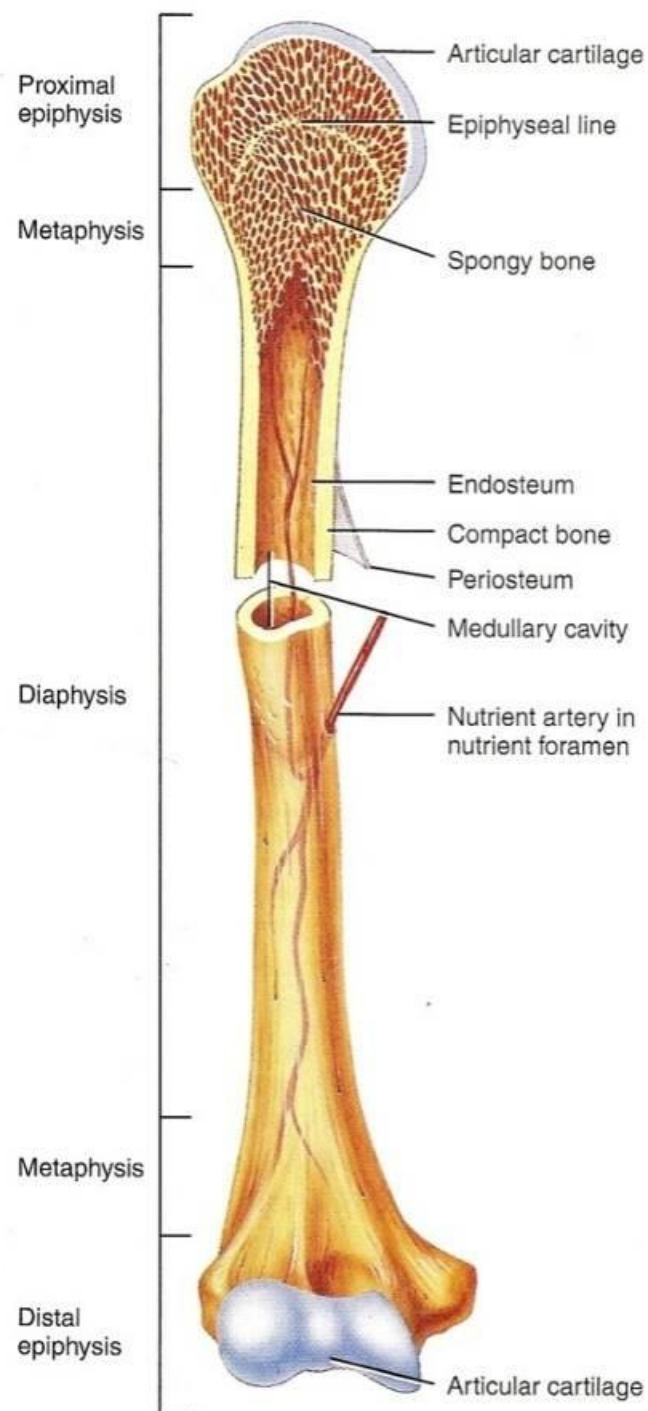
Bone or osseous tissue and the skeletal system have several basic functions including support, protection, assistance in movement, mineral homeostasis, blood cell production and fat storage. Bone is a fibre-reinforced, anisotropic, composite material that exhibits both inter- and intra-species variation, where both its composition and structure are dependent on anatomic location, physiological function, age, gender and species. Bone has a highly complex hierarchical structure (Table 2-1), which can be organised into the following levels: whole bone, macrostructural (cancellous or cortical), microstructural (osteons or trabeculae), sub-microstructural (lamellar arrangements of collagen fibrils), and nanostructural (collagen fibrils, non-collagenous proteins, apatite crystals and water). To correctly interpret measurements from the various biomechanical techniques, it is essential to understand the hierarchical structure of bone.

Table 2-1: Hierarchical structure of bone

<b>LEVEL</b>	<b>ELEMENTS</b>	<b>DIMENSIONS</b>
<b>Whole bone</b>	Femur, humerus, vertebra	cm
<b>Macrostructural</b>	Cortical or cancellous bone	1 – 5 mm
<b>Microstructural (Tissue)</b>	Osteons or trabeculae	20 – 500 $\mu\text{m}$
<b>Sub-microstructural (Lamellar)</b>	Lamellae, large collagen fibers	1 – 20 $\mu\text{m}$
<b>Nanostructural level</b>	Collagen fibrils & mineral components	2 nm – 0.5 $\mu\text{m}$

### 2.1.1 Whole bone level

Whole bone or bone as an organ comprises bone tissue, along with non-osseous cells, blood vessels, nerve fibres and bone marrow. The size and shape of bones varies according to anatomic location, however they are usually classified as either long bones (long tubular segments) e.g. the femur, short bones (short irregular structures) e.g. vertebra, or flat bones such as the pelvis and skull. Long bones are present in the appendicular skeleton, whereas flat bones are typically found in the skull, scapula, and pelvis and the short bones in the axial skeleton. In long bones, three different regions can be distinguished: the diaphysis, (central canal) which represents the longest part; the epiphysis, present at the two extremities; and the metaphysis, which lies between these two regions (Figure 2-1). A thin layer of articular cartilage covers the epiphyses where the bone forms an articulation with another bone. Exterior regions of the bone not covered by articular cartilage are enveloped in a tough sheath of dense irregular connective tissue called the periosteum. The interior surface of the diaphysis is lined with the endosteum, which contains osteoprogenitor cells, that can differentiate into osteoblasts and bone-lining cells.



**Figure 2-1: Partially sectioned humerus, an example of a long bone.. Hard compact bone forms a shell along the diaphysis and surrounds the metaphyses and epiphyses. The metaphyses and epiphyses comprise predominantly spongy bone. The outer surface is covered in a thin sheath known as the periosteum, with the inner surface lined by the endosteum [17]. (Reproduced with permission)**

### 2.1.2 Macrostructural level (cancellous vs cortical)

At the macrostructural level, two anatomically distinguishable types of bone exist: cortical (compact) and cancellous (spongy) bone (Figure 2-2). Cortical bone makes up the bulk of the skeleton (around 80% of total bone mass) with the remaining 20% comprising cancellous bone [18]; the distribution of each however varies greatly between individual bones. The ulna, for example, comprises 92% cortical and 8% cancellous bone, whereas a typical vertebra consists of 62% cortical and 38% cancellous bone [19].

Cortical bone appears as a solid continuous mass and makes up the hard outer compacta of all skeletal segments. Cancellous bone consists of a three dimensional lattice, with the interspaces occupied by marrow. The two types of tissue are classified on the basis of porosity and microstructure. Trabecular bone is highly porous, with a porosity ranging from 30% to more than 90% and an apparent density ranging from 0.1 to 0.9g/cm<sup>3</sup>; cortical bone is significantly denser with an apparent density of approximately 1.8g/cm<sup>3</sup> and a porosity ranging between 5 and 30% [20, 21].

Cortical bone makes up the external layer of all bones and the bulk of the diaphysis of long bones in the human body. Cortical bone tissue is arranged in units called *osteons* or *Haversian systems*, which run parallel to the axis of the bone. Cancellous bone is found in the epiphyseal and metaphyseal regions of long bones, as well as in the medulla of flat and short bones such as the vertebra. Unlike cortical bone, cancellous bone does not contain true osteons, but instead consists of trabecular packets comprising lamellae, which are arranged in an irregular lattice of rods and plates called trabeculae [17, 20-22]. The spaces between the trabeculae are filled with red marrow, through which the osteocytes receive nutrients from blood vessels passing through [23].

Because osteoporotic changes are generally initiated from cancellous bone, and fractures associated with osteoporosis most frequently occur in cancellous-rich regions, more attention is paid to investigating changes in cancellous bone rather than cortical bone. Consequently cancellous bone remains the focus of this dissertation.

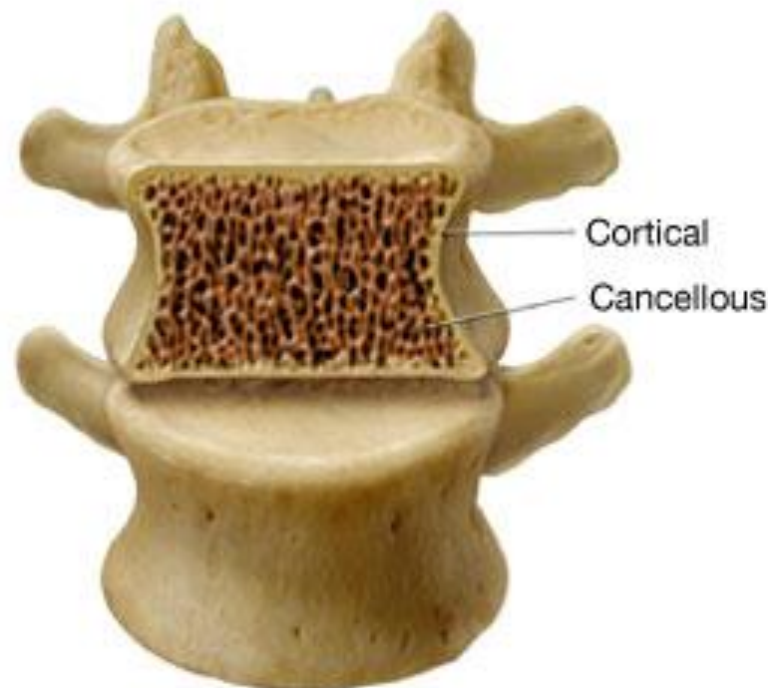


**Figure 2-2: Cortical and cancellous bone structures of the human vertebra.. Cortical bone makes up the dense outer shell which encloses the cancellous bone lattice network [24]. (Reproduced with permission)**

### 2.1.3 Microstructural level (osteonal vs trabecular bone)

Osteons are more or less cylindrical structures, with a diameter of 200-300  $\mu\text{m}$  and variable length of between 3 and 6 mm, both of which depend on species and age [20, 22]. The cylindrical structure comprises a central *Haversian* canal which runs longitudinally, surrounded by concentric rings of hard calcified matrix called *lamellae* (Figure 2-3). Osteons are renewed continuously due to the process of remodelling and as a result osteons of different degrees of calcification are always present; all of which contributes to the observed heterogeneity of mechanical properties in cortical bone.

Trabeculae are usually described as rod- or plate-like structures (Figure 2-4). The thickness of trabeculae ranges from 100 to 300  $\mu\text{m}$ , with the inter-trabecular spacings ranging from 0.3 to 1.5mm [25]. Whilst the microarchitecture of trabeculae appears random, their orientation is such that there is a “grain” direction, along which the mechanical stiffness and strength are greatest (Wolff’s Law) [26]; this grain corresponds to the direction of the most commonly applied loads. The micro-

architectural directionality results in both geometric and mechanical anisotropy at the microstructural level. Similar to osteons, microradiography shows different levels of calcification in trabeculae.

Both osteons and trabeculae are built up of unit layers of lamellae around 3-7  $\mu\text{m}$  thick [19], with the arrangement being described as similar to plywood. The lamellae are stacked at different orientations to form laminated structures. While in cortical bone the lamellae are arranged in concentric rings surrounding the longitudinal Haversian canal (Figure 2-3), the lamellae in cancellous bone tissue are preferentially aligned with the long axis of the trabeculae. Cement lines can be seen in the spicules separating groups of lamellae originating from different periods of bone generation and remodelling [22]. The groups of lamellae are called trabecular packets.

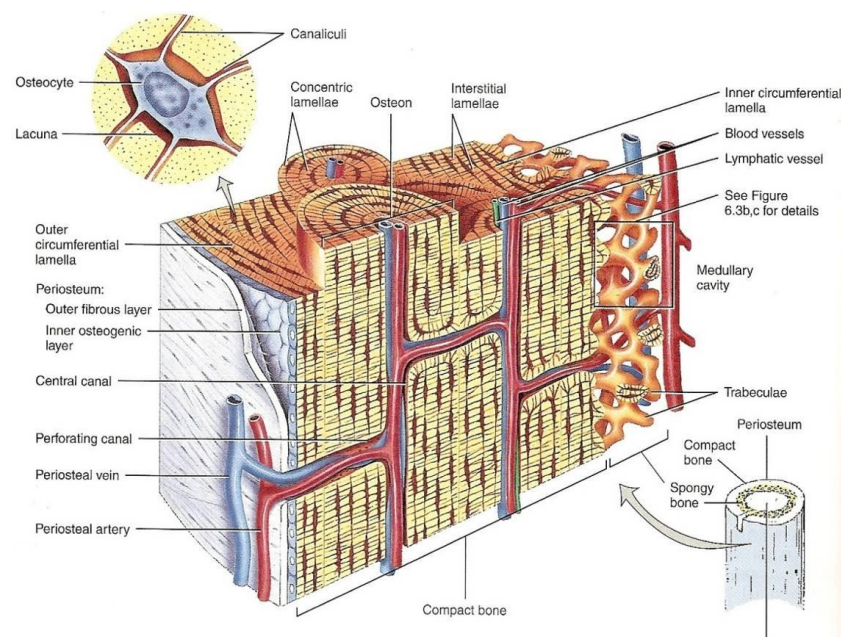


**Figure 2-3: Microstructure of cortical bone. Osteons are seen as concentric rings of lamellae. Blood and lymphatic vessels penetrate through the central canal of the osteons [17]. (Reproduced with permission)**

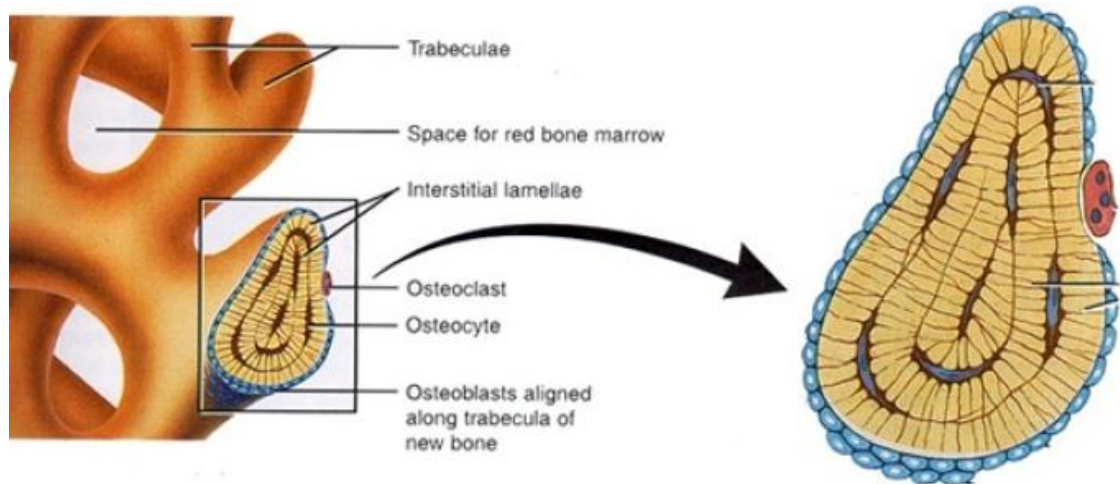


**Figure 2-4: Microstructure of cancellous bone. Lamellae are arranged along the long axis of individual trabecular spicules. The spaces in cancellous bone are filled with red bone marrow, which provides the blood supply via canaliculi [17]. (Reproduced with permission)**

#### 2.1.4 Sub-Microstructural level (lamellar)

At the sub-microstructural level, crystal reinforced collagen fibrils are arranged in a roughly parallel manner to form lamellae. Interspersed throughout the lamellae are small cavities (lacunae) which contain osteocytes (cells that maintain bone). The lacunae are connected with each other by a number of tiny channels called *canaliculi*. The canaliculi are filled with extracellular fluid and provide a vast network for nutrients and oxygen to diffuse through to the osteocytes and for wastes to diffuse back to the blood vessels [17].

At this level cancellous bone is not dissimilar to cortical bone in that it is an anisotropic composite composed of an organic phase and an inorganic phase. The organic phase makes up around 30% of the total bone mass, and consists primarily of type I collagen (90%), along with non-collagenous proteins, proteoglycans and phospholipids [19]. The collagen fibres have a relatively low modulus and contribute to the ductility and toughness of bone [27]. The fibres also act as an attachment and growth site for the mineral phase as well as providing ductile reinforcement [28, 29].

The mineral (inorganic) phase is made up of a calcium phosphate hydroxyapatite  $\text{Ca}_{10}(\text{PO}_4)_6(\text{OH})_2$  [21]. The mineral phase provides bone with strength and stiffness and comprises approximately 65% of the total mass of bone. The remaining 5% of total weight of bone is made up of water, located within collagen fibres, in the pores,

and bound in the mineral phase. Water plays an important role in determining the mechanical properties of bone; it has been shown that dehydrated bone samples have increased strength and stiffness, but reduced ductility and toughness [30].

### 2.1.5 Nanoscale level

At the nanoscale, the two main components of bone are the collagen fibrils (Figure 2-5(a)) and apatite crystals (Figure 2-5(b)). The collagen fibrils are about 100-200 nm in diameter, of a circular or ellipsoidal cross section and made of triple helix molecules about 1nm in diameter [31]. The exact shape and structure of the hydroxyapatite crystals is not fully known, but they are often described as tablet-, rod-, and needle-like crystals [32] with length and width in the order of a few hundred angstroms and 20 to 30 angstroms thick [22].

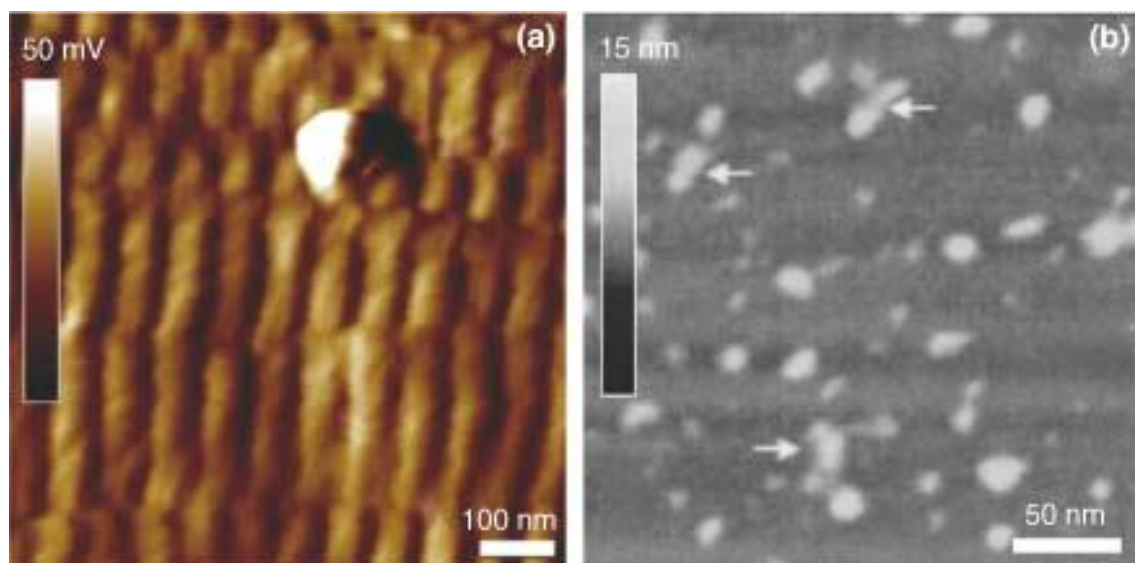


**Figure 2-5: Atomic force microscopy image of (a) collagen type I fibrils, and (b) hydroxyapatite mineral crystals extracted from bone [33]. (Reproduced with permission).**

## 2.2 Bone remodelling

Bone is a very dynamic and active tissue. Bone remodelling occurs on the periosteal, endosteal, Haversian canal and trabecular surfaces, and ensures bone is biomechanically and metabolically competent. The replacement of bone occurs by resorption, followed by formation of new lamellar bone. The signals for selection of sites to be resorbed are not completely understood. Osteoclasts (bone-resorbing cells) solubilise both the mineral and organic component of the matrix. Osteoblasts then synthesize and secrete collagen fibers and other organic components to build the unmineralised bone matrix or osteoid. Following the formation of osteoid, mineralisation occurs in two phases: primary mineralisation occurs as bone mineral is deposited during the remodelling cycle via enzymatic activity initiated by osteoblast secretions. During primary mineralisation, about half of the bone mineral accumulates within a few days. Secondary mineralisation proceeds more slowly during 6 months or more and further increases the bone mineral density [34].

In an average healthy adult, around 5-10% of the existing bone mass is replaced annually [35, 36]. The rate of turnover is much higher in cancellous bone compared to cortical bone; assuming normal rates of bone turnover, cortical bone has a mean age of 20 years and cancellous bone 1 to 4 years [37]. Under normal conditions, the remodelling process of resorption followed by formation is closely coupled and results in no or minimal net change in bone mass. It is believed that oestrogen levels inhibit bone resorption by decreasing osteoclastic activity [38]; in women, the onset of menopause causes a sudden decrease in oestrogen levels, which results in a significant reduction in bone mineral density after the age of 50.

## 2.3 Mechanotransduction in bone

The location for bone remodelling to occur is determined according to Wolff's law. Living bone adapts its mass and structure according to its mechanical requirements, to obtain a higher efficiency of load bearing. The role of the bone cells is to make and break-down the matrix in relation to the mechanical demands.

As bone is loaded, it produces a mechanical strain in the bone matrix. Pollack *et al* (1984) showed that strain-generated potentials are caused by strain-induced flow of interstitial fluid within the microporosity of bone [39]. Based on this theory and the cellular structure of bone, the osteocyte network and its accompanying lacuna-canalicular channels have been proposed as the mechanosensory system in bone [40, 41]. It is the role of the osteocyte to then translate the strain signal into a cellular signal to ensure either the formation or resorption of bone. This is achieved by the production of anabolic factors such as prostaglandins by the osteocyte [42]. It is assumed that these molecules are transported to the surface of bone via the lacuna-canalicular channels and at the surface of the bone they recruit new osteoblasts to lay down new bone matrix. The initiation of osteoclastic activation is not as clear; it has been suggested that underuse of bone or a reduction in bone loading reduces the nutrient supply and waste removal of the osteocytes. This in turn reduces osteocyte viability and may even lead to death. Osteocyte death may then be signal for osteoclastic recruitment [42]. It is also possible that osteocyte activity inhibits osteoclastic recruitment and that understimulation of osteocytes, by under-loading of bone, may lead to an absence of osteoclast-inhibiting signals [42].

## 2.4 Morphologic and mechanical properties of cancellous bone

The ability of bone to adapt to external conditions contributes to its heterogeneous and anisotropic nature. Whilst bone remodelling is a normal part of maintenance and repair, bone also undergoes constant, adaptational changes in response to local alterations in strain distributions. It is of common belief that trabecular bone architecture adapts so that its principal material axis is oriented along the most common loading direction [26]. The consequence of this is a structure which is both morphologically and mechanically anisotropic.

### 2.4.1 Morphologic parameters

The microstructure of cancellous bone is highly heterogeneous both within a single specimen and between species and anatomic locations. MicroCT was first validated as a method for the three-dimensional assessment and analysis of cancellous bone in 1998 by Müller *et al* [43] by comparing the morphometric results of conventional two-dimensional (2D) histomorphometry to microCT results. Their results showed excellent correlations between the 2D histology and the three-dimensional (3D) indices assessed. Since then, a standard set of 3D architectural descriptors has been developed to describe the structural arrangement of bone at the microstructural level. Listed below are the variables that are referred to in this dissertation, however a more extensive list and description of these can be found at [44]:

Bone volume fraction (BV/TV) represents the fraction of the volume of interest that is occupied by bone, where BV represents the bone volume and TV represents the total volume. TV is defined as the union of trabecular bone volume and marrow space volume.

Total surface (BS/TV) represents the bone surface area relative to the tissue volume of interest (VOI).

Trabecular thickness (Tb.Th) represents the mean thickness of trabecular elements; it is calculated using either model-dependent or model-independent measures of thickness.

Trabecular separation (Tb.Sp) is a measure of the separation between the edges of trabecular elements.

Trabecular number (Tb.N) is a linear density measure representing the number of intersections made across a trabecular structure for a linear path through the trabecular structure.

Trabecular pattern factor (Tb.Pf) quantitatively describes the ratio of trabecular connectivity by calculating an index of relative surface convexity or concavity. Low values for Tb.Pf indicates a well-connected structure whereas isolated trabeculae results in higher values [45].

Structure model index (SMI) quantifies the prevalence of plate-like and rod-like elements within a trabecular structure. In the case of an ideal plate and ideal cylinder, the SMI has values of 0 and 3 respectively [46]. Therefore a more plate-like structure exhibits SMI values closer to 0 and a more rod-like structure will exhibit SMI values closer to 3.

Whilst bone quantity (i.e. BV/TV) has been shown to be the strongest predictor of bone strength [47], substantial variability remains. Numerous studies have shown the contributions of other structural parameters to apparent strength; Ciarelli *et al* (2000), for example, found that bone from non-fracture subjects contained higher measures of BV/TV, TbN and connectivity compared to fracture cases [48].

#### **2.4.2 Mechanical properties**

At each of the structural levels discussed in section 2.1.3, bone exhibits different mechanical behaviour; therefore when reporting values such as modulus and strength, it is important to clarify the structural level under consideration.

Reported mechanical properties of cancellous bone generally refer to the macrostructural or what is commonly termed the *apparent* or *continuum* properties, with respect to a macroscopic sample. At this level, apparent properties refer to how the corresponding structure behaves as a whole. At the trabecular scale, we refer to the tissue properties that describe the bone matrix.

### 2.4.3 Apparent level properties

The apparent properties of bone are determined by the distribution of tissue properties and the structural morphology of the trabeculae. The basic requirement for the continuum assumption is that the minimum dimension of the sample must be significantly larger than the dimensions of its structural subunits. With regard to cancellous bone Harrigan *et al* (1988) reported that this criterion was satisfied when the apparent dimensions exceeded at least five times the average inter-trabecular spacing [49]. The apparent properties of cancellous bone are commonly measured by compression or tensile tests; a specimen is fixed at two ends and incrementally stretched or compressed, often to failure, while the load and resultant displacement are recorded. Normalising the force data by the cross-sectional area of the test specimen and the displacement by the original length gives a stress-strain plot. Figure 2-6 shows a typical stress-strain curve for both cancellous and cortical bone loaded in compression; from this it can be seen that cortical bone is both stiffer and stronger than cancellous bone. The average values of elastic modulus are several hundred MPa for cancellous bone, compared with 5 to 21 GPa for cortical bone [50].

Cancellous bone is both stronger and stiffer in compression compared to tension [51, 52]. Across anatomic sites and species, mean values of modulus and strength can vary by more than an order of magnitude (Table 2-2), with mechanical properties decreasing with age. Refer to An *et al* (2000) for a more detailed review of apparent mechanical properties of cancellous bone [50].

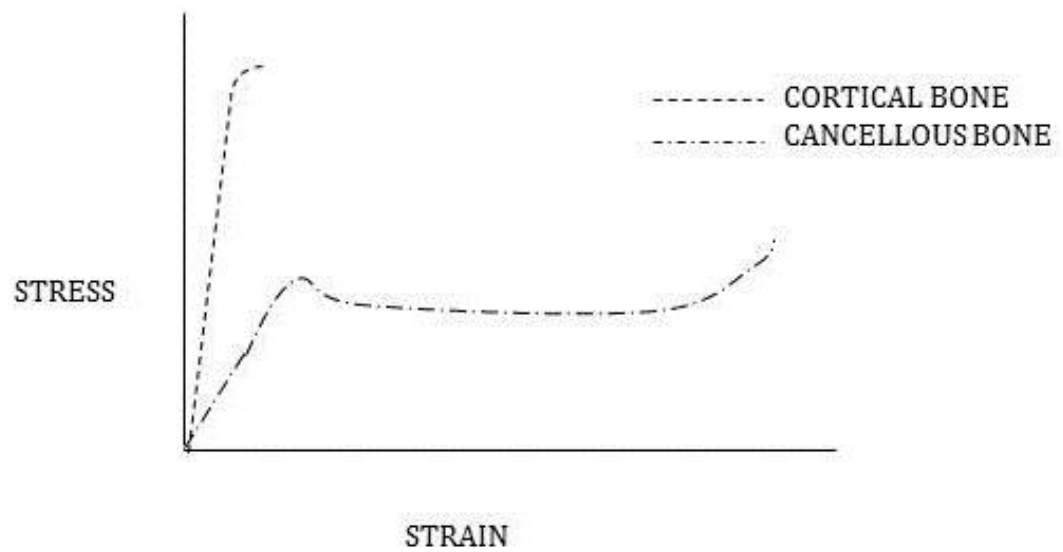


**Figure 2-6: Typical load-deformation curves for cancellous and cortical bone loaded in compression. The cancellous curve exhibits an initial elastic region followed by yield and then a non-recoverable plastic region. Yielding occurs as the trabeculae begin to fracture, and is followed by a long plateau region, created as progressively more and more trabeculae fail. The cortical curve exhibits a much stiffer elastic region, followed by a shorter plastic region due to the increased brittleness of cortical bone.**

Table 2-2: Mean (standard deviation) strength and modulus values for cancellous bone specimens

Species / Anatomical Site	Ultimate Strength (MPa)	Elastic Modulus (MPa)	Reference
Human			
Femoral neck	-	358.3 (338.1)	Matsuura 2008 [53]
Distal radius	-	304.6 (240.3)	Matsuura 2008 [53]
Vertebral body	-	165 (110)	Keaveny 1997 [54]
Bovine			
Proximal tibia	-	648 (430)	Rho 1997 [55]
Distal femur	8.5 (4.2)	117 (61)	Poumarat 1993 [56]
Canine			
Proximal tibia	2-24	106-426	Kang 1998 [57]
Distal femur	13-28	210-394	Kang 1998 [57]

#### 2.4.4 Tissue properties

At the tissue level, the mechanical properties are dependent on the material properties of bone itself. Biomechanically, bone tissue is regarded as biphasic, where the apatite is considered as one phase and the collagen and ground material substances as the other [23]. The consequence of this is that while bone tissue is essentially brittle, it also has a significant degree of elasticity, contributed by the collagen. The degree of mineralisation throughout trabecular tissue varies spatially, decreasing near trabecular surfaces [58]. The higher the mineral content, the stiffer the bone, therefore the elastic modulus of trabecular bone tissue varies across the width of a spicule [59]. Additionally, primary mineralisation is followed by secondary mineralisation, which occurs more slowly [34]; therefore older bone is stiffer than newly formed bone. This ultimately results in a material that is highly heterogeneous and anisotropic at the tissue level.

Originally cancellous bone tissue was believed to possess similar properties to cortical bone at the tissue level [60]; however the current consensus is that the elastic modulus of trabecular bone tissue is about 10 to 30% less than that of cortical bone [61, 62]. Determining the material properties of trabecular tissue is more complex due to the size of the test specimen. Some commonly used techniques for determining cancellous tissue properties include: (1) uniaxial micro-tensile testing of individual trabeculae [63, 64]; (2) ultrasonic measurements [63, 65]; (3) three- or four-point bending [62, 66, 67]; (4) nanoindentation [55, 65, 68-70]; and (5) back-calculation using 3D finite element models [71-78]. The values reported by these techniques are summarised in Table 2-3 and range from 0.8 to 18.7GPa; for a more detailed review of these and other techniques refer Guo *et al* (2009) [79].

Table 2-3: Average reported tissue properties ( $\pm$  standard deviation) of cancellous bone determined experimentally or by finite element analysis

Source	Species, site	Method	$E_{\text{Tissue}}$ (GPa)
Ryan <i>et al</i> (1989) [64]	Bovine distal femur	Microtensile	0.8 (0.4)
Choi <i>et al</i> (1990) [62]	Human proximal tibia	3-point bending	4.9 (1.8)
Rho <i>et al</i> (1993) [63]	Human tibia	Microtensile (dry)	10.4 (3.5)
		Ultrasonic	14.8 (1.4)
Reimer <i>et al</i> (1995) [80]	Human vertebra	Four-point bending	2.11 (1.89)
Rho <i>et al</i> (1997) [55]	Human vertebra	Nanoindentation	13.4 (2.0)
Ulrich <i>et al</i> (1997) [76]	Human femoral head	FEA	3.5 – 8.6*
Hou <i>et al</i> (1998) [72]	Human vertebra	FEA	5.7 (1.6)
Ladd <i>et al</i> (1998) [74]	Human vertebra	FEA	6.6 (1.0)
Turner <i>et al</i> (1999) [65]	Human femur	Acoustic microscopy	17.50 (1.12)
		Nanoindentation (dry)	18.14 (1.7)
Zysset <i>et al</i> (1999) [70]	Human femoral neck	Nanoindentation	11.4 (5.6)
Kabel <i>et al</i> (1999) [73]	Physeter Catodon vertebra	FEA	5.6 (0.2)
Niebur <i>et al</i> (2000) [75]	Bovine proximal tibia	FEA	18.7 (3.4)
Bayraktar <i>et al</i> (2004) [81]	Human femoral neck	FEA	18.0 (2.8)
Norman <i>et al</i> (2007) [82]	Human proximal femur	Nanoindentation	14.22 (1.07) <sup>a</sup>
Harrison <i>et al</i> (2008) [69]	Ovine vertebra	Nanoindentation	12.25 (1.01) <sup>b</sup>

Brennan <i>et al</i> (2009) [68]	Ovine proximal femur	Nanoindentation	8.3 (3.7)
Turner <i>et al</i> (2009) [33]	Various	Atomic force microscopy	15.9 – 24.8 <sup>c</sup>
Verhulp <i>et al</i> (2008) [83]	Bovine proximal tibia	FEA	6.5 (1.1)
Busse <i>et al</i> (2009) [66]	Human vertebra (normal)	3-point bending	2.16 (0.53)
	Human vertebra (osteoporotic)		1.20 (0.55)

<sup>a</sup> Inner medial region of trabecular spicule

<sup>b</sup> Outer region of trabecular spicule

<sup>c</sup> Only range given

#### 2.4.4.1 Uniaxial Tensile Testing

Significant technical difficulties are associated with tensile testing of small specimens. Alignment is critical to ensure a uniaxial state, but is almost impossible to achieve with irregular specimen geometry and such small specimen size. Additionally, the irregular geometry makes it difficult to determine accurate dimensions. Standard tensile test specimens are normally machined or cut along the middle segment of their free length so that stress and strain measurements can be made well away from the fixed ends, where edge effects and stress concentrations due to the grips are minimal [84]. The modulus for a standard specimen tested in tension can be determined by Equation 2-1, where  $E$  = Young's modulus,  $P$  = applied load,  $\delta$  = elongation of the reference length  $L$ , and  $A$  = specimen cross-sectional area. Based on this, it is obvious that specimen geometry will have a large impact on the measured elastic modulus and any inter-study comparisons would need to account for geometry variations. Using this method, Ryan & Williams [64] reported a modulus of 0.8GPa for wet bovine distal femoral bone, whereas Rho *et al* (1993) reported a modulus of 10.4 GPa, for dry human tibial trabecular tissue; highlighting the effects of hydration in bone strength [63].

$$E = \frac{P L}{\delta A}$$

Equation 2-1

#### 2.4.4.2 Ultrasonic measurements

The ultrasonic technique can be applied either to a continuum level cancellous specimen or to a micro-specimen to measure modulus. The rate at which sound travels through solid matter is dependent upon its elastic properties and density, based on Equation 2-2; where  $v$  = velocity,  $E$  = Young's modulus and  $\rho$  = density. Therefore if the density and sound velocities are known, Young's modulus can be extrapolated. A limitation of this technique is that the modulus value is an average measure over the entire specimen, neglecting the heterogeneous nature of cancellous tissue. Using this technique, Turner reported no difference between the elastic properties of cancellous and cortical bone, finding a tissue modulus of  $17.6 \pm 1.12$  GPa for human femoral cancellous bone and  $17.3 \pm 0.22$  for cortical bone [65].

$$E = \rho v^2$$

Equation 2-2

#### 2.4.4.3 Bending Tests

Bending tests are frequently used to determine the tissue modulus of cancellous bone tissue. The advantages of this method are that it is easy to implement and insensitive to specimen alignment, and bending is an important physiological deformation mode of trabecula. However studies that used this method have reported relatively low values for both cancellous and cortical tissue [62, 66]. Using varying size of specimens, Choi *et al* (1990) showed there is a significant size dependency of modulus measured by microbending tests [62].

#### 2.4.4.4 Nanoindentation

Nanoindentation can also be used to test the intrinsic mechanical properties of bone tissue and can achieve resolutions of between 1nm to 20  $\mu\text{m}$  [85]. Indentation tests are performed by driving a pyramidal diamond indenter into the specimen surface and dynamically collecting the applied force and displacement data; material properties are then derived from this data according to Equation 2-3, where  $S$  is the contact stiffness,  $E$  and  $\nu$  are the Young's modulus and Poisson's ratio, respectively, for the bone ( $b$ ) and indenter ( $i$ ), and  $A$  = contact area [86]. The high resolution of

this technique means it is possible to profile the modulus across the width of a trabecular strut. Using this technique, trabecular tissue modulus has been shown to increase from the periphery inwards [68, 87], which is consistent with the known process of bone formation which occurs on the surface.

$$S = 2\pi^{-1/2} \left[ \left( \frac{1 - \nu_b^2}{E_b} \right) + \left( \frac{1 - \nu_i^2}{E_i} \right) \right]^{-1} A^{1/2}$$

Equation 2-3

#### 2.4.4.5 Back-calculation using finite element models

The back-calculation procedure was first proposed by van Rietbergen (1995) [77]; the procedure involves generating an FE model from micro-CT data and applying an assumed initial modulus for the tissue,  $E_0$  (i.e. 5GPa). The bone is then mechanically tested to provide the stress-strain curve from which the apparent modulus,  $E_{Exp}$  can be determined. The FE model is then used to simulate the same test conditions and produce an estimate for the apparent modulus,  $E_{FE}$ . Based on the linear elastic assumption, the true elastic tissue modulus  $E_{Tis}$  can then be determined by:

$$E_{Tis} = \frac{E_{Exp}}{E_{FE}} E_0$$

Equation 2-4

The disadvantage of this technique is that similar to ultrasonic methods, it provides only an average tissue modulus, plus it requires an excised specimen so that the mechanical testing can be performed.

## 2.5 Density

The term “density” can be interpreted with various meanings. We can refer to density as a structural parameter which is a macroscopic measure, or we can consider the density with reference to the material properties, a more microscopic measure. At the macrostructural level, we use the term *apparent bone mineral density*; this is a measure of the amount of bone tissue within a given volume (which will contain soft tissue as well as bone tissue) and is measured in  $\text{g/cm}^3$ . At the material level, we are

referring to the degree of mineralisation of bone tissue. This is referred to as the *bone material mineral density* and is also measured in  $\text{g}/\text{cm}^3$ .

## 2.6 Osteoporosis

Osteoporosis is a growing global problem which affects over 2 million Australians [2] and more than 200 million people worldwide [1]. Osteoporosis is a skeletal disease caused by abnormal bone metabolism and characterised by a decrease in bone strength, leading to bone fragility and consequently greater risk of fracture. The etiology of osteoporosis is multifactorial and includes failure to achieve peak bone mass during growth and development, excessive thinness, calcium and vitamin D deficiency, alcohol abuse, corticosteroid use, smoking and other nutrition and lifestyle issues [88].

Osteoporosis is classified into two major groups: primary osteoporosis, which includes postmenopausal osteoporosis in women, age related or “senile” osteoporosis [89], and idiopathic osteoporosis in juveniles and young adults. Secondary osteoporosis is secondary to heritable or acquired abnormalities [90]. The most common cause of osteoporosis, however, is a result of decreased oestrogen with menopause, which is associated with increased osteoclast numbers and increased bone resorption [40]. The incidence of osteoporosis is much higher in women than in men; of those affected around 80% are women [19]. In Australia, total costs relating to osteoporosis are \$7.4 billion per year [91].

The World Health Organisation classifications use the term *osteoporosis* to define a bone mass value, as measured by dual energy X-ray absorptiometry (DEXA), greater than 2.5 standard deviations below the young adult mean. There is an imbalance in the remodelling process, which causes a resultant net loss in bone mass. Since bone turnover is significantly higher in cancellous bone (around 3% of cortical and 25% of cancellous bone is replaced annually) [92], skeletal regions containing predominantly cancellous bone tend to be more affected than regions of cortical bone. Bone material is lost from the struts and thin plates that make up trabecular bone (Figure 2-7), with bone mass becoming so depleted that bones fracture, commonly as a result of a fall, but also spontaneously.

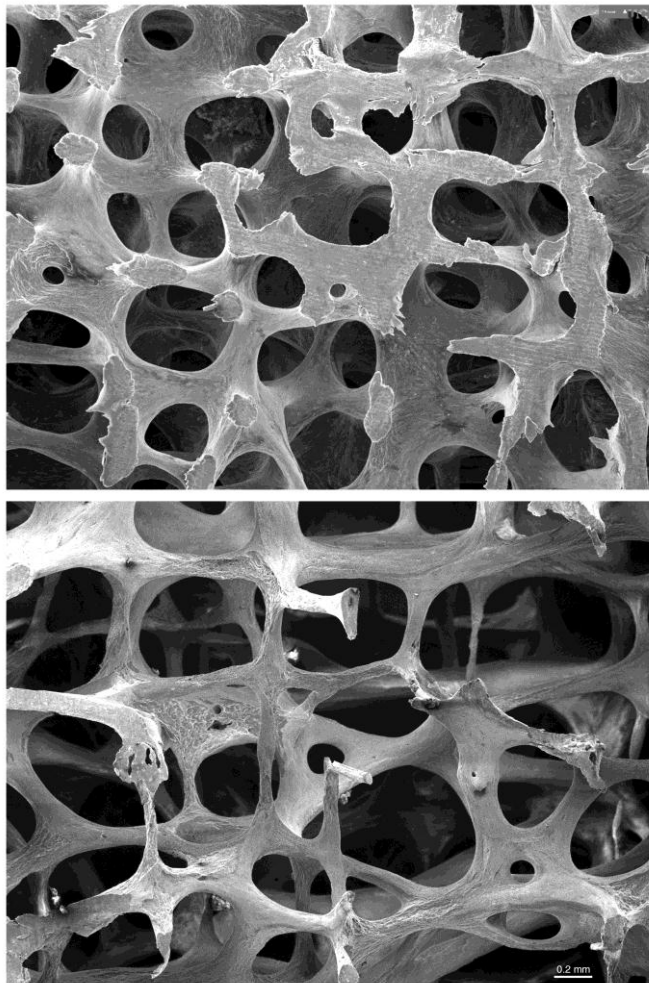


**Figure 2-7: Comparison of normal (top) and osteoporotic (bottom) bone architecture in the third lumbar vertebrae.. Marrow and other cells have been removed. Extensive pitting caused by osteoclasts in the osteoporotic bone is evident [93]. (Reproduced with permission).**

Previously, the reduced strength of osteoporotic bone was attributed to a reduction in bone quantity and changes in micro-architecture. However the mechanical strength of any material is dependent not only on structural properties but also on the properties of its constituent material. Recent literature suggests osteoporosis may affect not only structural parameters, but also tissue composition. Several authors have reported an increase in mineral content in osteoporotic cases compared to healthy tissue [66, 68, 94, 95]; however the geometry and size of the hydroxyapatite crystals do not appear to be altered in osteoporotic bone [41]. Zioupos *et al* (2008) found a negative relationship between trabecular and apparent density in osteoporotic bone, suggesting that as the cancellous bone becomes more porous there is a compensatory mechanism to increase the density of the tissue that is left [95].

Similarly, McNamara *et al* (2006) found significant increases in mineral content, yield strength and stiffness of ovariectomised rats compared to controls [94]. It is logical to assume that an increase in mineral content would be consistent with an increase in tissue modulus; but two recent studies reported the opposite. Brennan *et al* (2009) analysed the properties across trabeculae from proximal femoral ovine bone, comparing ovariectomised and control cases; they found no significant difference in hardness, but the elastic modulus was significantly lower in the ovariectomised cases compared to the controls [68]. Busse *et al* (2009) also reported a lower modulus and yield strength in osteoporotic cases compared to controls, testing human vertebral trabecular tissue in 3-point bending; this was despite the osteoporotic specimens having a significantly higher tissue density [66].

The reason for these discrepancies most likely lies in the heterogeneous nature of trabecular tissue. The observed increase in mineral density in osteoporotic tissue appears to be accompanied by a more heterogeneous mineral distribution and atypical lamellae structure [66, 68, 96].

The increase in cement lines and older more mineralised bone would cause an increase in measured mineral density and hardness, but may also provide the underlying reason for the reduction in stiffness and strength. Busse *et al* (2009) proposed the idea that more brittle bone supports the formation of micro-cracks in aged, hyper-mineralised areas, which can affect Young's modulus, fracture load and yield strength [66]. In summary there is a consensus that osteoporotic bone tends to be hyper-mineralised, but the mechanical effects of this are not fully understood.

## 2.7 Bone Fractures

Bone fractures can be classified by causation as either traumatic or pathologic. Pathologic fractures occur due to an underlying process that weakens the mechanical integrity of the bone. The causes of pathologic fractures include neoplastic (tumour related) and non-neoplastic conditions. The most non-neoplastic cause of pathologic fracture is osteoporosis [97].

Treatment of bone fractures can be classified as either conservative or surgical, the former referring to any non-surgical procedure such as immobilisation and pain management. Surgical treatment allows shorter hospital stays, enables individuals to return to function earlier and reduces the incidence of mal- or non-union [98]. For fractures to adequately heal, fixation devices must maintain anatomic alignment of fracture fragments, transmit compressive force whilst minimising motion across the fracture site and restrict shear forces across the fracture site [99]. However, when implants are used, there are localised effects on loading within the bone. For example, the application of fracture fixation devices such as a plate provides an additional load path and reduces the strain experienced by the underlying bone [85], a phenomenon known as “*stress shielding*”. Implants should be designed to minimise stress shielding, whilst ensuring adequate stabilisation of the fracture fragments.

The most common internal fixation devices include wires, pins, plates, rods or nails and screws, with bone screws the most commonly used internal fixation device [98]. Bone screws can be used alone to hold a fracture or in combination with plates, rods or nails. They are made from non-reactive materials that can be safely used inside a patient’s body. The screws are driven through the bone with the assistance of specialised surgical tools. Depending on the consistency of bone tissue and the type of fractures, various types of orthopaedic screws are available. Design variables for these screws include the root diameter, pitch, and thread profile [100], with cancellous bone screws having larger threads and pitch than cortical bone screws so that they are able to grip the widely spaced trabeculae.

## 2.8 Implant stability

Implant stability depends on the fixation of the implant and the amount and quality of peri-implant bone. Further stability of the implant is gained by osseointegration (the growth of bone into and around the implant). Internal fixation of fractures in younger people having dense cancellous bone rarely presents problems. In older patients with osteoporosis, however, many difficulties arise.

In osteoporotic bone, there is already a limited bone stock due to reduced bone mass in which fixation devices must find anchorage. In addition to this is the sole nature of osteoporosis whereby bone degradation outweighs bone synthesis. The reduced

ability to synthesize bone means that on top of an already weaker purchase by the screw, osseointegration is inadequate and future bone formation at the site may fail to solidify the construct, further reducing implant stability. Consequently, techniques of internal fixation using bone screws tend to have poor outcomes in osteoporotic bone [6] and osteoporosis is considered a risk factor for implant failure and poor functional outcome [7, 8]. Internal fixation of intertrochanteric fractures, for example, fails in around 10% of cases as a result of lag screw cut out from the trabecular bone of the femoral head [101].

Bone screw insertion during surgery requires the application of torque that advances the screw into bone until the head contacts the cortex or plate. Whether through a compression plate or a bone fragment, rotation after head contact produces tension in the screw, balanced by a shear stress in the bone surrounding the thread [11, 102, 103]. Insertion torque has been shown to correlate with the holding power of screws [104, 105] and is largely dependent on the density of the bone [106]. Since density is significantly reduced in osteoporotic bone, the insertion torque and holding strength of the screw are lower in osteoporotic bone.

Clinical torque tightening levels reach an average of 86% of the failure (stripping) torque ( $T_{stripping}$ ) [11]; however in cortical bone, over-tightening of the screw has been shown to reduce pull-out strength by up to 24% [107, 108]. Cleek *et al* (2007) found no statistical difference in pull-out strength when tightened to 50% or 70%  $T_{stripping}$  but pull-out strength was significantly lower when tightened to 90%  $T_{stripping}$  (Figure 2-8). This suggests there is a torque level at which the holding strength is optimised and over tightening past this level may compromise the stability of the implant construct. Whilst similar effects in cancellous bone have not been reported, it is most likely that a similar threshold would exist, beyond which the strength of the construct is compromised; however the threshold level may differ due to the differences in porosity.

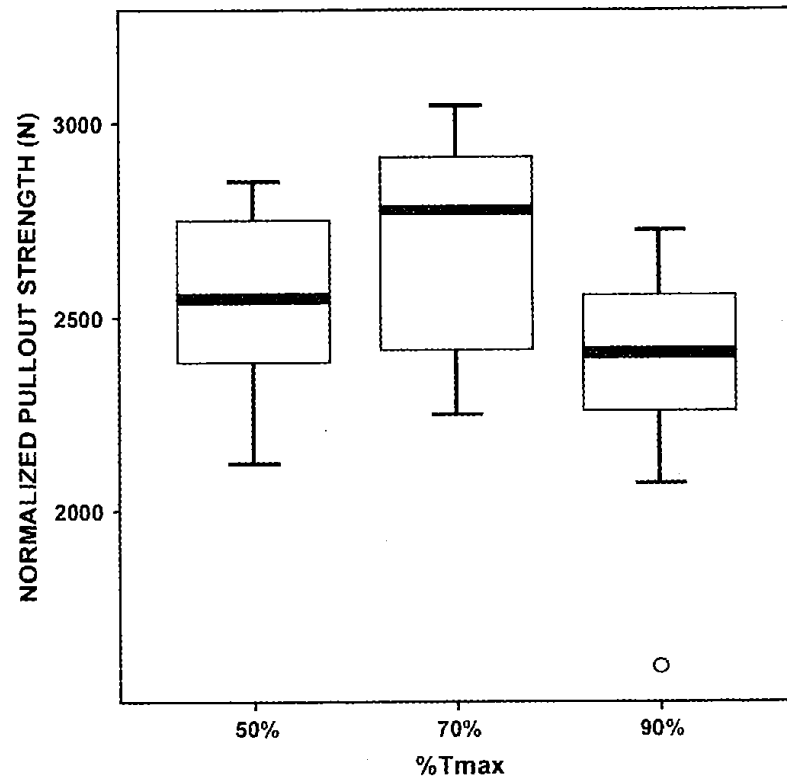


**Figure 2-8: Box plot indicating the median and quartile pull-out strengths. Pull-out strength was, normalised by cortical wall thickness, for screws inserted to either 50%, 70% or 90% of stripping torque in ovine tibial cortical bone [107]. (Reproduced with permission).**

# **3 THE FINITE ELEMENT METHOD**

The use of the FE method in orthopaedic research was first introduced in 1972 by Brekelmans *et al* [109]. Its superior ability to analyse structures and continua with highly complex geometries replaced the traditional mathematical tools for evaluation of stresses and strains in loaded bone; and in the past several decades it has become one of the most widely used tools for non-experimental analysis of bone.

The basic inputs for a FE model include a geometry, material properties, and boundary conditions that describe the loading configuration. The response of the system is then computed by simply summing the effects of all the elements that comprise the model. Because the behaviour of each element is known, the resulting system of equations is readily solved.

In terms of orthopaedic biomechanics, FE analysis is used as a non-destructive alternative to biomechanical testing of bone and analysis of bone-implant structures. When combined with medical imaging modalities, geometrically accurate models can be created. This offers a unique approach to characterising the mechanics of bone, without tissue damage. An advantage of its innate non-destructiveness is the ability to perform many tests on the same bone under different loading conditions and with different material characteristics. This has allowed the investigation of purely structural contributions to apparent level biomechanics, which was previously not possible. The following chapter provides an overview of the FE method as well as a review of the literature in terms of its application in biomechanical analysis of bone and bone-implants.

### **3.1 Principles of FEA**

When a structure is loaded, stresses are generated in its materials. The distribution, magnitudes and orientation of these stresses are dependent not only on the loading configuration but also on the geometry of the structure, the properties of its constituent materials as well as the interactions of the structure with its surrounding environment. Some assumptions that influence the accuracy of the FEA results include: (1) the geometry of the bone / implant, (2) material properties and (3) boundary conditions.

In terms of analysis, there are seven basic steps in the FE method that consists of the following:

#### Pre-processing phase

- 1) Discretisation of the solution domain into finite elements (i.e. dividing the geometry into nodes and elements).
- 2) Assume the shape function to represent the physical behaviour of an element
- 3) Develop equations for an element
- 4) Construct the global stiffness matrix
- 5) Apply boundary conditions, initial conditions and loading.

#### Solution phase

- 6) Solve the set of linear or nonlinear algebraic equations simultaneously to obtain nodal results such as displacement.

#### Post-processing phase

- 7) Obtain any extra information, i.e. principal stresses.

The equilibrium equation solved during an FE analysis is given below (Equation 3-1):

$$\mathbf{ku} = \mathbf{f}$$

Equation 3-1

Where  $\mathbf{k}$  is the known element stiffness matrix, and the vectors  $\mathbf{u}$  and  $\mathbf{f}$  vary according to the application being considered. In the case of bone,  $\mathbf{u}$  and  $\mathbf{f}$  represent the displacement and force vectors, respectively.

## 3.2 FE modelling of bone

Due to the abilities of the FE method in handling complex geometries, it has seen considerable use in the estimation of strength and stiffness of whole bones as well as cancellous bone, and in the computation of stress and strain distributions within the tissue. A clear advantage of the FE method is the implementation of parametric studies, which allows one to isolate the effects of a particular characteristic and assess their specific contributions to apparent mechanics.

### 3.2.1 Continuum Vs micro models

Continuum FE models have become standard computational tools for the evaluation of whole bone mechanical behaviour. Most commonly, cortical and cancellous bone are described as different materials with their geometries based on computed tomography (CT) or magnetic resonance imaging (MRI) scans. One of the requirements of continuum mechanics is that the minimum dimension of a sample that is treated as a material must be significantly larger than the dimension of its structural sub-units [110]. This restricts model sizes to specimens at least 5-10 mm in size in the case of cancellous bone [49] and slightly smaller for cortical bone. The limitations of the continuum assumption, however, appear in two areas: near biological interfaces and in areas of large stress gradients, such as the bone-implant interface.

This limitation can be overcome by the use of micro-FE models. Such models are able to incorporate the full trabecular architecture and structural anisotropy and afford one the ability to look inside the bone to see where stresses are localizing. For linear deformation conditions, high correlations have been found between biomechanical compression tests and micro-FE models, when a homogeneous isotropic tissue modulus is used [71, 74, 111-114].

To date, micro-FE analyses of cancellous bone have focussed on two main areas. The first area has looked at the relationships between apparent mechanical properties, trabecular architecture and the mechanical properties of trabecular tissue [115]. The second is in estimating distributions of stress and strain within trabecular tissue in response to loads applied at the apparent level. Due to the highly porous nature of the trabecular structure, a wide variety of tissue level strains occur, even under simple

loading conditions. The implications of this are currently a popular area of investigation.

### 3.3 Finite element modelling of cancellous bone

#### 3.3.1 Geometry

The first step in FE modelling is the computational representation of the geometry of interest. Trabecular micro-architecture is best captured by high-resolution magnetic resonance imaging (MRI) [116-121] or micro-CT images [71, 72, 75, 77, 78, 81, 83, 122-132]. Within the last decade there have been significant improvements in capabilities of imaging technologies and most current machines are capable of imaging at resolutions as high as 9  $\mu\text{m}$ . Higher resolutions, however, come at the cost of longer scan times, which can present an issue when imaging live animals. Generally scans acquired *in vitro* tend to be of a higher resolution than those obtained *in vivo* because of limitations with exposure time.

Once the image data has been acquired, image thresholding techniques are implemented to discriminate between bone and marrow or pore space in the image slices. The segmentation of bone is an important step and is most commonly achieved by a global threshold. This involves selecting a threshold level, above which all voxels are deemed bone and below which all voxels are deemed non-bone. The most accurate method to determine a suitable threshold level is by matching the BV/TV to that determined using Archimedes principle [133]. Archimedes principle states “*any object, wholly or partially immersed in a fluid, is buoyed up by a force equal to the weight of the fluid displaced by the object*”. For a fully submerged object, the density can be calculated by Equation 3-2; however applying this method can be time consuming and not always practical.

$$\frac{\text{density of object}}{\text{density of fluid}} = \frac{\text{weight}}{\text{weight of displaced fluid}}$$

Equation 3-2

Consequently the threshold is often determined visually, which itself is subjective and can be a source of errors. The threshold level chosen can have a large influence on, for example, BV/TV [134-136], however the reported effects of this are varied. Hara *et al* (2002) reported that a 0.5% change in threshold resulted in an error in BV/TV of up to 5% [134]; however Ruegsegger *et al* (1996) reported that a 10% change in threshold resulted in only a 5% change in BV/TV and no change in trabecular number [136]. It has been demonstrated, however, that the effects of threshold on BV/TV are less pronounced in cases with higher BV/TV, compared to lower BV/TV [134].

### 3.3.2 Discretisation

After segmentation the micro-FE model can be created by direct voxel conversion, which generates brick elements for every bone-containing-voxel in the stack of images [77]. To reduce model complexity the resolution of the images is often coarsened, however this comes at a sacrifice of accuracy. The optimum mesh will achieve accurate results whilst maintaining computational efficiency. Mesh sensitivity studies have been conducted and it is generally accepted that using a voxel resolution at least one-quarter of the average trabecular thickness will achieve numerical convergence in an adequate number of iterations whilst still maintaining a sufficient degree of accuracy [137, 138].

An advantage of the direct voxel conversion method is that all of the elements are geometrically the same and therefore the stiffness matrix for only a single element type needs to be stored [139]. One drawback of direct voxel conversion, however, is the jagged edges that result as a consequence of the hexahedral elements (Figure 3-1). This can introduce errors in tissue stresses and strains, particularly on boundaries [76]; however Van Rietbergen *et al* (1999) reported that although oscillations may occur in calculated stresses and strains, due to the jagged edges, these are less than 7% and their effect on average and standard deviations would be small [114]. The effects of the jagged edges can be somewhat reduced by using higher resolutions and smaller element sizes, or alternatively smoothing algorithms can be used to produce a smoother surface. To obtain a smooth surface, however introduces the use of tetrahedrons to the mesh. The combination of tetrahedral and hexahedral elements results in a mesh that is computationally less efficient. Similarly

a higher resolution increases the number of nodes and elements in the mesh, which results in a computationally more complex model.

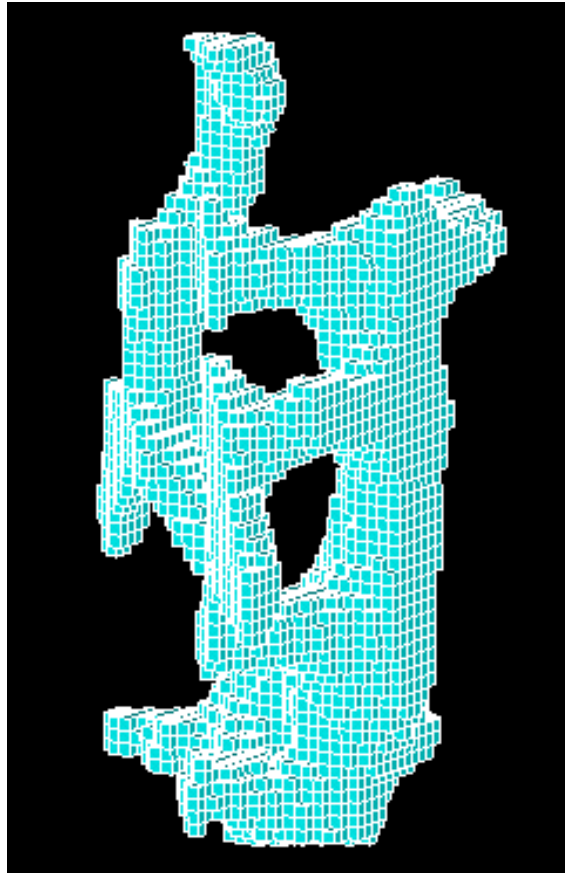


**Figure 3-1: FE mesh of trabecular bone. The model was created using 8-node brick elements. The jagged effects of using this type of element can be seen on the edges of the trabeculae.**

### 3.3.3 Material models

The material properties of cancellous bone are required for stress analysis of the bone-implant construct. As mentioned in the previous chapter, the true material properties of trabecular tissue are not fully known. Most studies assume the trabecular tissue to be a homogeneous, linear, elastic and isotropic material; requiring only two material constants, Young's modulus and Poisson's ratio. This elastic modulus can be determined by direct measurement (ie nanoindentation), or alternatively the material properties can be indirectly determined by back calculation using FEA [77]. Reported values for trabecular tissue range from 0.8 to 20GPa, varying with anatomic location, species and method of measurement [79]. Although it has not been verified experimentally, a Poisson's ratio of 0.3 is generally assumed for trabecular tissue [139]. The apparent properties of trabecular bone do not appear sensitive to variations in the value of the Poisson's ratio [74, 140].

The assumption of a homogeneous elastic modulus, however, is far from accurate. Bourne *et al* (2004) reported heterogeneous models were at least 8% more effective for predicting apparent modulus than models that used a homogeneous tissue modulus [58]. Models incorporating material heterogeneity apply material properties to individual elements based on the grey-scale value of its corresponding voxel in the image data. The application of grey-scale based material properties is commonly used for continuum models, however is limited in micro-models. Whilst numerous studies have demonstrated heterogeneity both along [70, 82, 141] and across [68, 142] trabecular spicules, and heterogeneous material models have reportedly produced more accurate results than homogeneous models [58, 69, 130, 141], limited data exists to relate greyscale values to modulus at the microstructural level. Consequently the assumption of a homogeneous tissue modulus for micro-FE models is customary.

More recent micro-FE models have incorporated non-linear material behaviour to attempt to predict apparent level yield and post-yield behaviour [71, 75, 78]. Whilst these models have shown good agreement with predicted and experimental yield data, they have had little success at simulating accurate post yield behaviour [78]. The incorporation of geometric nonlinearity has been an important omission in early studies. Geometric nonlinearity means that local deformations can be large for small

applied strains. Whilst the effects of omitting geometric nonlinearities are more pronounced in lower volume fraction specimens [143, 144], the SMI may also dictate the extent to which the model is affected [144]. Since significantly larger localised strains have been observed within the tissue for small apparent strains, this should be accounted for when performing micro-FE analyses of cancellous bone.

### 3.3.4 Loading and boundary conditions

When modelling excised volumes of bone, it must also be noted that boundary conditions *in situ* are different to those that occur when using a cubic or cylinder specimen. Whilst it is possible to replicate experimental conditions using FEA, it is not possible to simulate conditions that occur *in situ*. Van Rietbergen [114] (1999) pointed out that using such cubic samples provides information regarding the load transfer in the trabecular architectures, however it cannot be transferred to the situation of bone *in situ*, as boundary forces of the excised specimen aren't representative of the intact situation.

It is also necessary to highlight the importance of using experimental procedures that can be accurately replicated numerically and that minimise testing artefacts, when attempting to determine accurate tissue moduli, and when comparing FE results with experimental results. If experimental data are to be used to calculate specimen specific tissue moduli, then errors arising from experimental inaccuracies will be transferred to the resultant tissue properties. Some of the important areas subject to experimental error include but are not limited to issues arising from specimen size, shape and test protocol [145-150].

It is well established the mechanical tests designed to measure elastic modulus and strength of trabecular bone suffer from a number of experimental artefacts, with the 'end artefact' the most acknowledged. The phenomenon of end artefact occurs as a result of the damage incurred at the ends of machined specimens during specimen preparation. This damage produces an artificial increase in strain when specimens undergo compression testing with platens [146, 149, 151]. The effects of this can be minimised by replacing the use of platens with end caps [54, 152]. Side artefacts originate because the peripheral trabeculae lose their vertical load bearing capacity due to the interruption of the trabecular connectivity at the machined edges [150, 153]. Side artefact is an inevitable feature of biomechanical testing of trabecular

bone and is present in all excised specimens, however a correction factor has been proposed by Un *et al* (2006) [153].

Further, the aspect ratio and geometry of the test specimen have been shown to influence experimentally measured modulus and strength. Linde *et al* (1992) showed that experimental artefact in modulus measurements increases as aspect ratio decreases [148]. Keaveny *et al* (1993) extended on this to show that specimen geometry plays an important role too; higher correlation coefficients in linear regression models were observed for both modulus-density and strength-density regressions with the use of a 2:1 aspect ratio cylinder compared to a cube [154].

### 3.4 Current micro-FE models of cancellous bone: A review of the literature

FE analyses based on micro-CT image data have been used to study bone under various loading conditions [58, 71, 72, 75, 77, 83, 113, 114, 122, 123, 126-129, 144, 155, 156]. Such models have provided considerable insight into better understanding the material properties of cancellous bone at the tissue level, and their relationship to apparent level mechanics. The majority of studies, however, have focussed on high density bone from either bovine tibia or human femoral head. Few studies have considered low-density or osteoporotic bone. In light of recent revelations that suggest alteration of material properties as well as structural degradation as a consequence of osteoporosis, models assessing this are important.

In low density, human vertebral bone, Hou *et al* (1998) found excellent correlations between FE predicted apparent stiffness ( $E_{App-FE}$ ) and experimental stiffness ( $E_{App-Exp}$ ), reporting FE analysis was superior to any combination of morphometric measurements in predicting apparent stiffness and strength [72]. The adjusted  $R^2$  values for linear regression using  $E_{App-FE}$  were 0.89 and 0.87 for  $E_{App-Exp}$  and ultimate strength ( $\sigma_{Ult}$ ) respectively. In terms of morphometric parameters BV/TV was less reliable at predicting both  $E_{App-Exp}$  and  $\sigma_{Ult}$ , with  $R^2$  values of 0.79 and 0.80 respectively. Linear regression on the morphometric parameters only, showed the combination of BV/TV and the average eigenvalues ( $P_L$ ) was the best predictor of  $E_{App-Exp}$ , with an adjusted  $R^2 = 0.82$ , which was still inferior to the predictive power

of the FE model. Using back calculation, the average  $E_{\text{Tiss}}$  was found to be 5.7 GPa (1.6 GPa) with a range of 2.7 – 9.1 GPa.

Ladd *et al* (1998) conducted a similar experiment also in low density vertebral specimens, showing that using a single value for the tissue modulus resulted in differences between model and experiments that were less than the uncertainties within the experimental measurements. This indicates that the FE models are capable of predicting apparent modulus and strength, even if non-specimen specific tissue properties are implemented. Similar to Hou *et al* (1993) they too sought to find tissue modulus values for the lower density vertebral tissue and reported an average tissue modulus of 6.6GPa.

Chevalier *et al* (2007) utilized specimen specific tissue moduli measured directly from the specimen by nanoindentation. The authors found good correlations between FE and experimental predictions for apparent modulus in human proximal femoral cancellous bone specimens ( $R^2 = 0.985$ ) (Figure 3-2) [126]. Other studies have reported high reliability of FE models for predicting apparent modulus and stress even with the use of a general homogeneous and isotropic tissue modulus [78, 83, 124, 125, 129, 132, 144].

More recent studies have successfully incorporated material nonlinearity and tissue strength asymmetry to predict apparent yielding under uniaxial [71, 75, 83] and biaxial [129] loading with high degrees of accuracy. Niebur *et al* (2000) first proposed the biaxial nonlinear material model, incorporating a principal strain yield criterion in 2000 (Figure 3-3), based on the assumption that trabecular tissue had yield strains similar to those of cortical bone. Their results showed excellent agreement between model predictions and experimental measurements of yield strains and stresses under tensile, compressive and shear loading conditions [75].

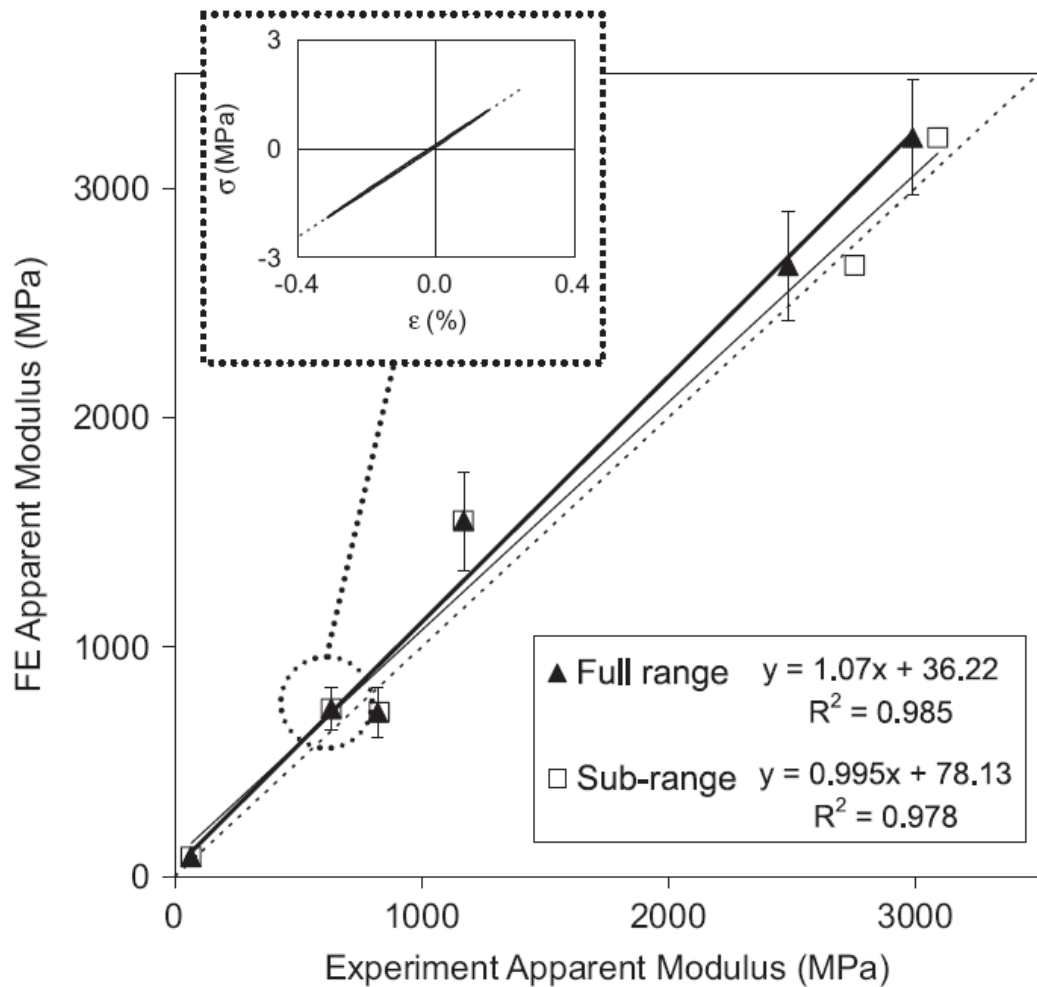


**Figure 3-2: Correlation between predicted and experimental uniaxial apparent modulus. The dotted line represents the desirable match between experimental and FE predictions. The inset shows a typical linear experimental nominal stress-infinitesimal strain curve; the regression was used to determine the experimental apparent modulus [126]. (Reproduced with permission).**

Bayraktar *et al* (2004) further explored the assumption of trabecular bone exhibiting similar yield properties to cortical bone using cortical and cancellous specimens taken from human femoral bone tissue. Their results found significant differences in yield stresses and strains between trabecular and cortical bone tissue, indicating that for the same tissue modulus, trabecular bone tissue possesses lower yield stresses and strains [71].

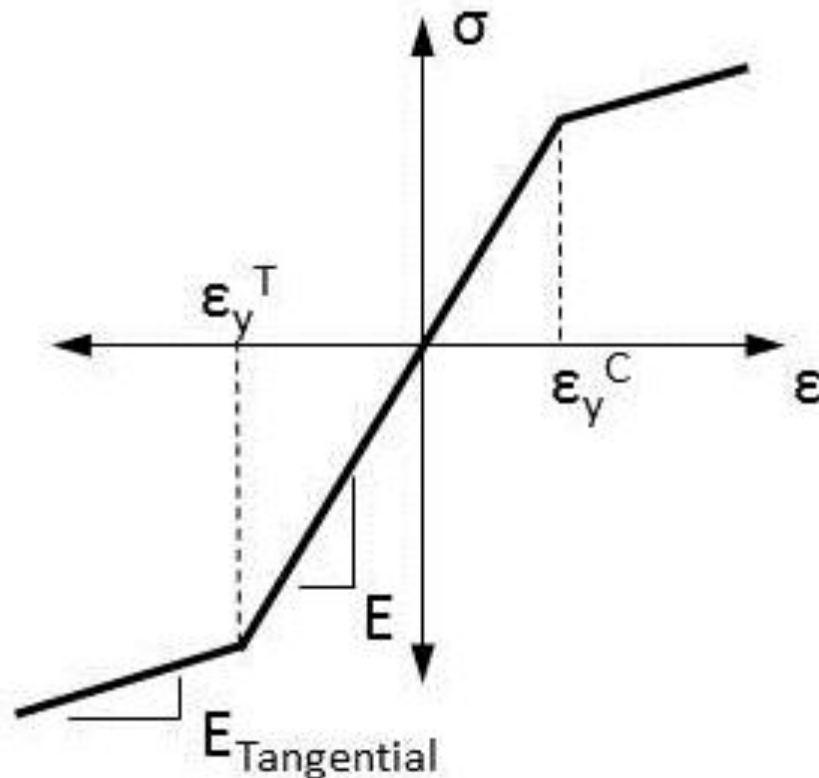


**Figure 3-3: Schematic of the bilinear tissue material model (not to scale). Elastic constants of the tissue were decreased isotropically when the principal strains exceeded either the tensile or compressive tissue yield strains, respectively. The initial elastic modulus was calibrated for each specimen [75]. (Reproduced with permission).**

Verhulp *et al* (2008) attempted to model the post yield apparent behaviour using FEA by incorporating an elasto-plastic model based on Hill's yield function [83]. They too concluded that effective failure properties of trabecular bone tissue cannot be accurately described using established material models for cortical bone tissue. Similar to the previous authors, they found good correlations between experimental yield data and the model data, once they had been calibrated from a small subset of specimens. The post yield behaviour could be modelled by defining only three parameters for the tissue properties: the initial tissue modulus, yield stress and post-yield modulus (minimal post-yield stress could also be incorporated to prevent the intersection of the x-axis, however this parameter had no influence on the simulated response of the specimen).

The studies discussed so far have all considered only compressive or tensile loading conditions. Recently, Wolfram *et al* (2010) conducted  $\mu$ FE analyses to study vertebral specimens under uniaxial tension, uniaxial compression and torsion. Implementing specimen specific tissue modulus values obtained from nanoindentation, they found no difference between experiment and simulations for apparent elastic modulus in tension or compression and shear modulus [156]. This study did however highlight the influence of hydration on bone material properties derived from nanoindentation, with dry tissue models showing distinctly lower R-values when comparing FE and experimental apparent modulus values, for all load cases [156].

The preceding studies have focused on deriving tissue material properties and using FE models to predict apparent biomechanical behaviour. However, it was noted earlier that a second and equally exciting avenue for  $\mu$ FEA is in estimating distributions of stress and strain within trabecular tissue in response to loads applied at the apparent level. Combining  $\mu$ FE analysis with histomorphometry or image based assessment has provided even further insight into the failure mechanisms of trabeculae. Nagaraja *et al* (2005) examined localised microdamage in bovine cancellous bone under apparent uniaxial compressive loading, using microCT images to visualise trabecular failure in conjunction with FE analysis [127]. They found good correlations between regions of high stress in the FE model with trabecular microdamage observed in the image data (Figure 3-4). Stresses in failed longitudinal trabeculae were predominantly compressive, leading to buckling failure; whilst stresses in failed transverse trabeculae consisted of both tensile and compressive stresses, consistent with failure in bending and shear.

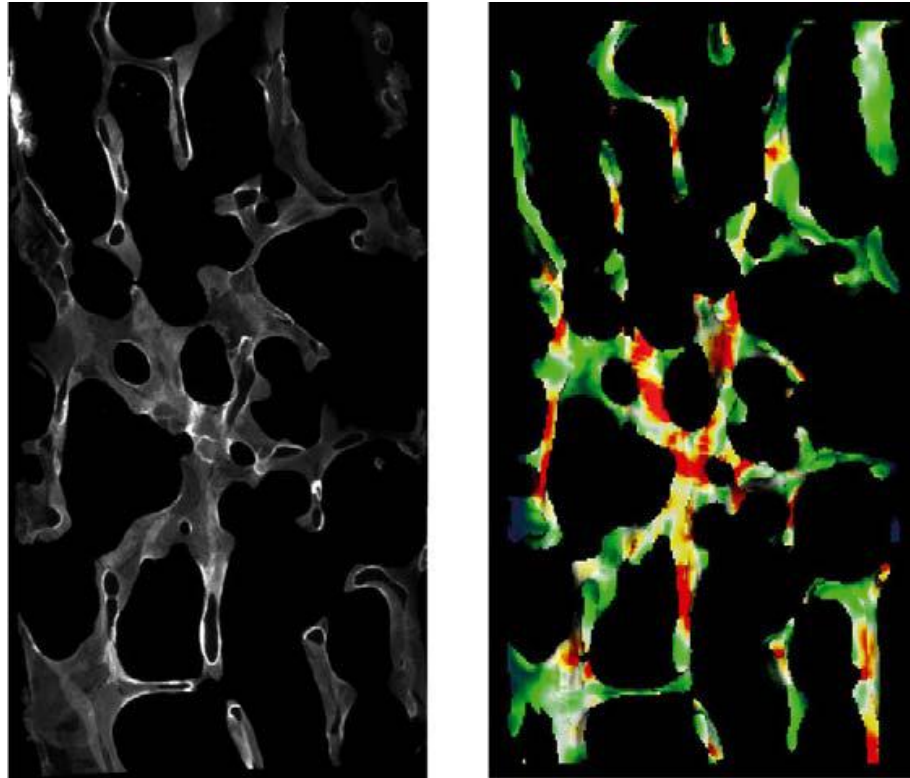


**Figure 3-4: Example of histology section (left) and FE section (right). The von Mises stress distributions can be seen in the FE section; the regions of high stress correlate with microdamage in the histology section [127]. (Reproduced with permission).**

A novel micro-compression device was devised by Müller *et al* (1998) that can sit inside a micro-CT scanner and provide time-lapsed visualisation of localised micro-damage in response to apparent loading; this introduced the term ‘image guided failure assessment’ [157]. The device has been used to perform stepwise compression of bone specimens, with image acquisition at desired intervals. This, in conjunction with micro-FE analysis has provided significant insight into fracture initiation as well as local failure mechanisms [128, 158].

However, most of these studies have concentrated on uniaxial loading conditions. Whilst these studies play an important role in improving our understanding of mechanical properties and failure mechanisms of trabecular bone, applying this knowledge to conventional loading conditions and modelling the behaviour of bone in conjunction with implants is an important development.

### 3.4.1 FE models of bone-implant constructs

Several studies have addressed the effects of implant configuration, geometry and loading using FEA, particularly in the area of dentistry [159-164]. Experimentally, the most common method for evaluating bone-screw holding strength is by pull-out test. Consequently, FE models of bone-implant constructs to date have concentrated on simulation of such tests.

Zhang *et al* (2004) constructed a simplified three-dimensional FE model of the bone-screw interface in the spine to investigate the effects of screw geometry (major and minor diameters, pitch and purchase length) on the pull-out strength [162]. The bone was modelled as a continuum using a rectangular block of cancellous bone (Figure 3-5). The bone was modelled with a Young's modulus of 100MPa, Poisson's ratio of 0.2 and yield stress of 2MPa. The screw was modelled as 316L stainless steel, with a Young's modulus of 193GPa, Poisson's ratio of 0.3 and yield stress of 250MPa. Failure of the bone-screw constructs occurred due to bone shearing with little or no damage to the screw.

A later study by the same author (2006) used a more refined mesh and incorporated a thin cortical shell to further analyse the behaviour of peri-implant bone during pull-out [164]. Results showed that the first thread experienced most of the force, with the remaining threads each undergoing similar forces. These models are simplistic, however in the modelling of cancellous bone as a continuum. The authors acknowledged that failure patterns can be quite different when the material properties of the two materials are similar. In the case of trabecular bone tissue, the material properties lie in the range of 5 to 20GPa, which is much closer to that of implants and as such the interactions may differ significantly at the microstructural level.

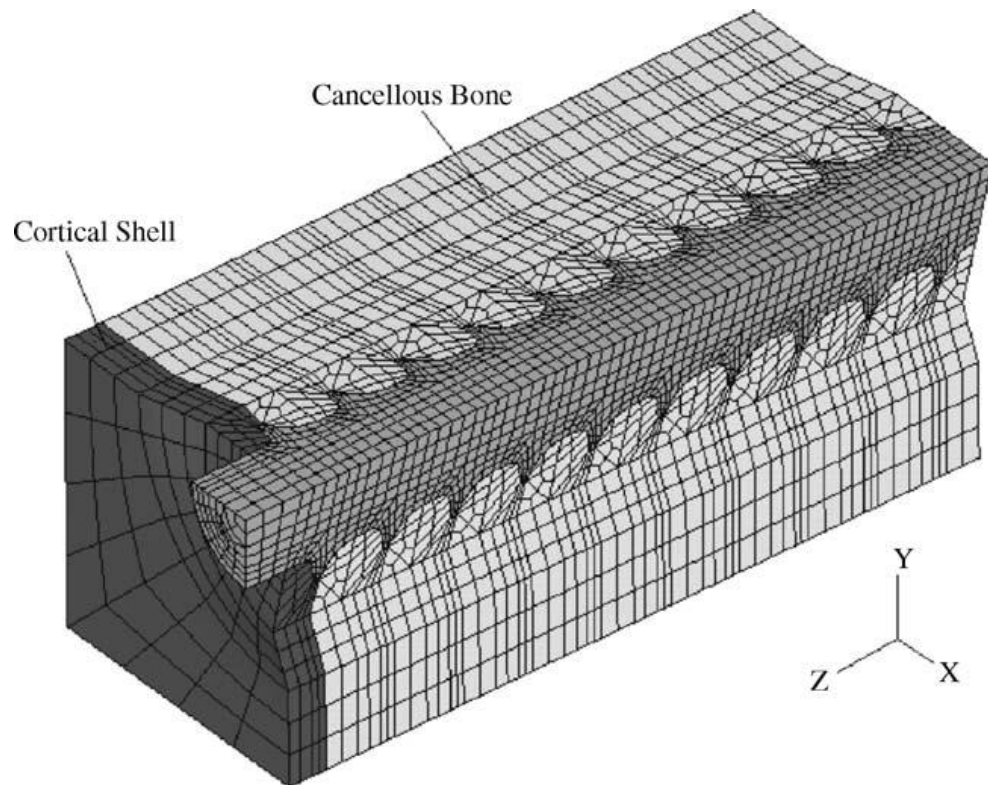


**Figure 3-5: FE model of vertebral bone with screw removed. The cancellous bone is modelled as a solid rectangular block with a thin layer of shells for the cortical bone [162]. (Reproduced with permission).**

Jaecques *et al* (2004) developed specimen specific micro-FE models of titanium implants in guinea pig tibiae, combining experimentation with the FE models to quantify peri-implant stresses and strains for controlled cyclic loading [165]. Although the models were quite sophisticated, the bone was modelled as a continuum, with cortical and trabecular bone tissue assumed to have the same Young's modulus. The authors did, however, implement a grey scale based application of tissue modulus, which attempts to incorporate the tissue heterogeneity due to mineralisation.

Cehreli *et al* (2006) explored the effects of torsion attempting to quantify stress distributions in the peri-implant bone at yield [161]. The authors developed an FE model, and applied a torque load to the model, which had been measured experimentally on the dental implant. At the time, this was one of the first models to consider stresses at the bone-implant interface under torsion; however their model was simplistic in that the surrounding bone was considered a continuum and the

helical continuity in the threads of the implant was not considered. An important finding from this study, however was that the distribution of stresses within the peri-implant bone was limited to 250  $\mu\text{m}$  radiating outwards from the implant.

Liao *et al* (2008) used FEA to investigate to what extent anisotropic elastic properties affect the stress and strain distribution around implants under physiologic loading, using a complete mandible model [160]. Their results were promising and provided a simplistic view of peri-implant stresses during implant loading, however again the peri-implant bone was modelled as a continuum.

All of the models discussed have considered the peri-implant bone as a continuum. Currently, few publications have considered the full trabecular architecture in the context of the bone-implant construct. To investigate the application of micro-FE models for assessing implant interactions with trabecular architecture, Wirth *et al* (2010) compared experimental and computational findings of pull-out tests in ovine spines [166]. Prior to experimental pull-out tests, the bone-implant constructs were micro-CT imaged at a resolution of 25  $\mu\text{m}$ . At such a high resolution, the resultant models comprised between 12.1 and 17.9 million elements, with up to 87.2 million degrees of freedom. The authors compared experimental and computational measures of stiffness of the bone-screw construct and pull-out force (with displacement as the applied boundary condition for the FE model). High correlations were observed for pull-out force ( $R^2 = 0.87$ ) using a VOI with a radius of 4.7mm, however the computationally derived stiffness values were significantly larger than those determined experimentally and were not correlated with experimental results.

In 2011 the same authors again looked at the interactions of the trabecular micro-architecture with respect to small implants, this time in human humeral heads [15]. This time, they looked specifically at the effects of varying implant placement within the head. The study was extensive in that screws were modelled at 25 separate locations within 12 humeral heads (Figure 3-6) totalling 300 micro-FE models. Screw pull-out tests were simulated and the stiffness of the constructs was found to be well correlated with several morphometric parameters (bone volume fraction, bone surface density, trabecular number, structure model index, and the percentage of osseointegration). The authors also found that small variations in implant position resulted in large changes in bone stiffness, with increasing stiffness of the bone-

screw construct as it was moved radially outward from the centre of the head. This is reflective of the large variability in microarchitecture within the humeral head, as strong correlations were observed between the stiffness of the construct and the local morphometry.

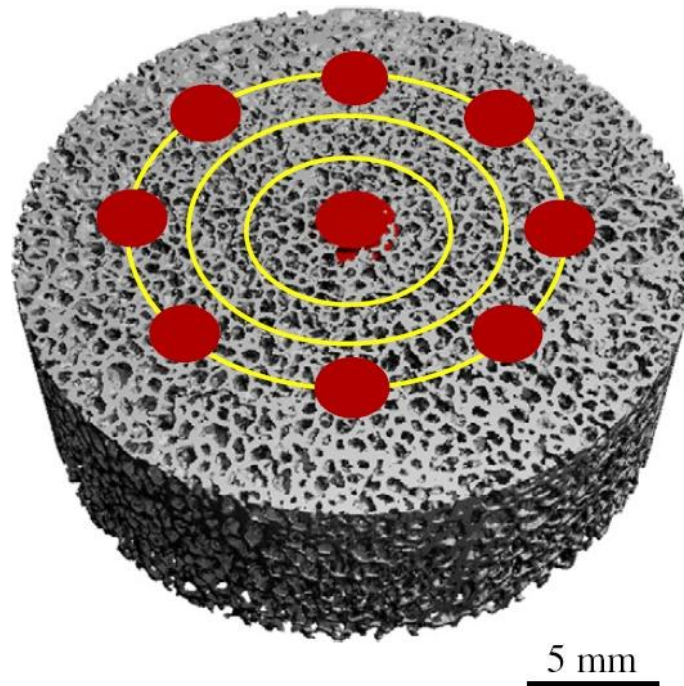


**Figure 3-6: Micro-CT image of humeral head. Indicated in red is the central screw position, and eight positions at a radial distance of 7.5mm from the centre. 2.5mm and 5.0mm distances from the centre are marked by concentric circles [15]. (Reproduced with permission).**

This was the first study to consider the influence of trabecular architecture on the stability of the bone-screw construct. Whilst the screws considered are not clinically used within the femoral head, the methodology provides an excellent example of the applications of micro-FE analysis for analysing bone-implant interactions. An important and relevant finding from this study was the distribution of the stress and strain fields surrounding the implant. Average element strain decreased with increasing distance from the implant, with an average reduction of 63% at a distance 2mm from the implant surface.

Wirth and colleagues were the first to consider the interactions of the microarchitecture of trabecular bone with implants, with previous studies treating cancellous bone as a continuum. To elucidate the importance of incorporating trabecular micro architecture, Wirth *et al* (2012) looked at how the strain distributions and load transfer varied between continuum and discrete models [16]. Two human humeral heads were considered, one a high density specimen and the other of low density. Three insertion depths were also considered (5, 10 and 15mm) as well as 2 different boundary conditions associated with the constraint of the external nodes. For each of these conditions, a continuum and discrete model was designed, totalling 12 micro-FE models for each head.

The continuum models used same volume of interest and identical element dimensions as the discrete models. A uniaxial load of 100N was applied to the head of the screw to simulate pull-out tests. For each model, the interface between bone and implant was modelled as fully bonded.

Comparison between the continuum and the discrete models revealed the continuum models consistently over predicting stiffness with differences as high as 104%. The most significant difference between the two models was the complex strain field observed in the discrete case and not in the continuum model, which instead showed a uniform and symmetric strain distribution. Strain concentrations only appeared close to the implant in the continuum model, whereas localised strain concentrations were observed at different locations for the discrete model. Histograms of the effective strain in the peri-implant bone had similar shapes for the two models; however absolute values differed, with the discrete models producing a lower range of strain distribution. Differences in strain distributions between the continuum and discrete models are illustrated in Figure 3-7, for each of the models considered. The most significant differences between the continuum and discrete models were observed for the low-density specimen. A high-density bone may exhibit more continuum-like behaviour, however differences of up to 30% were still observed between the continuum and discrete model. This highlights the importance of incorporating the micro-architecture of trabecular if one is to truly understand the load transfer at the bone-implant interface.

The two recent studies by Wirth and colleagues (2010, 2012) demonstrate the importance of incorporating the trabecular micro-architecture to accurately simulate macro-scale biomechanics of bone-implant interactions and relate these to micro-level stress and strain behaviour [15, 16]. With respect to screw insertion, the only study to consider torsion was that of Cehreli *et al* (2006); however they modelled the peri-implant bone as a continuum. Quantitative knowledge regarding tissue stress and strain distribution is essential to fully understand the mechanisms that contribute to implant failure.

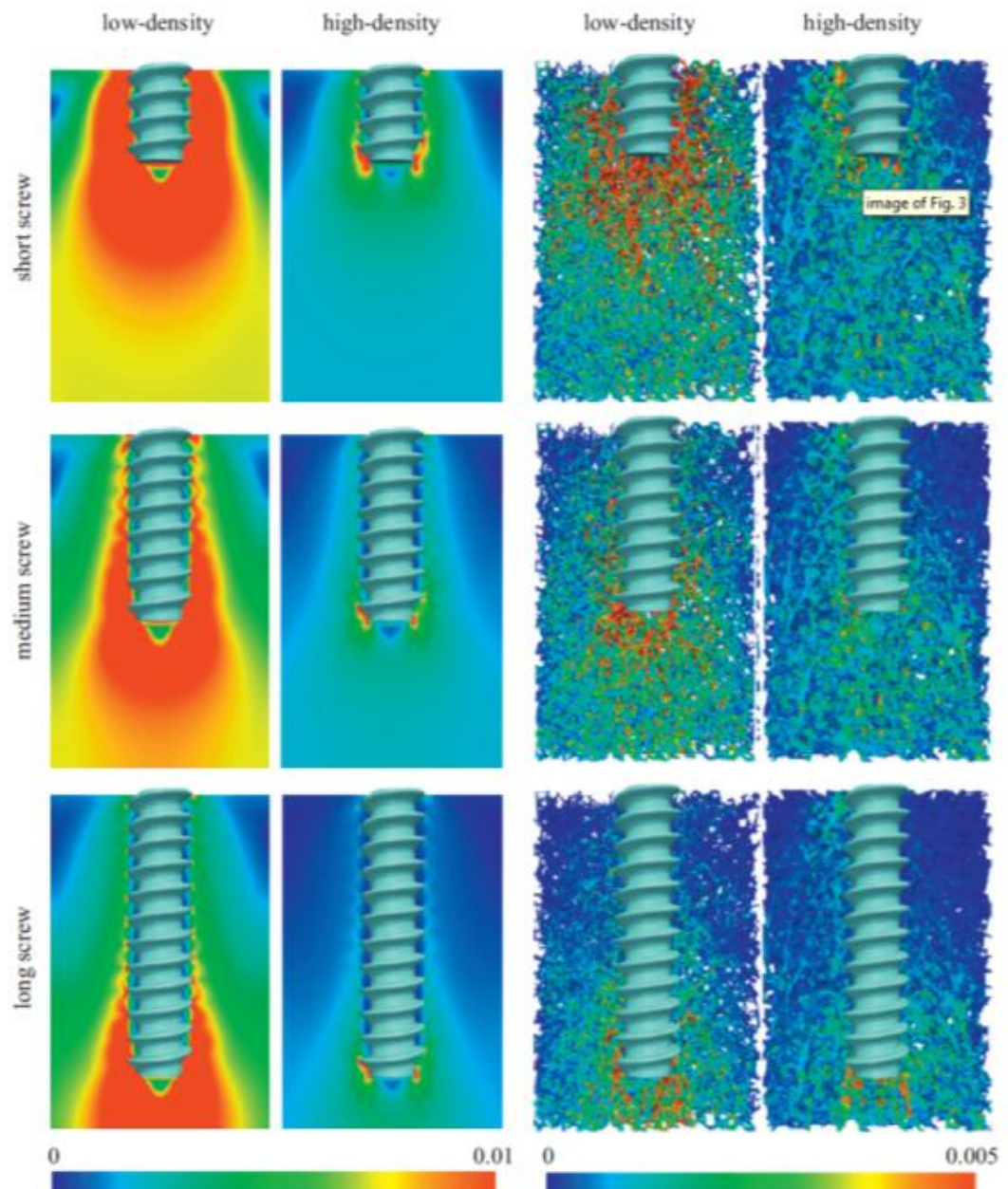


**Figure 3-7: Peri-implant strain in bone for the freely constrained continuum model (Left) and discrete model (Right). All screws were loaded with an axial loading force of 100N. Left columns: low density bone. Right columns: high-density bone. Top: 5mm insertion depth. Middle: 10mm insertion depth. Bottom: 15mm insertion depth. (Note: the scale bars differ between the two models) [16]. (Reproduced with permission).**

## **4 VALIDATION OF IMAGE BASED MICRO-FEA**

## 4.1 Introduction

High resolution FE models have the potential to provide non-invasive estimates of bone biomechanical properties in a more direct manner, compared to the current use of morphologic parameters. Additionally, stress and strain distributions within the trabecular architecture can be explored under several loading conditions. A major advantage of FEA is that it is non-destructive, which means that infinite tests can be performed on a single specimen and issues associated with inter-specimen variability are eliminated. FE models have now reached a level of fidelity that affords them the potential for use as surrogates for mechanical testing of excised specimens.

One of the difficulties associated with micro-FE models of bone is the selection of material properties such as Young's modulus. Although tissue-level elastic properties of trabecular bone have been reported in numerous studies (Table 2-3); see also Guo, 2001 [167] for a more detailed review), substantial discrepancies in the data remain. This is largely due to the technical challenges in obtaining such measurements with specimens at the micro-scale, as well as the inherent non-uniform nature of trabecular tissue. For example uniaxial tensile testing of individual spicules requires the extraction and machining of a geometrically uniform specimen; nanoindentation (an alternative method) can be affected by the heterogeneity of the trabecular tissue, analytical methods of determining elastic modulus from nanoindentation are derived under the assumption that the material is homogeneous and isotropic [168], which bone is not. An alternative approach to direct mechanical testing at the tissue level is the use of high-resolution FE models, which can provide an estimate of the average tissue stiffness [77], [73, 74].

Typically micro-FE models, used to determine tissue properties, contain millions of elements which produce huge stiffness matrices, and can be difficult for some desktop computers to handle. The development of element-by-element (EBE) iterative solvers takes advantage of the fact that all elements are identical [77]. This allows the model to be solved without constructing the entire stiffness matrix, saving on memory. The current standard linear equation solver in almost all bone  $\mu$ FE analyses uses a one level EBE - preconditioning conjugate gradient (PCG) method [169].

While the EBE-PCG solver is very memory efficient, the number of iterations required to reduce the residual can rise dramatically as the problem size increase. This can be overcome by the use of parallelisation, which is quite straightforward for EBE-PCG solvers. The accuracy of the EBE solver is dependent on the convergence tolerance selected. Convergence at each iteration is achieved when the norm of the residuals [15] (Equation 4-1) is less than the specified tolerance squared. Ideally the applied forces are equal to the product of the stiffness matrix and nodal displacements, however in practice there are some residuals.

$$\{\mathbf{R}_i\} = \{\mathbf{F}\} - [\mathbf{K}]\{\mathbf{u}_i\} \quad \text{Equation 4-1}$$

where  $\{\mathbf{F}\}$  is the nodal forces,  $[\mathbf{K}]$  is the stiffness matrix and  $\{\mathbf{u}\}$  represents the nodal displacements. The residuals dictate when convergence occurs, the tolerance of which can be manually set by the user, or a default option is also available through most software packages. In ANSYS (ANSYS Inc, Canonsburg, PA, USA), the EBE option for the PCG solver can be activated by simply issuing the “MSAVE,ON” command.

Additionally, to reduce model complexity, predictions of apparent stiffness and strength are often made based on sub-volumes of larger test-specimens, typically 5 mm x 5 mm x 5 mm. Numerous studies have been conducted on sub-volumes of bone to elicit tissue-level material properties [75, 123]. The size of the sub-volume is chosen such that it is large enough to satisfy continuum criteria. Harrigan *et al* (1988) reported that this condition is met for specimens that span at least five intertrabecular lengths. The use of sub-volumes, however, can be prone to errors due to intra-specimen variations of volume fraction and architecture, and also to specimen size-dependent errors due to mechanical testing methods [123, 126]. A majority of micro-FE studies have been conducted in high density bone; whereas only a small number have focussed on low-density human vertebral bone [72, 74, 124], which is of importance due to its clinical relevance to the effects of osteoporosis. In low density, osteoporotic bone, where the effects of altered mineralisation at the tissue level and the underlying architectural structure are not homogenous [66, 170], the effects of experimental artefact may be more pronounced. Since the overall goal of this thesis

was to develop a micro-FE model of screw tightening in osteoporotic bone, an understanding of the FE method and the ability to derive specimen specific tissue properties, specifically in lower density bone, is necessary. Consequently, the focus of this chapter was to establish a method for creating image-based micro-FE models of low density osteoporotic cancellous bone, and to derive tissue-level material properties from such models.

## 4.2 Aims

The overall goal of the study reported in this chapter was to develop image-based micro-FE models that can be used to estimate apparent level material properties and determine effective tissue moduli. This goal was performed with the following specific aims:

- 1) Assess the ability of the micro-FE model to predict experimental apparent modulus and strength with a homogeneous tissue modulus;
- 2) Establish whether a sub-volume, taken based on the criteria that the dimensions are at least as large as five inter-trabecular spacings, is an adequate surrogate for the full test specimen, in low density osteoporotic bone.

## 4.3 Methods

Image data from (n=12; 9 male, 3 female) vertebral cancellous bone specimens that had been used in a previous study conducted within our group were used [171]. In the previous study, cubic specimens were obtained from the centrum of lumbar vertebral bodies, from any of the T12, L1, L4 or L5 levels. The average (S.D) age of the specimens was 70 (11) years. The orientation of the specimens was controlled using  $\mu$ CT imaging to ensure that the principal trabecular orientation was aligned with the supero-inferior (SI) axis of the specimens. Specimens were mechanically tested to 10% apparent strain by uniaxial compression in the SI direction (at a rate of 1mm/min), using a standard platens test. In the study by Badieli *et al* (2008),

specimens were loaded in one direction followed by loading in the alternate direction (e.g. either supero-inferior (SI) followed by antero-posterior (AP) or vice-versa), consequently, the specimens could not be embedded in brass end-caps and as such the standard platen test was used [171]. Experimentally the specimens were constrained between two platens that were covered with a thin layer of rubber to minimise sliding of the specimen; further information on the testing methods can be found at Badiei *et al* (2008) [171].

#### 4.3.1 Image Processing

Prior to experimental testing, all specimens were  $\mu$ CT scanned (Skyscan 1072, Antwerp, Belgium) at an isotropic resolution of 15.6  $\mu\text{m}$ . The image data were used for the construction of the  $\mu$ FE models. Sections at the periphery of all faces were removed from each data set to ensure boundary artefacts due to cutting of the specimen were not present in the FE mesh. The noise of the resulting grey-scale images was removed using a basic three-dimensional Gaussian filter with a radius of one pixel. The image data were then coarsened to 40  $\mu\text{m}$  [137, 138]. To segment the bone from images, Otsu's automatic grey-level segmentation algorithm was used, implemented as a custom-written routine in Matlab (MathWorks Ltd, Natick, Mass, USA) (Figure 4-1), which used an average threshold value of 55 ( $\pm 3$ ) [172]. A preliminary analysis on the effects of threshold value was carried out on two specimens, one with a high BV/TV and one with a low BV/TV. Based on this analysis, the Otsu determined threshold level was accepted.

The segmentation technique resulted in some parts that were not connected to the main structure. Since these parts would not contribute to the stiffness in the FE-analysis, they were removed from the reconstruction by a custom programmed “*despeckle*” algorithm (CTAn, v1.6.11). Standard model-independent 3D algorithms were employed to calculate structural parameters including bone volume fraction (BV/TV), degree of anisotropy (DA), structure model index (SMI), trabecular number (TbN [ $\mu\text{m}^{-1}$ ]), trabecular thickness (TbTh [ $\mu\text{m}$ ]) and trabecular spacing (TbSp [ $\mu\text{m}$ ]). These parameters were computed using CTAn (v1.6.11) software provided by the manufacturer of the micro-CT system (Skyscan, Antwerp, Belgium). Previous work had analysed the “true” BV/TV by ash density [173]; to determine the effects of the threshold level chosen, the resulting BV/TV for each specimen was

compared to a “true” BV/TV as measured by ash density and was found to be adequate.

For the sub-volume models, a volume of interest (VOI) was selected from the raw image data, such that BV/TV of the sub-volume and full volume were within  $\pm 5\%$ . One model contained a highly heterogeneous structure and consequently a smaller VOI that reflected the full model could not be obtained; this model was not included in the sub-volume analysis. The sub-volume VOIs then underwent the same image processing and morphologic analysis as the full models.

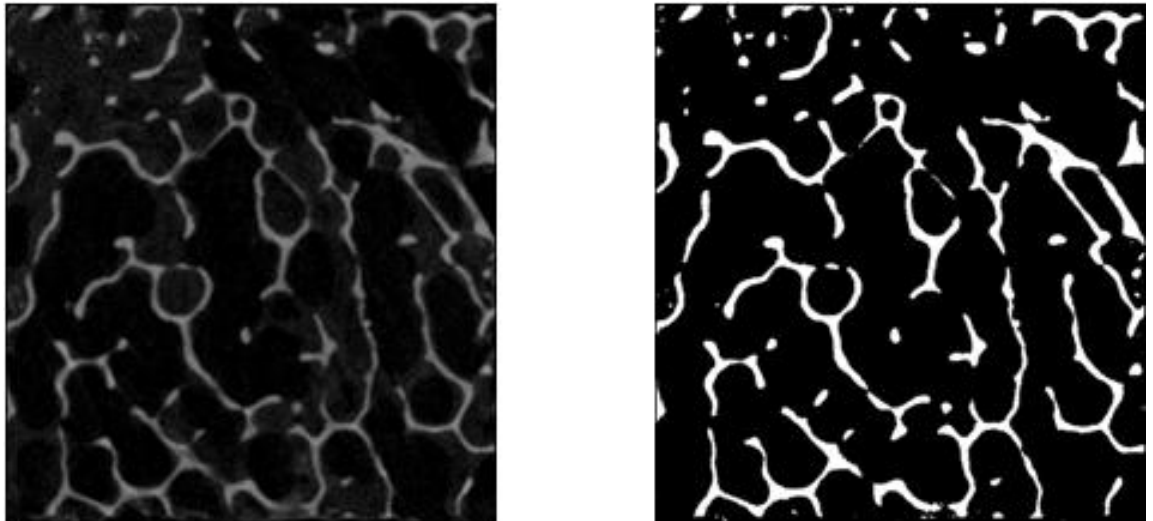


**Figure 4-1: Reconstructed micro-CT slice before image processing (left), and after image processing (right). The raw image underwent filtering and thresholding to segment bone from non-bone. Bone is displayed as white.**

#### 4.3.2 Experimental Analysis

All experimental stress-strain data were analysed by a custom program (Matlab version 7.6.0) to establish ultimate strength as well as yield strains and stresses. Ultimate strength was defined as the maximum stress obtained. Because the platens method had been implemented in the experimental stage, all stress-strain curves were adjusted for the non-linear “toe” region as follows: A third order polynomial was fit to the experimental data to smooth the curve and eliminate experimental artefact. The

toe region was removed by continuing the stress-strain curve along the linear path from where the experimental curve started to deviate. After removal of the toe, the curve was shifted to the left so that the new curve passed through the origin. The 0.2% offset method was then used to establish yield strains and stresses [174], whereby experimental yield stress and strain were defined by the intersection of the 0.2 % strain offset line with the adjusted experimental curve (Figure 4-2).

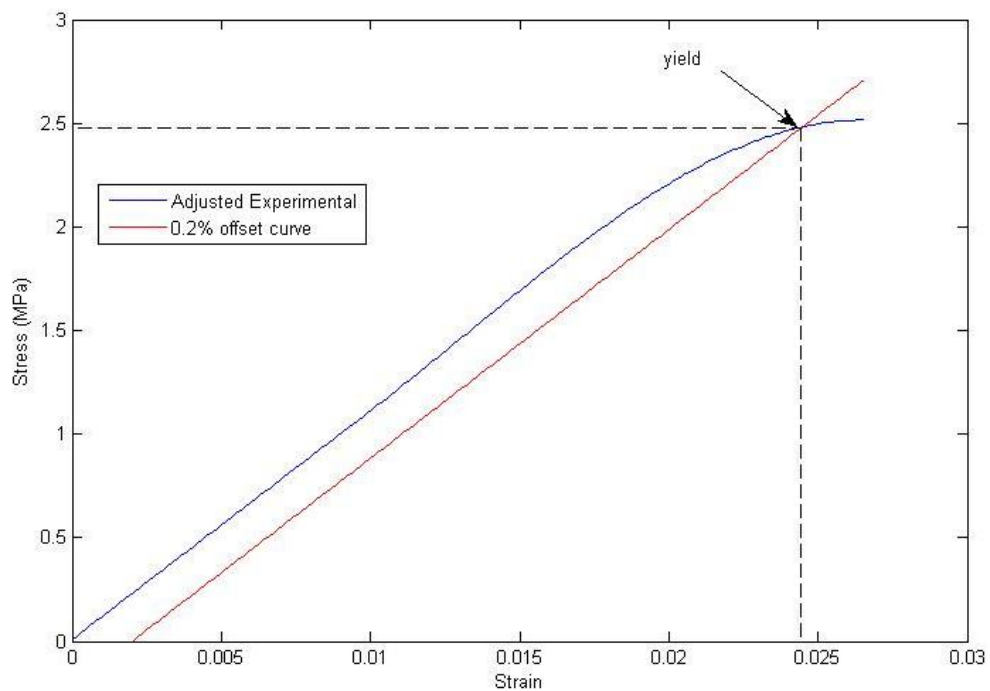


**Figure 4-2: Typical stress-strain curve for the experimental uniaxial compression tests. The 0.2% offset method was used to establish yield stress and yield strain. Yield stress and strain were defined at the point the 0.2% offset curve intercepted the data curve.**

### 4.3.3 FE models

To construct the micro-FE models a commercial mesh generation software package was employed (Simpleware Ltd., UK, 5.0). The binarised images were imported into the program and coarsened to 40  $\mu\text{m}$  resolution. This resolution was chosen, such that a minimum of four voxels spanned the average trabecular thickness (0.171 mm); this is a resolution suggested to reduce the complexity of the model but ensure numerical convergence [137, 138]. Coarsening of images was performed using the

nearest neighbour algorithm, where each interpolated output pixel is assigned the value of the nearest sample point in the input image.

After coarsening, any segments that were no longer connected to the main structure were removed. Voxels containing bone were then converted to eight node linear elastic hexahedral brick elements. Element material properties were assumed to be linear, homogeneous and isotropic. A Young's modulus of 5GPa and Poisson's ratio of 0.3 were assumed for all elements [72].

To simulate the experimental tests, a compressive displacement boundary condition was applied to all nodes on the top face equivalent to 0.2% apparent strain. All nodes on the bottom face were fully constrained in all directions (Figure 4-3). Models were implemented using the (PCG) iterative solver with the memory save option activated. This option implements the EBE approach and the global stiffness matrix is not assembled, reducing memory during the solution.

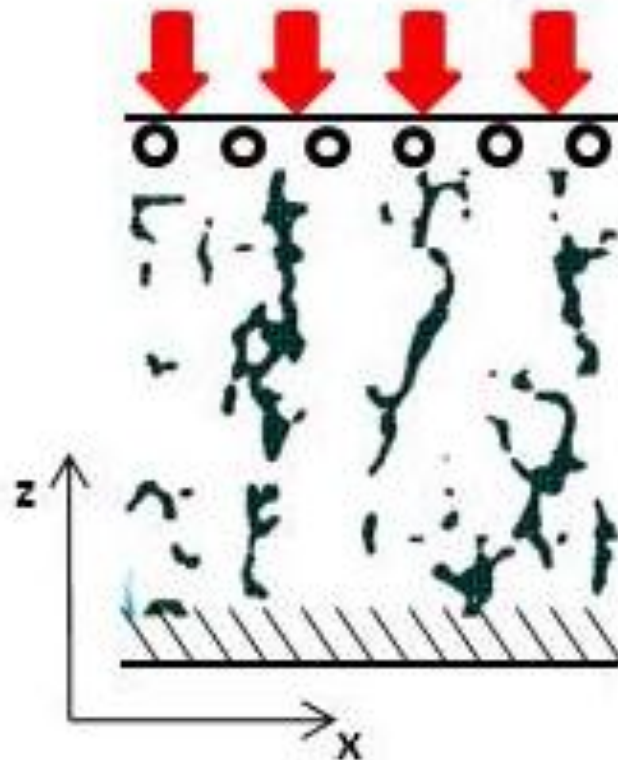


**Figure 4-3: Diagram showing the compressive displacement boundary conditions for the FE model. The bottom face was constrained in all directions; the top face was displaced 0.2% in the z direction.**

The convergence criteria for the PCG iterative solver were analysed using one of the sub-volume models and the same boundary conditions as stated above. The Euclidean norm of residuals was used and accuracy was measured by comparing the results from the iterative solver to those of the direct solver. All models were solved using Ansys12.0. Sub-volume models were solved on a single core desktop PC, however larger models were solved using the parallel processing module available from Ansys and super computer facilities. The FE apparent stress ( $\sigma_{app}^{FE}$ ) and FE apparent modulus ( $E_{App}^{FE}$ ) were then calculated from nodal reaction forces [77]. The effective tissue modulus ( $E_{Tiss}$ ) was calculated for each model by scaling the FE apparent modulus to match the experimental apparent modulus ( $E_{App}^{Exp}$ ) [77].

#### 4.3.4 Statistical Analysis

All statistical analyses were performed using the SPSS statistical package (version 18.0; SPSS, Inc., Chicago, IL). All reported p-values are two-tailed, with  $p < 0.05$  considered statistically significant [175]. Shapiro-Wilk tests ( $p > 0.05$ ) were used to check data was normally distributed. Based on the tests for normality, for statistical analysis, linear regression was used to compare the FE and experimental methods; linear regression analyses were also performed on material and architectural properties to establish any relationships. Paired *t*-tests were used to compare differences in morphological parameters between sub- and full- volume models, as well as any differences in the apparent elastic modulus of the FE models.

## 4.4 Results

### 4.4.1 Convergence

Accuracy of the iterative solver was determined by varying the tolerance level and comparing the calculated apparent modulus to the direct solver result. The errors in calculated modulus are listed in Table 4-1; the error was less than 1% for tolerances set to  $10e^{-4}$  or lower. Consequently, a tolerance of  $10e^{-5}$  was used for both full- and sub-volume analyses, resulting in less than 0.01% error.

Table 4-1: Output results of PCG iterative solver

Solver	Tolerance	Error (%)
Direct	-	-
PCG	$10e^{-9}$	0
.	$10e^{-7}$	0
.	$10e^{-5}$	0.0012
.	$10e^{-4}$	0.0545
.	$10e^{-3}$	3.26
.	$50e^{-3}$	29.36
.	$10e^{-2}$	75.7

#### 4.4.2 Thresholding

Volume fractions determined from ashing ranged from 0.07 to 0.11, which is typical for osteoporotic cancellous specimens [176, 177]. Linear regression indicated good agreement between BV/TV of the models and BV/TV as measured by ash density, for both the full- and sub-volume models ( $R^2 = 0.84$ ,  $R^2 = 0.83$ ,  $p \leq 0.001$ , respectively).

#### 4.4.3 Comparison of full-models and mechanical tests

Regression analysis showed a strong relationship between  $E_{App}^{FE}$  and  $E_{App}^{Exp}$ , ( $R^2 = 0.82$ ,  $p \leq 0.001$ ) (Figure 4-4); however the FE model tended to over predict the apparent modulus ( $E_{App}^{Exp} = 0.527 * E_{App}^{FEA} - 12.122$  MPa). A strong relationship was observed between  $E_{App}^{FE}$  and ultimate strength ( $\sigma_{Ult}$ ) (Figure 4-5) ( $R^2 = 0.88$ ,  $p < 0.001$ ). The average effective tissue modulus ( $E_{Tiss}^{full}$ ) was 2.2 GPa ( $\pm 0.36$  GPa). Based on linear regression analysis, no structural parameters correlated with effective tissue modulus. There was no statistically significant relationship between apparent density measured by dual X-ray absorptiometry (DXA) and effective tissue modulus ( $R^2 = 0.08$   $p = 0.397$ ), or ash ( $\rho_{Ash}$ ), ( $R^2 = 0.21$ ,  $p = 0.156$ ).

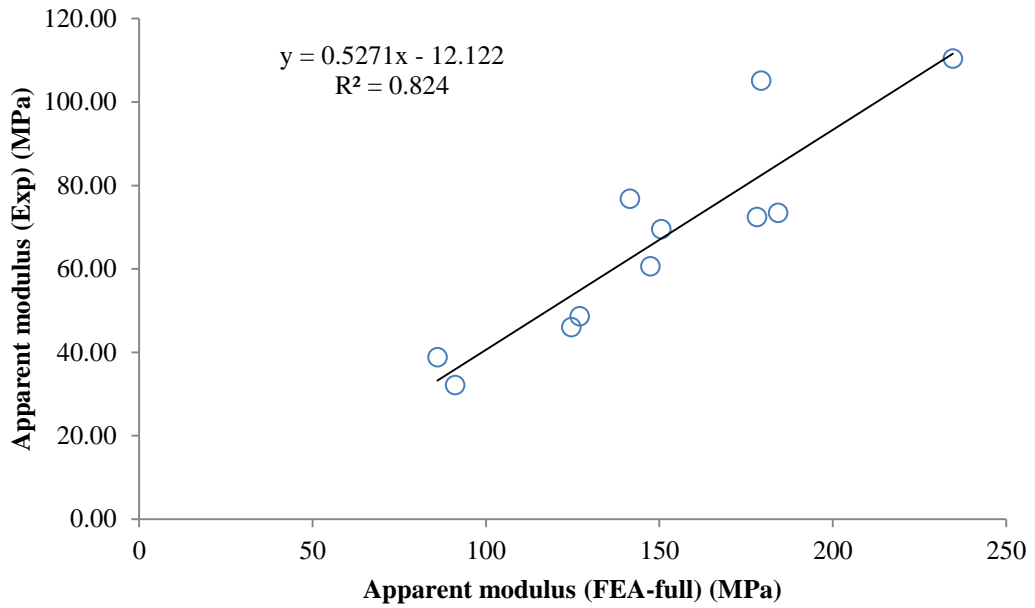


Figure 4-4: Apparent modulus determined experimentally ( $E_{App}^{Exp}$ ) vs apparent modulus predicted by the full FE model ( $E_{App}^{FE}$ ).

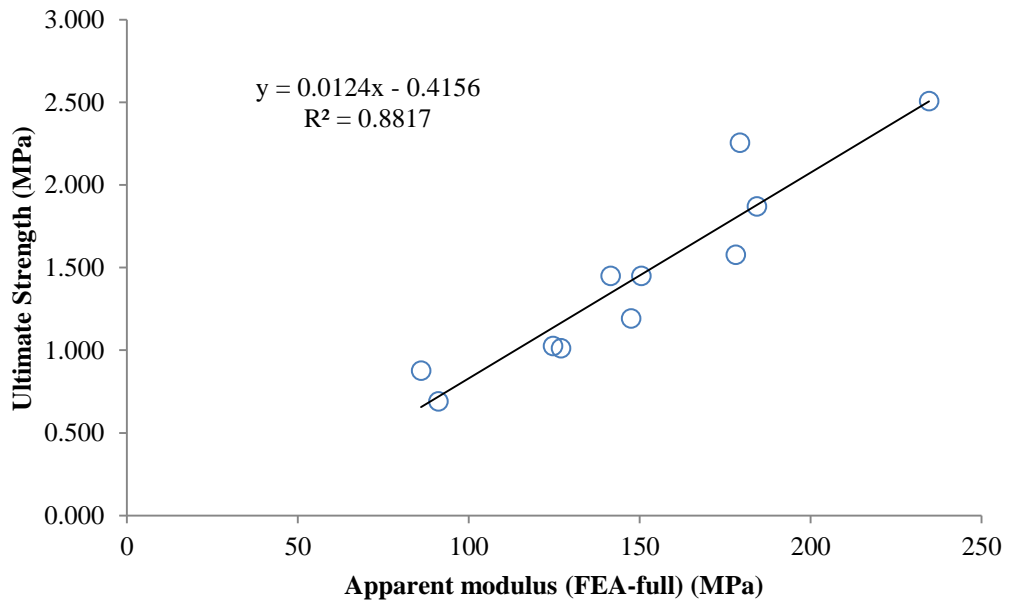


Figure 4-5: Apparent ultimate strength determined experimentally vs the FE predicted apparent modulus ( $E_{App}^{FE}$ ) for the full-volume models .

#### 4.4.4 Comparison of full- and sub-volume models

With regard to the sub-volume, morphologic parameters when compared to the full-volume model were almost the same for all parameters except for trabecular separation (Table 4-2). The trabecular separation was smaller in the sub-volume model, for all cases; however this was not statistically significant ( $p = 0.22$ ). Selecting a sub-volume reduced the size of the models in terms of node number on average by 74%; the sub- and full-volume models contained 500,000 and 2,000,000 nodes and 300,000 and 1,200,000 elements respectively. The average  $E_{App}^{FE}$  was 140MPa ( $\pm 38.8$ ) and 149MPa ( $\pm 43.6$ ) for the sub- and full-volume models respectively. The FE calculated apparent moduli tended to be lower for the sub-volume models compared to the full-volume models; however the difference was not statistically significant ( $p = 0.71$ ) (Figure 4-6).

There was a strong linear relationship between  $E_{App}^{FE}(\text{sub})$  and  $E_{App}^{Exp}$ , ( $R^2 = 0.89$ ,  $p \leq 0.001$ ) (Figure 4-6); however regression analysis again showed that, similar to the full-models, the sub-volume model over-predicted the experimental apparent modulus ( $E_{App}^{Exp} = 0.614 * E_{App}^{FEA} - 19.67$  MPa) (Figure 4-7). A strong relationship was also observed between  $E_{App}^{FE}(\text{sub})$  and ultimate strength ( $\sigma_{Ult}$ ) (Figure 4-8) ( $R^2 = 0.91$ ,  $p < 0.001$ ). The average effective tissue modulus ( $E_{Tiss}^{full}$ ) measured was 2.32 GPa ( $\pm 0.36$  GPa). The effective tissue modulus calculated by the sub-models was slightly higher than that measured by the full-volume models but the difference not statistically significant ( $p = 0.46$ ). Similar to the full-volume models, there was no significant relationship between  $E_{Tiss}^{FE}(\text{sub})$  and any architectural parameters or apparent density measured by dual X-ray absorptiometry (DXA). There was, however, a moderate relationship between  $E_{Tiss}^{full}$  and ash density ( $\rho_{Ash}$ ) ( $R^2 = 0.32$ ,  $p = 0.07$ ).

Table 4-2: Structural parameters for the full- and sub-volume models ( $n=11$ ) . The parameters were calculated using the standard Skyscan software package.

Parameters <sup>†</sup>	Full model	sub model	p-value
	mean (SD)	mean (SD)	
BV/TV	0.091 (0.013)	0.090 (0.013)	0.82
Tb Pf (mm <sup>-1</sup> )	5.653 (0.923)	5.733 (1.016)	0.92
Tb Th (mm)	0.171 (0.016)	0.170 (0.016)	0.92
Tb Sp (mm)	1.051 (0.109)	0.995 (0.097)	0.22
Tb N (mm <sup>-1</sup> )	0.537 (0.065)	0.534 (0.071)	0.92
SMI	1.723 (0.204)	1.735 (0.235)	0.94
DA	2.367 (0.305)	2.361 (0.319)	0.95
E <sub>1</sub>	0.713 (0.027)	0.718 (0.034)	0.95
E <sub>2</sub>	0.629 (0.031)	0.621 (0.034)	0.68
E <sub>3</sub>	0.306 (0.039)	0.309 (0.034)	0.95

<sup>†</sup> BV/TV = bone volume fraction; Tb Pf = Trabecular pattern factor; Tb Th = trabecular thickness; Tb Sp = trabecular spacing; TbN = Trabecular number; SMI = structural model index and DA = degree of anisotropy; E<sub>1,2,3</sub> = Eigenvalues determined from tensor describing the anisotropy ellipsoid.

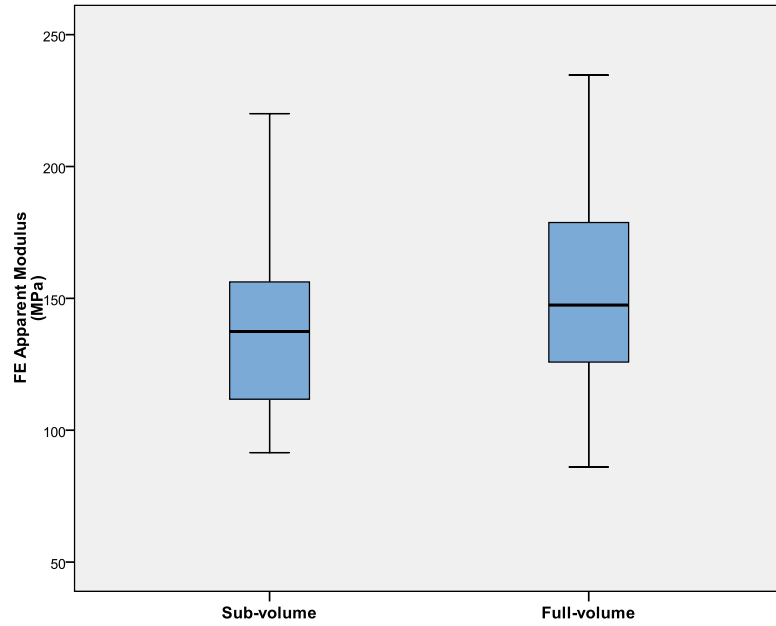


Figure 4-6: FE calculated apparent modulus for the full- and sub-volume models. Material properties were assumed to be linear, isotropic, and homogenous with a tissue modulus of 5GPa and Poisson’s ratio of 0.3

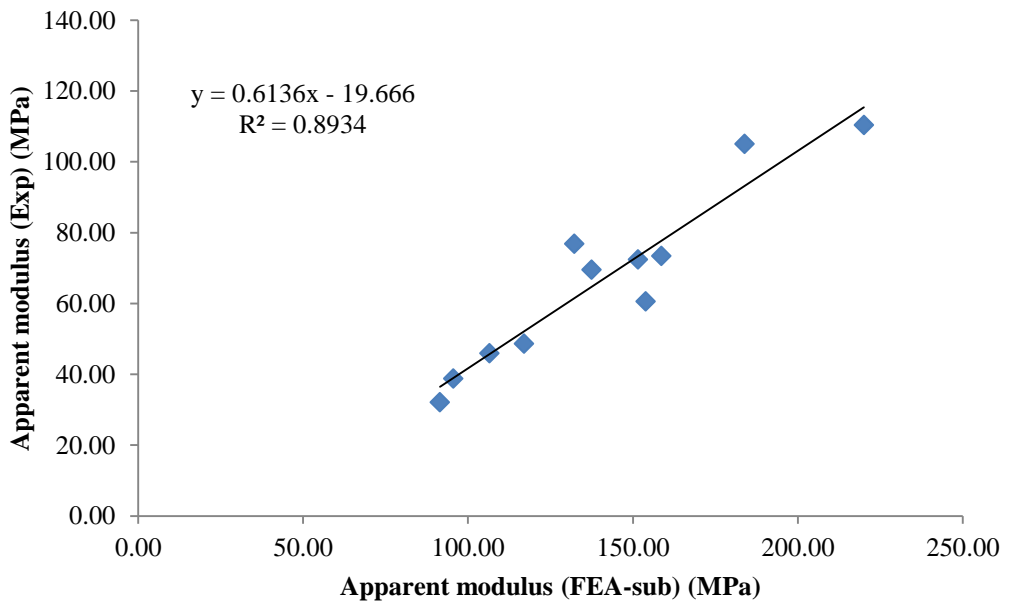
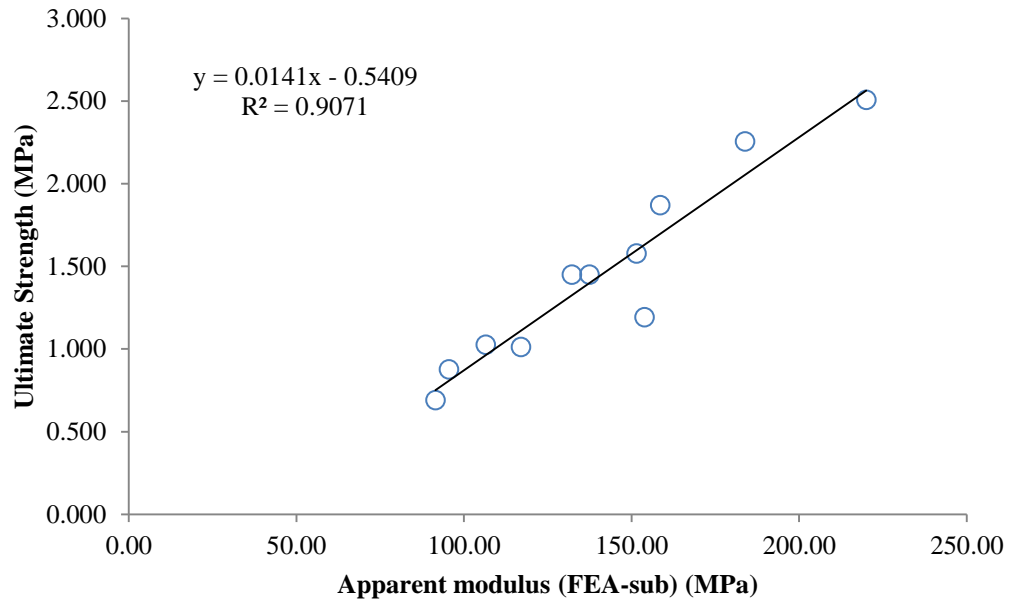


Figure 4-7: Apparent modulus determined experimentally ( $E_{App}^{Exp}$ ) vs apparent modulus predicted by the sub-volume FE model ( $E_{App}^{FE}$ ).



**Figure 4-8: Apparent ultimate strength determined experimentally Vs the FE predicted apparent modulus ( $E_{App}^{FE}$ ) for the sub-volume models.**

## 4.5 Discussion

The main aim of this study was to establish a valid method for constructing image based  $\mu$ FE models that could be used to estimate apparent level material properties. Some of the limitations of this study need to be noted. Firstly, we used a global threshold to segment the bone matrix. Segmentation of bone voxels from non-bone is a necessary step in image based FE models; the global threshold technique is the most widely used technique [72, 77, 138, 178-180]; the threshold value is chosen either visually by analysing the histogram of CT numbers or by forcing the resulting binary data set to have the same BV/TV as measured by an independent method, such as the Archimedes test. The first technique is faster, however the latter appears to produce more accurate results [134]. Different thresholds can produce variations in local bone morphology [173, 181]; and whilst there is evidence to suggest that BV/TV may be sensitive to variations in threshold [173, 181], when Archimedes test cannot be used, the use of a visually determined threshold is common [72, 77, 138, 179, 182-184].

Second, all trabecular bone voxels in the FEA were assigned an isotropic and homogeneous tissue modulus. Newly remodelled regions of trabecular bone are less mineralised than older segments, and consequently, trabecular tissue tends to decrease in stiffness from the core outwards [68]; therefore estimates of local stress and strain values would be expected to vary in regions of high or low density bone tissue. These effects, however, would be expected to influence the analysis of individual trabeculae more so than the results averaged over an entire subsection. To account for heterogeneity, material properties can be scaled from grey-scale values of the micro-CT images and assigned on an element by element basis [58, 185], however this was not incorporated for this analysis. We assumed linear behaviour for all elements, even though trabecular tissue is known to yield at relatively low strains (reportedly less than 1%) [71, 75, 123, 124, 129]; however the loading was restricted to 0.2% apparent strain and at this level local tissue yielding would be minimal and the linear assumption is reasonable.

Another limitation is the use of the platens method in obtaining the experimental data. It is well known that mechanical test methods used to measure elastic modulus and strength of excised trabecular bone specimens suffer from various experimental artefacts, with ‘*end-artefact*’ being the most reported [54]. The end-artefact is caused by damage that occurs at the ends of specimens during machining; this damage produces an artificial non-linearity and increase in strain when the specimens are tested in a standard platens compression test [54, 146, 151]. The result is an underestimation in measured apparent modulus [54].

In addition to this end-artefact, a “*side-artefact*” originates from the sides of the specimen, due to the disruption of the trabecular network at the periphery. The effects of the side-artefact are dependent on anatomic location and tend to increase with decreasing bone volume fraction [186]. Side artefacts underestimate the true (i.e. in situ) mechanical properties. Un *et al* (2006) reported a reduction in modulus by up to 50% in human vertebral bone [153].

Experimentally the specimens were constrained between two platens. This frictional boundary was implicitly modelled, by fixing all nodes on the bottom face and restricting the nodes on the top face to movement in the z-direction only (Figure 4-3). The implicit modelling of the boundary conditions may be seen as a potential source

of error, however, Bevill *et al* (2009) reported that the calculated effective tissue modulus showed no dependence on boundary conditions modelled explicitly or implicitly [155].

Finally, any inferences from this study need to be considered in light of the sample size. The small sample size has a greater probability that any observations were by chance; however, strong relationships were observed with high statistical significance.

Despite these limitations, high correlations were observed between experimental data and micro-FE model data. The resultant BV/TV of the models compared well with the experimentally derived values for BV/TV, indicating that the threshold level chosen was acceptable. The greatest discrepancies were observed in specimens with lower bone volume fractions; this was not unexpected with several studies reporting specimens with lower BV/TV to be more sensitive to variations in threshold [126, 134].

To solve the models, an EBE-PCG solver was implemented. This has the advantage over a direct solver in that it is much faster; however the accuracy is dependent on the convergence tolerance used. One of the sub-volume specimens was used to assess the accuracy of the PCG solver and determine the optimum tolerance level that would provide an adequate convergence rate. By increasing the tolerance, the model is more likely to converge faster but with lower accuracy. The sub model was used to assess the accuracy, because it was small enough to be solved on a desktop PC. The accuracy of the EBE-PCG solver used was greater than 99% for tolerances set to  $10e^{-4}$  or lower. For these linear analyses, the PCG tolerance was set so to  $10e^{-5}$ , so that the highest accuracy was achieved.

The main aim of this study was to assess how well the micro-FE model could predict apparent stress and elastic modulus, using a single tissue value taken from the literature. An initial tissue modulus of 5GPa was assigned based on previous work using vertebral cancellous specimens [72]. The resulting FE predicted apparent modulus was significantly higher than the experimentally determined modulus; however there was a strong relationship between the  $E_{App}^{Exp}$  and  $E_{App}^{FE}$  (Figure 4-4). The most likely reason for the discrepancy is that the measured experimental

modulus is erroneous due to end artefact issues. As mentioned previously the use of the platens method results in an underestimation of apparent modulus, which is dependent on anatomic location; Keaveny *et al* (1997) showed that the use of platens can result in an underestimation of modulus as high as 86%; with an average error of 36.3% ( $\pm 29.6$ ) in human lumbar cancellous bone [54]. The FE model over-estimated apparent modulus by 50%; if the FE model is a better representation of the true apparent modulus, then an error of 50% is within the reported error range for platens testing of human vertebral cancellous bone. The fact that a strong, statistically significant relationship still existed between the FE and experimental results suggests that the error is systematic and common to all tests.

There is a known strong linear correlation between the stress at which trabecular bone fails and the corresponding elastic modulus [187]. Linear regression analysis showed that  $E_{App}^{FE}$  determined using an estimated tissue modulus of 5GPa was a strong predictor of ultimate strength, for both the full- ( $R^2 = 0.88$ ) and sub-volume models ( $R^2 = 0.91$ ). The coefficients for the relationship, determined by linear regression analysis for this and other studies, are listed in Table 4-3. The majority of studies have used the end cap method for experimental testing and as a result the slope of the regression line is much smaller compared to this study. However Yener *et al* (2001) considered human vertebral bone, and found the relationship was dependent on the test method employed [184]. For the end cap method, their slope was similar to other studies that had analysed human vertebral bone [188]. For the platens method, the slope of the regression line was similar to that found for both the full- and sub-volume models of this study. The regression slope of the experimental modulus is approximately double that found for the FE model and reported by Yener *et al* (2001); this is further evidence that a systematic error most likely exists in the experimental data, which is in all likelihood associated with the use of the platens method.

The average  $E_{\text{Tiss}}$ , of 2.2 GPa, determined from the FE models was within the reported range of 1-20GPa, albeit at the lower end of the scale. Studies that have reported tissue moduli values at the upper end of the scale however, have tended to be in high density bovine bone (Table 2-3). Reported tissue moduli for human vertebral cancellous bone range from 1.2 to 13.4 GPa (Table 4-4), and the calculated average tissue modulus is still within this range.

Table 4-3: Linear regressions ( $\sigma_y = mE_{\text{App}} + c$ ) of the yield strength of cancellous trabecular bone under uniaxial compression against Young's modulus ( $E$ ).  $m$  is the slope of the regression line and  $c$  is the constant.

Author	Specimen	$m$ [c]	$R^2$
Keaveny <i>et al</i> (1994)[152]	Bovine tibial (end cap)	$9.6e^{-3}$ [-1.49]	0.85
	Bovine tibial <sup>†</sup> (end cap)	$5.6e^{-3}$ [0.81]	0.95
Fyhrie <i>et al</i> (2000)[188]	Human vertebral (end cap)	$6.3e^{-3}$ [-0.039]	0.89
	Bovine cortical (end cap)	$6.0e^{-3}$ [-10.919]	0.92
Yener <i>et al</i> (2001)[184]	Human vertebral (platens)	$10.3e^{-3}$ [0.0148]	0.96
	Human vertebral (end cap)	$4.4e^{-3}$ [9.29]	0.71
Current study	Human vertebral (FE-full) (platens)	$12.0e^{-3}$ [-0.416]	0.88
	Human vertebral (FE-sub) (platens)	$14.0e^{-3}$ [-0.541]	0.91
	Human vertebral (exp) (platens)	$22.0e^{-3}$ [-0.041]	0.95

<sup>†</sup>Performed in tension

Table 4-4: Mean (SD) tissue elastic modulus values for human vertebral trabecular tissue

Author	Test method	Mean Tissue modulus ( $\pm$ SD) (GPa)
Riemer <i>et al</i> (1995)[67]	Four-point bending	2.11 (1.89)
Rho <i>et al</i> (1997)[55]	Nanoindentation	13.4 (2.0)
Hou <i>et al</i> (1998)[72]	FEA	5.7 (1.6)
Ladd <i>et al</i> (1998)[74]	FEA	6.6 (1.0)
Homminga <i>et al</i> (2002)[140]	FEA	10.6 (1.4) <i>Control</i> 10.1 (1.8) <i>Fracture case</i>
Bevill <i>et al</i> (2008) [125]	FEA	10
Busse <i>et al</i> (2009)[66]	Three-point bending	2.16 (0.53) <i>Normal</i> 1.20 (0.55) <i>Osteoporotic</i>

Ladd *et al* used a similar population of specimens to this study (BV/TV: 0.083 vs 0.09; average ( $\pm$ SD) age: 69.6 (8.6) vs 70 (11)) [74]. Still, they reported an average apparent modulus almost double that reported for the present study (102.4 Vs 63.5 MPa). Since the tissue modulus is directly derived from the experimental apparent modulus, a difference of 50% would be expected to result in a similar difference in tissue modulus, as reported herein.

A number of studies have investigated the tissue level effects of osteoporosis. Earlier studies reported no difference between healthy and osteoporotic tissue material properties [140, 189]; however more recent studies suggest that a significant reduction in both elastic modulus and strength occurs in osteoporotic bone tissue [41, 66, 68, 96], which may also have contributed to the reported lower tissue modulus. Bone loss in osteoporosis is caused by increased resorption and decreased new bone formation, resulting in an overall reduction in bone mineral content. In bone structural units (BSUs), mineralisation begins with a rapid primary mineralisation followed by a secondary mineralisation phase, which is much more gradual [190]. The degree of secondary mineralisation is largely dependent on the rate of remodelling. When the remodelling rate is low, there is more time for mineralisation to proceed; in the case of osteoporosis however, where bone-turnover is increased, recently formed bone is removed before prolonged secondary mineralisation can occur. Since mineralisation contributes significantly to both stiffness and strength, the rate of bone turnover is an important factor influencing bone mechanical properties.

At the sub-microstructural level, there is thought to be no difference in the size and morphology of the hydroxyapatite crystals in osteoporotic trabecular tissue compared to healthy tissue [41, 191]. However Rubin *et al* (2005) observed there was a more random distribution of crystals in osteoporotic tissue [96]. They also reported that within the lamellae, the collagen organisations were similar between healthy and osteoporotic cases, but atypical lamellar structures and more cement lines were present in the osteoporotic cases.

At the microstructural level, Brennan *et al* (2009) measured the stiffness and hardness at three locations (core, intermediate, periphery) across the width of individual trabeculae [68]. The specimens were taken from ovariectomised and

control ovine femurs; results for both groups were consistent with previous findings that the stiffness and hardness of the trabeculae decreased from the core to the periphery. Interestingly they reported that whilst hardness was not different between groups, tissue modulus was significantly lower in the ovariectomy cases in all three locations.

Busse *et al* (2009) performed 3-point bending tests on singular trabecular spicules taken from human trans-iliac and vertebral specimens and reported a reduction in modulus in cases of osteoporosis [66]; and specimens were classed as either skeletally intact (healthy) or fracture cases (osteoporotic). Similar to Rubin *et al* (2005), backscattered images showed increased disorganisation in the lamellae arrangement in the fracture cases. The atypical lamellae arrangement is most likely due to additional bone remodelling in the osteoporotic cases, and the formation of several cement lines and trabeculae packets. Busse *et al* found the cement lines contained a higher mineral content, which may explain the observed increase calcium content in this and other studies in osteoporotic bone [66, 94]. Their results, however, showed that despite higher calcium content in the osteoporotic cases, mineralisation was more heterogeneous and tissue material properties were lower. These results appear to allude to the fact that osteoporosis can no longer be seen as a purely structural disease and that there are alterations at both the microstructural and sub-microstructural levels that do in fact impair tissue level material properties.

Finally it is also important to note the large intra-specimen variation in tissue modulus. It has been shown that intra-specimen coefficient of variation of the elastic modulus, measured by nanoindentation, can range from 8% [82] to 63% [70] in human femoral trabecular tissue. Since bone turnover is higher in osteoporosis, it is reasonable to assume that this variation may be even larger in osteoporotic trabecular tissue.

The last aim of the study was to elucidate whether the use of a sub-volume was appropriate for low density osteoporotic bone. To reduce the complexity of micro-FE models it is common practice to select a sub-region for analysis [75, 123, 126, 155, 186, 192]. To ensure that this was appropriate for use in low-density bone where the structure is less uniform, FE analyses were conducted on both full- and sub-volume models. The sub-volumes were chosen to ensure the dimensions were equal to at

least five inter-trabecular lengths [49] and that BV/TV of the sub- and full-models were within 5%. Results show that when this criterion is used, the sub-volume is morphologically an accurate representation of the full-volume (Table 4-2). The largest difference was seen in trabecular spacing, which was on average lower in the sub-volume group; however this was not significant. No statistical difference between FE calculated apparent and tissue moduli was observed for the sub- and full volume models. Differences in apparent modulus between full- and sub-volume models can range from 20 to 43% in low density bone [126] however in the present study the average (SD) difference in apparent modulus was 8.28% (4.92). This error may, however, be larger in nonlinear analyses. Regardless, this along with the morphological data suggests that the sub-volume is an adequate surrogate even in low density osteoporotic bone, where the structure can be highly non-uniform. Due to the heterogeneous structure it was difficult to match the BV/TV of the sub-volumes for the full-model in some cases; however a larger difference in BV/TV did not necessarily translate to a larger difference in apparent modulus.

In summary, the established method found strong correlations between  $E_{App}^{Exp}$  and  $E_{App}^{FE}$ , indicating trabecular tissue is well described by a homogeneous isotropic tissue modulus. At the tissue level the effects of osteoporosis remain in dispute; mineral heterogeneity results in intra-specimen variations in tissue modulus that may influence mechanical properties at both the microstructural and apparent level [141, 185]. If the end cap method cannot be used in the experimental work, using an established global tissue value rather than specimen specific value may offer better results. The errors reported in this study highlight the importance of vigilance during experimental testing for validation of FE models.

Nonetheless, when appropriate material properties are used, the FE models constructed appear to be adequate surrogates for estimating apparent level biomechanics of trabecular bone. The models' ability to estimate strength suggests they are "as good as" current experimental methods that predict strength from an experimentally determined modulus. The use of a sub-region appears valid for linear models.

These data, however, looked only at the case of uniaxial loading along the principal axis. An FE model assessing torsional loading (as will be the case with screw tightening) will involve localised loading conditions that are not as trivial as uniaxial loading. It is therefore necessary to assess whether a homogeneous tissue modulus is adequate for simulating off-axis loading conditions. Additionally, in some cases, it is not possible to derive a tissue modulus directly from the specimen under investigation. In such a case it would be necessary to apply a non-specific tissue modulus reported in the literature for the anatomic location of interest. However it may be possible to derive tissue properties from an adjacently located trabecular specimen, which may provide more accurate results. The following chapter investigates these issues.

# **5 TESTING THE ASSUMPTION OF ISOTROPY FOR CANCELLOUS BONE TISSUE ELASTIC MODULUS**

## 5.1 Introduction

As discussed in the previous chapters, the material properties of trabecular bone at the tissue-level are not well understood, primarily due to the difficulty in testing specimens at such a small scale, as well as trabecular tissue's inherent heterogeneity. micro-FEA is now an established method for indirect determination of an average tissue-level Young's modulus. However, this method relies on accurate experimental measurements, since the scaling factor for the tissue modulus is derived from experimental data.

Several areas have been identified as potential sources of error in experimental data obtained from compression testing of excised specimens of trabecular bone including, but not limited to, specimen size, shape and test protocol [145-150, 154]. To minimise the effects of “*end-artefact*”, the use of end-caps has replaced the standard platens test as the gold standard method for determining apparent Young's modulus from uniaxial compression tests [54]. However some test methods restrict the use of end-caps. For example, the case of modelling the insertion of a screw into the femoral head ideally would utilise the entire head, to replicate real-life interactions of the bone and screw. However the ability to use a specimen-specific modulus in the model would produce the most accurate macro-mechanical behaviour of the bone-implant construct [58]. In such a case, the selection of tissue modulus would need to be taken from the literature.

Current micro-FE models of cancellous bone assume an isotropic tissue modulus. Cortical bone is known to exhibit at least orthotropic elastic properties [193] and it has been suggested that trabecular tissue is anisotropic at both the apparent and tissue levels [194]. However, most micro-FE models, assume the tissue level properties to be isotropic [77, 78, 83, 114, 123, 124, 129, 138]. If trabecular tissue does possess a directional dependence at the material level, the isotropic assumption may affect apparent behaviour during simulations of off-axis loading. Using micro-FE analysis, Van Rietbergen *et al* (1997) demonstrated that the effective tissue modulus ( $E_{\text{Tiss-eff}}$ ) is capable of predicting apparent stiffness in each orthogonal plane [131], which implies the mechanical anisotropy observed at the apparent level is primarily determined by the structural anisotropy of the trabeculae within the excised specimen and the assumption of an isotropic tissue modulus is valid. van Rietbergen's study,

however, was conducted in high-density human tibial bone specimens, and the results may be different in lower density bone specimens where material properties may play a more significant role.

To investigate the effects of off-axis loading, specimens from the vertebra are well suited. The spinal column and vertebra are subjected primarily to axial loading; consequently the principal material coordinate system tends to be closely aligned with anatomic supero-inferior (SI), antero-posterior (AP) and medio-lateral (ML) directions. Additionally, the trabecular structure of the vertebra comprises thick vertical columns and thinner horizontal struts ranging from 200  $\mu\text{m}$  to 220  $\mu\text{m}$  and 90  $\mu\text{m}$  to 180  $\mu\text{m}$  respectively, depending on age [195]. With ageing and the onset of bone diseases such as osteoporosis, there is a significant degradation in the trabecular architecture associated with an increase in structural and mechanical anisotropy. In general the transverse trabeculae tend to become even thinner and fewer in number, while the longitudinal struts remain virtually unchanged [111, 195, 196]. Accordingly, the tissue modulus determined from supero-inferior (SI) loaded specimens could be viewed as reflective of the longitudinal trabecular tissue modulus, whereas tissue moduli values determined from antero-posterior (AP) loaded specimens would be more reflective of the transverse tissue modulus.

Thus the main aims of this chapter were to explore anisotropy with respect to effective tissue moduli derived from micro-FE models. Understanding differences in micro-mechanical behaviour under different loading conditions in low-density bone could provide insight into the factors that initiate macro-mechanical yield and fracture susceptibility. Therefore a secondary goal was to gain an understanding of tissue strain distributions in vertebral trabecular bone under both on-axis and transverse loading.

## 5.2 Aims

The overall goals were achieved by addressing the following research questions:

- 1) Is the effective tissue modulus derived by indirect determination from micro-FE models dependent on loading mode in low density trabecular bone?
- 2) Is there a difference in the trabecular tissue strain distributions under SI vs AP loading?

## 5.3 Methods

Vertebral cancellous bone specimen pairs (n=2 female, n= 8 male) from a previous study were analysed [171]. Specimens were taken from any of the T12, L1, L4 or L5 levels (Table 5-1). The orientation of the specimens was controlled using micro-CT to ensure that the principal orientation was aligned with the axis of the specimens. One specimen from each pair was randomly assigned to either supero-inferior (SI) or antero-posterior (AP) mechanical testing groups using a random selection process. Since cube pairs were collected from adjacent vertebral bodies, once one of the pair was assigned to the SI group, the adjacent cube was automatically assigned to the AP group. All specimens were mechanically tested to 10% apparent strain by uniaxial compression in the direction to which they were assigned (Figure 5-1). Further information regarding the experimental methods can be found at Badiei *et al* (2007) [171].

For the SI group, the specimens analysed in chapter 0 were used; two specimens however were not included, one specimen was disregarded because an adjacent specimen pair was not available for analysis, the second specimen was not included because a sub-volume model representative of the full-volume could not be obtained. This resulted in a total of 10 specimen pairs. The experimental data for the AP group was analysed according to the method set out in chapter 0.

Prior to mechanical testing, all specimens were scanned at an isotropic resolution of 15.6  $\mu\text{m}$  in a micro-CT scanner (Skyscan 1072, Antwerp, Belgium). For the FE modelling, image data was coarsened to 40  $\mu\text{m}$  [137, 138] and the architecture was quantified using standard micro-CT software provided with the scanner (CTAn, Skyscan, Antwerp, Belgium).

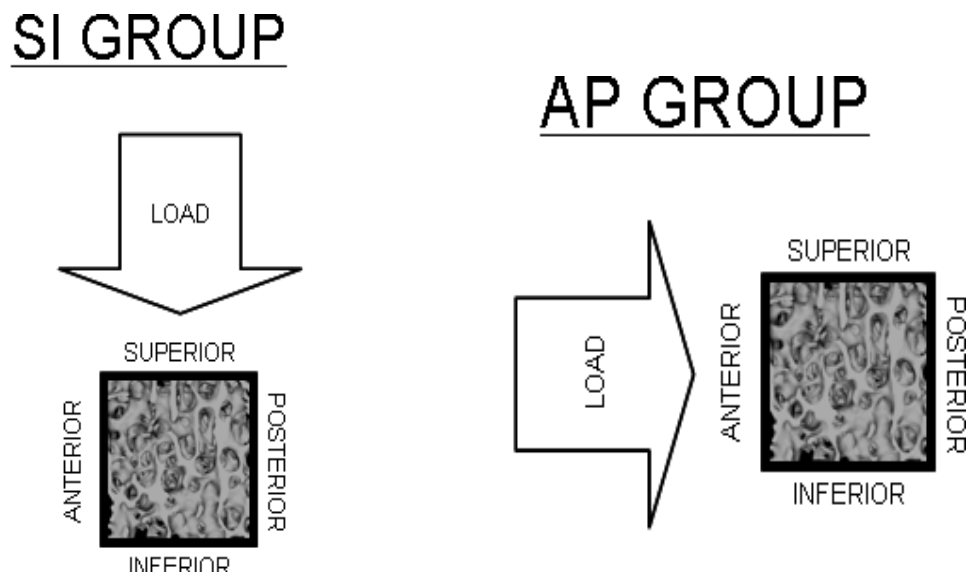


**Figure 5-1: Schematic illustrating loading conditions for the vertebral specimens in either the supero-inerior (SI) or anteroposterior (AP) group[171]. (Reproduced with permission).**

Table 5-1: Specimen pairs indicating vertebral level each specimen was taken from and BV/TV . Values listed are of both the full-volume of the cube and the sub-volume used in the FE analysis.

Specimen Pair	Supero-inferior (SI)			Antero-posterior (AP)		
	Vertebral level	Specimen BV/TV (full)	Specimen BV/TV (sub)	Vertebral level	Specimen BV/TV (full)	Specimen BV/TV (sub)
1	L5	0.0879	0.0846	L4	0.0752	0.0753
2	T12	0.0795	0.0791	L1	0.0733	0.0755
3	T12	0.0897	0.0866	L1	0.087	0.0901
4	L5	0.1095	0.1097	L4	0.0877	0.0879
5	L1	0.0959	0.0952	T12	0.0822	0.084
6	T12	0.1108	0.1078	L1	0.1048	0.1097
7	L4	0.089	0.0864	L5	0.0915	0.0918
8	L4	0.0717	0.0748	L5	0.1077	0.1041
9	L1	0.0938	0.091	T12	0.1124	0.1156
10	L4	0.0744	0.0735	L5	0.081	0.082

### 5.3.1 FE Analysis

Chapter 3 demonstrated no difference in apparent modulus between the full and 6mm models, for a given tissue modulus. A cube of these dimensions is large enough to satisfy continuum criteria [49] and consequently 6mm sub-volumes were used for all analyses. The sub-volumes were selected such that the bone volume fraction (BV/TV) matched BV/TV of the full volumes within  $\pm 5\%$  (Table 5-1).

The specimen specific tissue moduli calculated in chapter 3 were used for the SI group. Specimen specific tissue moduli were calculated for the AP group following the same method, however loading was oriented in the AP direction. Element material properties were assumed to be linear, homogeneous and isotropic. A Young's modulus of 5GPa [72] and Poisson's ratio of 0.3 were assumed for all elements. A compressive displacement boundary condition was applied to all nodes on the anterior face equivalent to 0.2% apparent strain. All nodes on the posterior face were fully constrained in all directions. Models were implemented using the preconditioned conjugate (PCG) iterative solver, with geometric non-linearity and the memory save option switched on to employ the EBE approach [197]. Following the same methods as described in chapter 3; the AP effective tissue modulus ( $E_{Tiss}$ ) was calculated by scaling the FE apparent modulus to match the experimental apparent modulus ( $E_{App}^{Exp}$ ).

To elucidate the ability of the tissue modulus derived from one adjacent vertebra to simulate apparent behaviour in an adjacent vertebra, the effective tissue modulus derived from the SI group (SI- $E_{Tiss}$ ) was assigned to its adjacent pair and the FE simulation was repeated. Apparent modulus (AP- $E_{App}^{FEA}$ ) using this tissue modulus was then calculated from the reaction forces and applied displacements.

The SI and AP models were then loaded in 0.5 % increments until the applied strain exceeded the experimental apparent yield strain, using the specimen-specific tissue moduli derived from their respective loading condition. Tissue stresses and strains were evaluated at each interval of 0.5 % strain. At each incremental strain level, the volume of yielded tissue in both tension and compression was evaluated. The volume of yielded tissue at apparent yield was extrapolated for each specimen by fitting a third order polynomial to the incremental FE data. A third order polynomial was chosen, because it provided the best fit for the FE output (Figure 5-2). Elements were

considered yielded if the principal strains exceeded either -0.69 % or 0.33 % for compression and tension respectively [125]. If both levels were exceeded, the largest magnitude was used to define whether the element was in tension or compression.

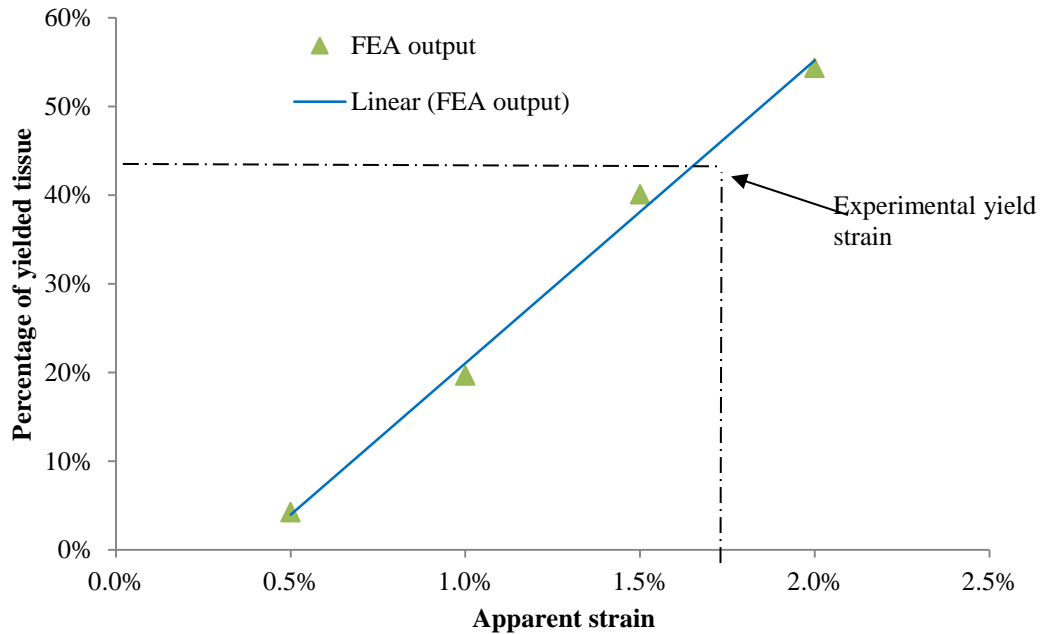


**Figure 5-2: Determination of percentage of total tissue yielded for one of the SI specimens. The percentage of total tissue yielded at experimental yield strain was extrapolated from the fitted linear curve.**

### 5.3.2 Statistical Analysis

All statistical analyses were performed using the SPSS statistical package (version 18.0; SPSS, Inc., Chicago, IL). All reported p-values are two-tailed, with  $p < 0.05$  considered statistically significant. Shapiro-Wilk tests ( $p > 0.05$ ) were used to check data was normally distributed. Based on the tests for normality, linear regression and paired t-tests were used to compare results between the two groups.

### 5.3.3 Results

The morphology of the trabecular architecture was not statistically different between specimen pairs (Table 5-2). Paired t-tests found apparent experimental yield strain was significantly higher for the AP group compared to the SI group ( $p=0.006$ ). Mean (SD) apparent yield strains were 1.9 % (0.18) and 2.94 % (1.1) for the SI and AP groups respectively. There was also significantly less variability in the yield strain data for the SI group compared to the AP group (coefficient of variance (COV) = 0.10 vs 0.37). Apparent yield stress and ultimate strength were both significantly higher for the SI group (average yield stress: 1.22 MPa, SD: 0.51; average ultimate strength: 1.4 MPa, SD: 0.59) compared to the AP group (average yield stress: 0.22 MPa, SD: 0.14; average ultimate strength: 0.30 MPa, SD: 0.12)

Table 5-2: Average morphological parameters for SI and AP groups

Parameters <sup>a</sup>	SI Mean (SD)	SI Range	AP Mean (SD)	AP Range	p- value
BV/TV	0.091 (0.012)	0.075 – 0.11	0.09 (0.014)	0.08 - 0.12	0.75
TbTh ( $\mu\text{m}$ )	168.7 (17.7)	148.3 – 210.8	174.3 (28.3)	147.0 – 242.8	0.62
TbN (/mm)	0.541 (0.067)	0.445 – 0.667	0.523 (0.073)	0.435 – 0.647	0.81
TbSp ( $\mu\text{m}$ )	999.8 (90.8)	880.0 – 1126.5	994.3 (80.3)	878.9 – 1142.3	0.67
TbPf (/mm)	5.51 (1.0)	4.44 – 7.20	5.82 (1.15)	3.96 – 7.77	0.64
SMI	1.68 (0.23)	1.41 – 2.07	1.77 (0.29)	1.40 – 2.17	0.55
DA	0.572 (0.06)	0.455-0.649	0.549 (0.05)	0.447 – 0.614	0.28

### 5.3.4 FEA

The average ( $\pm$  SD) axial tissue modulus calculated from the SI group was 2.32GPa (0.38), which is at the lower end of the reported range for vertebral trabecular tissue of 1.2 to 13.4GPa (Table 4-4). Student's t-tests revealed the average transverse tissue modulus calculated from the AP group was not significantly different ( $p = 0.18$ ), but had a greater variance, with an average (SD) of 2.17GPa (0.77).

As reported in Chapter 0, using a general tissue modulus of 5GPa resulted in a strong coefficient of determination for the linear regression of the FE calculated SI apparent modulus ( $SI-E_{App}^{FEA}$ ) and the experimentally determined SI apparent modulus ( $SI-E_{App}^{Exp}$ ) ( $R^2 = 0.90$ ,  $p < 0.001$ ). For the AP group, using the same tissue modulus, linear regression between the FE calculated apparent modulus ( $AP-E_{App}^{FE}$ ) and the experimentally determined apparent modulus ( $AP-E_{App}^{Exp}$ ); revealed only a weak coefficient of determination ( $R^2 = 0.26$ ), which was not statistically significant ( $p = 0.13$ ). For both groups an initial tissue modulus of 5GPa resulted in an overestimation of apparent modulus. A strong coefficient of determination was also observed between  $SI-E_{App}^{FE}$  and experimental SI ultimate strength ( $R^2 = 0.96$ ,  $p < 0.001$ ); however for the AP loading condition, only a weak coefficient of determination was found between the  $AP-E_{App}^{FE}$  and experimental ultimate failure strength (UFS) and this was only approaching statistical significance ( $R^2 = 0.35$ ,  $p = 0.07$ ).

When the tissue modulus derived in the SI direction from each adjacent pair was used, only a weak coefficient of determination was observed between  $AP-E_{App}^{FE}$  and  $SI-E_{App}^{FE}$ , and this was only approaching significance ( $R^2 = 0.33$ ,  $p = 0.086$ ). Linear regression between  $AP-E_{App}^{FE}$  and the ultimate apparent AP strength revealed a moderate coefficient of determination ( $R^2 = 0.6$ ,  $p < 0.001$ ).

Using the tissue modulus derived from an adjacent vertebra produced coefficients of determination between  $E_{App}^{FE}$  and  $E_{App}^{Exp}$  and ultimate strength that were similar for both groups. For apparent modulus the coefficient of determination was 0.33 for both groups, however it was larger for ultimate strength for the A-P group compared to the SI group (0.6 vs 0.35, Table 5-3). Coefficient of determination for  $E_{Tiss-eff}$  and apparent mechanical properties are also presented in Table 5-3.  $E_{Tiss-eff}$  was

significantly correlated with UFS for the SI group ( $R^2=0.55$ ,  $p=0.01$ ), but not for the AP group.

Table 5-3: Linear regression results (coefficient of determination,  $R^2$  (p-value)) of FE predicted apparent modulus and effective tissue modulus with experimental mechanical properties (n=10).

	Mechanical				Tissue	
	SI- $E_{App}^{FE}$ ( $E_{Tiss} =$ 5GPa)	AP- $E_{App}^{FE}$ ( $E_{Tiss} =$ 5GPa)	SI- $E_{App}^{FE}$ ( $E_{Tiss} =$ SI- $E_{Tiss}$ )	AP- $E_{App}^{FE}$ ( $E_{Tiss} =$ AP- $E_{Tiss}$ )	SI- $E_{Tiss}$	AP- $E_{Tiss}$
SI- $E_{App}^{Exp}$	0.90 ( $<0.001$ )	0.07 (0.46)	0.33 (0.09)	0.33 (0.08)	0.64 <sup>‡</sup> ( $<0.01$ )	-0.02 (0.73)
SI- $\sigma_{Ult}$	0.91 ( $<0.001$ )	0.10 (0.38)	0.35 (0.07)	0.37 (0.06)	0.55 (0.01)	-0.01 (0.80)
AP- $E_{App}^{Exp}$	0.012 (0.72)	0.26 (0.13)	0.40 (0.05)	0.33 (0.09)	0.001 (0.93)	0.48 (0.03)
AP- $\sigma_{Ult}$	0.32 (0.09)	0.35 (0.07)	0.37 (0.06)	0.60 ( $<0.01$ )	0.61 (0.25)	0.10 (0.37)

### 5.3.5 Micromechanical Behaviour

Significantly more tissue yielded at each strain increment when specimens were loaded in the SI direction, compared to the AP direction (Figure 5-3). At experimental apparent yield strain, on average 52% of the hard tissue had yielded for the SI group, compared to only 21% for the AP group ( $p < 0.001$ ), this was despite the higher average apparent yield strain for the AP group. The micromechanical yield behaviour was also distinctly different between the two groups. For the SI group, tissue yielding was predominantly tensile at the first strain increment, but following this significantly more tissue yielded in compression compared to tension for all strain increments from 1.0% onwards (Figure 5-3). In contrast, the AP group experienced approximately equal amounts of tensile and compressive tissue yielding at all strain increments (Figure 5-3).

At each strain increment, the average tensile and compressive tissue strains were significantly higher for the group loaded in the SI direction compared to those loaded in the AP direction (Figure 5-4). However the maximum tensile and compressive tissue strains were not found to be significantly different for the two groups, at each strain increment.

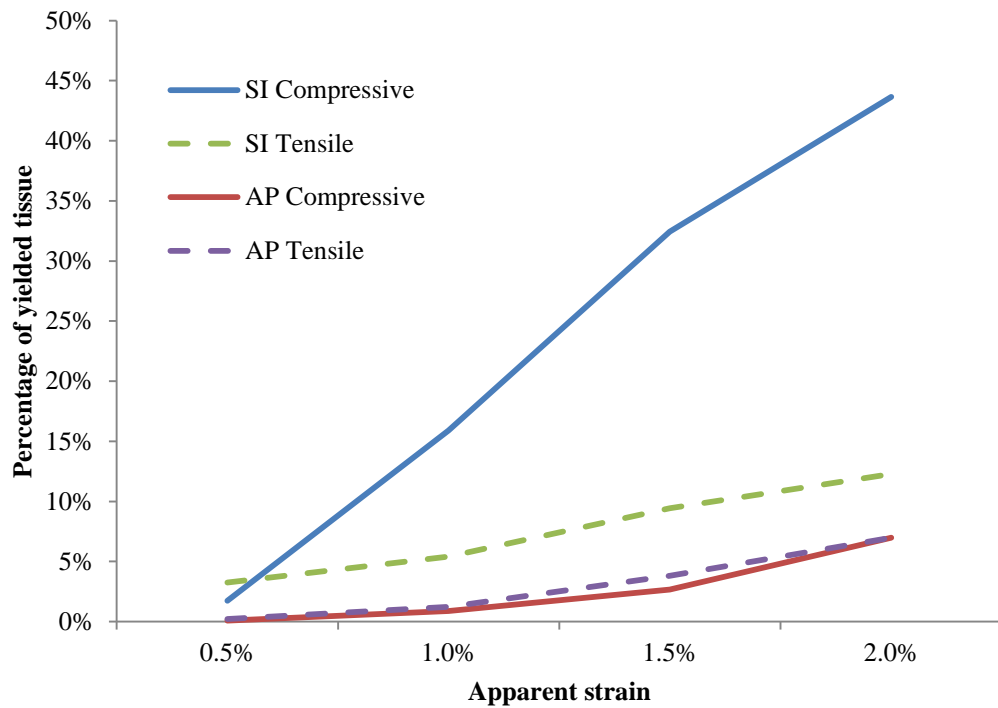


**Figure 5-3: Percentage of tissue yielded in compression and tension at apparent strain increments from 0.5 to 2.0 %. Specimens (n=10) were loaded in compression in the supero-inferior direction under quasi-static loading conditions.**

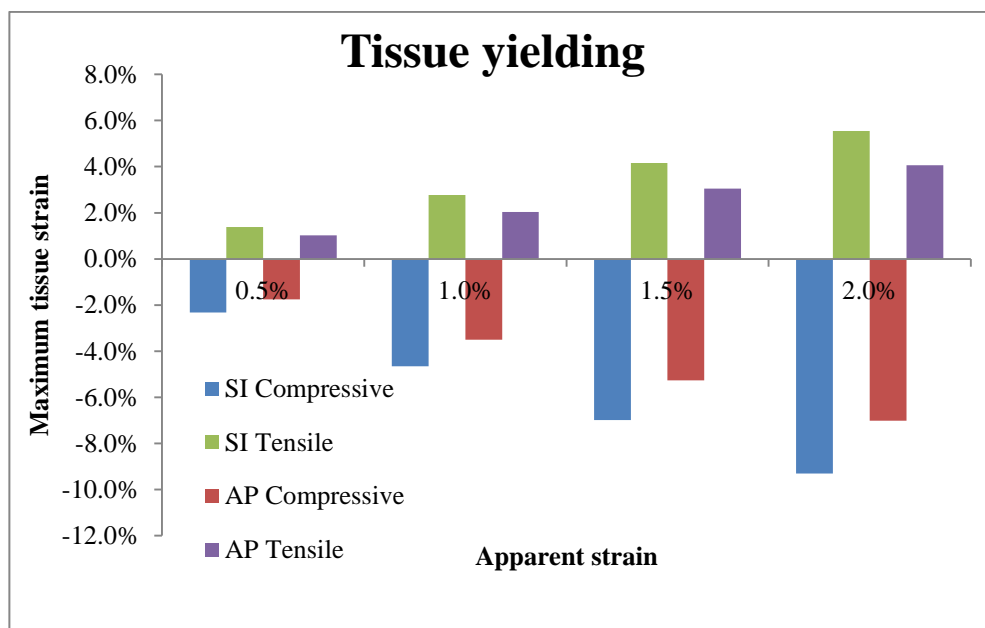


**Figure 5-4: Maximum compressive and tensile tissue strains at each strain increment up to 2.0% apparent strain for vertebral specimens loaded in either the SI or AP directions.**

## 5.4 Discussion

The main aim of this study was to elucidate whether the effective tissue modulus derived from micro-FE models of trabecular bone specimens was dependent on loading direction. To explore this, effective tissue moduli values were derived for adjacent vertebral pairs loaded in either the AP or SI directions. FE analyses revealed that although the tissue moduli values were significantly lower than more recent reported tissue moduli values for cancellous bone tissue [72, 74, 125, 140]; there was no statistically significant difference between the SI and AP modulus. Van Rietbergen [194] reported that the tissue modulus is stiffest in the SI direction, and weakest in the AP direction; however the values were reported for only one specimen and therefore little can be drawn from this. The results from this study found that the average tissue modulus in the AP direction was slightly lower than the average tissue modulus in the SI direction; however this was not statistically significant. The assumption of an isotropic tissue modulus has yielded accurate results at the apparent level in both on-axis and off-axis loading conditions [124, 129]; this, along with the results from this study, indicates that the common assumption of an isotropic modulus in micro-FE models is a valid one.

For the specimens loaded in the SI direction, using a 5GPa tissue modulus resulted in  $E_{App}^{FEA}$  that was equally as good at predicting  $E_{App}^{Exp}$  as BV/TV. However for the group loaded in the AP direction, the relationships between the  $E_{App}^{FEA}$  and  $E_{App}^{Exp}$  and UFS were not statistically significant. When the tissue modulus from the adjacent vertebra was used, a statistically significant relationship was only observed between the  $E_{App}^{FEA}$  and UFS and not  $E_{App}^{Exp}$ . This relationship, however, was much weaker than that observed between BV/TV and both  $E_{App}^{Exp}$  and UFS. Since no difference was observed between the tissue moduli between adjacent specimens, it was surprising that only a moderate coefficient of determination was observed for linear regression between the experimental apparent modulus and the apparent FE modulus for the AP group, when the tissue modulus from the adjacent specimen was used. Since a general tissue modulus of 5GPa was adequate for simulating on-axis apparent behaviour, it is possible that in low-density bone, off-axis mechanics are more sensitive to variations in tissue moduli. In terms of simulating apparent behaviour, BV/TV was a much better predictor of  $E_{App}^{Exp}$  than the FE model (using

either of the tissue moduli values) for the AP group, whereas the SI model (using a 5GPa tissue modulus) was equally as good as BV/TV.

The micromechanical behaviour was distinctly different between the two groups. At each strain increment, significantly more tissue yielded in the SI group, compared to the AP group, indicating a greater portion of tissue yielding was necessary for apparent failure in the SI direction compared to AP. The average experimental yield strains (1.86% and 2.94% for the SI and AP groups respectively) are significantly higher than those reported in the literature for vertebral cancellous bone [124]. This is most likely due to the errors associated with the use of platens in the experimental testing [54].

The errors in yield strain are further evidenced when considering the volume of yielded tissue at apparent yield. At apparent experimental yield strain, on average 56.7% ( $\pm 6.5$ ) of hard tissue yielded for the SI load case compared to 36.1% ( $\pm 9.1$ ) for the AP load case. These volumes are significantly larger than values reported by others. At apparent yield Niebur *et al* (2002) reported on average 13% of hard tissue yielded in bovine tibial specimens for on-axis loading, while only 4.2% yielded in transverse mode [129]. Bevill *et al* (2009) also found total tissue failure at apparent yield, was higher for the on-axis load case compared to off-axis, but the volumes of yielded tissue were closer to those reported by Niebur *et al* than those reported for this study; approximately 10% and 3% for on-axis and off-axis ( $45^\circ$ ) in vertebral bodies [124]. There was a similar trend for the femoral neck specimens in their study, with on-axis tissue failure significantly larger than off-axis (16 vs 4.5%). The values reported by Bevill *et al* for femoral neck are similar to those reported by Niebur *et al* for the bovine tibial specimens. Since both femoral neck and bovine tibial bone have a significantly larger BV/TV this suggests that in higher density bone more tissue needs to fail to initiate apparent yield. To investigate this, both high and low density bone could be analysed, and with the percentage of tissue failed normalised by BV/TV. There is a similar trend across all three studies, however, in that more tissue yields in on-axis loading than off-axis loading at apparent yield.

To enable a comparison with the studies by Niebur *et al* (2002) and Bevill *et al* (2009), and since apparent yield strains reported for vertebra are in the range of 0.7 [124] to 1.45% [52], the volume of yielded tissue was evaluated at the 0.5% and

1.0% apparent strain increments for the SI load case and 1.0% and 1.5% for the AP load case. Several investigators have demonstrated that apparent yield strains are isotropic for compressive, tensile and torsional loading of on-axis, transverse and off-axis specimens in high density bone [123, 198, 199]. However work in low-density human vertebral bone, where the structure is distinctly less homogeneous and more rod-like than plate-like and there is relative conservation of stiffness in the axial direction compared with the transverse directions [200], it has been reported that an anisotropy of failure strains may exist [124, 201]. Experimentally, higher yield strains were observed for the AP load case compared to the SI load case; consequently, the slightly higher strain range was chosen for the AP load case.

Over the 0.5 to 1.0% apparent strain increment, the quantity of yielded tissue increased from 5.0% to 21.3% for the SI group, which is consistent with the values reported by Niebur *et al* (2002) and Bevill *et al* (2009). For the AP group, the average volume of yielded tissue increased from 0.2% to 6.5%, over the strain increment from 1.0% to 1.5%. This is also consistent with previously reported values [124, 129]. At each strain increment, significantly more tissue yielded in the SI load case (Figure 5-3), which is in agreement with previous observations [124, 129, 202].

The tissue yield behaviour was also distinctively different between the loading directions. Significantly more tissue yielded in compression than tension at each strain level, after the 0.5% strain increment for the SI load case. For the AP group, however, there was no statistical difference between the volume of tissue that yielded in tension or compression at each strain increment. Niebur *et al* (2000), showed a similar trend [203]; the transverse behaviour is similar, with tensile yielding only slightly higher; however the on-axis behaviour is distinctly different from the SI behaviour in this study. In the high density bovine bone, compressive yield was dominant at lower strains, but nearly equal amounts of tissue exceeded tensile and compressive yield limits at apparent yield point. Bevill *et al* (2009) reported the ratio of tissue failure in tension versus compression tended to increase with off-axis loading and increasing BV/TV [124]. This demonstrates that with low BV/TV, compression is the dominant tissue failure mode under on-axis loading, indicative of crushing failure as opposed to buckling. This is in contrast to the off-axis loading cases, where tensile and compressive loading approached similar volumes, which is

similar to the results reported in this study. Similarly, Shi *et al* (2009) reported significantly more hard tissue regions underwent compressive yielding than tensile at all apparent strain levels under on-axis loading; but during transverse loading, approximately equal amounts of tissue yielded due to tensile and compressive loading [204]. The difference in tensile and compressive tissue failure under on-axis loading was not as marked as in our study; however their study was performed in bovine tibial specimens.

The reasons behind the tissue failure asymmetry are best understood by considering the underlying architecture of the vertebra. Figure 5-5 illustrates the typical failure that occurred in each load case. For the SI load case, vertical columns failed principally in compression, with a scattering of tensile stresses seen through the transverse rods. As can be seen from the same figure, the vertical columns are much thicker, whereas the transverse reinforcing rods are thinner. This is in keeping with previous findings that a highly significant decrease in average thickness of the horizontal trabeculae occurs with age, but no change in average thickness of the vertical trabeculae [195].

The pattern of failure is distinctly different for the group loaded in the AP direction. The thicker vertical columns contain similar volumes of tissue yielded in tension and compression; indicating that for AP loading, significant bending occurs. Under off-axis loading, Bevill *et al* (2009) found that the specimens tended to have less total tissue failure and increased failure in the horizontal trabeculae [124], which is similar to these results. The off-axis loading in Bevill's study, however, was applied at 15 and 45° from the longitudinal axis and not 90° as in our case. Off-axis loading may result in different types of tissue failure, as we observed combination of tensile and compressive forces in both horizontal and vertical struts indicative of bending, for the AP load case, whereas in the SI case, the vertical struts were subjected almost purely to compression, suggesting buckling as the failure mode.

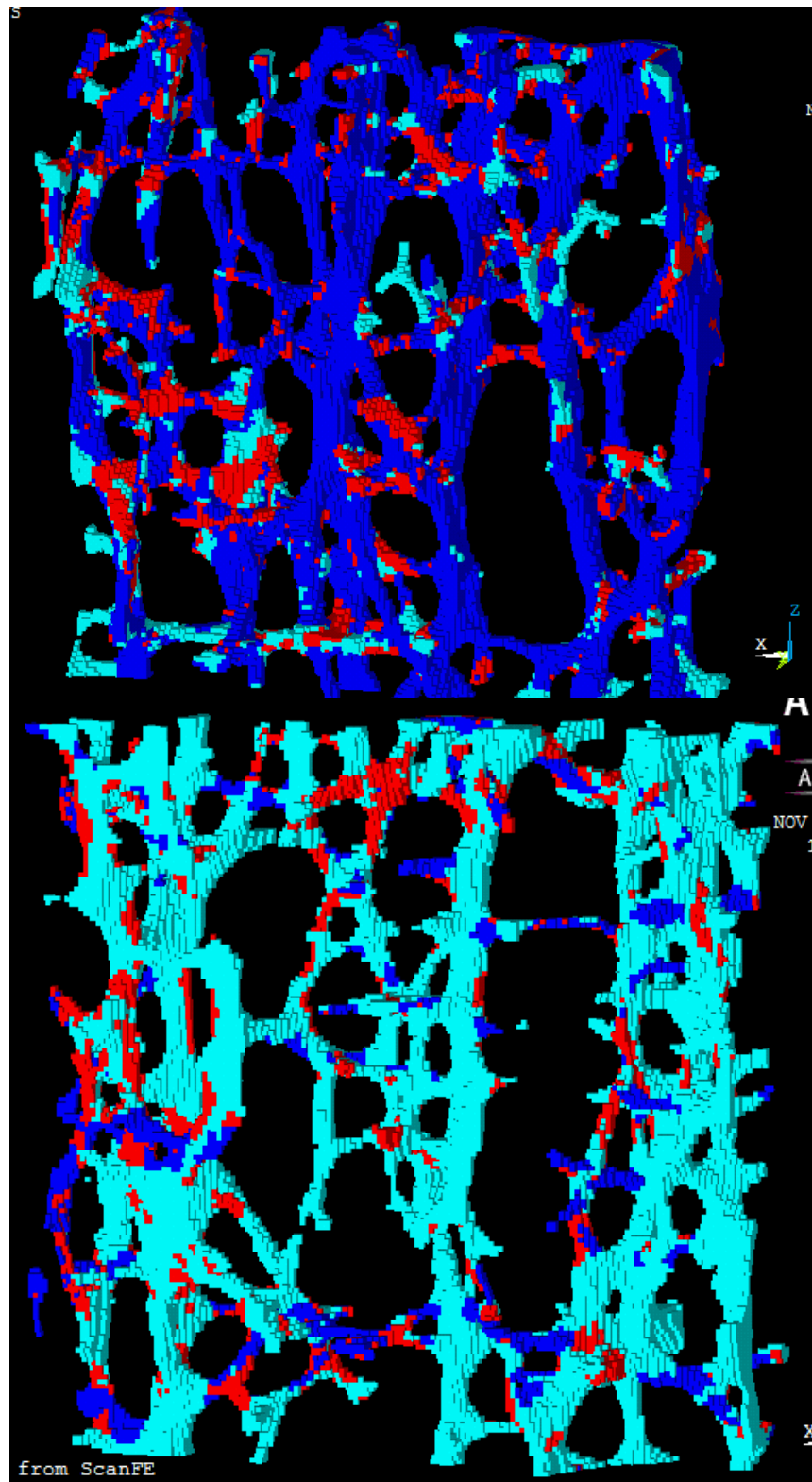


**Figure 5-5: 3D renderings of bone slices taken from a 60 year old female specimen. The slices were taken from the L5 vertebra (top) and loaded in the SI direction to 2.0% apparent strain; and from the L4 vertebra (bottom) and loaded in the AP direction to 5.5% apparent strain. Red regions indicate tissue yielded in tension, blue regions indicate tissue yielded in compression. The specimens are oriented anatomically so that the slice is viewed anteriorly and the most superior region of bone is located at the top.**

Local failure mechanisms are strongly governed by the micro-architecture. From a mechanics point of view, buckling is defined as an instability of equilibrium in structures that occurs from compressive loads or stresses [174]. The critical load that will cause a pinned column to buckle is dependent on the unsupported length of the column:

$$P_{crit} = \frac{\pi^2 EI}{L^2} \quad \text{Equation 5-1}$$

Where  $P_{crit}$  is the maximum axial load on the column just before buckling,  $E$  is the modulus of elasticity for the material,  $I$  is the least moment of inertia for the column's cross-sectional area and  $L$  is the unsupported length of the column (whose ends are pinned). The transverse struts in vertebra are thinner in comparison to the vertical columns, and therefore the critical load to initiate failure is lower for the transverse struts.

It is believed that under SI loading in the vertebra, the transverse struts act as supports to prevent the vertical trabeculae from buckling [139]. The cross bracing provided by the transverse struts reduce the unsupported length of the column. From Equation 5-1, it can be seen that this would increase the maximum axial load the column could withstand.

However, in low density bone, with the age related thinning of the transverse struts and the reduced strain limit of trabecular tissue, the transverse struts cannot withstand loads as high and appear to fail first, as is evident in this study. Figure 5-3 demonstrates that tensile tissue yielding dominates at the beginning, as the thin transverse reinforcing struts fail. Once these struts fail, increased loads are transferred to the vertical columns. Given that the vertical columns are subjected to compressive failure (Figure 5-5), the most likely failure mode of these columns is either via tissue yielding due to direct compression, or by buckling. In higher density bone, with the presence of plate-like structures and an increase in the number and thickness of the transverse struts, failure has been seen to occur instantaneously, with bending and buckling not present [157]. This would explain the equal ratios of tensile and compressive tissue yielding observed by Niebur *et al* (2002) [129].

Most studies that have aimed to quantify tissue yielding and describe the micromechanical failure mechanisms have been in high density bovine bone; with few focusing on low density bone. Similar to Bevill *et al* (2009), who looked at both high and low density specimens [124], our results suggest that failure modes may be different for low density bone. The AP tissue failure behaviour was similar to that reported by others for off-axis loading conditions [129, 204], with approximately equal amounts of tissue yielding in tension and compression, despite differences in volume fractions. However, the on-axis tissue failure behaviour was different to that reported for high-density bone; but consistent with Bevil *et al* (2009) who also looked at low density bone [124].

The most important outcome from this work is highlighting the important role of the transverse struts. Micro-damage appears in the transverse struts at low apparent strains. Since most vertebral fractures have a gradual onset and are thought to be the result of normal daily loads rather than traumatic events [205], it is therefore possible that it is the cumulative and progressive damage to the transverse struts that initiates fracture. The fast deterioration and disconnection of transverse struts has been proposed as a trigger for fractures [202]. This emphasises the important role of the transverse trabeculae in not only providing transverse support, but also in preventing the longitudinal trabeculae from buckling under axial loading [206, 207]. As such, preservation of the transverse trabeculae may play a crucial role in reducing fracture risk as a consequence of ageing as well as in osteoporosis.

Finally, it is necessary to remark on the limitations of this study. An important aspect is the errors in experimental data, associated with the test methods employed. The impacts on the use of platens as opposed to end-caps are noted extensively in Chapter 4. Consequently the tissue moduli values observed are at the lower end of the scale, albeit within the range reported for vertebral cancellous bone. In terms of apparent yield, when this was corrected for, similar volumes of tissue failure were observed compared to the literature.

Furthermore, the AP and SI loading regimes were applied to adjacent specimens. It is possible that variations in tissue modulus exist between adjacent levels. It has been suggested that bone tissue properties do vary across anatomical location [125]; however there is little in the literature with regards to variations in properties across vertebra. However it is most likely that variations between adjacent vertebra would be less than variations between specimens of the same level from a range of cadavers; hence, adjacent vertebra were used.

The yield criteria applied to determine tissue yielding is also worth noting. Whilst there has been no qualitative validation of tissue level stresses between experiment and FEA, regions of high von mises stresses in FE models have been shown to correspond to regions of microdamage under loading [127]. Additionally, the implementation of constitutive models with asymmetric yield criteria based on principal strain has been shown to produce accurate predictions of apparent level yield behaviour under on-axis, off-axis and biaxial loading [129]. Consequently, the general agreement between models and experiments [124, 125, 129, 208] suggest that while exact tissue level mechanics may vary, the current assumptions are valid.

Also of note is the use of homogeneous material properties; this is despite the well-established knowledge that trabecular tissue tends to decrease in stiffness from the core outwards [68]. Trabecular tissue also tends to contain “packets” of remodelled bone, that differ in degree of mineralisation and hence stiffness depending on age, as well as regions that are unmineralised. Furthermore, it has been suggested the cement lines possess a higher calcium content [66], which would add to tissue level material heterogeneity. However such influences would be expected to affect the analysis on individual trabeculae more so than the results averaged over an entire subsection. The incorporation of material heterogeneity, however, may alter the tissue level failure mechanics. Finally, any inferences from this study need to be considered in light of the sample size; however, strong relationships were observed with high statistical significance.

Despite these limitations, this study provides important insight into the tissue-level mechanics of low-density cancellous bone. The results suggest that at the micro-structural level the assumption of an isotropic effective tissue modulus is valid; however off-axis loading may be more sensitive to variations in tissue modulus. Additionally, differences in tissue yielding under SI or AP loading conditions have been identified. This is notable, as it highlights the importance of the transverse struts in the vertebra. However it should be noted that these models only incorporated linear material properties. To further explore the tissue failure behaviour, the incorporation of non-linear material properties is necessary, which is addressed in the following chapter. The direction of screw insertion into the femoral head is aligned with the principal direction of the trabeculae; consequently the axial loading applied by the screw would mostly be in the longitudinal direction of the trabeculae and the assumption of an isotropic tissue modulus in the final FE model of the bone-screw interface would be valid.

# **6 NONLINEAR MICRO-FE MODELLING OF HUMAN VERTEBRAL BONE UNDER UNIAXIAL COMPRESSION**

## 6.1 Introduction

Linear elastic micro-FE models provide a simple and straightforward relation between stress, strain, and material properties. Fully linear models are limited however, because they cannot explicitly simulate apparent-level failure. Nonlinear models, whilst more complex, are far more descriptive of the true biomechanical behaviour.

Micro-FE models have been used to predict apparent yield properties, by incorporating both material and geometric non-linearity [71, 75, 83]. Niebur *et al* (2000) successfully predicted apparent yield properties with the implementation of an asymmetric bilinear material model for specimens under compressive, tensile and shear loading [75]. The tissue level yield properties, based on the principal yield strain criterion, were calibrated from a single specimen and then applied to the remaining specimens with outstanding comparisons to experimental data.

Based on the study by Niebur *et al* (2000), Bayraktar *et al* (2004) explicitly calibrated tissue yield criteria so that the resultant FE apparent yield behaviour matched within 0.1% of the experimental apparent yield behaviour [71]. This was conducted in both cortical and cancellous bone specimens from human femora; their results found yield strains of trabecular tissue were around 17% lower than that of cortical, with average tensile and compressive yield strains of 0.41% and 0.83% respectively.

Unlike Bayraktar [71] and Niebur [75], Verhulp *et al* (2008) implemented an isotropic elasto-plastic material model based on Hill's yield function, using cancellous bone specimens extracted from a single bovine proximal tibia [83]. Averaging their results, they reported a tissue yield strain of 3.02% and ultimate strain of 5.20%. A 2.0% yield strain was used in tension and not adjusted, as less than 10% of elements were found to be in tension and the effects of modifying tensile yield strain were found to be negligible.

The studies performed by Niebur *et al* (2000) and Verhulp *et al* (2008) were performed in bovine bone and the calibration study by Bayraktar *et al* (2004) was conducted in specimens taken from human femora, all of which are locations of high density trabecular bone. Bevil *et al* (2006) postulated that that high-density cancellous bone most likely fails by tissue level yielding, whereas the failure of low-density bone can be attributed to excessive bending or buckling [144]. A search of the literature revealed

that only one other study has implemented nonlinear micro-FE models to analyse low density vertebral bone [124]. This study by Bevill *et al* (2009) looked at the anisotropy of yield strains in both on- and off-axis loading of trabecular specimens from the femora and vertebra. Implementing specimen specific calibrated tissue moduli and strength asymmetry, with material properties dependent on anatomic location, the authors produced exceptional results with respect to the FE model's ability to predict apparent yield under both loading conditions.

Consequently, the purpose of this chapter was to replicate the work by Bevill *et al* (2009), by incorporating nonlinear material properties into the models analysed in chapter 5. Since the calibrated specimen specific effective tissue moduli determined in the previous chapters were found to be most likely affected by experimental protocols used, the study sought to compare the implementation of these specimen specific tissue moduli values, with material properties obtained from the literature. The issue that arises from this is the large range of values reported for trabecular tissue. The consensus is that the stiffness of trabecular bone tissue is lower compared to cortical bone [61, 62] but to what degree is not fully known. A review of the literature revealed substantial variation in trabecular tissue modulus values for vertebral bone (Table 4-4). However when considering only those studies that utilised FEA for determining tissue modulus, two distinct values stood out as most common. Consequently, we investigated tissue modulus values of 5GPa [72, 74] and 10GPa [125, 140] as well as the specimen specific values derived in chapter 4.

## 6.2 Aims

The specific aims of the study were as follows:

- 1) Implement nonlinear micro-FE models using three different material models, and compare the FE apparent yield properties against experimental data;
- 2) Quantify the volume of yielded tissue at apparent yield and ultimate strength.

### 6.3 Methods

Vertebral cancellous bone FE models (n=2 female, n=8 male) that were analysed in chapter 5 were modified to incorporate both material and geometric nonlinearity. Only models that were loaded in the SI direction were used. Specimens were taken from either T12 or the lumbar region. The material model used for the bone tissue was modelled using the cast iron plasticity model available in Ansys (version 12.1, Pennsylvania, USA). This material model was chosen because it uses a composite yield surface, which allows elasto-plastic behaviour with different yield strengths in tension and compression [75]. In tension, the Rankine maximum stress criterion is used; and in compression the von Mises yield criterion is implemented. The elastic behaviour is isotropic and is the same in both tension and compression.

Three analyses were run for each specimen. In an attempt to parameterise the apparent yield behaviour of trabecular tissue, Verhulp *et al* (2008) identified three parameters that influence the apparent behaviour: The effective elastic modulus controls the initial slope of the apparent stress-strain curve; the tissue yield stress controls the point at which the apparent stress-strain curve starts to deviate from a straight line; and the post-yield modulus controls the slope of the remainder of the curve. Consequently, the first model (model 1) used the specimen specific initial tissue modulus derived from the linear analyses. Since the experimental yield strains were quite high, in order to replicate the experimental stress strain curves, a yield strain of 3% in compression ( $\epsilon_y^c$ ) and 1.5% in tension ( $\epsilon_y^t$ ) were used. The second and third models used tissue properties taken from the literature; model 2 used an initial tissue modulus of 5 GPa [72, 74]; and model 3 used an initial tissue modulus of 10 GPa [124, 125, 209]. Both literature based models also incorporated a bilinear axisymmetric yield criterion, which was again implemented with the cast iron material model. For models 2 and 3, however, compressive and tensile yield strain ( $\epsilon_y^c$  and  $\epsilon_y^t$ , respectively) were taken from the literature and set to 0.69% and 0.33% [125]. The post yield modulus for all models was set to 5% of the initial tissue modulus (Figure 6-1) [75].

The cast iron plasticity model results in a sparse unsymmetric element stiffness matrix, and as such the sparse direct solver with unsymmetric storage was used. Because linear elements were used, enhanced strain formulation was implemented, which introduces 9 internal Gauss integration points and helps in preventing shear locking in bending dominated problems [210] which, it has been suggested, may produce better results for the bending expected in the trabeculae [211]. Displacement conditions equivalent to 2.0% apparent strain were applied to the top face of the specimen using roller boundary conditions, and all nodes on the bottom face were fully constrained. At such low levels of apparent strain, and in low density bone such as the vertebra, self-contact of the bone micro-structure was not considered [81]. Geometric nonlinear effects were included in the analysis [212]. The nonlinear system of equations was solved at each increment using the Newton-Raphson method [75]. All micro-FE analyses were performed with the FE package Ansys Structural (version 12.1, Pennsylvania, USA), implementing the distributed memory option. Models were solved on a 64-bit dual quad core intel Xeon with 48.0Gb RAM @ 2.66GHz.

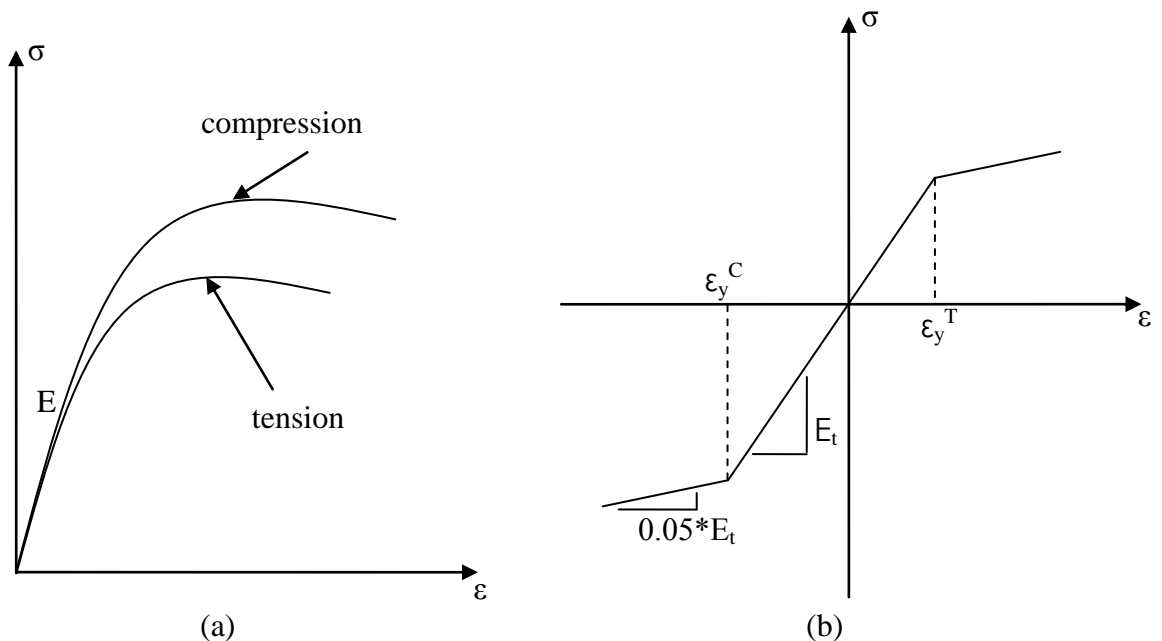


**Figure 6-1: Schematic of the idealised material model for cast-iron plasticity (a) and the bilinear material model implemented for the nonlinear FE analyses (b).  $E_t$  was set to either 5GPa or 10GPa or a specimen specific tissue modulus; axisymmetric yield strains were implemented for tension and compression. The secant modulus was set to 5% of the initial tissue modulus.**

Tissue strains were found from the incremental solutions. FE apparent modulus ( $E_{\text{App}}^{\text{FEA}}$ ) was determined from the first sub-step. At each sub-step apparent stress ( $\sigma_y$ ) was calculated from the nodal reaction forces and apparent area; stress-strain curves were then generated by interpolation of the stress data as a function of the applied apparent strain by a cubic spline. Apparent yield properties were determined by the 0.2% offset method [174], and ultimate strength ( $\sigma_{\text{Ult}}$ ) was taken as the maximum stress. Regions of tissue that had yielded due to exceeding the compressive or tensile strain limits were identified at all sub-steps. If the tissue strains were such that both limits had been exceeded, the limit that was exceeded by the greater proportion was used [204]. The percentage of bone volume yielded due to either tension or compression was extrapolated at 0.2% increments to apparent yield strain.

### 6.3.1 Statistical Analysis

All statistical analyses were performed using the SPSS statistical package (version 18.0; SPSS, Inc., Chicago, IL). All reported p-values are two-tailed, with  $p < 0.05$  considered statistically significant; strength of relationships was determined according to Cohen *et al* (1988) [175]. Shapiro-Wilk tests ( $p > 0.05$ ) were used to check data was normally distributed. Based on the tests for normality, linear regression was used to compare all FE and experimental methods, as well as comparisons between bone volume fraction (BV/TV) and tissue yielding. Student's paired t-tests were used to identify differences in compressive and tensile tissue yielding.

## 6.4 Results

The nonlinear models required between 113 and 273 iterations to converge. Convergence could not be achieved for one specimen using the specimen specific tissue modulus and so was excluded from that part of the analysis; however FE analyses using a tissue modulus of 5 and 10 GPa were included for that specimen. Therefore 9 models were generated with a specimen specific initial tissue modulus and 10 each with an initial tissue modulus of 5 and 10 GPa. The mean (SD) apparent modulus, yield strain and yield and ultimate stress for each of the models and from the experimental data are listed in Table 6-1.

Since the only difference between models 2 and 3 was the tissue modulus, the correlation coefficient for comparison of apparent modulus with  $E_{App}^{Exp}$  was equally as strong ( $R^2=0.89$ ,  $p<0.001$ ), and both produced strong linear relationships (Figure 6-2). Since the apparent modulus was used to scale the specimen specific modulus, regression analyses was not performed for apparent modulus of model 1 and experimental data.

Table 6-1: FEA results for the three different models tested. Apparent modulus was taken from the first substesp, yield data and ultimate strength was calculated from an interpolated curve. Values reported as mean (SD).

	Tissue Modulus	Apparent modulus (MPa)	Yield strain (%)	Yield stress (MPa)	Ultimate Strength (MPa)
Experimental	-	66.02 (26.43)	2.3 (0.13)	1.39 (0.58)	1.40 (0.49)
Model 1 (n=9)	Specimen specific	65.79 (24.27)	1.6 (0.25)	0.96 (0.50)	1.10 (0.55)
Model 2 (n=10)	5 GPa	131.34 (39.89)	0.73 (0.04)	0.7 (0.25)	0.84 (0.33)
Model 3 (n=10)	10 GPa	262.70 (79.78)	0.73 (0.04)	1.40 (0.49)	1.68 (0.65)

Linear regression revealed strong, positive, linear relationships between all three models and the experimental data for apparent yield stress (Figure 6-3) and ultimate strength (Figure 6-4). Model 2 underestimated apparent yield stress by almost half ( $\sigma_y^{\text{FEA}(5)} = 0.43 * \sigma_y^{\text{Exp}} + 0.11$ ,  $R^2=0.97$ ,  $p<0.001$ ), whereas models 1 and 3 were better predictors of the experimental data ( $\sigma_y^{\text{FEA}(SS)} = 0.87 * \sigma_y^{\text{Exp}} + 0.32$ ,  $R^2=0.92$ ,  $p<0.001$ ;  $\sigma_y^{\text{FEA}(10)} = 0.84 * \sigma_y^{\text{Exp}} + 0.23$ ,  $R^2=0.97$ ,  $p=0.024$ ; respectively). Similarly models 2 and 3 were better at predicting ultimate strength, whilst model 1 underestimated it by approximately 40% (Table 6-2). No statistically significant relationships were found for the yield strain data produced by any of the FE models and the experimental yield strain data.

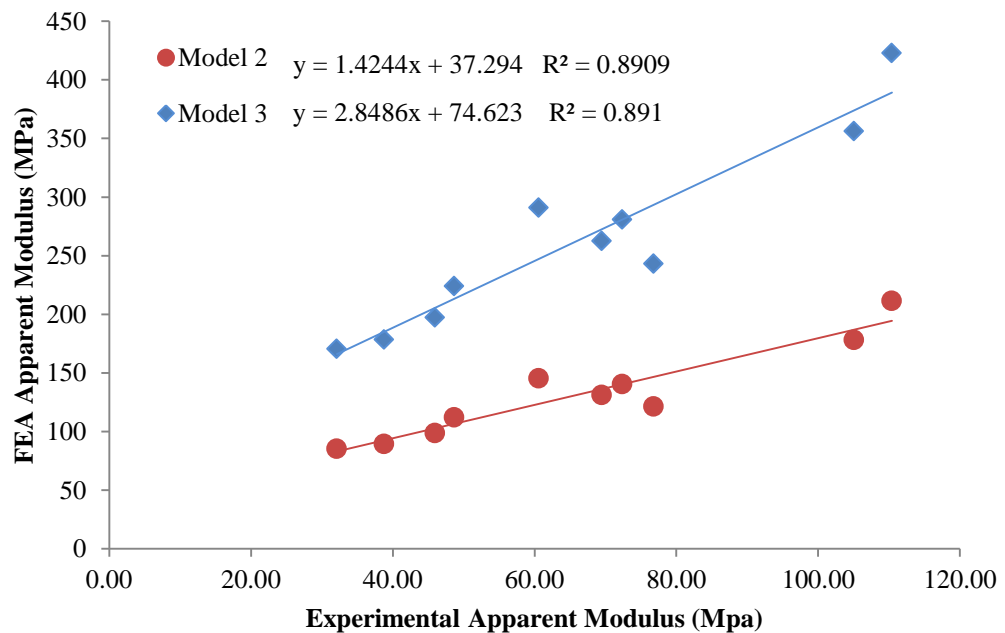


**Figure 6-2: Experimentally determined Vs FE model apparent modulus for material models 2 and 3. An initial tissue modulus of 5GPa was used for model 2 and 10GPa for model 3.**

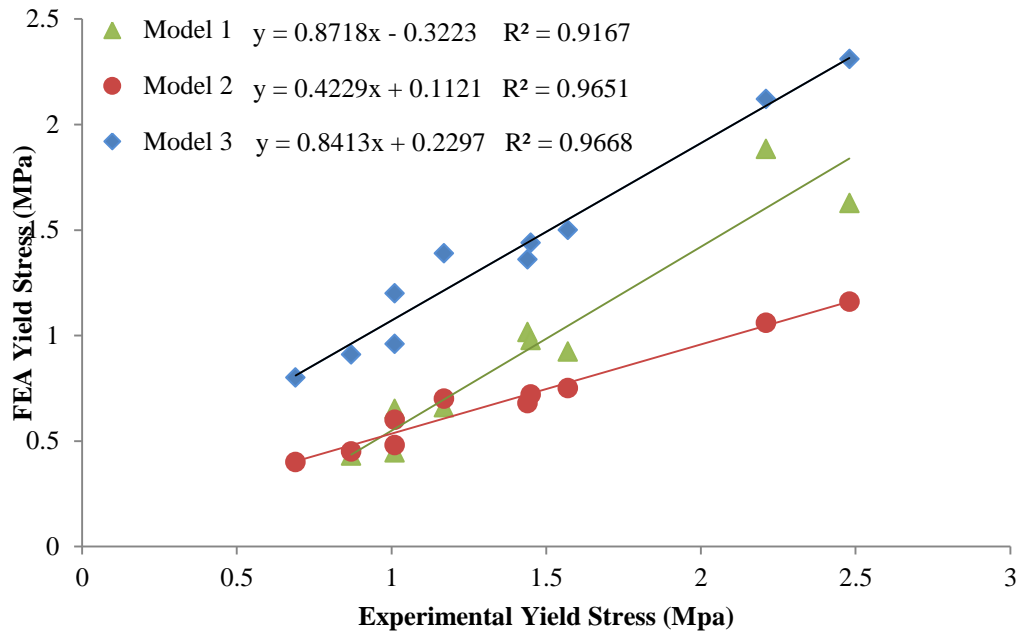


Figure 6-3: Experimentally determined Vs FE apparent yield stress for the three material models analysed. A specimen specific tissue modulus was used for model 1, 5GPa for model 2 and 10GPa for model 3

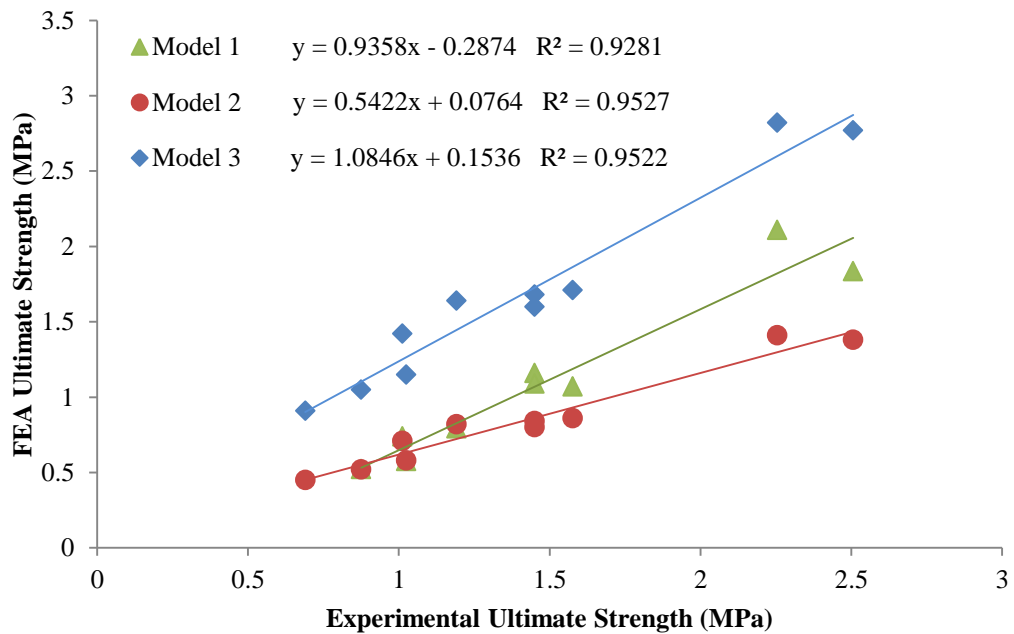


Figure 6-4: Experimentally determined Vs FE apparent ultimate strength. A specimen specific tissue modulus was used for model 1, 5GPa for model 2 and 10GPa for model 3.

Since the yield and ultimate stress data from model 3 best reflected the experimental data, only model 3 was analysed for tissue level yielding. The average apparent yield strain for model 3 was 0.72%. The percentage of yielded tissue was evaluated at six strain increments up to apparent yield and then interpolated to determine the percentage of tissue yielding at apparent strain for each individual model. On average (SD), at apparent yield strain, 2.1% (0.9) of the tissue had undergone compressive tissue yielding, whilst 1.9% (0.9) of the tissue had undergone tensile yielding; the average compressive tissue yield strains ranged from 0.20% to 0.32% (mean = 0.25, SD = 0.15), whilst the average tensile yield strains ranged from 0.11% to 0.23% (mean = 0.15, SD = 0.04). The maximum compressive tissue strains observed at yield ranged from 1.06% to 1.49% (mean = 1.27, SD = 0.15); and the maximum tensile tissue strains ranged from 0.53% to 1.11 (mean = 0.82, SD = 0.17).

Table 6-2: Linear regression relationships between the FE models and the experimental data for yield stress and UFS

	$a*\sigma_y^{Exp} + b$	$R^2$ (p-value)	$a*\sigma_{ult}^{Exp} + b$	$R^2$ (p-value)
Model 1 (n=1)	$0.8718x - 0.3223$	0.92 (p < 0.001)	$0.9358x - 0.874$	0.93 (p < 0.001)
Model 2 (n=1)	$0.4229x + 0.1121$	0.97 (p < 0.001)	$0.5422x + 0.0764$	0.95 (p < 0.001)
Model 3 (n=1)	$0.8413x + 0.2297$	0.97 (p < 0.001)	$1.0846x + 0.1536$	0.95 (p < 0.001)

Although not a primary aim, linear regression was also performed to explore any possible relationships between the percentage of yielded tissue at apparent yield and BV/TV. A strong positive linear relationship was observed between BV/TV and the percentage of tissue yielded in compression ( $R^2 = 0.83$ ,  $p < 0.001$ ) (Figure 6-5). The percentage of yielded tissue in tension, however was virtually independent of BV/TV, with a single outlier (Figure 6-6).

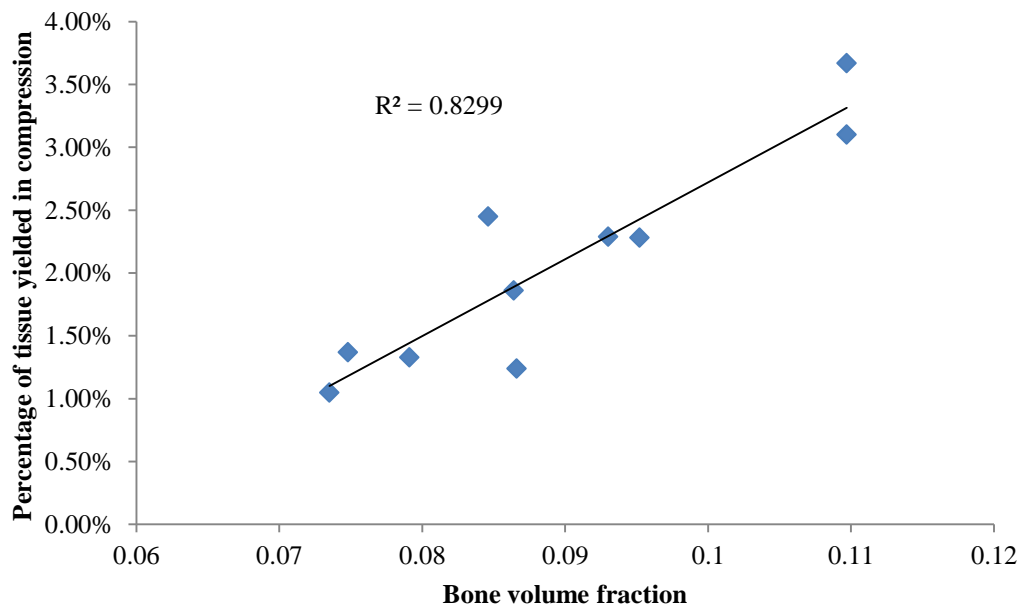


**Figure 6-5: Percentage of compressive tissue failure at apparent yield strain versus BV/TV. The model implemented material model 3, which used an initial tissue modulus of 10GPa and tissue compressive and tensile yield strains of 0.69% and 0.33%, respectively.**

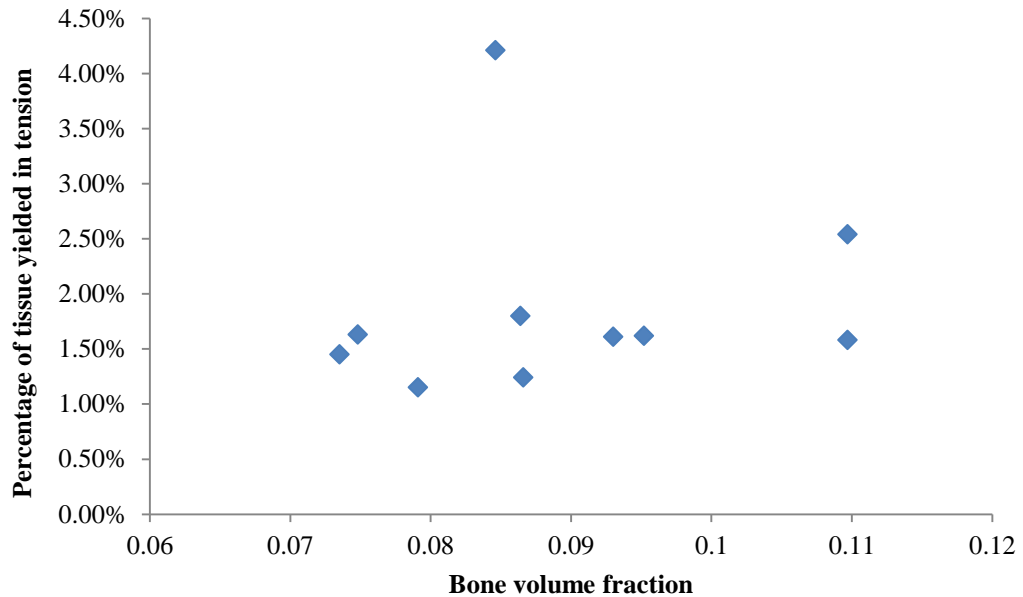


**Figure 6-6: Percentage of tensile tissue failure at apparent yield strain versus BV/TV. The model implemented material model 3, which used an initial tissue modulus of 10GPa and tissue compressive and tensile yield strains of 0.69% and 0.33%, respectively.**

## 6.5 Discussion

The main aim of this study was to implement geometrically and materially non-linear micro-FE models with material properties reported in the literature and test the validity by comparing apparent modulus and yield properties with experimental data. There is still a degree of uncertainty as to the true material properties of trabecular tissue and the values reported in the literature vary from 2 - 13GPa [55, 66, 67, 72, 74, 125, 140], consequently, three material models were implemented. None of the three models were able to simulate apparent yield strains that were related to the experimental apparent yield strains.

Verhulp *et al* (2008) identified that three basic tissue parameters control the overall apparent behaviour; tissue modulus influences apparent modulus, tissue compressive yield strain determines apparent yield, and the post-yield tissue modulus dictates apparent post-yield behaviour [83]. Since the experimental apparent yield strain averaged 2.3%, the compressive tissue yield strain was set to 3.0%, with the tensile tissue yield strain slightly lower. The models however produced an average apparent yield strain below the experimental, of 1.6%. This is still, however higher than yield

strains reported in the literature for vertebral cancellous bone [52, 213]. Since models 2 and 3 implemented the same yield criteria, the yield strains for models 1 and 2 were the same with an average of 0.73%, which is more consistent with published data (

Table 6-3).

Linear regression found no statistically significant relationship between the FE and experimental yield strains for any of the models. The FE determined yield strain was identical between models 2 and 3, which implies that the under uniaxial compression, apparent yield strain is independent of tissue modulus and solely dependent on tissue yield strain. This is consistent with Verhulp *et al*, who reported that under uniaxial compression, the effective tissue elastic modulus controls the initial slope of the apparent stress-strain curve, the tissue compressive yield strain controls point at which the curve starts to deviate from a straight line and the post yield modulus controls the slope of the remainder of the curve [83].

The fact that no statistically significant relationship could be observed between experimental and FE data yield strain data is most likely a further implication of the platens method used experimentally. It is now well-established that artifactual errors arise in the measurement of cancellous bone compressive modulus when a specimen is compressed between platens and the strains are based on the relative motion of the platens [146-149, 154, 214-217]. The experimental data used here reports yield strains in the order of 2.0% and greater, whereas using end-cap testing methods, cancellous bone reportedly yields at much lower strains [152, 188]. The over-estimation of apparent yield strain is associated with the toe-region present in platens test data. It is likely that the true apparent yield strain values are closer to those exhibited by the 5 GPa and 10 GPa models.

Results from this study showed that both model 1 and model 2 produced apparent moduli that were positively and linearly associated with the experimental modulus, however significantly larger (Figure 6-2). Doubling the initial tissue modulus from 5 GPa to 10 GPa simply resulted in a two-fold increase in the FE modulus, since the apparent modulus is taken from the linear region of the stress-strain curve. Although the FE apparent modulus for both models was significantly larger than experimentally

determined values, they were well within the ranges of apparent moduli values reported in the literature (

Table 6-3). The 5 GPa model, however, produced results more reflective of experimental data that had implemented the platens method [72, 74] and the 10 GPa model of studies that had used end-caps [124, 125, 209]. Since it is now well established that the use of end-caps significantly reduces experimental error it is most likely that the true tissue modulus of vertebral tissue lies somewhere closer to values reported in the 10 GPa range, than those reported in the 5 GPa range. Since the experimental apparent modulus is used to scale the specimen specific modulus, no regression analysis was performed on the FE apparent modulus for the specimen specific tissue modulus.

Bevill (2008) reported that trabecular tissue properties may be anatomic site dependent, with average values of tissue modulus of over 18GPa in the femoral head and closer to 10 GPa in the vertebra [125]. Eswaran *et al* (2009) implemented micro-FE models of human vertebral trabecular specimens with a tissue modulus of 18.5 GPa but comparison with continuum models suggested this was too high for vertebral trabecular tissue; the authors also noted that subsequent tests in their laboratory found the effective tissue modulus of trabecular bone to be closer to 10 GPa [209].

Table 6-3: Average (SD) mechanical properties of human vertebral cancellous bone specimens under uniaxial compressive loading.

Author	Age	Apparent Modulus (MPa)	Apparent ultimate strength (MPa)	Apparent yield stress (MPa)	Apparent yield strain (%)
Mosekilde <i>et al</i> (1990) [218]	50-75  > 75	-	F = 1.35 (0.64), M= 1.86 (0.89)  F=0.93 (0.4), M=0.93 (0.55)	-	-
Keaveny <i>et al</i> (1997) [54]	46-91	165 (110) <sup>†</sup>  121 (97) <sup>‡</sup>	-	-	-
Kopperdahl & Keaveny (1998) [52]	32-65	291 (113) <sup>†</sup>	2.23 (0.95)	1.92 (0.84)	0.84 (0.06)
Banse <i>et al</i> (2002) [213]	44-88	352 (145) <sup>†</sup>	2.37 (1.14)	-	1.19 (0.26)*
Current study					
5GPa <sup>FEA</sup>	53-82	131.31 (40)	0.84 (0.33)	0.70 (0.25)	0.73 (0.04)
10GPa <sup>FEA</sup>		262.70 (80)	1.68 (0.65)	1.40 (0.49)	0.73 (0.04)
Specimen specific <sup>FEA</sup>		65.79 (24)	1.10 (0.55)	0.96 (0.50)	1.60 (0.25)

<sup>†</sup> End plates used; <sup>‡</sup> platens used; \*only ultimate strain given.

The validity of a tissue modulus closer to 10 GPa is further supported when the yield and ultimate strengths produced by the two models are considered. The apparent yield stress and ultimate strength values obtained from the experimental data are consistent with the literature [52, 188]. The results for the 10GPa model are excellent, with the FE model only slightly underestimating experimental yield stress (Figure 6-3); the relationship is further improved when the intercept of the trend line is set to 0, ( $\sigma_y^{\text{FEA}} = 0.98 * \sigma_y^{\text{App}}$ ,  $R^2=0.93$ ) and the strength of the relationship is only slightly reduced. A similar result was seen for ultimate strength, where the 10GPa FE model was an excellent predictor of experimentally determined ultimate strength (Figure 6-4). For all of apparent modulus, apparent yield strain and apparent ultimate strength, reducing the initial tissue modulus by half to 5GPa, simply resulted in a 50% reduction in all parameters. The results for model 1 were also statistically significant, but similar to the 5GPa model; in general model 1 underestimated both yield stress and ultimate strength, by up to 50% and 40% respectively. Accordingly, model 3 was the best at simulating apparent behaviour that was most reflective of that which is reported in the literature, strengthening the supposition that vertebral trabecular tissue modulus is in the range of 10GPa and yields at low strains.

The second aim of the study was to quantify the volume of yielded tissue at apparent yield strains. Only model 3 was selected for this analysis, which implemented a tissue modulus of 10GPa and compressive and tensile yield strains of 0.69% and 0.33%, respectively. For all models, tensile tissue yielding was the primary mode of tissue failure at very low yield strains. However at yield, there was no distinct pattern as to the ratio of tensile or compressive tissue strain domination. When the ratio of tensile to compressive tissue failure at yield, however, was plotted against BV/TV, a moderate negative relationship was observed, indicating that with decreasing BV/TV, tensile tissue yielding is more dominant at yield, whereas as BV/TV increases, compressive tissue yielding becomes the more dominant mode of failure. The pattern of all specimens suggests that initial tissue yielding is dominated by tensile tissue failure, which is most likely due to the loading of the transverse struts in bending. In the very low-density specimens, this is enough to initiate overall yield of the structure. In specimens with a larger volume fraction, once the transverse struts are subjected to a certain amount of tensile yield, the load is transferred to the vertical struts and an increase in compressive tissue yielding occurs. For these specimens a certain amount of

tissue yielding in these vertical columns is required before apparent yield is initiated. It could be argued that tensile tissue yielding dominates early due to the two-fold reduction in tensile vs compressive yield strain in the material model. Bevill *et al* (2009) reported that in vertebral bone, compressive tissue failure dominated over tensile failure at yield, despite the tissue-level tension-compression asymmetry. However the cohort of specimens considered had an average (SD) BV/TV of 11% (0.02), which is slightly higher than that considered here. It is possible that with the slightly higher BV/TV, the tissue-level behaviour is different, as we observed that with increasing BV/TV the compressive tissue yielding also increases, whereas tensile tissue yielding was independent of BV/TV.

Finally, it is important to note some of the limitations of this study. Simulation of nonlinear behaviour is hampered by a number of challenges; firstly, the CPU time requirements for FE analyses that incorporate geometric and material nonlinearity are significantly more than required for nonlinear analyses. Secondly, little data exists regarding the yield and post-yield behaviour of trabecular bone tissue. Therefore it is not known what failure model should be used, or the parameters to input to these models, and this information is commonly based on cortical bone. This is despite the fact that cancellous bone tissue properties are known to differ from cortical bone [55, 70]. Yield properties that had been reported by Bevill *et al* (2009) were implemented and shown to produce good results that correlated well with experimental data [124]. However that study implemented a material model that employs a principal failure criterion for both tensile and compressive failure. Within Ansys, the material model available to simulate yield asymmetry is the cast-iron plasticity model which uses the Rankine maximum stress criterion for tensile yield but in compression, the von Mises yield criterion is applied. Since the von Mises yield stress is a combination of the three principal stresses, this value will always be lower than the principal stress and so compressive tissue failure will be somewhat less, compared to if the maximum stress criterion had been used, as in the case of Bevill *et al*'s mode. This may have contributed to the reason that the current study observed more tensile yielding early on than compressive yielding. However under uniaxial compression, it is most likely that tissue loading is predominantly pure tension or compression, and shear loading is unlikely. In this case, the von Mises stresses will be closer to principal stress values.

Von Mises yield criterion is recommended for isotropic, dense and ductile materials, whereas the Rankine criterion is more suited to brittle materials, such as ceramics. In higher density bone such as bovine tibia, and younger bone, the von Mises yield criterion may therefore be more suited. In osteoporotic bone, which is of lower density and where the mineral distribution is more heterogeneous and the tissue more brittle [66], the Rankine criterion may be a better representation of the tissue properties. Any differences in material models for healthy versus osteoporotic bone, however, have thus far not been explored.

Additionally, the post-yield behaviour of these models was not explored. To date the majority of models that have incorporated material non-linearity have implemented a post-yield modulus set to 5% of the initial tissue modulus, which was based on the behaviour of cortical bone [75, 124, 125, 155]. However none of the models has been effective at modelling apparent post-yield behaviour. Verhulp *et al* (2008) attempted this, relatively successfully, by implementing an isotropic elasto-plastic material model based on Hill's yield criteria [83], which is a modified von Mises surface. They validated their results by comparing micro-CT images of the post-yield specimens with the FE models and found good correlations between regions of high strain in their model, and localised damage in the micro-CT data. However, they reported tissue yield strains as high as 3%, and moduli values of 6GPa for bovine tibial bone, which is significantly different to that reported by Niebur *et al* (2000) [75]. This highlights the effects of experimental procedures in inter-study comparisons, with Verhulp *et al* (2009) using similar bone, but different specimen sizes, method for strain measurement and applied strain rate. This demonstrates that the derivation of tissue properties using FE models and experimental data is highly dependent on the experimental protocol, and should be considered in light of this. Consequently, in this study, in order to replicate apparent behaviour, low tissue moduli values and higher tissue-yield strains were necessary, although the models were still not able to accurately replicate apparent yield strains. Finally, only a small number of specimens were analysed. However since the data used here was taken from a previous study with a different goal, the sample size was limited to what was available. Additionally, implementing non-linear models is both CPU time and memory intensive, so larger sample sizes are problematic.

In summary, three models were implemented with varying tissue moduli and yield strains. Models 1 and 3 were best at simulating apparent yield stress and ultimate strength, but implementing a specimen specific modulus in model 1 reproduced that apparent modulus, whereas implementing a homogeneous 10GPa tissue modulus produced apparent moduli values significantly higher than the experimental data, but consistent with literature that has used the end-cap method for compression testing. The implementation of nonlinear material properties enables the investigation of apparent level yield behaviour, as well as analysis of tissue-level stress distributions under various loading conditions; however any comparisons to experimental data need to be considered in light of the experimental methods implemented. Tissue moduli values that are determined from micro-FE models calibrated by experimental test data should be interpreted with consideration for the experimental test methods used, as any errors associated with test methods can confound the resultant tissue moduli. The tissue-stress distributions observed in this study suggest tensile tissue loading is dominant in low-density bone, but this should be considered in light of the asymmetrical material model and yield criteria used.

This and the preceding two chapters have explored the methods involved in micro-FE modelling of cancellous bone, as well as micro-mechanical tissue behaviour under uniaxial loading conditions and with alternative material models. This has provided an understanding of trabecular behaviour, and considerations for selecting appropriate material models and tissue modulus values for micro-FE modelling of cancellous bone. This chapter has highlighted the effects of experimental set up when using experimental data to derive a tissue modulus for FE analysis. As a consequence, due to time and resource constraints the FE model of the bone and screw will use material properties taken from the literature as opposed to trying to derive specimen specific tissue moduli through experimentation.

The overall goal of this dissertation was to develop a micro-FE model of the bone-screw interface, which is the focus of the remainder of this thesis. The following chapter focuses on the experimentation required to achieve this.

# **7 DETERMINING THE RELATIONSHIP BETWEEN INSERTION AND STRIPPING TORQUES**

## 7.1 Introduction

A screw is a mechanical device that converts applied torque into a compressive force between the two components it is placed through. Many kinds of screws are used in orthopaedics and dentistry for the attachment of implants to bone, for bone to bone fixation, or for soft tissue fixation or anchorage. Such procedures may involve the vertebra or epiphyseal and metaphyseal regions (e.g. the femoral head, femoral condyles, or proximal and distal regions of the tibia), which comprise primarily cancellous bone. The main objective of fracture fixation devices is to obtain maximum stability at the fracture site, whilst allowing favourable mechanical and biological conditions for healing (i.e. rotational stability and adequate compression across the fracture line) [219].

Generally the strength of fixation is described in terms of screw pull-out strength or insertion torque, which are directly related [220-222]. The strength of the bone-screw construct is largely influenced by the friction generated between the bone and plate or washer to maintain stability [223]. The magnitude of this friction is determined by the coefficient of friction between the two materials and the normal (compressive) force between the two surfaces, which itself is proportional to the screw's insertion torque [224].

Screw pull-out strength is widely considered to be the most important parameter for optimisation of bone-screw constructs. This strength is defined as the maximum uniaxial tensile force applied to a screw to cause failure of either the bone or screw. Factors affecting screw holding strength include the major diameter of the screw, the length of engagement of the thread, the shear strength of the material into which the screw is embedded and the thread shape factor (TSF) which accounts for screw thread depth and pitch [225].

There are three major phases of screw placement: insertion, tightening and stripping. During the first phase, insertion, a gradual rise in torque occurs as a result of the increasing friction between the bone and the screw as it cuts the threads. The second phase, tightening, occurs as the head of the screw comes into contact with the bone or plate. The threads of the screw are forced against the newly formed threads in the bone, resulting in an increased resistance to the applied torque; this is characterised by a steep

increase in slope of the torque versus screw rotation (or time) trace. The final phase, stripping, shows a decrease in torque as the screw threads shear through the bone material [226] (Figure 7-1).

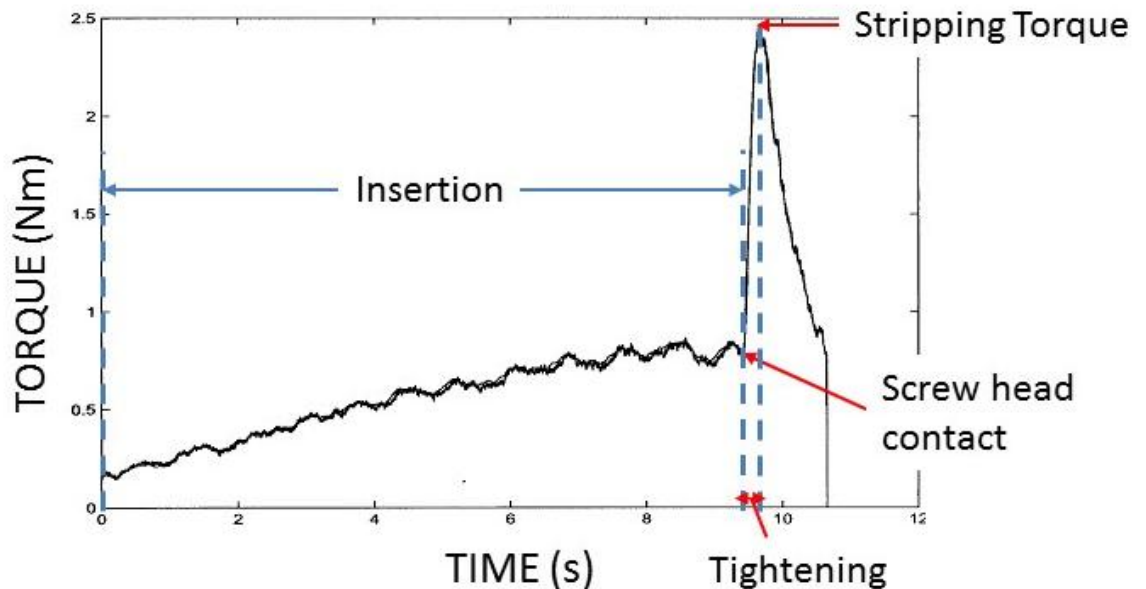


**Figure 7-1: The three phases of screw placement. A torque trace measured during insertion of a bone screw into cancellous bone. Three distinct phases are evident: the first phase (insertion) is a result of the increasing friction between the bone and screw as the threads are cut. The second phase (tightening) is quite short and occurs as the threads of the screw are forced against the newly formed threads in the bone. The final phase (stripping) is characterised by a negative slope in the torque trace. The stripping torque is defined as the maximum torque achieved.**

Because screws produce very high amounts of axial force, it may not be necessary to tighten to maximum torque to produce adequate compression [13]. Surgeons manually tighten bone screws until they subjectively feel that adequate purchase has been obtained; clinically, this equates to approximately 86% of maximum torque [11]. Screws can fail during insertion by over-torqueing if the surgeon attempts to apply maximum torque [13, 227]. In cortical bone, inserting screws beyond 70% of the maximum torque can compromise pull-out strength [107, 108], so it is highly important that the surgeon is well educated in judging the correct torque level. Over tightening that leads to stripping of the screw can reduce pull-out strength by as much as 80% [108, 228] and may not be recognised by the surgeon. This means that patients may leave surgery with an unstable fixation.

Osteoporosis further complicates fracture treatment because screws are unable to obtain an adequate purchase in the reduced bone stock. In situations where the metaphyseal bone quality is poor or osteoporosis is present, screw stripping can occur before sufficient torques are achieved, leaving the construct unstable [224]. Screw failure during insertion increases operation time and requires the drilling of several holes in bone. Since drilling a hole into a bone reduces its strength by 10-40% depending on the screw/bone diameter ratio [99, 229, 230], it is essential to avoid screw failures during operations [219]. An automated tool that could reduce or eliminate over tightening would be highly beneficial, especially in circumstances of osteoporotic bone.

Previous work has established a strong relationship between the insertion torque prior to head contact ( $T_{\text{plateau}}$ ) and stripping torque [231]. This is a significant finding, because it means that the stripping torque ( $T_{\text{stripping}}$ ) can be estimated purely based on the torque required to achieve head contact. However there is no indication as to the ideal level of tightening with respect to  $T_{\text{stripping}}$ . In cortical bone it has been reported that there is little gain in pull-out strength by increasing insertion torque above 50% of  $T_{\text{stripping}}$  [107]. However the effects in cancellous bone have not been addressed.

To utilise the relationship between head contact torque and  $T_{\text{stripping}}$  it is necessary to understand the effects on the peri-implant bone with increased application of torque (i.e. along the tightening phase of screw placement trace (Figure 7-1)). The overall goal of this dissertation was therefore the development of a technique to accomplish this. To achieve this goal, it was proposed to use the known relationship between  $T_{\text{plateau}}$  and  $T_{\text{stripping}}$  to predict  $T_{\text{stripping}}$ , stop screw insertion at predefined positions along the torque versus rotations curve (Figure 7-2) and obtain image data.

Whilst the relationship between  $T_{\text{plateau}}$  and  $T_{\text{stripping}}$  has been established for a stainless steel screw in femoral head cancellous bone [231]; the plan to incorporate micro-CT imaging, would require the use of a radio-translucent material. The presence of a metal screw in a micro-CT scanner presents a number of problems that include but are not limited to beam hardening, scatter and non-linear partial volume effects [232]. Due to the density of the metals that are currently used for surgical screws (namely stainless steel and titanium), it is difficult to examine bone or soft tissue that is near the screw. The screw causes significant artefact in the immediate region surrounding the screw. The artefacts introduced by metallic hardware are associated with the composition of

the metal, as well as the shape and orientation of the hardware [233] and acquisition and reconstruction parameters [234].

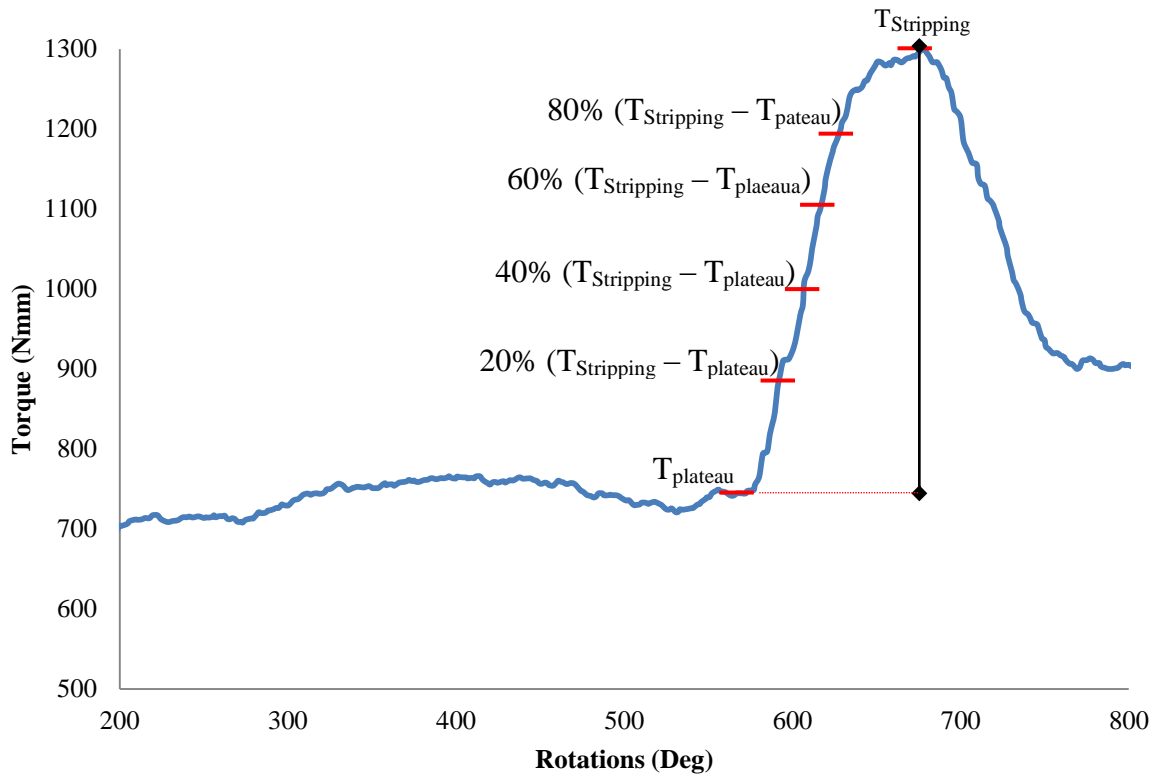


**Figure 7-2: Torque versus rotation curve for an aluminium screw inserted into cellular polyurethane foam (Sawbones, Seattle, WA). The red ticks indicate equally-spaced points along the trace between  $T_{plateau}$  and  $T_{stripping}$ . Assuming a relationship between  $T_{plateau}$  and  $T_{stripping}$ , these can be pre-programmed such that the device will stop once these torque thresholds are reached to allow image acquisition during screw insertion.**

## 7.2 Screw Material

Consequently, an initial analysis was conducted to verify an adequate screw material for micro-CT imaging of the bone-screw interface. Three screw materials were investigated (Figure 7-3). The first screw was a medical grade stainless steel cancellous bone screw with an outer diameter (OD) of 7.0 mm and inner diameter (ID) of 5.2 mm (Catalog No. 7111-9106, Smith and Nephew, London, UK). The second screw was the same Smith & Nephew screw made from titanium. Finally, a custom made screw was manufactured in house from polyether ether ketone reinforced with carbon-fibres (PEEK), and based on the geometry of the Smith & Nephew screws. All screws had a thread length of 16 mm, inner diameter (ID) of 5.2 mm, outer diameter (OD) of 7.0 mm and pitch of 2 mm. The specifications of each material are described in

Table 7-1.



**Figure 7-3: Three screw types were investigated. From left to right the materials investigated were titanium, stainless steel and PEEK. The stainless steel and titanium screws are commercially available Smith and Nephew screws; the PEEK screw was custom manufactured in-house, with the Smith and Nephew screws used as the basis for the screw geometry.**

Table 7-1: Material properties materials investigated.

Material	Density (g/cm <sup>3</sup> )	Youngs Modulus (GPa)
Stainless Steel (316L)	8.0	193
Titanium (Ti6Al4V)	4.42	110
PEEK – CA30	1.31	3.45

### 7.2.1 Identification of Optimal Screw Material for micro-CT Imaging

Each of the three screws was inserted into the centre of individual bovine tibial specimens. Micro-CT imaging (SkyScan model 1072, SkyScan, Kontich, Belgium) was performed at an isotropic resolution of 17.4  $\mu\text{m}$  pixel size. The scanner settings were optimised for each of the specific materials and are detailed in Table 7-2. The resultant images were reconstructed and the greyscale images were compared visually to determine the optimum material for viewing the bone-implant interface.

The results from the initial image analyses are shown in Figure 7-5. As can be seen in the images, the most severe artefact is seen in the image containing stainless steel, followed by the titanium. The PEEK was completely radio-translucent and provided the best visualisation of the trabeculae at the bone-implant interface. Consequently, this was chosen as the initial material; however subsequent testing in the femoral head specimens resulted in shearing of the threads during insertion, due to the low Young's modulus (see Figure 7-6). Based on these findings, an alternative material was explored and aluminium was subsequently chosen as a material that allowed the acceptable visualisation of the bone-implant interface, yet had a Young's modulus significantly higher than PEEK (Young's modulus for aluminium = 70 GPa, density = 2.7 g/cm<sup>3</sup>). Custom manufactured screws were subsequently fabricated using this material and the remainder of the testing was performed using the aluminium screws (Figure 7-4). The scanning parameters used for the aluminium screw are listed in Table 7-2.

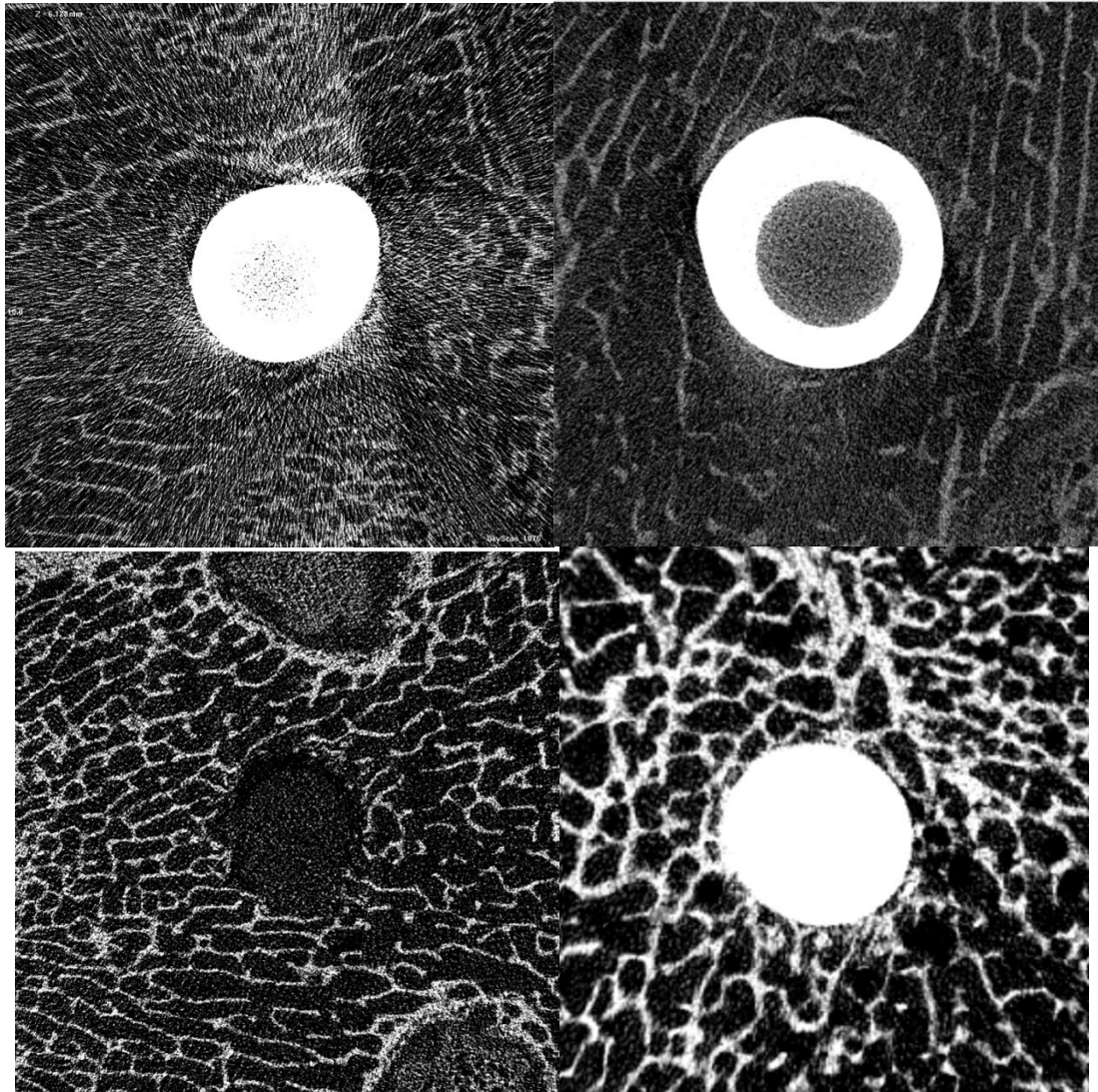




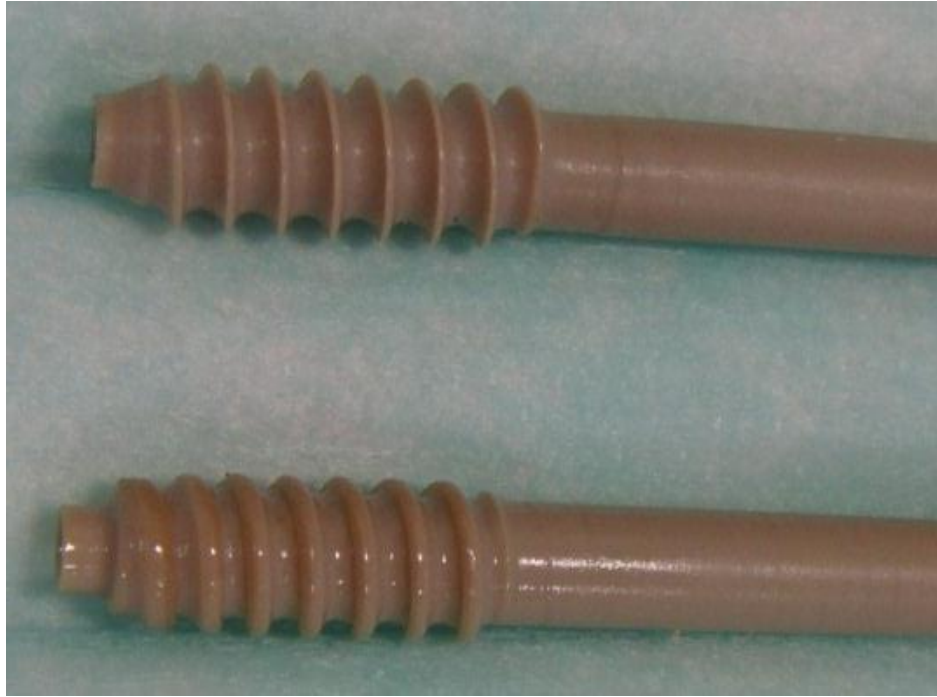
**Figure 7-4: Aluminium screw used for testing in cancellous femoral head bone. The geometry of the screw was modelled on the Stainless Steel and Titanium screws used in the analysis of screw material, and screws were manufactured in house.**

Table 7-2: Scanning acquisition parameters

Material	Voltage (kV)	Current (micro-A)	Filter (mm)	Frame averaging	Step size (deg)	Scan time (mins)
Stainless Steel (316L)	100	80	Al 1.0	4	0.4	35
Titanium (Ti6Al4V)	100	80	Al 1.0	4	0.6	26
PEEK – CA30	100	80	Al 1.0	4	0.4	26
Aluminium (6061T6)	100	80	Al 1.0	2	0.5	23



**Figure 7-5: Cross-sectional Micro CT scans of a 7.0mm cancellous bone screw. The images demonstrate the varying attenuation coefficients of Stainless Steel in bovine tibiae (Top Left); Titanium alloy in bovine tibiae (Top Right); PEEK (Bottom Left); and Aluminium (Bottom Right). Scan acquisition parameters are listed in Table 7-2. The bone-screw interface is best discernible in the bottom left image, however the PEEK screw is less apparent.**



**Figure 7-6: PEEK screws. The screws are shown prior to insertion (Top) and after one insertion (Bottom) into femoral head bone. The limitation of this material is evident by the shearing of the threads in the bottom screw.**

With the aluminium screw, the relationship between  $T_{\text{plateau}}$  and  $T_{\text{stripping}}$  would most likely differ from that previously determined with a stainless steel screw due to the different screw materials and potentially minor differences in screw geometry due to custom manufacturing. Therefore to perform the ultimate goal of step wise screw insertion with micro-CT, the relationship between  $T_{\text{plateau}}$  and  $T_{\text{stripping}}$  for the specific screw under consideration would be required.

## 7.3 Aims

The maximum (stripping) torque, generated during screw placement is dependent on the screw geometry and material, as well as the properties of the surrounding material. The compressive, tensile and shear strength of the peri-implant bone is governed by the quantity and quality (including micro-architecture) of bone present [235]. Consequently the goals of this study were two-fold:

- 1) To determine the relationship between plateau torque and stripping torque during placement of a custom manufactured 7mm cancellous bone screw into osteoporotic femoral head cancellous bone;
- 2) To test whether any relationship exists between screw insertion variables (plateau torque, yield torque, stripping torque and maximum compression) and local bone morphology (Tb N, Tb Sp, Tb Pf, SMI, BS/BV).

## 7.4 Methods

### 7.4.1 Tissue Collection

Eight human femoral head samples (males=4; females=4) were collected from routine hemi- or full-arthroplasty cases from patients who had suffered an osteoporotic fracture, from the Orthopaedics and Trauma department at the Royal Adelaide Hospital, Adelaide, South Australia. Cases were excluded if there was any evidence of hepatitis or HIV from patient history or a blood test of arterial blood taken at the time of surgery. Femoral heads were collected from donors, flensed and immediately wrapped in saline soaked gauze, sealed in plastic bags and stored fresh at  $-20^{\circ}\text{C}$  until required. Average (S.D.) age of donors at time of surgery was 75 (12) years.

### 7.4.2 Ethical Approval

All donors of the specimens had given their consent for use in research and ethical approval was obtained from relevant institutions for use in this project (Project ID 208/08, Flinders Clinical Research Ethics Committee).

### 7.4.3 Specimen Preparation

The lateral face of all femoral heads were sectioned using a surgical hand saw to ensure a minimum specimen height of 35 mm and a smooth surface for gluing to the specimen holder (Figure 7-7). Specimens were prepared whilst frozen for ease of cutting and immediately returned to the freezer.

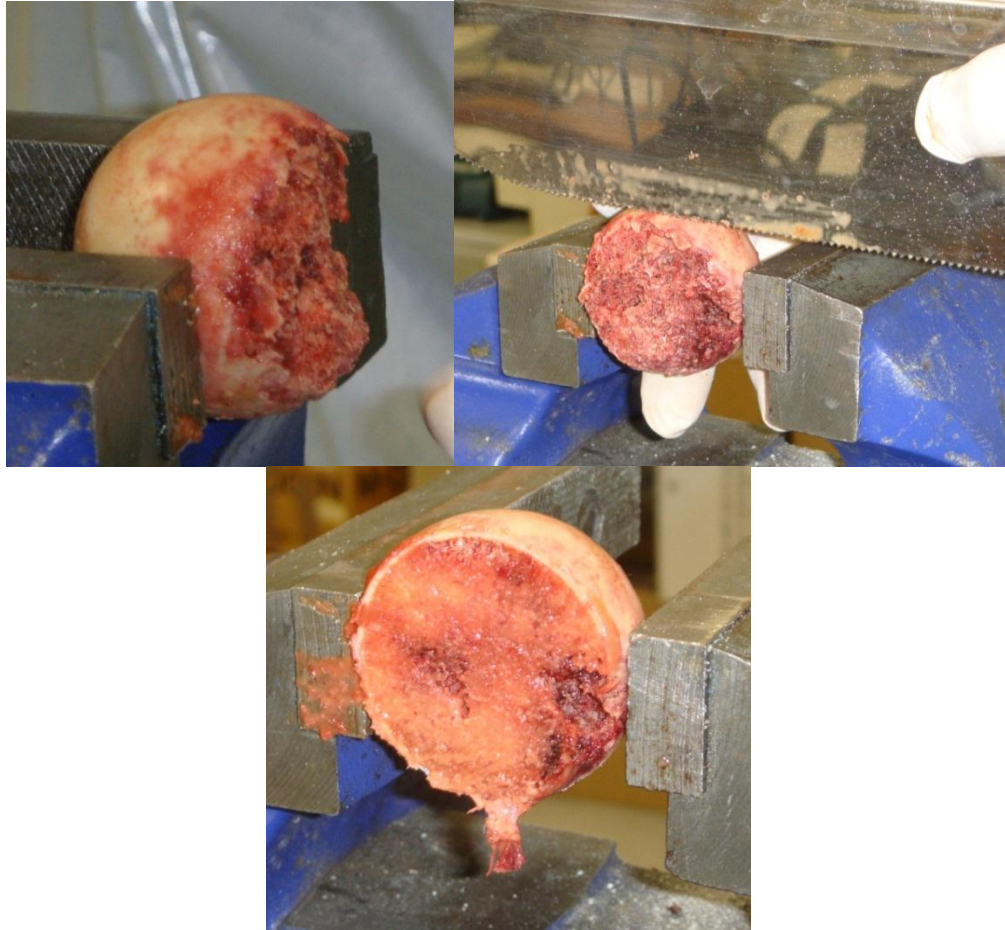


**Figure 7-7: Specimen preparation. Top Left: As received femoral head in clamp; Top Right: Sectioning of the lateral face using a surgical hand saw to ensure a smooth face for gluing; Bottom: Femoral head with smooth lateral face after being trimmed.**

#### 7.4.4 Micro-CT Imaging of Bone Specimens

Prior to testing, all specimens underwent micro-CT imaging (SkyScan model 1072, SkyScan, Kontich, Belgium) at an isotropic resolution of 17.4  $\mu\text{m}$  pixel size, operating at 100kV, 80  $\mu\text{A}$ , 1 mm aluminium filter with 2 frame averaging and a 0.5° step size. Tomographic images were obtained by cone-beam reconstruction using a modified Feldkamp algorithm [236] (NRecon, SkyScan).

The noise of the resulting grey-scale images was reduced using a basic three-dimensional Gaussian filter with a radius of one. A global threshold derived by Otsu's method was then used to segment the bone from the marrow [237]. Cubic volumes of interest (VOI's) (400 x 400 x 400 pixels) were obtained from the approximate area of screw insertion. For each specimen, the following microarchitectural parameters were determined over the VOI (CT-An, SkyScan): bone volume fraction (BV/TV [%]), trabecular thickness (Tb.Th [mm]), trabecular separation (Tb.Sp [mm]), trabecular number (Tb.N. [ $\text{mm}^{-1}$ ]), structural model index (SMI), and bone surface / volume ratio (BS/BV [ $\text{mm}^{-1}$ ]) [238, 239].

#### 7.4.5 Test-Rig

A custom-designed test rig was used for the final screw insertion and tightening phases (Figure 7-8). The test-rig comprised: a 1,100N compression load cell (Model Number: THB-250S, Transducer Techniques, CA, USA) that sits under the head of the screw; the screw and driver; an 11 Nm torque transducer (Model number: TRT-100, Transducer Techniques, CA, USA); a 32mm diameter A-max 20W motor with graphite brushes (Model number: 23667, Maxon motor AG, Switzerland) coupled with a ceramic planetary gearhead (Model number: 166939, Maxon motor AG, Switzerland); and a 500 CPT encoder (Model number: 110513, Maxon motor AG, Switzerland) to determine the number of rotations. The torque and compression transducers were calibrated by a NATA accredited lab prior to use (Norbar Torque Tools, SA, Aust). The specimen was glued to a polymer base plate, which was screwed into the gantry of the test rig. The base plate was designed to minimise any fixation or loading points on the bone and enable easy representation of the boundary conditions for FE modelling. The specimen was constrained purely by glueing the medial face to the base plate with cyanoacrylate. Preliminary testing was conducted to determine an optimal adhesive and drying time for the glue to the base plate. The base plate was connected to the test rig by three screws to

ensure rigid fixation. The test-rig was designed to fit inside the micro-CT scanner and manufactured from aluminium to ensure no metal artefact in the images. The system was computer controlled using custom written software (Labview, V8.2, National Instruments Corporation, Austin, Tx, USA), such that the system could remain completely inside the scanner whilst screw tightening was performed.

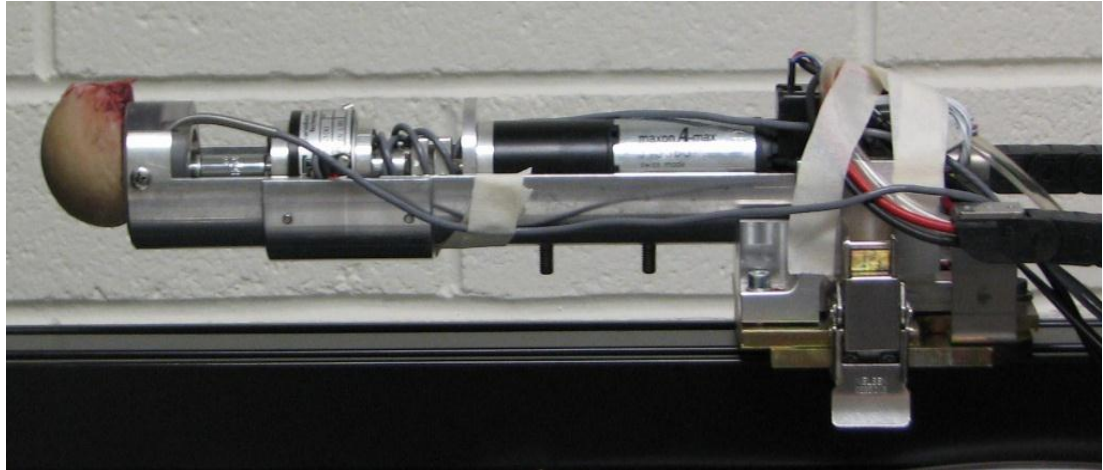
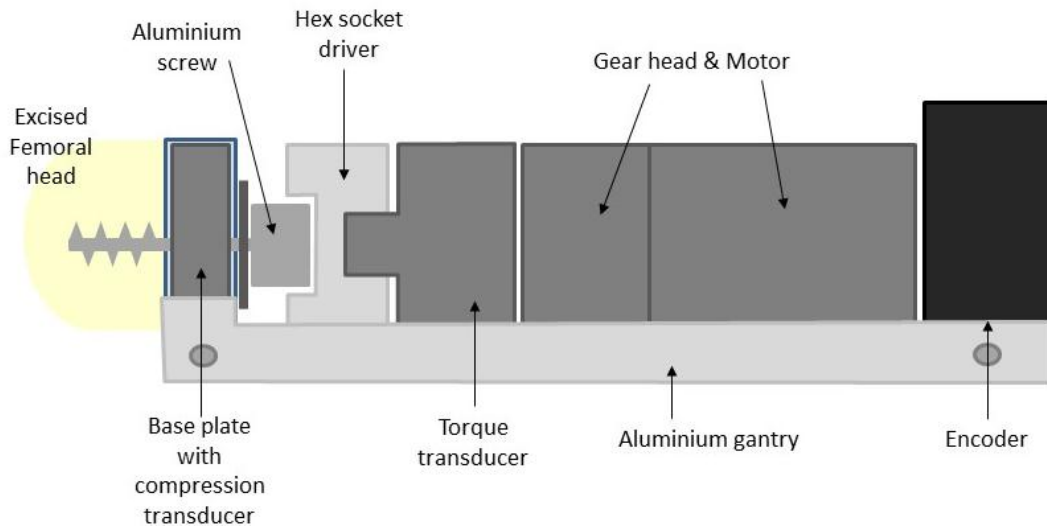


**Figure 7-8: Custom designed test rig, block diagram (top) and actual test rig set up in microCT scanner (bottom). The test rig comprises a polymer base plate that incorporates a 1.1 kN load cell; a hex socket driver and 11 Nm torque transducer; 20W motor and gear head; and encoder and polymer base plate. The rig is computer controlled with custom developed software. Both torque and compression under the head of the screw are simultaneously measured at 25kHz during screw tightening.**

#### 7.4.6 Screw Insertion

In some specimens, an extraction hole was present in the femoral head. Depending on its location with respect to the insertion holes, between one and three screws were inserted into each femoral head to ensure the insertion hole did not impact screw placement. Screws were positioned in a pattern similar to the inverted triangle used clinically for fixation of neck of femur fractures using cancellous bone screws [240] (Figure 7-9). Taking into account whether the heads were left or right, hole 1 was created in the anterior superior aspect of the femoral head, hole 2 in the posterior superior aspect and hole 3 in the central inferior aspect. Anatomic locations were based on the ligament teres located on the medial side of the head.

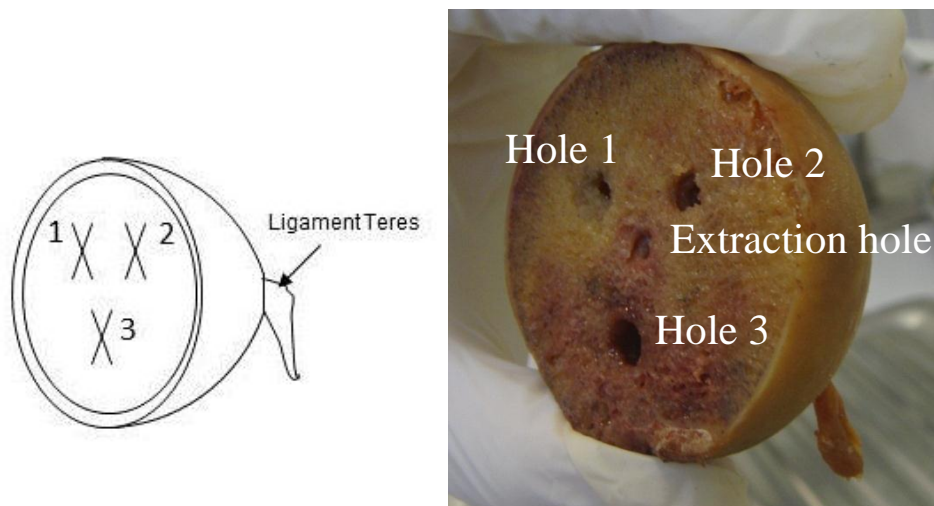


**Figure 7-9: Femoral head indicating the location of the holes for screw insertion. Schematic (left) and a single specimen after three insertion tests (right). The ligament teres, located on the medial side of the head, was used as the anatomic land mark to position the three holes.**

On the day prior to insertion, specimens were removed from the freezer and thawed at 3°C overnight. To ensure that the specimen would adhere to the base plate, the lateral face was prepared in the following manner; excess moisture was removed from the face using paper towels, the face was sanded and wiped with alcohol and allowed to dry. The face was then marked to identify the three insertion points (Figure 7-9). The specimen was glued to the base plate using cyanoacrylate and clamped for 15 minutes to ensure a strong bond.

Once the specimen was glued and a good adherence had been achieved, the base plate was clamped in a vice, and a 5.2mm pilot hole was drilled to a depth of 35mm using a table top drill press (ZQJ-4116, Ledacraft, Aus) (Figure 7-10). To ensure that the screw was perfectly aligned with the hole, the bone specimen was not removed and the drill bit was replaced with a hex drive to insert the screw. Prior to insertion, a stainless steel washer and load cell was inserted under the head of the screw. The head of the screw was inserted into the hex drive and the screw was inserted by manually rotating the chuck of the drill press. The screw was manually tightened until approximately 10 mm of clearance between the screw head and washer remained. This last component of the insertion phase would provide an adequate range to determine plateau torque over (Figure 7-10).

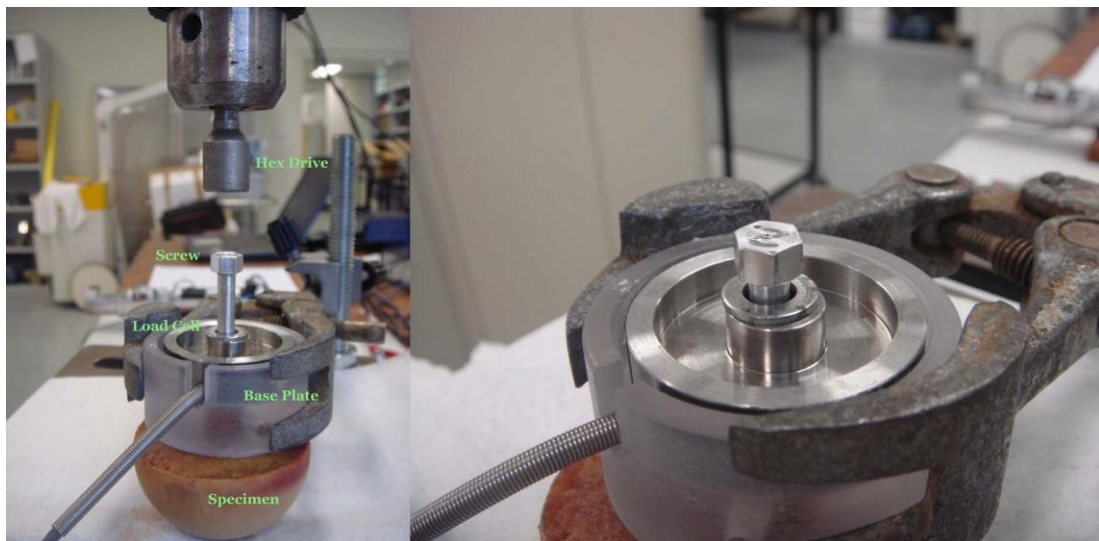


**Figure 7-10: Screw placement in the femoral head. A 1,100N load cell was inserted under the head of the screw and the screw was tightened to within approximately 10mm of head contact.**

For the final insertion of the screw, the custom-designed test rig was used. Each screw was inserted at a rate of 5 rpm, whilst torque and compression under the head of the screw were simultaneously measured at a sample rate of 25 kHz. The screw was inserted continuously until failure occurred. Failure was determined by monitoring the torque trace and identified once the maximum torque had been achieved and the slope of the torque trace was negative Figure 7-11.

Specimens that had more than one screw inserted, were removed after the test and the base plate and specimen face were cleaned, sanded and prepared as described above for the next insertion test.

#### 7.4.7 Signal analysis

The torque and compression traces were analysed using a custom written program (Matlab, MA, USA). The point of head contact was achieved when the slope of the compression trace exceeded a predefined threshold level (10 N/°). The threshold for the slope was varied between 1 and 20, to obtain a value that selected head contact most accurately for all specimens. Using lower values for the threshold to detect head contact, sometimes resulted in the software incorrectly detecting head contact early. Setting the threshold to 10 N/deg, achieved the best result for all specimens. At head contact, three plateau torque values were determined as follows: the torque at the “Head Contact” time point ( $T_{HC}$ ) and also by averaging the torque trace over the preceding 60° ( $T_{60}$ ) and 180° ( $T_{180}$ ) from head contact (Figure 7-11). Stripping ( $T_{Stripping}$ ) was defined as the maximum torque measured by the torque transducer (Figure 7-11). The maximum compressive force ( $F_{max}$ ) was defined as the maximum force measured by the load cell.

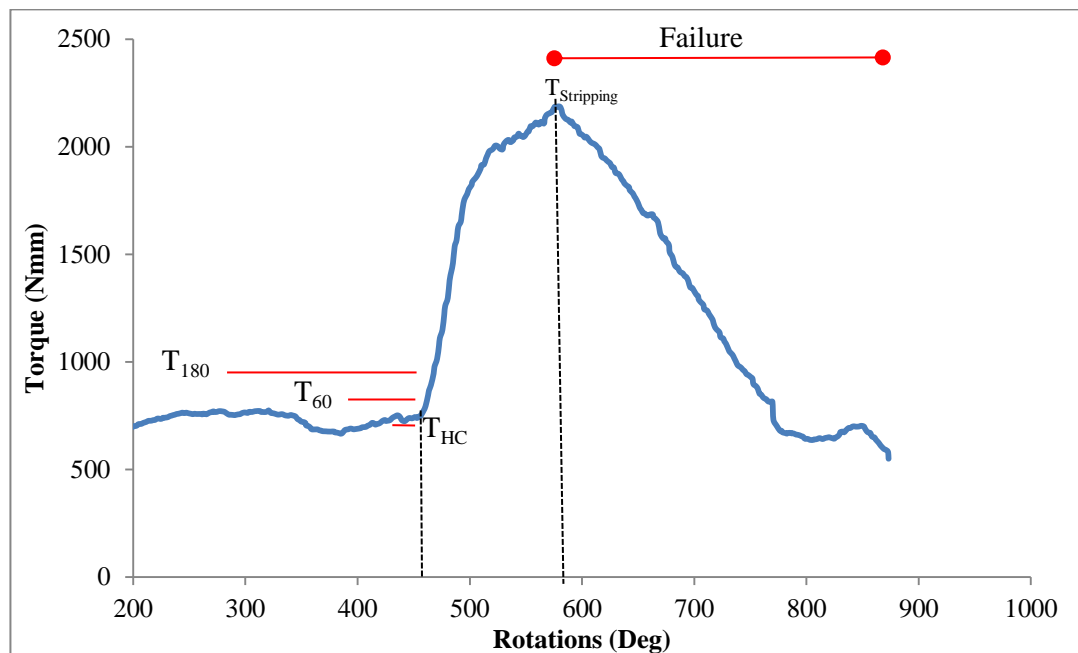


**Figure 7-11: Torque versus rotation trace indicating the three different regions plateau torque was calculated over. Failure is defined once a negative slope occurs (i.e. after  $T_{stripping}$ ).**

The slope of the insertion torque trace and yield torque were determined by a custom written Matlab routine (Matlab, v7.14). Firstly a moving average filter with a span of 5 was applied to the torque trace to smooth the curve and eliminate experimental artefact. The 'linear' region of the curve was defined as the region of the curve between the tenth and sixtieth percentiles of plateau torque ( $T_{60}$ ) to stripping torque.  $T_{60}$  was chosen because this had the strongest relationship with  $T_{stripping}$ .

A straight line was fit to the 'linear' region of the smoothed curve and a line was then constructed parallel to the 'linear' region of the torque-rotation curve and offset. For materials where the point at which a material yields is often difficult to define, and a yield point cannot easily be identified based on the shape of the stress-strain curve, an '*offset yield point*' is sometimes used. The value for this is commonly set at 0.1 or 0.2% of the strain [241]. Although the plots in this case were not stress versus strain, but torque versus degrees of rotation, we employed the offset method to identify the point where the curve begins to deviate from linearity. For the curves under consideration, the offset value was varied between 0.2 and 2 degrees and little difference in resultant yield torque was detected (Appendix A). The offset value was selected as 2 degrees. The offset yield torque was then defined as the torque at which the constructed line intersected the smoothed torque-rotations curve as shown (Figure 7-12) (Individual plots for each specimen are available in Appendix B).

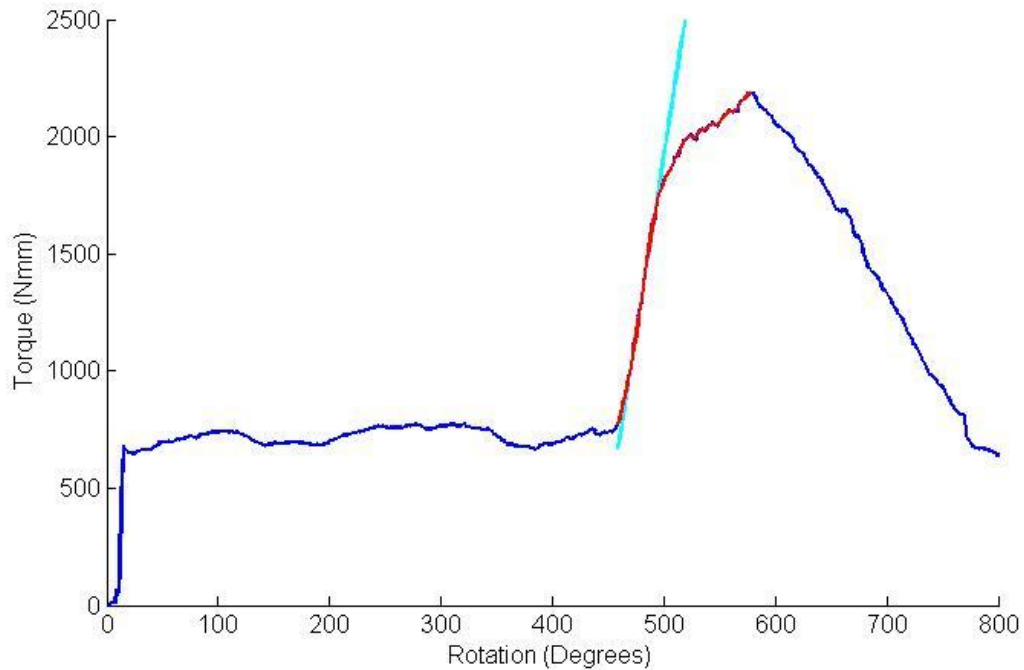


**Figure 7-12: Output traces of torque versus rotation. The blue line represents the original data, the red line represents the smoothed trace and the cyan line represents the offset line. The yield torque was defined as the intersection of the offset line with the smoothed curve.**

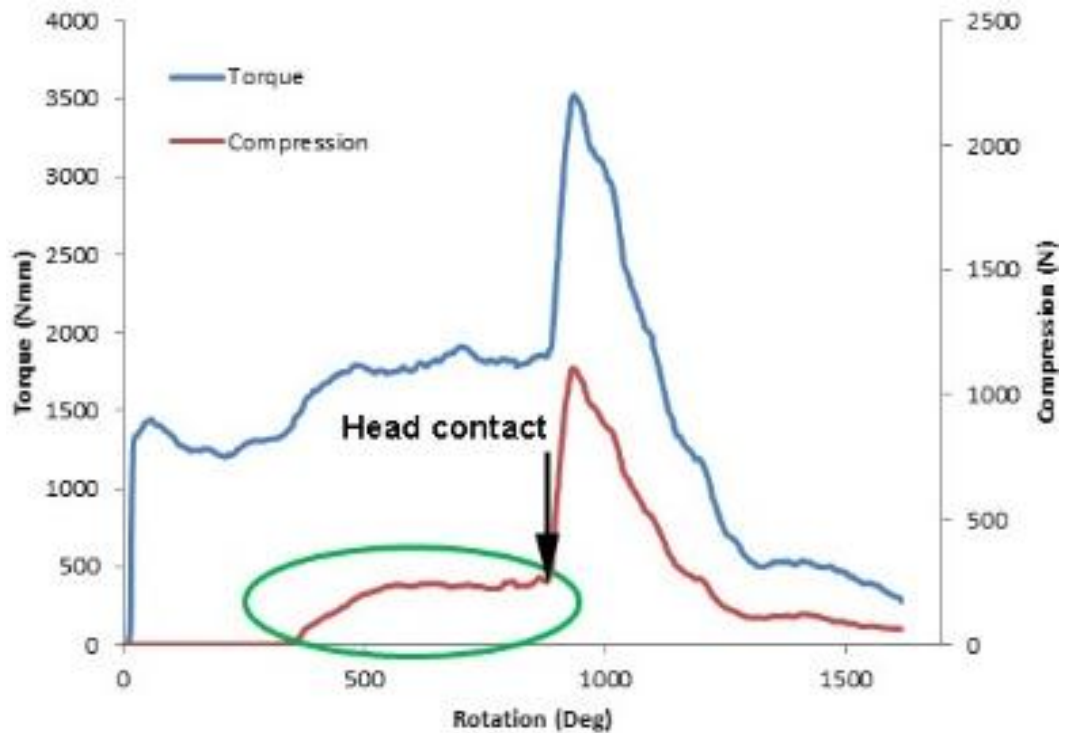
#### 7.4.8 Statistical Analysis

The morphometric test data showed a normal distribution ( $p > 0.05$ , Shapiro-Wilk tests); therefore parametric statistical tests were used for analysis. A one way ANOVA with Bonferroni post-hoc correction was used to compare the averages of the three methods for determining plateau torque, and also for establishing whether there were any differences in morphology and insertion variables for the three different insertion sites. Linear regression was performed to determine if a linear relationship existed between stripping torque and plateau torque. Bivariate correlation was used to explore any relationships between morphometric data and insertion variables including plateau torque, compression and stripping torque. All statistical analyses were performed using SPSS statistical package (version 18.0; SPSS Inc, Chicago, IL). All reported p-values are two-tailed, with  $p < 0.05$  considered statistically significant; the strength of relationships was determined according to Cohen *et al* (1988). Post-hoc power analyses were performed where significant differences were not found.

## 7.5 Results

The aims of this chapter were two-fold, firstly to establish a relationship between plateau torque and stripping torque and then to explore the relationship between screw insertion variables and the local bone morphometry. To achieve this, twenty-one screws were inserted into the eight specimens, sixteen of which were micro-CT scanned prior to insertion. In thirteen cases, the washer would apply pressure to the load transducer prior to true head contact. This is because the washer hung “freely” between the screw head and load cell. If it was not perfectly flat, or moved slightly during the initial tightening phase, an increase in the compression trace prior to head contact was detected (Figure 7-13). However, as can be seen from the plots, head contact coincides with a sharp increase in slope for both the compression and torque traces.

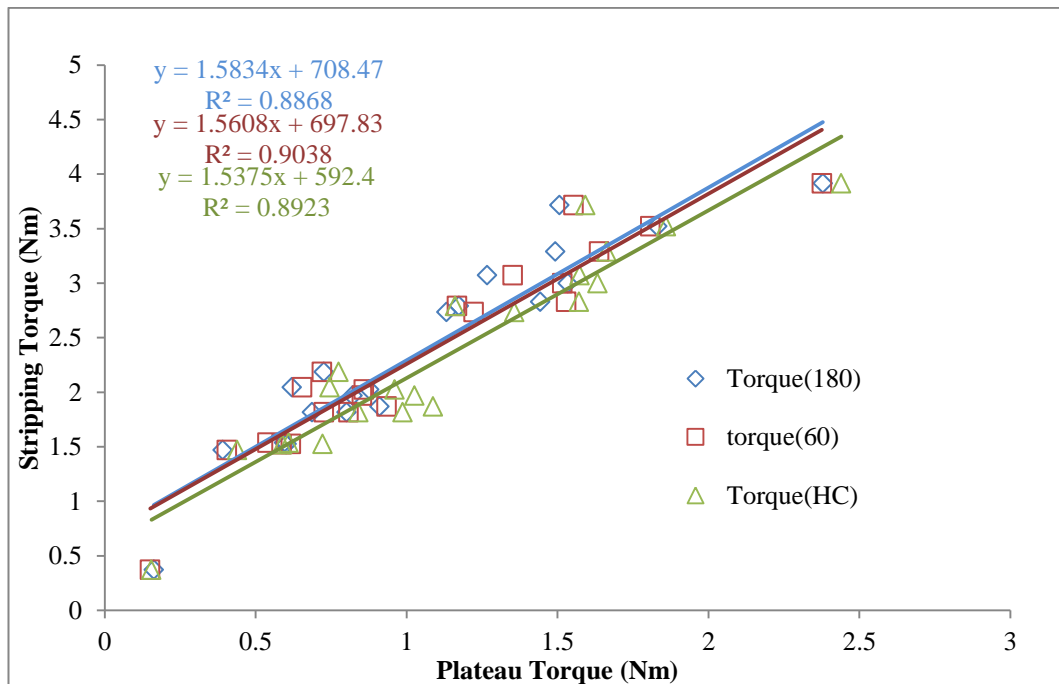
The mean (SD) plateau torques, using the three different methods of calculation were:  $\tau_{HC} = 1.13$  (0.55) Nm;  $\tau_{60} = 1.05$  (0.54) Nm and  $\tau_{180} = 1.03$  (0.53) Nm. One way ANOVA found no statistical difference between the three methods of determining plateau torque ( $p=0.801$ ). The measured stripping torque ranged from 0.37 – 3.91 Nm with an average (SD) of 2.33 (0.89) Nm. The peak compression measured ranged from 117–1,300 N with average (SD) of 766 (307) N. Figure 7-13 illustrates the recorded torque and compression traces for a lone specimen. The average (SD) plateau torque equated to 47.1% (8.3), 43.2% (7.8) and 42.5% (7.7) of stripping torque for  $\tau_{HC}$ ,  $\tau_{60}$  and  $\tau_{180}$  respectively.



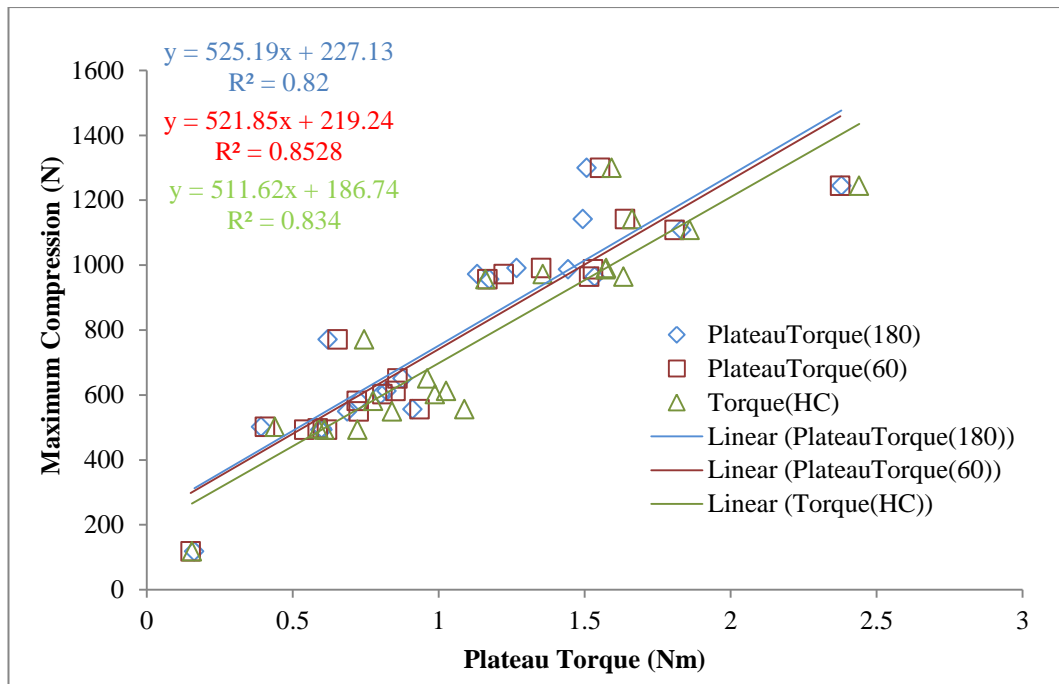
**Figure 7-13: Torque and compression versus screw rotation.** The Aluminium screw was inserted into the anterior superior aspect of the femoral head of a 94 year old male. An artificial increase in compression is seen between 400 rotations and head contact (identified by the green circle). This is due to a misalignment of the washer which results in a registration of load by the load cell. True head contact (denoted by an arrow) occurs at the steep increase in slope of both the torque and compression traces.

Figure 7-14 illustrates the strong linear relationship observed between the plateau and stripping torques, similar to results previously observed within our lab [231]. A strong linear relationship was observed between the plateau torque and peak compression measured under the head of the screw (Figure 7-15). The slope of the linear regression was almost indistinguishable for the plateau ranges determined over 60 and 180 degrees and only slightly lower for the plateau torque taken at the exact point of head contact. The average (SD) maximum compression ( $C_{max}$ ) measured under the head of the screw was 766N (307). Compression versus insertion torque traces for each test are available in Appendix C.

The average (SD) stiffness measured from the torque-rotation curves was 0.023 Nm/deg (0.009). The average (SD) yield torque was 2.1 Nm (0.86); the average (SD) ratio of  $T_{\text{yield}} : T_{\text{Stripping}}$  was 88.86 % (7.15) of the stripping torque. On average (SD) it took 49.96 (22.25) degrees of rotation from head contact to yield torque, and a further 57.00 (33.28) degrees between yield torque and  $T_{\text{Stripping}}$ . Varying the offset between 0.2 degrees and 2 degrees resulted in an increase in average yield torque from 2.04 Nm to 2.13 Nm; the ratio of  $T_{\text{yield}} : T_{\text{Stripping}}$  increased from 86.38 % to 90.23 % (Appendix A).



**Figure 7-14: Plateau versus stripping torque.** The cannulated aluminium cancellous bone screws were inserted into excised femoral heads. Plateau torque was defined as the torque at head contact ( $T_{\text{HC}}$ ), the average torque over 60° of rotation prior to head contact ( $T_{60}$ ) or the torque averaged over 180° prior to head contact ( $T_{180}$ ).



**Figure 7-15: Plateau torque vs maximum compression.** The cannulated aluminium cancellous bone screws were inserted into excised femoral heads. Plateau torque was defined as the torque at head contact ( $Torque_{HC}$ ), the average torque over  $60^\circ$  prior to head contact ( $Torque_{60}$ ) or the torque averaged over  $180^\circ$  prior to head contact.

Seven screws were inserted into hole 1, six into hole 2 and eight into hole 3, in the 8 specimens. One-way ANOVA found no statistically significant difference in plateau torque for each of the hole locations (Figure 7-16). To check whether the morphology of the bone varied in the three locations, one-way ANOVA was also performed on each of the morphological parameters but no significant differences were found (Appendix D).

No morphological parameter was found to be statistically associated with plateau or yield torque, although BV/TV was approaching statistical significance (Table 7-3). BV/TV was the only morphological parameter to have any statistically significant relationship with the maximum compression measured under the head of the screw. A post-hoc power analysis revealed that the study was underpowered for the current sample size (Table 7-3). The number of specimens required to achieve a power of 0.8, for each morphological parameter, is listed in Table 7-3.

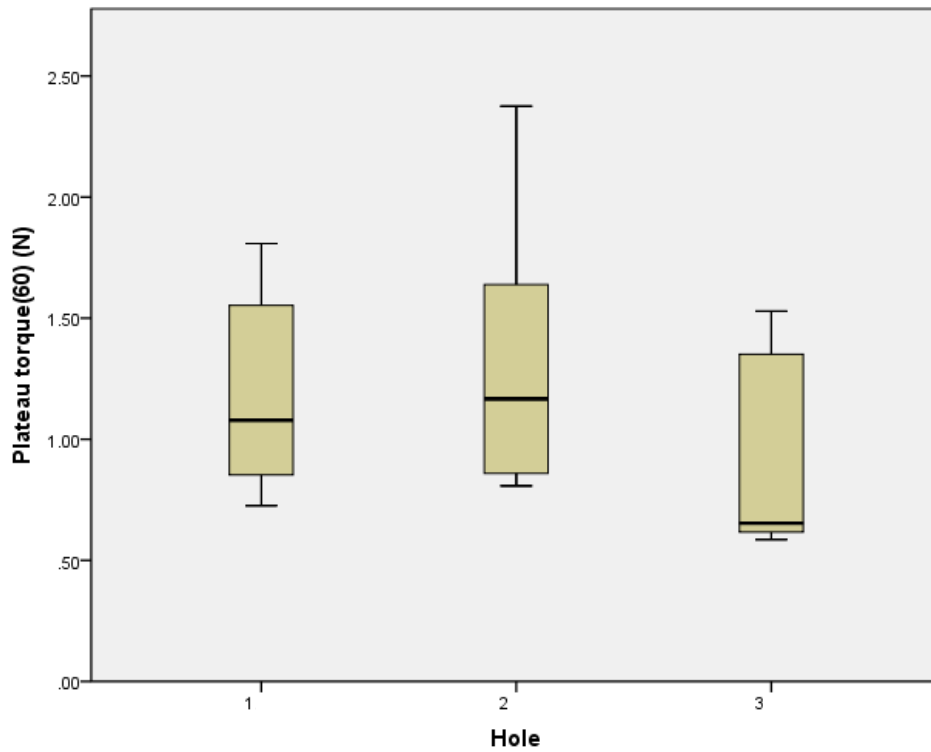


**Figure 7-16: Box plot indicating the difference in plateau torque in the three hole locations . The plateau torque was determined by averaging the torque trace over the 60 degrees prior to head contact.**

Table 7-3: Bivariate correlation of morphological and insertion variables . The results show the coefficient of determination ( $R^2$ ), p-value. A post-hoc power analysis was also performed to determine actual power and the number of specimens that would be required to achieve a power of 0.95 (N-sig). Statistically significant relationships are indicated with a \* symbol.

	Plateau Torque <sub>HC</sub>	Plateau Torque <sub>60</sub>	Plateau Torque <sub>180</sub>	Yield Torque	slope	T <sub>Stripping</sub>	C <sub>max</sub>
BV/TV R <sup>2</sup>	0.226	0.213	0.206	0.283	0.03	0.223	0.253
p-value	(0.06)	(0.07)	(0.08)	(0.03)*	(0.51)	(0.07)	(0.05)*
power	0.62	0.59	0.57	0.	0.16	0.61	0.67
N-sig	26	27	28		204	26	23
TbTh R <sup>2</sup>	0.046	0.023	0.01	0.04	0.14	0.030	0.038
p-value	(0.42)	(0.57)	(0.72)	(0.43)	(0.15)	(0.52)	(0.40.7)
power	0.20	0.14	0.10	0.19	0.43	0.16	0.18
N-sig	133	267	616	153	42	204	161
TbN R <sup>2</sup>	0.135	0.151	0.169	0.18	0.14	0.149	0.161
p-value	(0.163)	(0.138)	(0.114)	(0.10)	(0.15)	(0.14)	(0.12)
power	0.42	0.46	0.50	0.52	0.43	0.45	0.48
N-sig	44	39	35	33	42	40	37
TbSp R <sup>2</sup>	0.090	0.114	0.130	0.141	0.21	0.100	0.117
p-value	(0.26)	(0.20)	(0.17)	(0.15)	(0.08)	(0.23)	(0.19)
power	0.31	0.37	0.41	0.43	0.58	0.33	0.38
N-sig	67	52	46	42	28	60	51
TbPf R <sup>2</sup>	0.184	0.145	0.124	0.21	0.03	0.184	0.203
p-value	(0.097)	(0.145)	(0.181)	(0.08)	(0.54)	(0.098)	(0.080)
power	0.53	0.44	0.39	0.58	0.16	0.53	0.57
N-sig	32	41	48	28	204	32	29
SMI R <sup>2</sup>	0.094	0.071	0.058	0.13	0.06	0.104	0.124
p-value	(0.248)	(0.318)	(0.369)	(0.17)	(0.35)	(0.223)	(0.182)
power	0.32	0.26	0.23	0.41	0.23	0.35	0.39
N-sig	64	85	105	46	101	58	48
BS/BV R <sup>2</sup>	0.074	0.046	0.030	0.08	0.13	0.066	0.076
p-value	(0.31)	(0.42)	(0.52)	(0.30)	(0.17)	(0.34)	(0.30)
power	0.27	0.20	0.16	0.29	0.41	0.25	0.28
N-sig	82	133	204	75	46	92	80

Statistically significant ( $p < 0.05$ )

## 7.6 Discussion

### 7.6.1 Screw material

The preliminary component of this study was to identify an adequate screw material that would allow imaging of the bone-screw interface. The presence of materials with attenuation properties significantly higher than bone and the surrounding soft tissues results in an increased absorption of the photons in the higher attenuating material. Consequently fewer photons reach the detector, which results in typical “streaking” in the reconstructed images (Figure 7-5). Since titanium alloy has a lower attenuation coefficient than stainless steel, visualisation of bone-implant structures can be somewhat improved by using titanium in place of stainless steel [234]. Whilst several metal artefact correction software programs exist, the usefulness of these are somewhat limited; although streaking effects distant from the implant are removed, there still remains a loss of detail around the metal-tissue interface [242]. At the micro level, the beam hardening effects of titanium, whilst not as severe as stainless steel, were still evident and the bone-implant interface specifically was not discernible [243]. Using a filter, such as the aluminium filter used in the scans, can harden the x-ray beam before it passes through the bone to reduce the effects of beam hardening; however Figure 7-5 demonstrates the persistent inability to discriminate the implant from bone in micro-CT scans containing either the stainless steel or titanium.

PEEK is a radiolucent polymeric biocompatible material that is currently used for load-bearing spinal implants [244]. The PEEK screw provided the best image data to enable segmentation of bone and screw, and was initially selected as the material of choice. Preliminary testing of the PEEK screws into the femoral head specimens, however, resulted in shearing of the PEEK (Figure 7-6).

The elastic modulus of femoral head cancellous bone tissue reportedly lies in the range of 5-15GPa [65, 70, 71, 76, 82], which is around 3-4 times higher than that of PEEK. The yielding of the screw, which occurred before sufficient torque could be generated, would be attributed to the two to three times higher modulus of bone compared to PEEK.

Aluminium, whilst not biologically inert and not clinically used as an implantable material in the body, possesses an acceptable attenuation coefficient such that the signal to noise ratio is higher, and allows for the segmentation of bone. The Young's modulus is significantly larger than that of bone tissue, (70GPa Vs 10GPa) so that during screw tightening the peri-implant bone yields before the screw. Consequently aluminium was chosen as the material of choice and all testing was performed on custom manufactured aluminium screws. The images reveal that there is still some noise present at the leading edge of the thread, however this was deemed to be the best possible outcome, whilst still maintaining a material strong enough to cut through the bone tissue. Subsequent goals of the thesis were to perform step-wise insertion of the screw and image at designated points along the torque tightening curve. Since the mechanical integrity of the bone will affect the bone-screw interactions it was necessary to minimise scan time [128]. Thus the imaging settings were chosen to maximise the signal to noise ratio (SNR) at the bone-implant interface, whilst minimising scan time.

It may be argued that any results are not clinically relevant; however the aims here were to produce preliminary data to allow an initial FE model to be generated from micro-CT image data. As such the screw material is of little importance. Future models will not require stepwise imaging, and a lone scan will suffice for generation of the FE model. As such, the image acquisition time will not be applicable and there is potential for clinically used materials to be imaged. Additionally, a valuable benefit of the FE model is that the effects of screw material can be investigated by altering the material properties within the model. By using the same bone model and keeping all other parameters the same, the direct effects of the screw material can be analysed.

### 7.6.2 Establishing a relationship between $T_{\text{plateau}}$ and $T_{\text{stripping}}$

The primary aim of this chapter was to determine the relationship between plateau torque and stripping torque for the custom designed aluminium screw. To accomplish this, femoral heads obtained during routine full- or hemi-arthroplasty were used. Femoral heads comprise primarily cancellous bone and are readily available and therefore pose good specimens for testing of cancellous bone screws.

No statistical difference was found between the three methods for determining plateau torque; although the value taken directly at the point defined as head-contact was slightly higher than the other two methods. Some traces also exhibited a spike as head contact occurred; using an average over the preceding 60 or 180 degrees of rotation allowed the effects of this spike to be smoothed.  $T_{60}$  was chosen, since it displayed the highest correlation coefficient between plateau and stripping torque.

As expected from previous work [231] there was a strong linear relationship between the plateau torques and the stripping torque. These linear relationships found the stripping torque to be approximately 1.5 times the plateau torque, with an offset. The differences in the observed regression slopes between this study and the previous study (Figure 7-17) highlights the effects of the different material properties between stainless steel and aluminium and differences in thread geometry. The previous test data used a 6.5 mm stainless steel cancellous bone screw with the same thread length (16 mm), which was inserted into femoral head cancellous bone. The femoral heads from that study had been retrieved from patients who had undergone hemi- or full-arthroplasty for either osteoporosis or osteoarthritis.

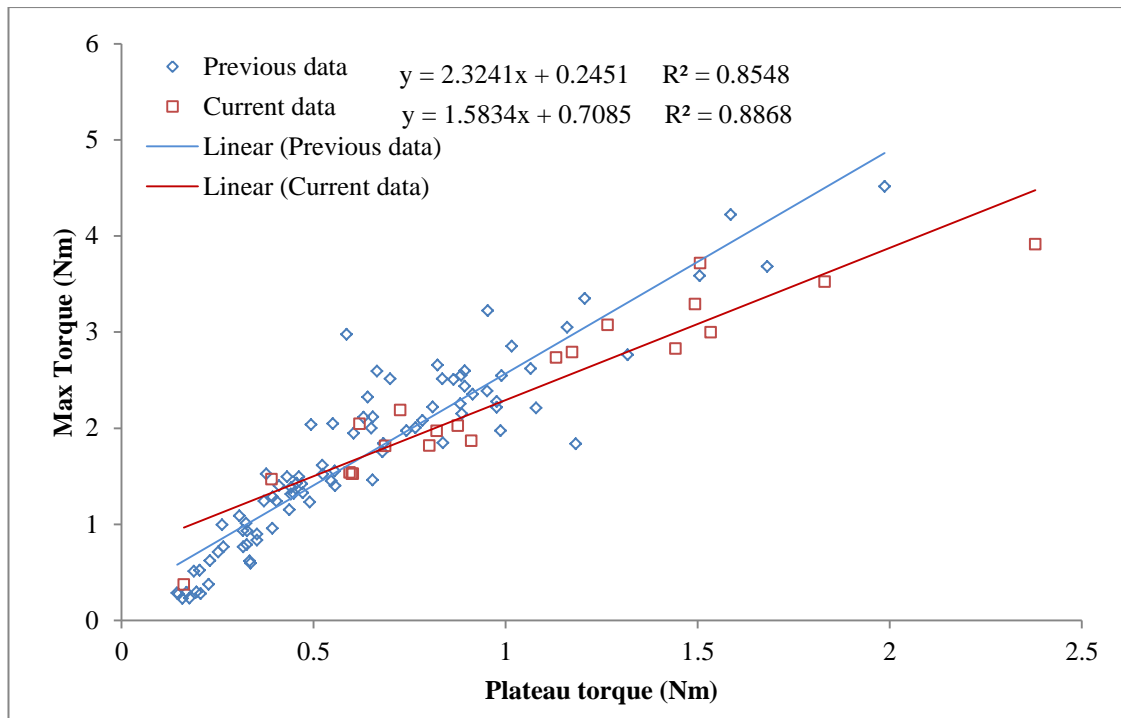


**Figure 7-17: Comparison of previous and current data for plateau torque Vs Stripping torque.. Both data considered femoral head cancellous bone. For the current data, a 7.0mm aluminium screw was used; the previous data used a 6.5mm stainless steel screw.**

A strong linear relationship was also observed between the plateau torque and peak compression measured under the head of the screw (Figure 7-15). However the relationship was slightly weaker than that observed between plateau and peak torque (Figure 7-14). Approximately 40% of the insertion torque applied to a conventional 4.5mm cortex screw during tightening is transformed into axial force [13]. Compression is important, because it provides fracture stability & facilitates primary bone healing by limiting strain and shear forces along the fracture site [245]. We also observed a linear relation between compression and insertion torque for each test independently (Appendix C).

One of the most interesting findings from this study was the ratio of yield torque to stripping torque. Only two other studies have looked at the ratio of clinical tightening torque to stripping torque [11, 12], with both studies reporting surgeons tighten to within 86% of stripping torque in cortical bone. The point of adequate tightening is determined by tactile judgement of the surgeon. It is likely that the surgeons are detecting the onset of tissue yielding, and this is what determines the point to stop

tightening [107]. This study supports this hypothesis, with our data showing an average yield torque of 88% stripping torque; however five of the twenty-one specimens displayed a yield torque greater than 95% of stripping torque. Additionally of significance is the number of rotations between yield and  $T_{\text{Stripping}}$ ; whilst on average this occurred over 57 degrees, there was a large variation in this, with two specimens having less than 10 degrees of rotation between yield and  $T_{\text{Stripping}}$ . This demonstrates that even if surgeons are able to accurately detect yield and stop before stripping very little additional energy needs to be absorbed before potential failure of the bone-implant construct. Prevention of over-tightening relies on the surgeon's ability to accurately detect the onset of the tightening phase, both visually and by the feel of the rapid increase in torque [226]. Figure 7-13 illustrates the steep slope of the tightening phase; this, in conjunction with a more brittle failure mode in the torque-rotation curve, means that the tightening phase occurs on average (SD) over as little as 106 (33) degrees. This allows only a small margin of rotation for obtaining the optimum tightening torque. A slight under or over rotation of even 10 degrees can mean a significant difference in the resultant torque (Figure 7-1). Over-tightening can result in micro-failure of the peri-implant bone; this may lead to targeted remodelling and screw loosening, or, particularly in osteoporotic bone, outright failure of the material around the threads and immediate loss of fixation [246]. However under-tightening may have equally deleterious results. A study by Terrier *et al* (2010) reported the average clinical tightening torque was only 60% of the stripping torque [247], which suggests a number of screws may potentially leave the clinic under-torqued. If adequate torque is not achieved, then sufficient compression at the fracture site may result in instability of the bone-screw construct.

It has been shown here, along with in a previous study [231], that the stripping torque can be determined from the plateau torque. Therefore it is possible to develop an algorithm for an automated screw insertion device that will stop tightening at a safe level after head contact but before stripping. The question remains however, as to what is the optimum tightening torque, such that the screw is neither under- or over-torqued. Previously, pull-out studies conducted in cadaver bone have not yielded strong correlations between tightening torque and pull-out strength [248, 249], however this may be due to the variability in tightening torque levels applied.

### 7.6.3 Morphological influences on screw insertion

The secondary goal of this study was to investigate the existence of any relationship between screw insertion variables and local bone morphometry. Equation 8-1 demonstrates the strong linear relationship between the shear strength of the host material and the holding strength of screws. Since BV/TV, TbTh, TbSp, TbN, and SMI, have all been shown to be linearly related to the shear strength of cancellous bone [47, 250], it was hypothesized that some relationship may then exist between these parameters and plateau torque, which itself is correlated with pull-out strength. However no morphological parameter was found to be statistically associated with plateau torque. BV/TV, however was approaching statistical significance for all of the torque parameters (Table 7-3). Since BV/TV is the strongest structural parameter for predicting both modulus and strength [73, 122, 144, 152, 171, 251], it is not surprising that this parameter was the most influential on the insertion and stripping torques. The fact that no statistically significant relationships were observed between any other parameters was surprising. TbTh, TbSp, TbN, and SMI, however, play a lesser role in their effects on shear strength; and since shear strength is only one of the variables affecting insertion and stripping torque, to find a statistically significant contribution between these and insertion or stripping torque would require a substantially larger sample size as shown in Table 7-3. Based on these assumptions and this preliminary data, a recent study undertaken in our laboratory, considered a larger number of specimens (n=46) and statistically significant relationships were found between plateau torque and the following architectural parameters: BV/TV, SMI, BS/TV, Tb.Th, Tb.Sp and Tb.N. The strongest relationship being between plateau torque and SMI ( $R^2=0.67$ ,  $p<0.001$ ) and BV/TV ( $R^2=0.64$ ,  $p<0.01$ ) [252].

The results between local bone morphology and insertion variables observed in this study are consistent with other literature. Terrier *et al.* (2010) looked only at BV, but found a linear relationship between BV and stripping torque [247]. However, similar to this study, the observed relationship was only approaching statistical significance and only considered a small number of specimens (n=12). Again, increasing the number of specimens may have improved the statistical significance of BV with respect to stripping torque. Although Reitman *et al* (2004), considered BMD and not morphology, they found a strong linear relationship ( $R^2=0.7$ ) between BMD and stripping torque [248].

Terrier *et al* also found a strong correlation between BV and Fmax ( $R^2=0.69$ ) [247]. In this study, BV/TV was found to be the only morphological parameter statistically associated with the peak compression. Since both BV and BV/TV are strongly associated with uniaxial compressive strength, this is not surprising. Since the loading under the head of the screw essentially applies a uniaxial compressive force to the bone specimen it would be expected that some relationships would exist between the measured force and parameters such as TbSp, TbTh, TbN, which are associated with strength and modulus under uniaxial compressive loads [47, 76, 196, 203, 253-259]. Therefore it was surprising that no relationships could be identified between maximum compression and any other parameters. Similar to the plateau torque relationships, it is possible that other variables do influence the resultant compression; trabecular pattern factor for example was approaching statistical significance for both maximum compression and insertion and stripping torque. However in order to identify these, an increased number of samples would be required.

In this study, the average maximum compression measured under the head of the screw was 766 (307) N, which is almost double that measured by Terrier *et al* [247]. However comparison is not straight forward, as their study considered cadaveric scapulae, whereas this study used femoral heads, which would have a larger BV/TV and consequently a higher ultimate strength and stiffness.

The only other author to our knowledge to look at bone morphology with respect to screw construct stability is Wirth *et al* (2011) [15]. In their study they compared the same morphological parameters, but looked at pull-out strength, in humeral head specimens, whereas this study considered morphology and insertion torque in femoral head specimens. Their study found statistically significant relationships ( $p<0.001$ ) for all of the following parameters (BV/TV, BS/TV, SMI, TbTh, TbSp, TbN). Given the reported relationship between insertion torque and pull-out strength [248, 249, 260], it is likely that micro-architectural parameters that influence pull-out strength would also play a role in insertion and maximum torque. The most likely reason this study was unable to elucidate such relationships is that our study was under powered with only 16 specimens.

The main limitation of this study is the small sample size. The availability of human bones as test specimens is a limiting factor as well as costs associated with micro-CT imaging. Imaging was performed for all specimens; however it was only possible to confidently determine approximate screw locations for sixteen of the screw insertion tests. Since scanning was done only prior to screw insertion, the VOI of interest that the screw was inserted into could only be estimated. To explore potential problems with this, a single specimen was analysed within the lab to investigate regional variations within the femoral head. However no statistically significant difference was found between five locations, (central, antero-superior, antero-inferior, postero-superior, and postero-inferior). Post-hoc power analyses revealed that considerably larger sample sizes would be required to establish statistically significant relationships between morphology and insertion parameters, this has been demonstrated however in a recent paper [252]. The main aim of the study, however, was to establish a relationship between the plateau torque and stripping torque and despite the small sample size; a statistically significant relationship was defined with a strong coefficient of determination.

Furthermore, as mentioned previously, the location of the VOI within which the morphology was analysed could only be estimated with respect to the actual screw insertion. A scan of each femoral head was performed prior to, but not post screw insertion. Landmarks such as extraction holes already present in the bone were used to locate the approximate region that the screw was inserted into and the VOI's were created there. Potential effects of this have been addressed previously.

In summary, although no morphological parameters were found to be statistically associated with insertion or tightening torque due to a low sample size, subsequent work within our lab has identified a strong correlation between BV/TV and plateau torque as well as weak but statistically significant relationships between plateau torque and BS/TV, SMI, TbTh, TbSp, TbN.

# **8 MICRO-FE OF THE BONE-IMPLANT INTERFACE**

## 8.1 Introduction

The biology of bone fracture repair is a complex process. Poor implant stability can lead to micro-motion of the implant; primary bone healing occurs when there is rigid stabilisation of the fracture site [261]. It is well known that some degree of mechanical loading can be advantageous as it promotes tissue repair and growth [262]. Small amplitudes of micro-motion ( $< 20 \mu\text{m}$ ) have been shown to produce no influence on the bone healing, whereas amplitudes greater than 40-150  $\mu\text{m}$  can produce tensile and shear stresses in the peri-implant bone, which stimulates the formation of a fibrous membrane around the implant [263-265]. A persistent fibrous membrane can lead to loosening of the prosthesis due to bone resorption caused by the presence of macrophages in the membrane [14, 266] and ultimate failure of the implant [267-270]. Consequently, implant stability is important for long term fracture healing.

Cancellous lag screws are commonly used for fracture fixation of sub-capital neck of femur fractures [271]. A surgeon's ability to accurately gauge the appropriate level of tightening torque depends heavily on experience [227], as there is no quantification as to what this tightening torque should be.  $T_{\text{stripping}}$  of bone screws in cancellous bone lies in the range of 1-3 Nm, depending on screw geometry, screw material, anatomical location and bone quality [12, 104, 221, 224, 231, 247, 248, 272]. In low density osteopenic and osteoporotic bone, inadvertent stripping of the bone surrounding the threads occurs before sufficient torque is generated in up to 45% of cases [14, 272].

In cortical bone, studies have indicated that tightening beyond 50% of  $T_{\text{stripping}}$  has little effect on the pull-out strength of the bone-screw construct [107, 108, 273]; and tightening beyond  $T_{\text{stripping}}$  can reduce pull out strength by at least 50% [108, 228]. Cortical bone, however, is highly compact. The high porosity of cancellous bone means that the effects of tightening beyond 50%  $T_{\text{stripping}}$  may be different compared to cortical bone. The presence of large spaces between trabecular spicules lend themselves to a more elastic response. However it has also been demonstrated that once trabeculae are broken or completely perforated it is not possible to recreate these structures – even with treatment [274]. The perforation and loss of trabecular spicules is associated with a far greater reduction in strength compared to an equivalent reduction in mass due to thinning alone [275]. Together these suggest that minimal trabecular deformation,

whilst achieving maximum insertion torque, would provide the optimum holding strength.

The previous chapter demonstrated a strong linear relationship between plateau torque and stripping torque, for a custom manufactured aluminium screw in femoral head specimens. For a given screw type, the ability to predict stripping torque from plateau or insertion torque means that it is possible to tighten to a desired tightening torque as a function of predicted  $T_{\text{stripping}}$ . The question remains however, as to what is the optimum tightening torque. Chapter 7 found that yield torque occurs on average at 88% of  $T_{\text{stripping}}$ , which is coincident with reported levels of clinical tightening torque [11, 12]. However, there is little evidence to suggest that this level of tightening torque provides the optimum holding strength of the bone-screw construct. A previous study from our laboratory found that in ovine tibial bone, peak pull-out strength occurred at 70 % of  $T_{\text{stripping}}$  [107]. A more recent study, in human humeral bone, also reported no significant difference in pull-out strength of screws tightened to 50, 70 or 90%  $T_{\text{stripping}}$  [273]. Both of these studies suggest little is gained in tightening past 70% of  $T_{\text{stripping}}$ , however both were performed in diaphyseal bone, which is primarily cortical. The effects of tightening to various levels of  $T_{\text{stripping}}$  in cancellous bone have not been reported.

The test-rig described in chapter 7 allows sequential image acquisition during stepwise screw insertion in excised specimens of bone. This allows us to visually observe the behaviour of the trabecular network surrounding the screw. Additionally, these images can be used to generate micro-FE models to quantify the stresses and strains induced within the trabeculae with increasing levels of torque. FE models of trabecular bone typically use a continuum representation to model the bone. These however are inappropriate, especially in osteoporotic bone where single, weak structural elements play an important role in determining the mechanical competence of a specimen [276]. Two recent studies by Wirth *et al* (2010, 2012) demonstrate the importance of incorporating the trabecular micro-architecture in FE models [15, 16]. However any computational model is a simplified representation of a real-life set-up and the quantitative values cannot be fully interpreted without some type of experimental validation. Therefore the overall goal of this chapter was to develop a computational model to simulate the tightening phase of screw insertion, which was validated by macro-experimental data.

## 8.2 Aims

The overall goal of this thesis was to investigate the micro-mechanical behaviour of the peri-implant bone during the tightening phase of screw placement. The previous chapter established the strong, linear relationship between plateau torque and stripping torque, for the custom manufactured screws in femoral head cancellous bone. The established algorithm allows stepwise screw insertion for visualisation of the interactions between the bone and the screw during tightening. Therefore the specific aims of this chapter were as follows:

- 1) Perform time-elapsd insertion of a custom made 7 mm aluminium bone screw into femoral head cancellous bone, in conjunction with micro-CT image acquisition, at increments of 20% between  $T_{\text{plateau}}$  and predicted stripping torque;
- 2) Develop a micro-FE model of the bone-screw interactions during the tightening phase, based on micro-CT data acquired at head contact, validated by matching the measured insertion torques.
- 3) Analyse the micro-mechanical behaviour of the peri-implant bone during the tightening phase of screw placement using the FE model.

## 8.3 Methods

### 8.3.1 Specimens

A femoral head specimen was obtained from the Orthopaedics and Trauma department at the Royal Adelaide Hospital, Adelaide, South Australia. The head was retrieved from a routine arthroplasty case of a 76 year old male who had suffered an osteopenic fracture. Following removal, the specimen was flensed and immediately wrapped in saline soaked gauze and stored fresh at  $-20^{\circ}\text{C}$ . Prior to the day of screw insertion, the lateral face of the specimen was sectioned, whilst still frozen, using a surgical hand saw according to the methodology outlined in section 7.3.4.

### 8.3.2 Screw Insertion

On the day prior to insertion, the specimen was removed from the freezer and thawed at  $3^{\circ}\text{C}$  overnight. The specimen was prepared and glued to the base plate according to the methods described in section 7.3.7. However, prior to the drilling of a pilot hole, the specimen was connected to the test rig and placed inside the scanner and a micro-CT image was taken ('Pre-drill' image).

After the acquisition of the first image dataset the specimen was removed, the pilot hole drilled and the screw inserted to 5-10mm prior to head contact, according to the methods established in section 7.4.6. Since only one screw was to be inserted, and no difference in insertion parameters between the three positions had been detected in the previous chapter, the screw was inserted into the central location of the femoral head.

For the final tightening of the screw, the custom test rig was again used, and torque, compression and screw rotation were measured simultaneously at a sample rate of 25 kHz. The real time data were averaged every 1000 samples and then saved at a sample rate of 20 Hz. Implementing the custom written software, the screw was inserted until head contact was detected. Whilst the analysis in the previous chapter had defined head contact as an increase in slope of the compression trace above a given threshold, the implementation of this in real time was non-trivial. Consequently for the real time detection of head contact, a threshold of 2N measured by the load cell was defined. At this time point a second image dataset was obtained ('Head Contact' image).

Based on the linear regression analyses in chapter 7, the following algorithm was implemented to predict stripping torque based on insertion torque:

$$T_{max} = 1.56 * T_{insert} + 0.698$$

**Equation 8-1**

where insertion torque was defined as the average torque over 60 degrees of rotation prior to head contact. By implementing this algorithm, and without removing the specimen from the scanner, the screw was then inserted step-wise at intervals of 20%, 40%, 60%, 80% and 100% of the difference between predicted stripping torque and the plateau torque ( $T_{plateau}$ ) (Figure 7-2). At all time-points, the specimen was micro-CT imaged to acquire datasets at '20 %', '40 %', '60 %', '80 %' and 'post failure'. All micro-CT images were acquired using the SkyScan 1072 micro-CT scanner (SkyScan, Kontich, Belgium) at an isotropic resolution of 17.4  $\mu\text{m}$  pixels, operating at 100 kv, 80  $\mu\text{A}$ , with a 1mm aluminium filter, 2 frame averaging and a step size of 0.5°. Tomographic images were obtained by cone-beam reconstruction using a modified Feldkamp algorithm [236] (NRecon, SkyScan).

### 8.3.3 Post-Analysis

To analyse the torque and compression traces, the spikes of the signal were first removed and both the compression and torque traces underwent a second moving average filter with a span of 20 to remove any noise in the signal. The signals were then analysed using the same method as described in section 7.4.7.

### 8.3.4 Image Processing

Following screw insertion, the image datasets were reconstructed by cone-beam reconstruction using the software supplied by the scanner (NRecon, Skyscan). Using the head-contact scans, a cylindrical volume of interest (VOI) centred about the screw, with a radius of 11.23mm was defined. 11.23mm was selected as the diameter of the VOI as it included a 2mm annulus outside the outer diameter of the screw (Figure 8-1). The VOI was then applied to all image data sets, including the 'pre-drill', '20%', '40%', '60%', '80%' and 'post failure' images. For morphological analysis, the noise of the images was reduced using a basic three-dimensional Gaussian filter with a radius of 1 voxel, and bone segmented from the marrow by implementing Otsu's automatic threshold technique in 3D (CTAn, v1.10.11). The following morphological parameters

were calculated using CTAn: Bone volume ( $\text{mm}^3$ ) (BV), bone volume fraction (%) (BV/TV), trabecular thickness (mm) (Tb.Th), trabecular separation (mm) (Tb.Sp), trabecular number ( $\text{mm}^{-1}$ ) (Tb.N), and bone surface density ( $\text{mm}^{-1}$ ) (BS/TV), assuming a rod-like structure.

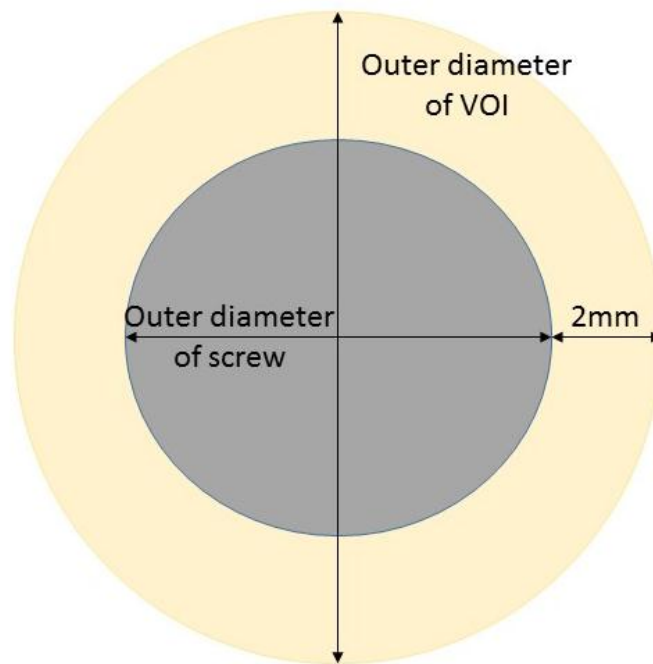


**Figure 8-1:** Schematic of region of interest selected to create the volume of interest (VOI). The outer diameter of the VOI extended 2.0 mm outside the outer edge of the screw.

### 8.3.5 Image guided failure assessment

For qualitative assessment of the stepwise screw insertion, full data sets were analysed in Simpleware (ScanIP) as follows: A median filter ( $r = 5$  voxels) was applied to the three-dimensional (3D) image stack. The bone, screw and marrow were differentiated by implementing Otsu's multi-level threshold technique, which generates three distinct masks for each medium (the bone, the screw and the marrow). A flood-fill filter was then applied to both the screw and bone to remove any components not connected to the main structure. Due to artefact at the bone-screw immediate interface, a morphological dilation filter was applied twice ( $r = 1$  voxels) to artificially expand the mask of the screw [277]. At a resolution of  $60 \mu\text{m}$ , the dilation equated to expanding the diameter of

the screw by 0.12 mm. A Boolean subtraction was then applied to the bone and screw masks. All image processing was performed using ScanIP. The resultant overall volume of bone and screw at each time point was also calculated to establish any differences between time points. Two-dimensional cross sectional images of the resultant bone and screw are shown in Figure 8-2.

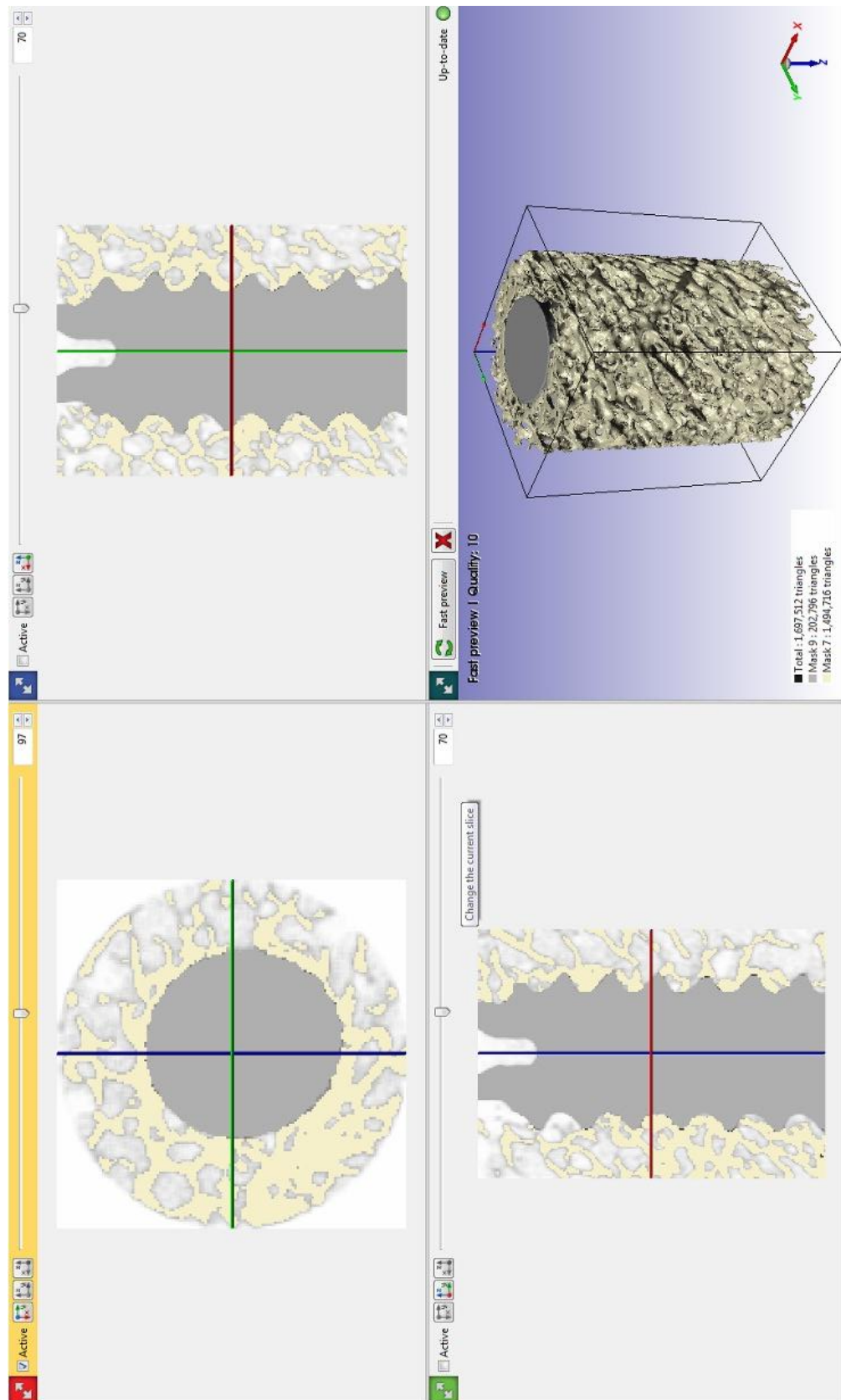


**Figure 8-2: Cross sectional two-dimensional slices of the bone and screw. The white mask represents the component of the image segmented as bone and the grey mask represents the component segmented as screw.**

### 8.3.6 FEA

The methods described in section 8.3.5 allowed generation of the bone and screw geometries; however the debris and noise present at the bone-screw interface meant that the screw geometry could not be accurately segmented. In an attempt to generate the most accurate representation of the screw geometry, images were first coarsened to an isotropic resolution of 60  $\mu\text{m}$ , followed by the filtering and segmentation steps as listed in section 8.3.5. The orientation of the screw was then determined by virtually importing a CAD model of the screw such that it was optimally aligned with the slice images of the screw from the ‘head contact’ image data set (ScanCad, Simpleware). The orientation of this placement was then used to virtually place the screw in the exact same location in the ‘pre-drill’ image data set. A Boolean subtraction was then performed between the CAD screw mask and bone mask.

To construct the FE models, the external meshing software ScanIP was employed. Whilst most micro-FE models of trabecular bone implement direct voxel conversion to generate the FE mesh, this creates a jagged surface along the edge of the bone. When attempting to simulate rotation of the screw and the contacts between the bone and the screw, this can cause localised regions of high stress, which may lead to large fluctuating residuals and issues with convergence. Consequently a smoothed tetrahedral mesh was implemented. The geometry of the trabecular structure was modelled using fully linear tetrahedral elements (solid185) with reduced integration. The surface of the screw was meshed using fully linear triangular shell elements (shell181). To ensure the smoothest surfaces between the two bodies, 25 iterations of surface pre-smoothing was implemented. The “Free” mesh generation tool in ScanIP was implemented.

To model the contact between the bone and screw, the bone elements in contact with the screw as detected by the ScanIP software were defined as the “bone contactable” elements (i.e. the only elements that would come into contact with the screw); and the entire surface of the screw was defined as elements that could potentially come into contact with bone. Contact elements conta173 and targe170 (available in Ansys) were used to model the contact surfaces. Since the bone has a lower modulus of elasticity compared to the screw, the bone was defined as the contact surface and the screw as the target surface. The contact was defined as a non-bonded standard contact, with a friction coefficient of 0. The default augmented Lagrange contact algorithm was

implemented, which is a variation of the pure penalty method. The advantage of the augmented Lagrange over the pure penalty algorithm is that the results are less sensitive to the value of the contact stiffness ( $kn$ ). The contact stiffness was updated each iteration. Contact detection was implemented as the surface projection from nodes. Contact surfaces were initially closed using the default “ICONT” value; using this parameter, any contact points lying within the zone defined by ICONT, are shifted to the target surface to “close” the gap.

Similarly to vertebral bone tissue, large variation exists as to the reported tissue modulus for femoral head trabecular bone tissue (Table 8-1). Based on the values reported in Table 8-1 the bone and screw were modelled as linear isotropic, with Young’s modulus of 15GPa and 70GPa, respectively, and both with a Poisson’s ratio of 0.3. In an attempt to minimise the model complexity, the screw was modelled as a rigid body.

Table 8-1: Average reported tissue properties ( $\pm$  SD) of cancellous bone.

Source	Species, site	Method	ETissue (GPa)
Mente & Lewis (1989)	Human, femoral head	Experiment - FEA	$7.8 \pm 5.4$
Ulrich <i>et al</i> (1997)	Human, femoral head	Experiment – FEA	3.5 - 8.6a
Turner <i>et al</i> (1999)	Human, distal femur	Acoustic	$18.1 \pm 1.7$
		Nanoindentation	$17.5 \pm 1.1$
Zysset <i>et al</i> (1999)	Human, femoral neck	Nanoindentation	$11.4 \pm 5.6$
Bayraktar <i>et al</i> (2004)	Human, femoral neck	Experiment-FEAb	$18.0 \pm 2.8$

a Only range given

b Endcaps used

A rotational degree of freedom equivalent to that measured experimentally was applied to the pilot node of the screw. All external faces of the bone were constrained by an elastic constraint with a stiffness of 0.09 MPa. To simulate the elastic constraint, three COMBIN14 elements were attached to all nodes on the outer surface of the bone, aligned with each of the x, y, and z planes (Figure 8-3). The resultant reaction moment and axial force at the pilot node were recorded and compared to those obtained experimentally. The model was solved using the sparse direct solver.

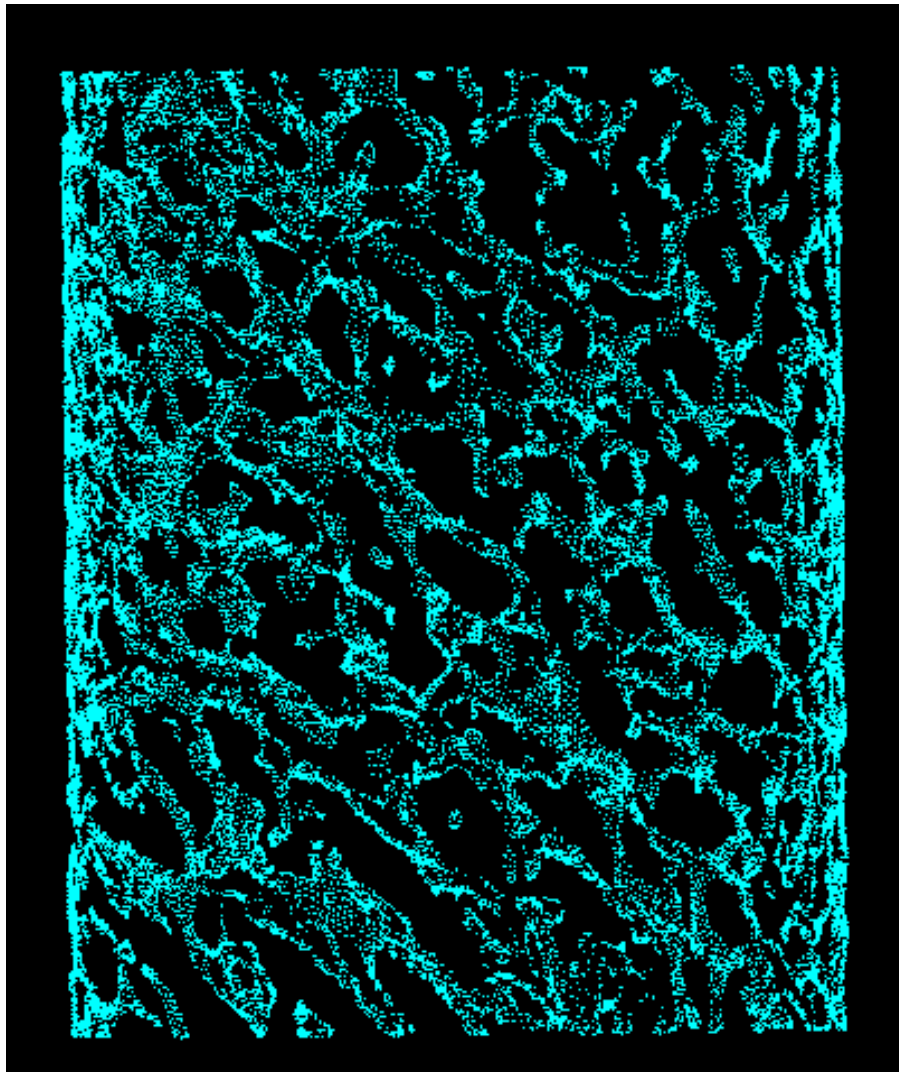


**Figure 8-3:** The nodes representing the outer surface of bone. Springs were applied to these nodes to simulate an elastic boundary condition. The springs were implemented using three COMBIN14 elements, each aligned with the x, y, or z axis. A spring constant of 0.09MPa was defined.

## 8.4 Results

### 8.4.1 Experimental analysis

The previous chapter had used a change in slope by a given threshold as the detection method for head contact, however to implement this in real time is non-trivial and consequently a threshold level of the compression trace was implemented. To determine the effects of this, the test specimens ( $n=7$ ) from the previous chapter that had a zero compression trace up to head contact (i.e. no issues associated with the washer) were analysed. As can be seen from Figure 8-4 the detection of head contact using the compression threshold as opposed to the slope method detects head contact slightly earlier. As a result,  $T_{\text{plateau}}$  would have been marginally lower and hence the device may slightly underestimate  $T_{\text{stripping}}$ .

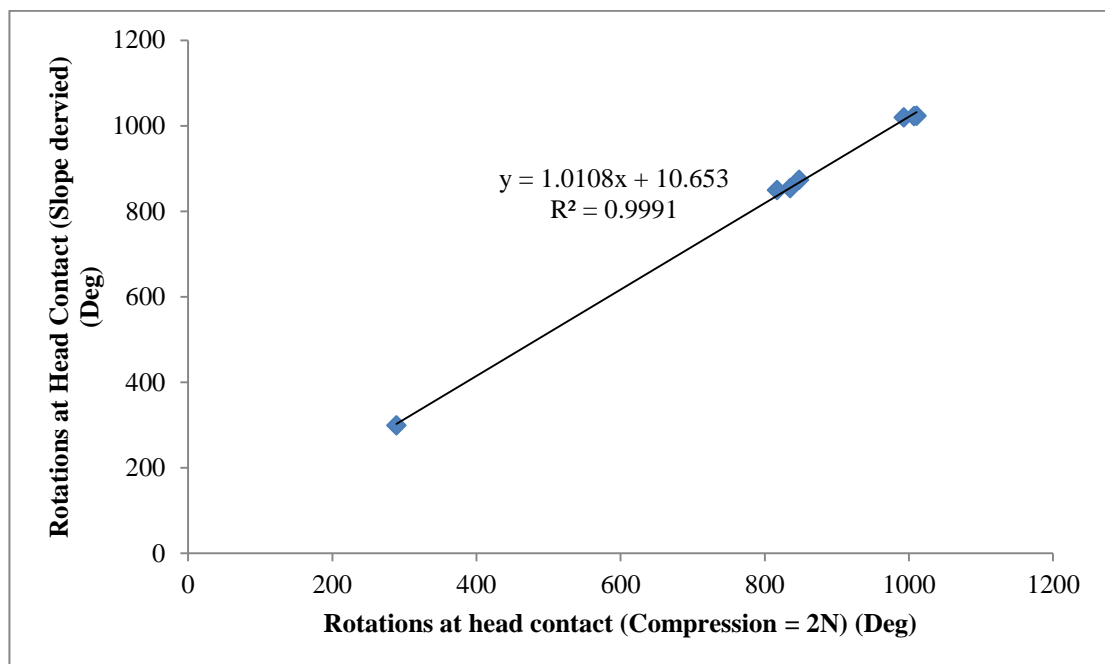


**Figure 8-4 : Comparison of the head contact detection methods implemented. The micro-test rig defined head contact as when the compression transducer registered a load exceeding 2N. The post analysis software defined head contact as an increase of slope greater than 10N/deg.**

The post analysis software established the insertion torque to be 1.43Nm. According to Equation 2 1, the predicted stripping torque was estimated to be 2.92 Nm. The equivalent torques at 20 %, 40 %, 60 % and 80 % of the difference in torque between plateau and stripping torque, as estimated by the software and the actual torques at which the motor stopped for each interval and the rotations from head contact are

recorded in Table 8-2. The overshoot in torque measurements are due to the time delay in the system detecting the desired torque level and the motor's ability to stop. However the algorithm accurately predicted the stripping torque of the bone-screw construct.

Table 8-2: Comparison of the algorithm predicted and actual torque levels for stepwise screw insertion.

$\% T_{\text{stripping}} - T_{\text{plateau}}$	Predicted	Actual torque	Error (%)
20	1.72	1.90	9.5
40	2.02	2.28	11.4
60	2.33	2.40	2.9
80	2.62	2.65	1.1
100	2.92	2.93	0.0

The resultant torque and compression vs degrees of rotation can be seen in figure (Figure 8-5), the spikes observed in each of the traces occur at the time points at which the image datasets were acquired. Once the motor is switched off, the torque trace drops; there is then an overshoot as the motor starts up again. The motor did not stop at the predicted stripping torque, as the predicted value was 2.92Nm, analysis of the trace found the maximum recorded torque to be 2.9326Nm. Consequently once it was observed that failure had occurred, the motor was stopped and the final image acquired post stripping.

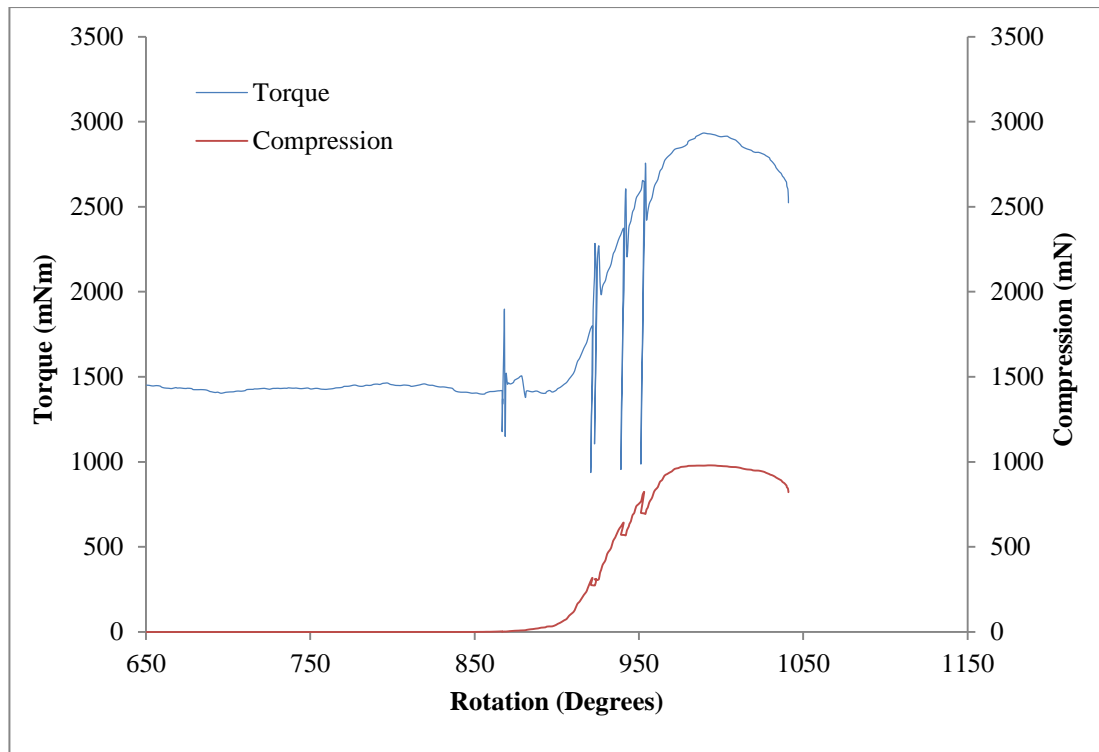


**Figure 8-5: Output traces from software. Torque vs degrees of rotation shown in blue and compression vs degrees of rotation shown in red.**

The smoothed traces for both torque and compression are shown in Figure 8-6 and Figure 8-7. Smoothing was performed using a moving average filter (Refer 8.3.3). As can be observed in the traces, smoothed traces retained the overall shape of the compression and torque traces. The resultant slopes of the linear regions of the torque and compression traces were found to be 28.63 Nmm/deg and 16.36 N/deg respectively. The torque at head-contact, maximum torque, torque at yield, maximum compression, and compression at yield were: 1.49 Nm, 2.92 Nm, 2.49 Nm, 979 N, 702 N respectively. The yield torque equated to 85.38 % of  $T_{stripping}$ , which is consistent with the findings of chapter 7.

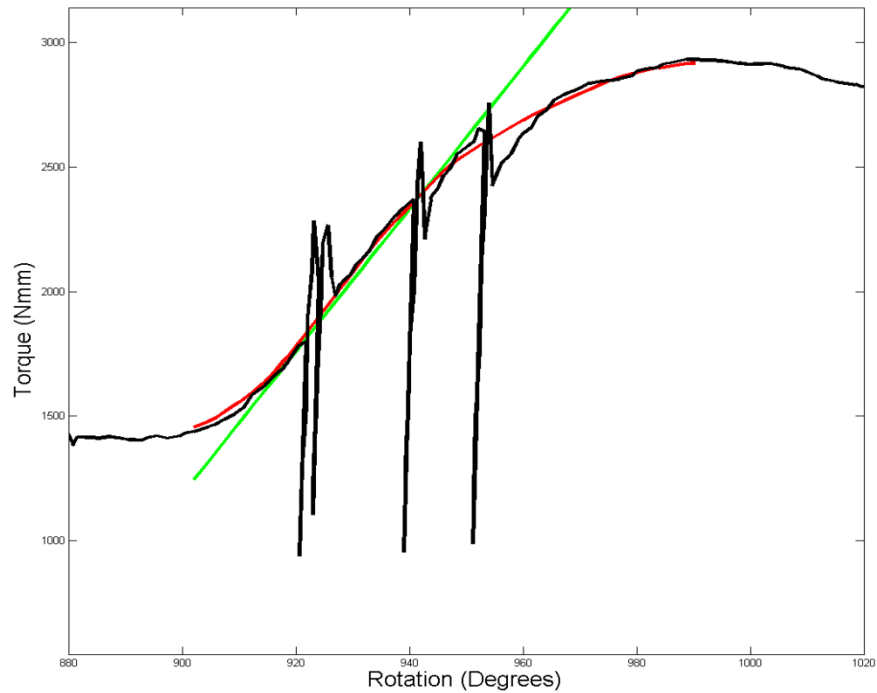


**Figure 8-6: Torque versus rotation. The original trace is shown in black, and the smoothed trace in red, which used a moving average filter. The 2 degree offset line in green was used to define yield.**

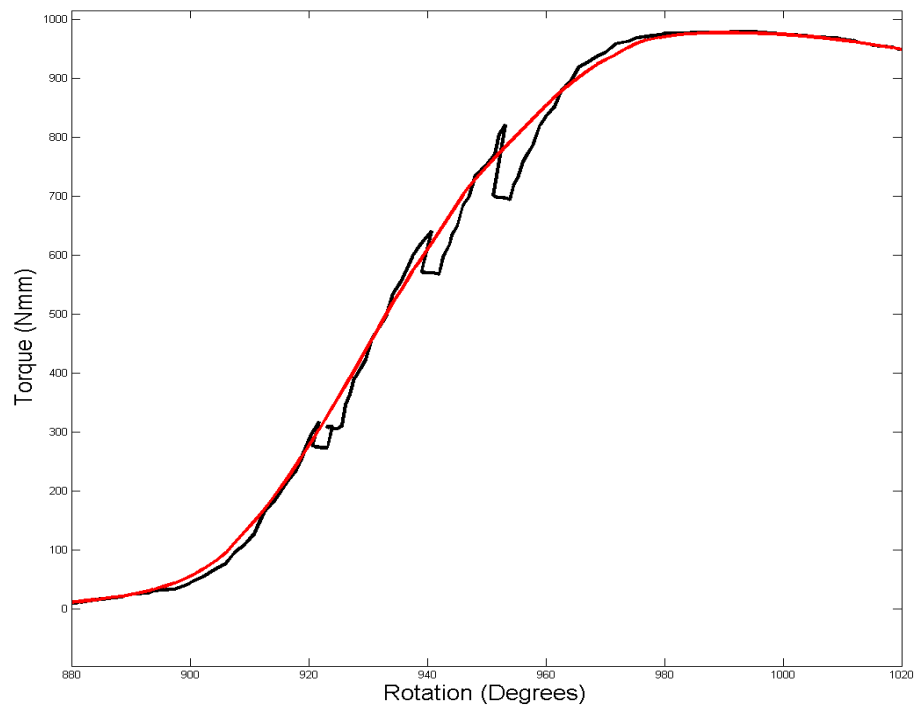


**Figure 8-7: Compression versus rotation. The original trace is shown in black, with the smoothed trace in red. Smoothing was performed using a moving average filter.**

#### 8.4.2 Morphological assessment

The grey-scale Otsu derived threshold level was 100. The morphological assessment for the specimen found the following:  $BV = 436 \text{ mm}^3$ ;  $BV/TV = 28.30 \%$ ;  $BS/TV = 3.63 /\text{mm}$ ,  $TbTh = 0.265 \text{ mm}$ ;  $TbN = 1.07 / \text{mm}$ ;  $TbSp = 0.644 \text{ mm}$ .

#### 8.4.3 Image guided failure assessment

The image dataset obtained at 40 %  $T_{\text{stripping}}$  was corrupted and could not be reconstructed. Successful data sets, however, were obtained for the predrill image, at head contact, and at 20 %, 60 %, 80 % of  $(T_{\text{plateau}} - T_{\text{stripping}})$  (equating to 49 %, 65 %, 82 %, 91 % of  $T_{\text{stripping}}$ ), and post failure. The mask volumes and screw volumes at each time point are shown in Table 8-3. An example of the 3D rendering possible from the image datasets is shown in Figure 8-8.

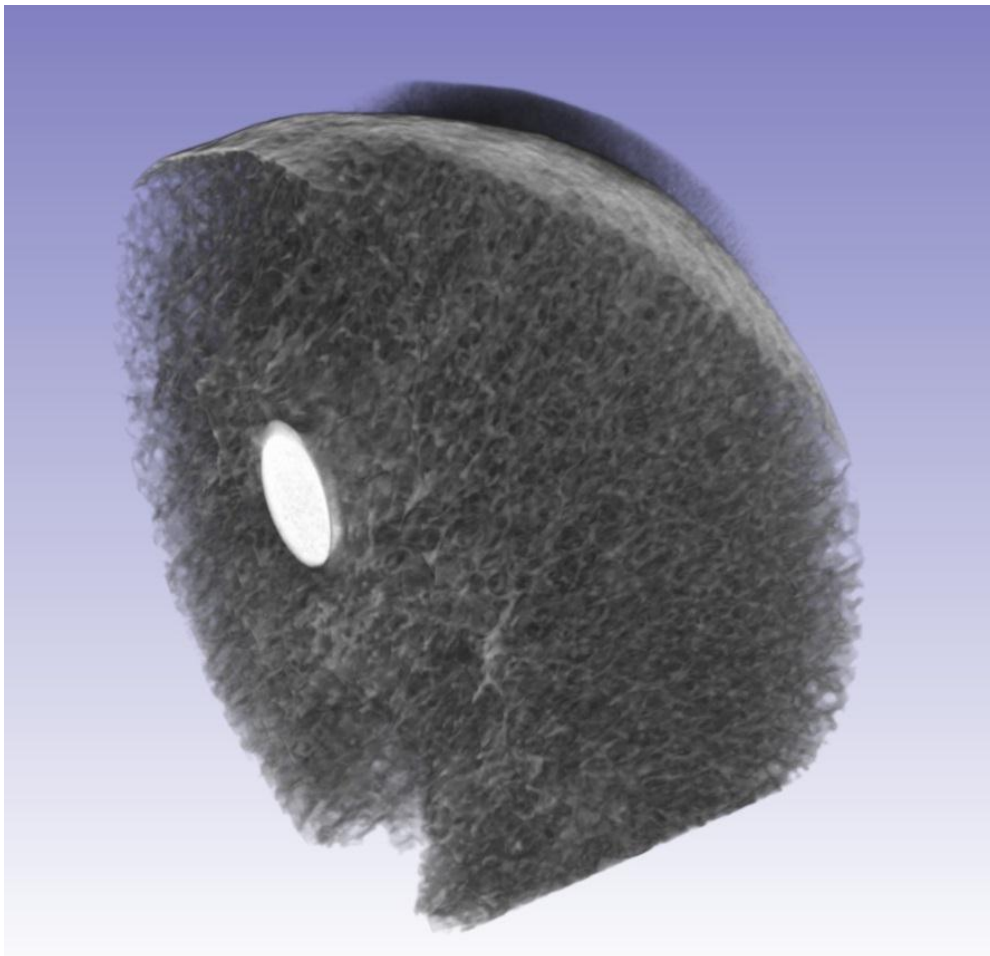


**Figure 8-8: 3D rendering of the screw in the femoral head. Images were acquired at head contact and the 3D representation was generated using Simpleware.**

Table 8-3: Bone and screw volumes for step-wise acquired image data sets

	Bone volume (mm <sup>3</sup> )	Screw volume (mm <sup>3</sup> )
Head contact (49 % T <sub>stripping</sub> )	3,660	475
65 % T <sub>stripping</sub>	3,670	481
82 % T <sub>stripping</sub>	3,680	482
91 % T <sub>stripping</sub>	3,670	481
Post failure	3,720	480

Trabecular deformations occurred along the thread profile and could be visualised in 2D (Figure 8-9) and 3D (Figure 8-10). An example of the visualisation of the trabecular bone deformation at each time point is show in Figure 8-11. Additionally, masks were overlaid on the preceding time point to identify trabecular deformation between sequential images (Figure 8-12). Very little deformation occurred between “Head Contact” and the 80 % time point, however significant trabecular deformation was observed between the 80 % time point and post-failure. However a significant amount of the deformation was elastic, as once the screw rotates around, the trabeculae are seen to “move back” to where they were pushed out from by the leading edge of the thread. The radial displacement appears to recoil once the load applied by the leading edge of the thread is removed and the significant deformation is best seen in the slice along the axis of the thread, where the peri-implant trabeculae are forced towards the head of the screw (Figure 8-10).

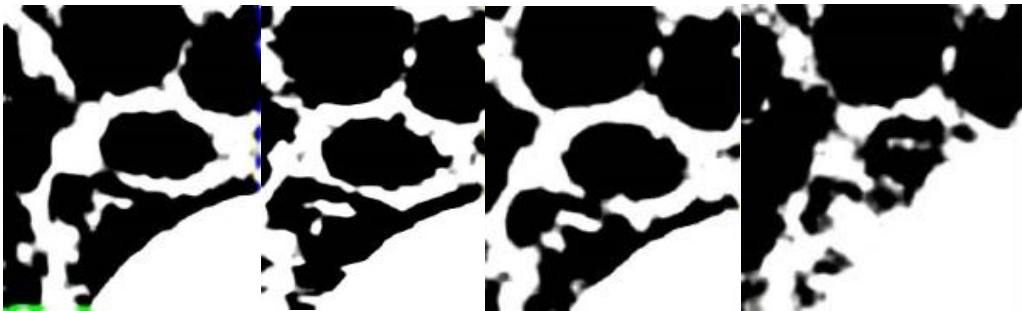
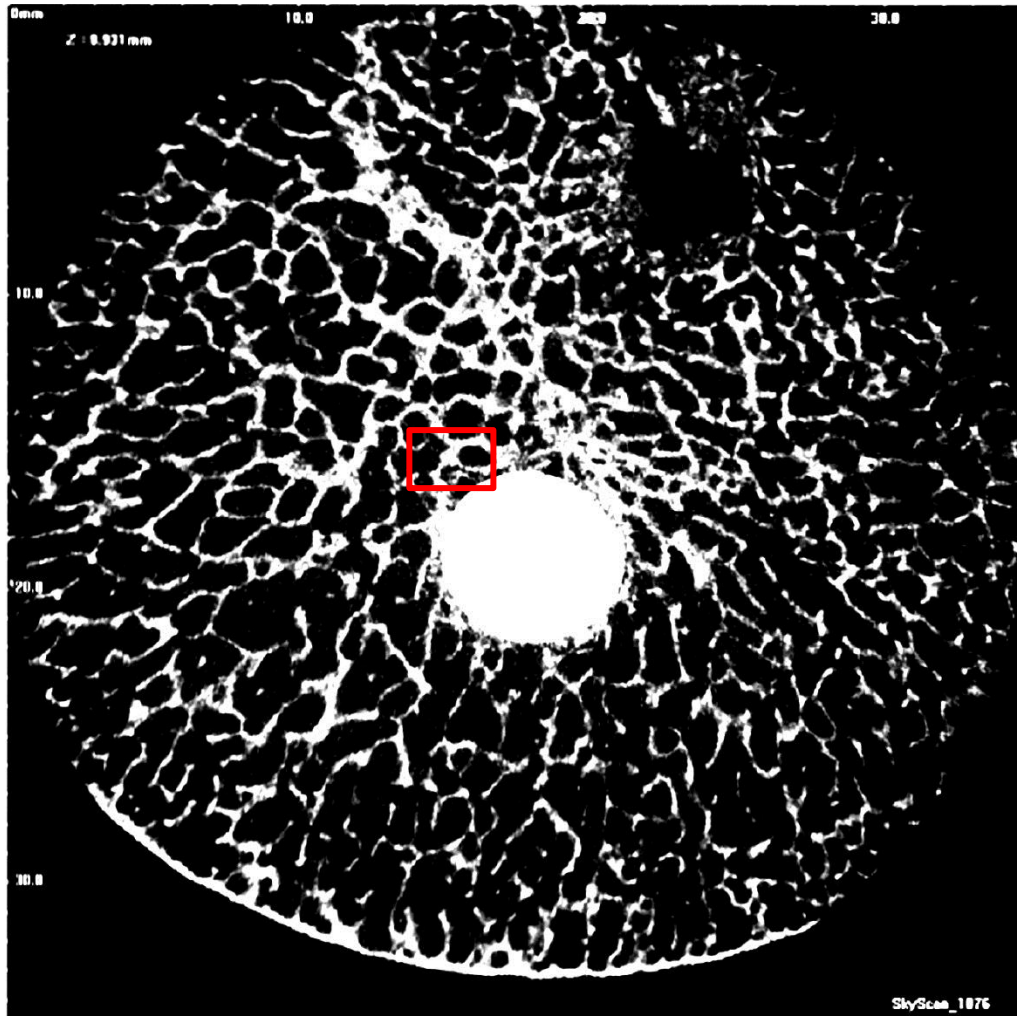


**Figure 8-9:** 2D time-elased images of the screw in the femoral head. The top image is taken at head contact. The red square depicts where the ROI is taken from that is shown in the bottom images. The bottom images show the ROI at 20 %, 60 % 80 %  $T_{HC} - T_{Max}$  and post failure.

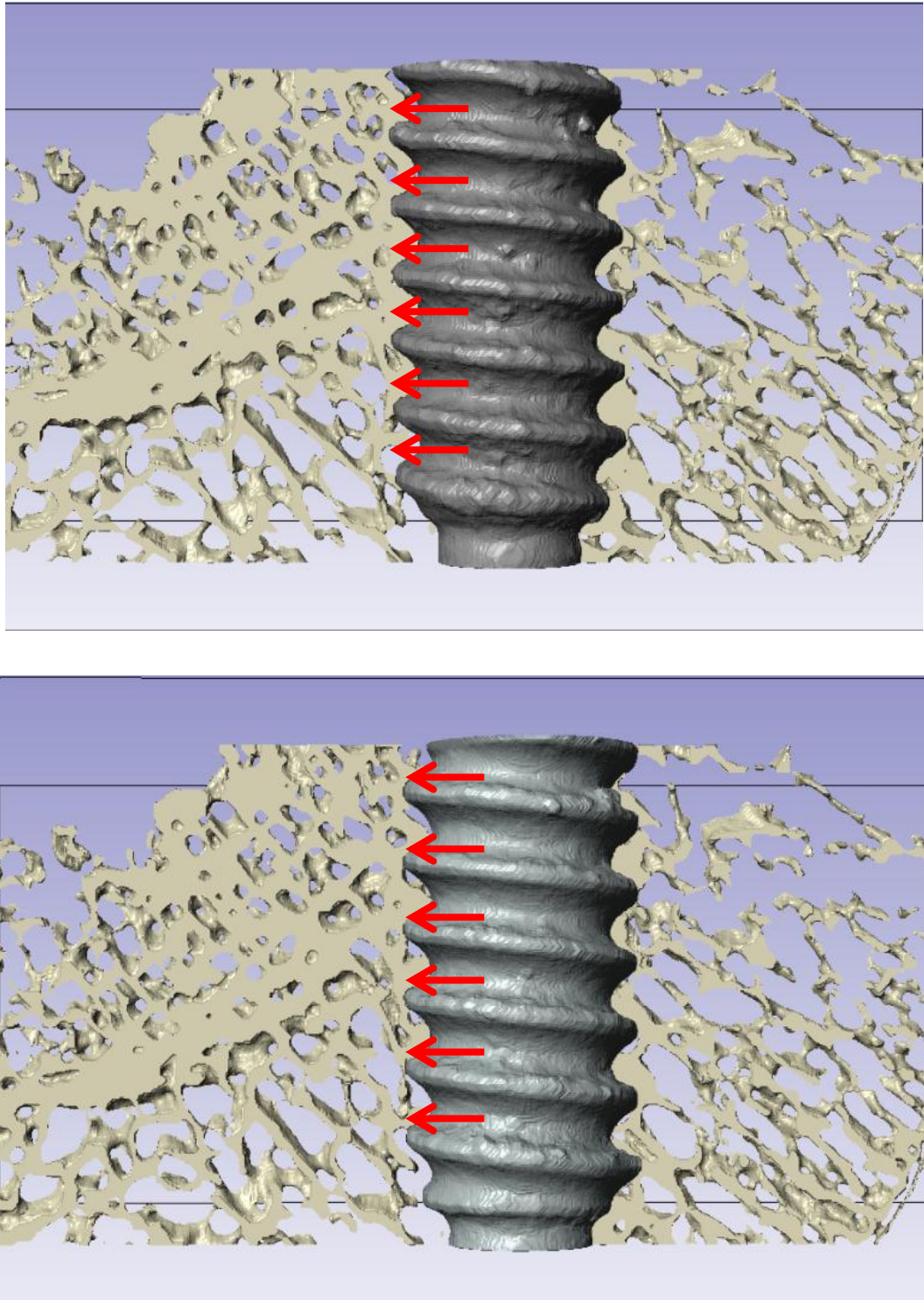


**Figure 8-10: 3D time elapsed slices of bone during screw tightening. The time points are taken at head contact (top) and after failure (bottom). Trabecular deformation is evident along the top face of each of the threads, which extends further than just within the threads of the screw.**

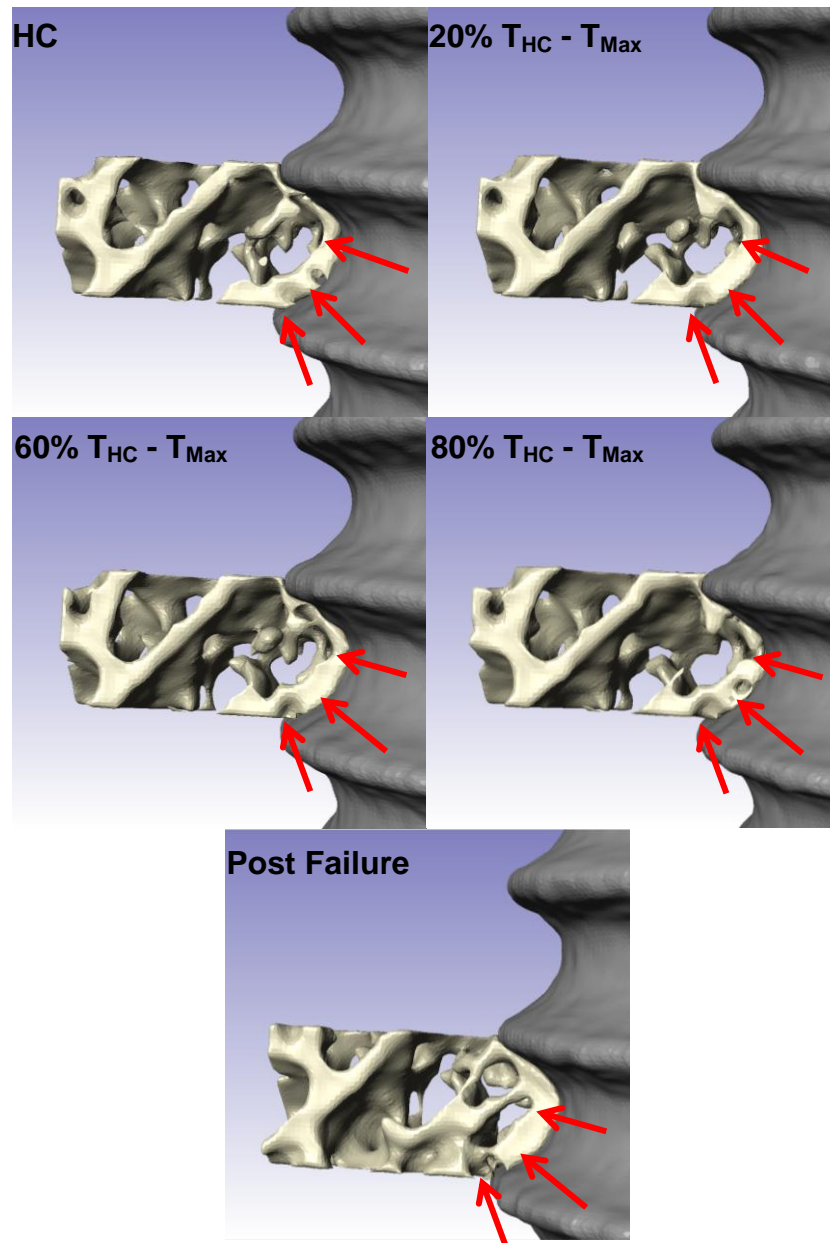


**Figure 8-11: Typical deformation observed in a trabecular spicule surrounding the screw thread. The rendered images were taken at time points specified in the top left corner of each image. Red arrows are used to highlight regions of trabecular deformation.**

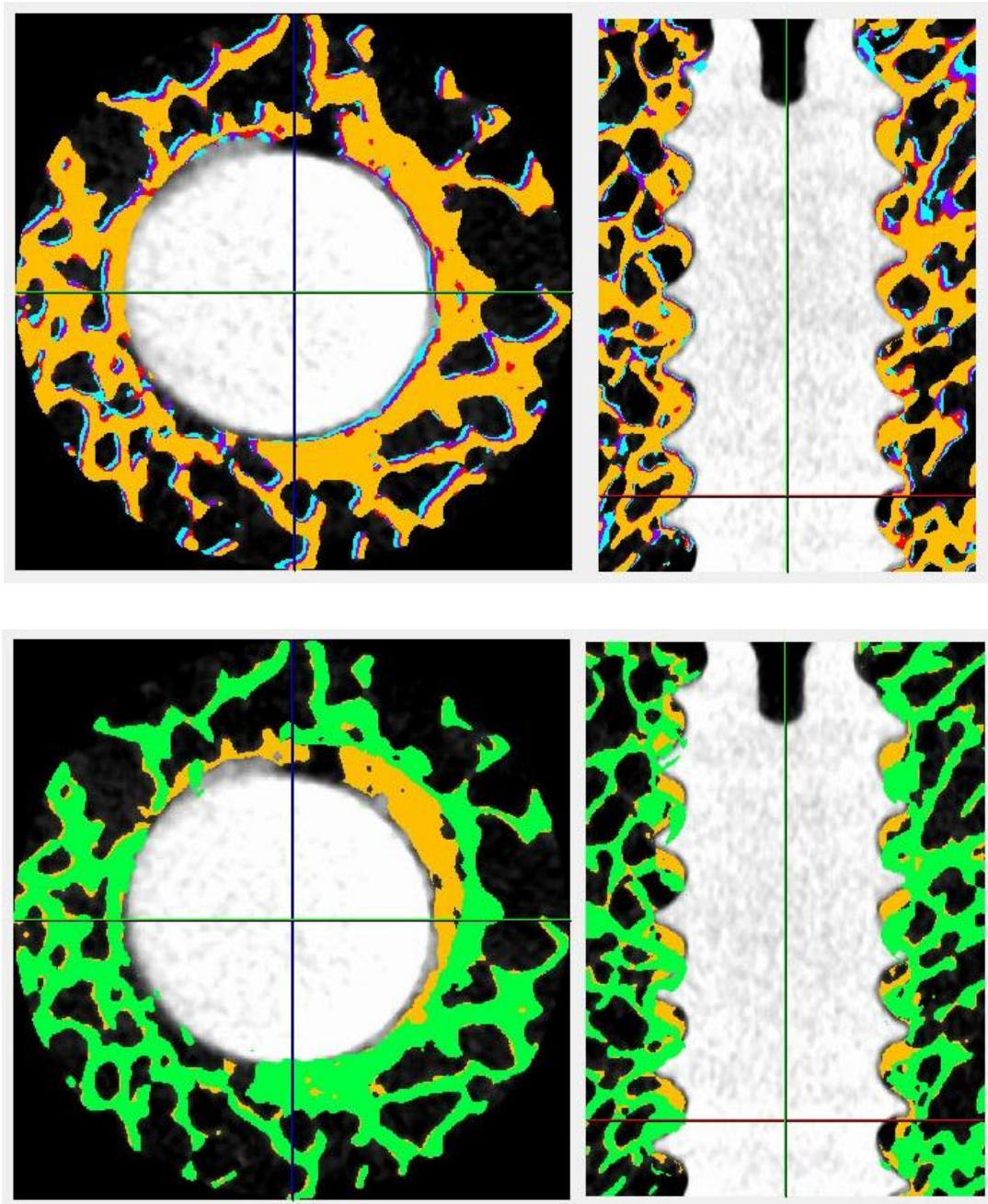


**Figure 8-12: Step-wise acquired masks from micro-CT data sets are overlaid to visualise the trabecular deformations. The column on the left shows a cross section slice through the screw and the column on the right shows a slice along the axis of the screw. Top: the images obtained at head contact (cyan), 65 %  $T_{stripping}$  (purple), 82 %  $T_{stripping}$  (red), 91 %  $T_{stripping}$  (yellow) are overlaid and demonstrate little deformations. Bottom: images obtained at 91 %  $T_{stripping}$  and post failure are overlaid on each other.**

#### 8.4.4 Validation of the micro-FE model

Issues in the FE model generation were encountered as a result of the external meshing software. When meshing in Scan IP some “sticky nodes” were generated that were common to both the bone and screw bodies. When attempting to simulate the rotation, these common nodes resulted in large localised regions of high strain, as the bone tried to move with the screw. This has been identified as a bug within the scanIP software. To eliminate this, nodes that were common to both the bone and screw were identified and bone elements that contained these nodes were removed. The bone was removed, as opposed to the screw, to avoid creating holes in the screw surface and leave a continuous surface for the screw. In total, 3,140 elements were deleted. The resultant FE model consisted of 928,623 nodes and 3,278,207 elements overall, including 802,959 nodes and 2,920,048 elements representing bone and 42,289 nodes and 84,574 elements representing the screw. To check the initial contact status, a zero load analysis, revealed all 21,064 bone elements were in initial contact with the screw (Figure 8-13).

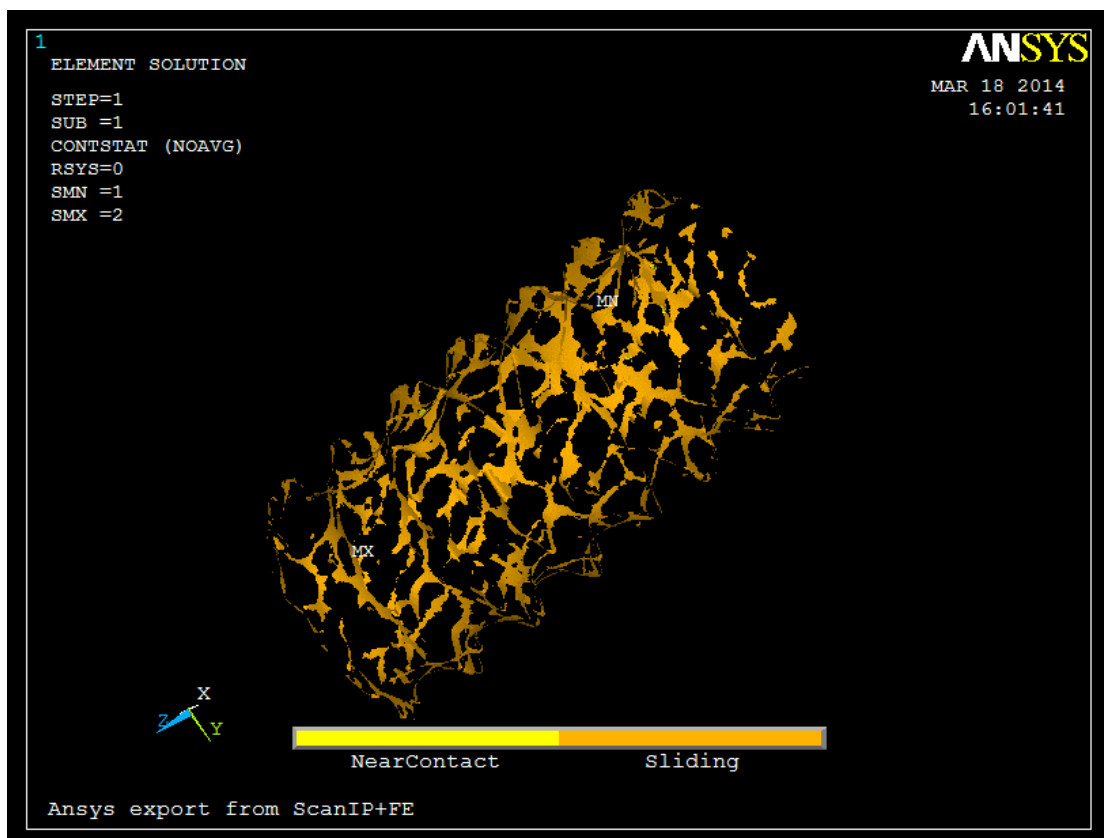


**Figure 8-13: Contact status of contact elements representing the surface of bone in contact with the screw. A zero load is initially prescribed to determine the initial contact status. Contact status is displayed as either “near contact” or “sliding”.**

To simulate the bone-screw interactions, a rotational displacement of 20 degrees was applied. Previous “test” models had demonstrated convergence issues after approximately 20 degrees of rotation, most likely associated with the linear material properties implemented. Consequently a rotational load of only 20 degrees was applied to try to simulate the apparent behaviour over the initial linear region of the torque versus rotation curves observed experimentally. With the above parameters, the FE model took 301 total iterations to complete, however could only achieve 10 degrees of rotation. After this, the model experienced convergence issues. Whilst convergence issues can be addressed by increasing the number of sub-steps the load was applied over, the initial slope of the torque versus rotation curve had already exceeded that observed experimentally and furthermore, geometric nonlinearities had been omitted. Based on the results from chapter 5, which considered geometric and material nonlinearity, the slope of the system at the macro level was largely influenced by the material properties of the underlying bone. Therefore to attempt to reduce the slope of the torque / rotation curve, the elastic modulus of the bone was reduced from 15GPa to 10GPa, which is still within the reported range for femoral head cancellous bone (Table 8-1) and geometric nonlinearity was included. With the tissue material modulus reduced, a rotational load of 50 degrees was applied.

The resultant FE determined torque and compression traces for the model that incorporated geometric nonlinearity and a 10GPa tissue modulus are displayed in Figure 8-14, along with the experimental data. The model took 264 total iterations to complete, however after 20 degrees of rotation, the model again experienced convergence issues due to errors in the element formulation. To try to overcome this, elements with a large von mises strain ( $> 10\%$ ) were selected and deleted and the analysis resumed. This resulted in the deletion of 1,067 bone elements. However element formulation errors again developed after only a further 1.8 degrees of rotation and the model was terminated. The model took 27 days to run, on a .2.40GHz i7-3630QM CPU. Comparison of the FE and experimental data found a similar output for the tightening torque versus degrees of rotation (Figure 8-14). The slope of the compression trace, however greatly exceeded that measured experimentally (85.38 Vs 15 73) (Figure 8-15).

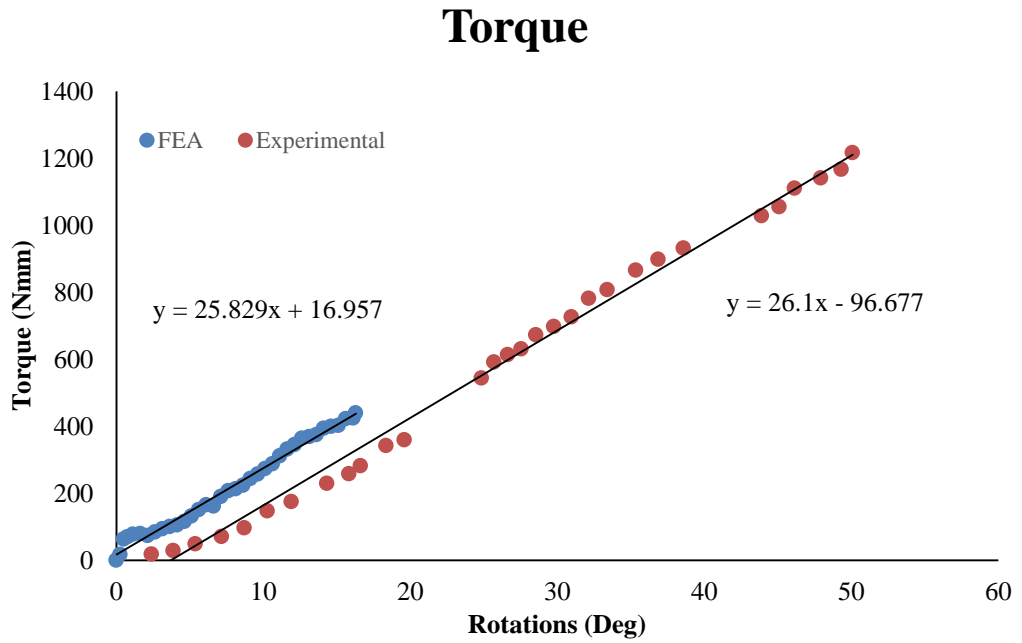


Figure 8-14: Experimental and FE Torque versus Rotations curves.

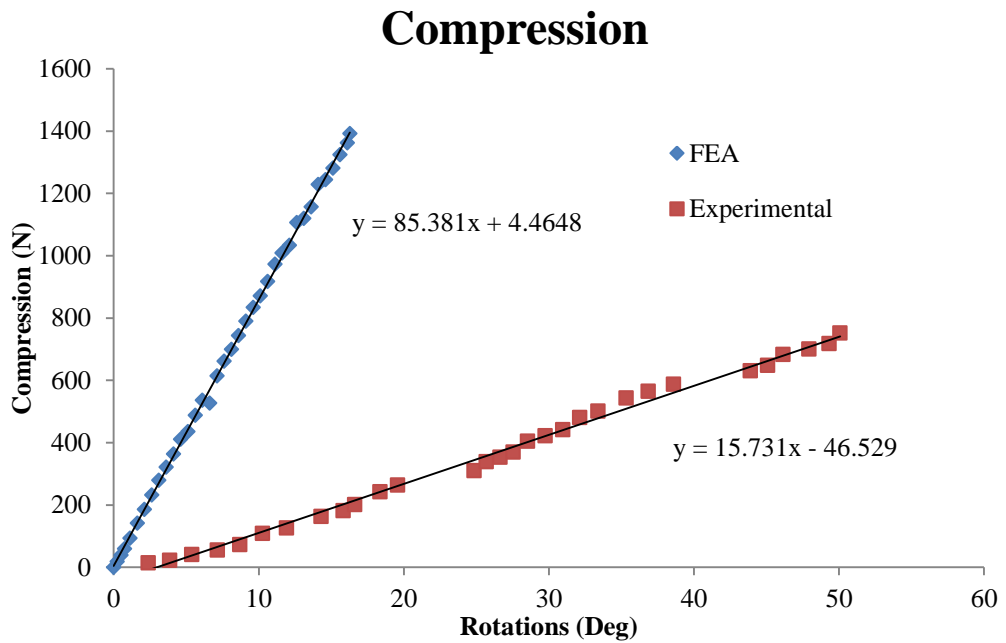
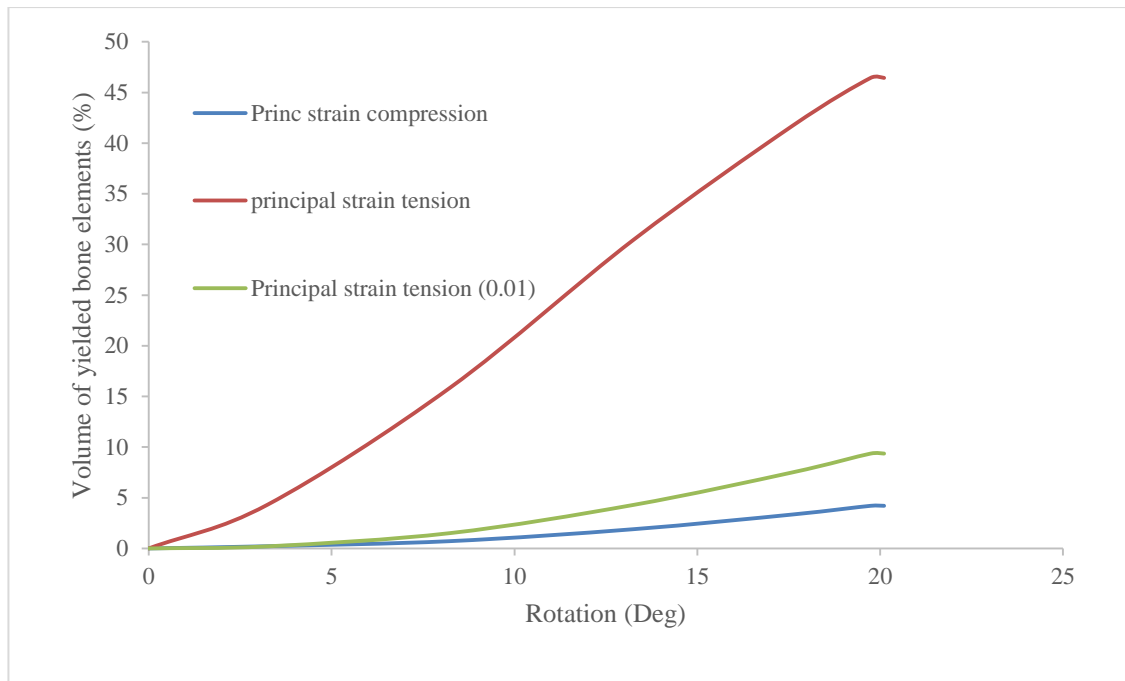


Figure 8-15: Experimental and FE Compression versus Rotations curves.

### 8.4.5 Biomechanics of the peri-implant bone

Similar to Chapter 6, volumes of tissue that had exceeded tensile or compressive yield limits were quantified at each sub-step. Asymmetric yield strains with a tensile yield strain of 0.33% and a compressive yield strain of 1.0% found tensile loading as the dominant mode of tissue failure (Figure 8-16). Applying a symmetric yield criterion (principal strain of 1.0%) still confirmed tensile yielding as the dominant form of tissue failure (Figure 8-16). Plotting the element von Mises strains revealed that initial tissue yielding occurred around the top thread and propagated down the screw with increasing torque (Figure 8-17). The strain field was not constrained to the peri-implant bone, but extended the total width of the VOI.



**Figure 8-16: Volumes of yielded tissue over 20 degrees of rotation from head contact. The elements were considered yielded if the principal strain had exceeded either 1.0% in compression or 0.33% in tension. The volume of tissue yielded as defined by 1.0% in tension is also plotted.**

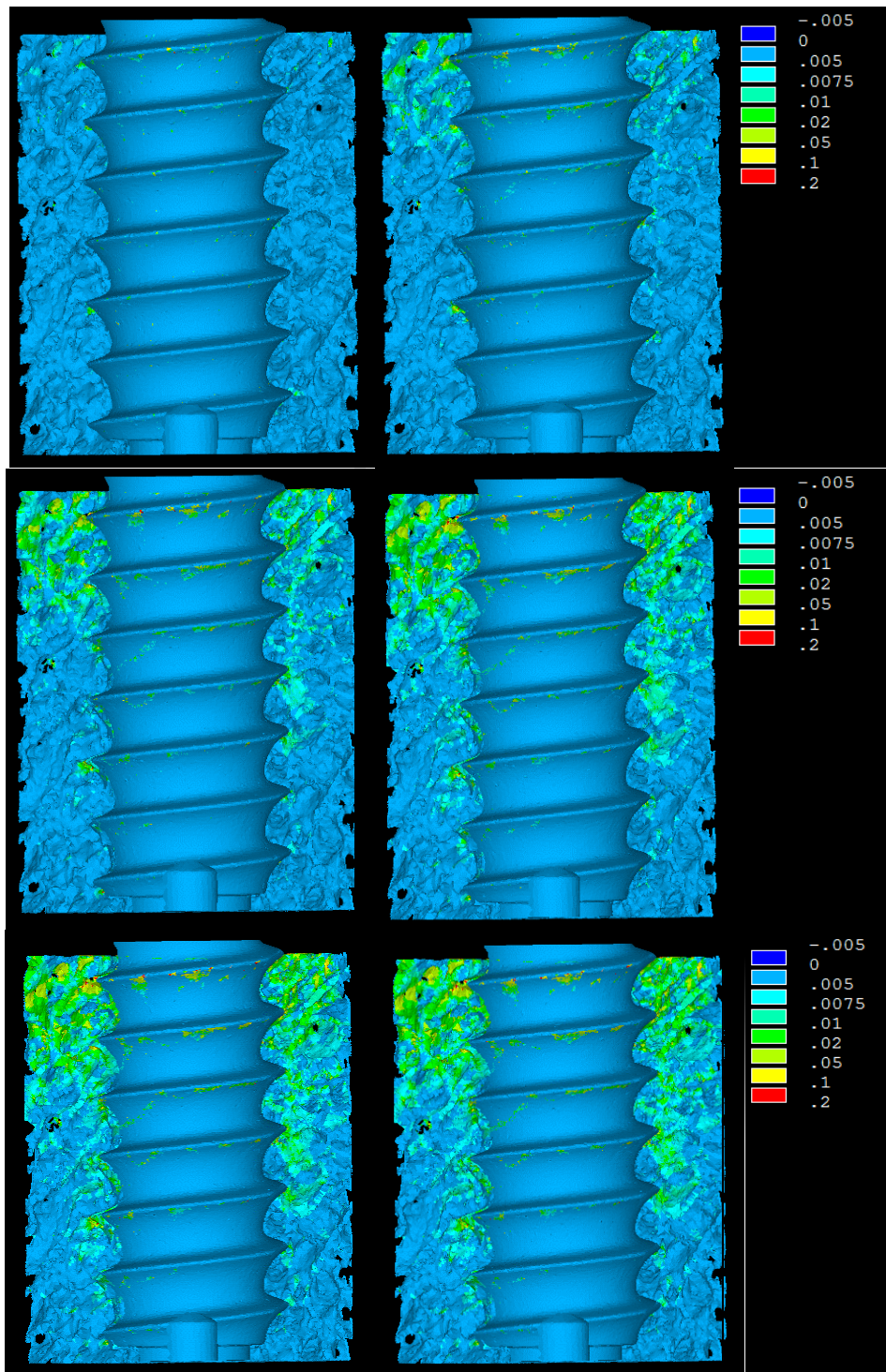


**Figure 8-17: Time-elased von mises strain field of the peri-implant bone. The strain is concentrated around the top of the screw and extends further along the thread towards the tip with increasing applied torque. The rotation angle for each image is: 3.2 deg (Top Left); 8.2 deg (Top Right), 13.2 deg (Centre Left); 17.6deg (Centre Right); 19.7 deg (Bottom Left) and 20.1 deg (Bottom Right)**

A rotation of 20 degrees with a screw which has a pitch of 2mm would be expected to result in an axial translation of 0.11mm. However, if the screw is restricted in axial translation, then an equivalent displacement would be expected in the bone. Figure 8-18 illustrates the axial displacement along the axis of the screw, which ranged from -0.014 up to 0.13 mm, as expected for a 2mm pitch. The largest displacements occurred at the tip of the screw, decreasing in size towards the top of the screw.

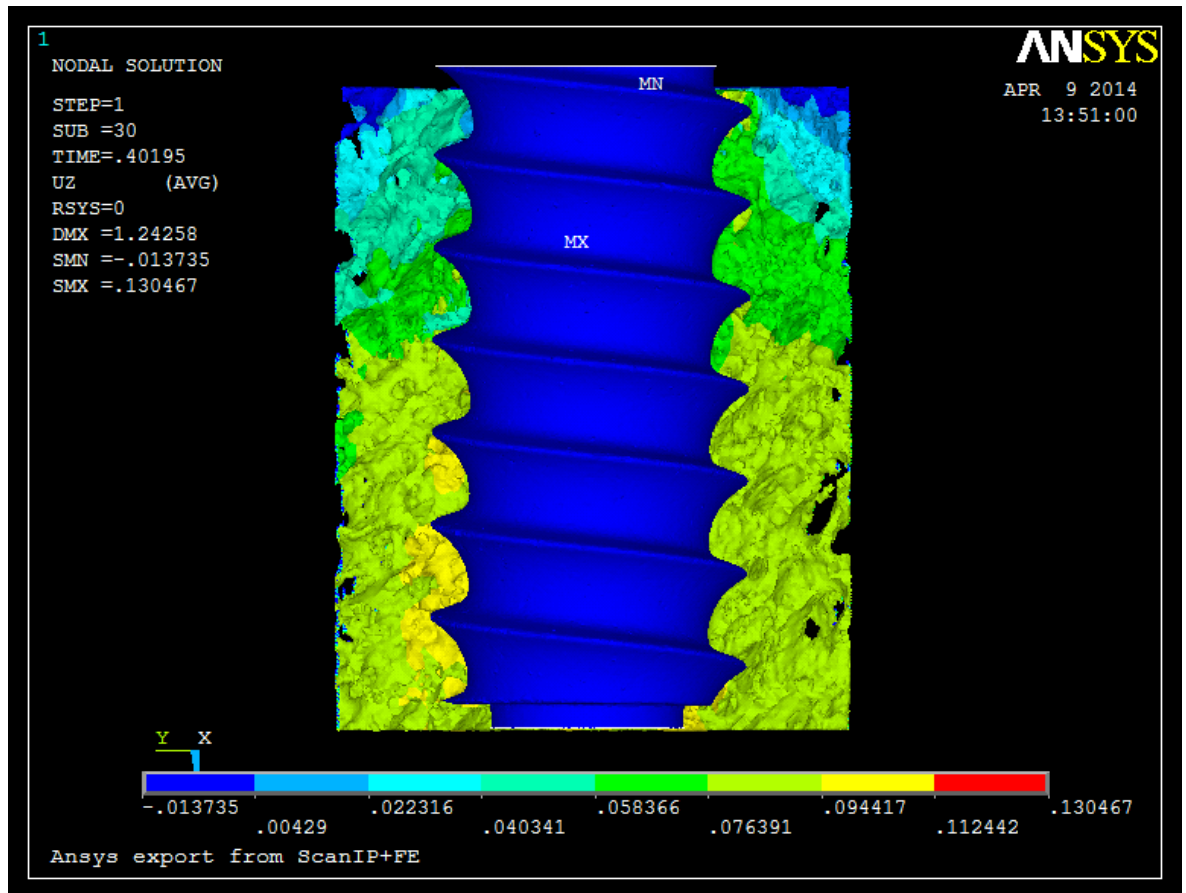


Figure 8-18: Axial displacement field after 20 degrees of rotation. The trabecular deformation is largest at the tip of the screw.

## 8.5 Discussion

Image based assessment of bone under various loading conditions is a novel technique, which to date, has only been conducted on bone specimens under uniaxial compression [128]. This procedure provides the ability to step inside the bone and visualise local failure mechanisms. Previous work that has analysed screw insertion variables has been performed at the macro-scale; to date no other work has analysed the behaviour of

trabeculae at the micro-structural level. The development of the micro-test rig and the procedures described herein provides a unique method to visualise the trabecular deformations during the tightening phase of screw placement.

Although only one specimen was analysed, the device and methodology described herein has demonstrated, for the first time, visualisation of the trabecular behaviour during the tightening phase of screw insertion. It has also verified the ability to accurately predict stripping torque based purely on the torque obtained up to head contact, as well as the capacity to stop at predefined points along the torque versus rotation curve between head contact and  $T_{\text{stripping}}$ .

The step-wise insertion was performed for a single specimen of a 74 year old male. The morphometry of the bone specimen considered is typical for that of the femoral head [278, 279]. Image data were successfully acquired at head contact, 65 % of predicted stripping torque, 82% of predicted stripping torque, 91% of predicted stripping torque and post failure. Torque and compression data were continuously collected during screw tightening.

The stripping torque of 2.93 Nm is within the reported range for bone screws in cancellous bone [104, 221, 224, 247, 248, 272]. The correlation between the theoretical prediction and actual occurrence of stripping was excellent, with the error tending to decrease as the torque approached stripping torque (Table 8-2). This suggests that the stepwise insertion in conjunction with the imaging at each time step had little effect on the overall behaviour of the trabeculae. This is consistent with the findings of Nazarian *et al* (2004) who investigated the effects of step-wise versus continual uniaxial compression testing of cetacean (whale) vertebral cancellous bone specimens and highly porous aluminium alloy cylinders; in the study, the correlation between continuous and the step-wise testing was very high with 98 % of the continuous test behaviour explained by the step-wise compression test [128].

Head contact according to the software occurred at 868 degrees of rotation after the start of recording, however head contact defined by the custom Matlab program, which used a change in slope, detected head contact at 902 degrees of rotation. The effect on measured torque was an increase of 0.03Nm from 1.46Nm at 868 degrees to 1.49Nm at

902 degrees of rotation. Averaging over the preceding 60 degrees at each time point resulted in no difference in plateau torque (1.43Nm).

Using the software post analysis defined point of head contact at 902 degrees, head contact to  $T_{stripping}$  occurred over approximately 91 degrees of rotation. The region from head contact to 91% of  $T_{stripping}$ , however occurred over 50 degrees, and the point from 91%  $T_{stripping}$  to  $T_{stripping}$  occurring over a further 41 degrees. Yield was identified as occurring at 85% of  $T_{stripping}$ , suggesting that trabecular bone tissue exhibits some amount of ductility.

Trabecular bone has been shown to exhibit large amounts of strain prior to micro-cracking [280, 281]. From 3-point bending tests, Jungman *et al.*, 2011, showed trabecular tissue yielding occurred at 1.6% strain, whereas failure did not occur before 12% strain [280]. Szabo *et al.*, 2011, reported similar values for trabecular tissue yield strain, but that strain at trabecular failure ranged from 14.2 up to 61.65% [281]. Together these suggest trabecular tissue is a highly ductile material, especially in comparison to cortical bone tissue, which would explain the ductile behaviour observed in the torque versus rotation traces. The degree of ductility would most likely be affected by factors such as degree of mineralisation as well as increased cement lines [66]. The torque versus rotation traces for individual tests (Appendix B) illustrate this, with some specimens displaying more ductile behaviour between yield and failure compared to others.

The consistency in bone and screw volumes between sequential data sets (Table 8-3) verifies that differences in the architecture between steps is a result of the screw tightening and not caused by image analysis and segmentation techniques. The regions highlighted by the red, yellow and blue circles in Figure 8-9 demonstrate the ability to identify deformation of individual spicules in the sequential image data. 3D segmentation and visualisation of individual spicules, however, is more challenging. Figure 8-11 shows the compaction of a trabecular spicule isolated from the leading edge of one of the threads. Together this demonstrates the ability to obtain sequential image data during screw insertion using the custom designed test rig described herein.8

The image data shown here, along with the analysis from chapter 7 verifies that the majority of plastic trabecular deformation occurs just prior to  $T_{stripping}$ . The effects of

this were further explored by overlaying sequential masks on top of one another and the results showed significant amount of elastic deformation even after failure (Figure 8-12). Only minor trabecular deformation occurs up to the 91 %  $T_{\text{stripping}}$  time point; in the step between 91 %  $T_{\text{stripping}}$  and failure the trabecular tissue within the threads is forced up towards the head of the screw. The peri-implant bone provides the resistance to the shear forces generated along the axis of the screw. A larger volume of bone tissue and the architectural arrangement of the peri-implant bone would be expected to influence the resistance to stripping. Additionally, the ductility of the tissue would influence this; a more ductile tissue would potentially allow more rotations to failure compared to a brittle material. The effects of osteoporosis are not fully understood, however Busse *et al* (2009) suggests that osteoporosis increases the brittleness of bone tissue and this along with the reduced bone mass, would reduce the opposing force against the threads with increasing applied torque. The tissue properties (i.e. modulus, ductility, architectural arrangement) as well as the quantity of tissue most likely all contribute to the holding strength but further investigations are required to better understand their contributions. The region of trabecular tissue damage initiated at the top of the thread and extended down to the tip with increasing torque (Figure 8-17). This is not surprising, since many studies, with respect to screws, have demonstrated that the first engaged thread carries 38% of the load, the second 25%, the third 18% with the seventh free of load [222].

To our knowledge the only other work that has demonstrated an ability to visualise time-elapsd interactions of trabeculae with implants is that performed by Mueller *et al.*, 2013. In their work, they implemented a similar device but performed screw-push in tests as opposed to screw tightening, and considered a dynamic hip screw (DHS) whereas we considered lag screws [277]. Both their analysis and this study demonstrate an extremely novel technique in being able to visualise the interactions of individual trabeculae at the bone-screw interface.

The generation of the FE model is a complex process. Most micro-FE models of trabecular bone use direct voxel conversion, whereby each voxel in the image dataset is translated into an 8-node brick element. However this would create jagged edges at the bone/screw interface, which can lead to regions of high stress, especially under the rotational loading condition applied here. Consequently the bone was meshed using a

tetrahedral mesh to would allow smooth surfaces to interact with the screw. The tetrahedral mesh however means that an iterative solver cannot be used and requires a direct solver, which is highly memory intensive. Therefore the VOI that could be modelled was restricted in size to a cylinder of bone containing the screw that was 11.23mm in diameter and 49mm in length, which contained nearly 1 million nodes and over 3 million elements. A study by Basler *et al.* developed a similar FE model to simulate screw push-in in human femoral heads [282]. Their models considered the entire head, and consisted of up to 63 million elements; due to the model size, they required 1500 CPU's of a Cray super computer system. Such processing power was not available for this work, and consequently a smaller VOI was considered.

The final model required a tissue modulus of 10 GPa, and the inclusion of geometric nonlinearity to accurately simulate the slope of the torque versus rotation curve for the overall bone-screw construct. The model, however, was only able to simulate up to 20 degrees of rotation before element formulation errors lead to a lack of convergence for the model. A tissue modulus of 10GPa is well within the reported range for human cancellous bone of the femoral head (Table 8-1). The importance of incorporating geometric nonlinearity into micro-FE models of bone was highlighted by Stolken and Kinney (2003) [143]. Whilst reducing the elastic modulus from 15GPa to 10GPa resulted in a 20% decrease in the slope of the torque versus rotation trace from 411 to 515 Nmm/deg; it was the incorporation of geometric nonlinearity that further reduced it to within a range comparative to that measured experimentally. Stolken and Kinney, 2003, however highlighted that the true failure mechanisms of trabeculae is a result of a complex coupling between material yielding and structural instability [143]. The incorporation of material nonlinearity and the yield criteria implemented would have a significant impact on the load distribution as well as the failure mechanisms.

To try to simulate the extra bone that was present in the experiment an elastic boundary condition was implemented, which contained all nodes on the exterior surface of the bone (Figure 8-3). The stiffness was initially applied such that it matched an elastic modulus of 15GPa (i.e. 90 MPa). However this resulted in both compression and torque traces that were excessively stiff. Consequently, the spring stiffness was another parameter that was adjusted to assist in matching the FE output to the experimental data. On review of the model, it was also noted that the lower face of the bone was freely

constrained; an elastic boundary condition should also have been included on the lower face, as this face was structurally supported by more bone. This may account for the largest displacements observed at the tip of the screw (Figure 8-18). This may also provide a support for the construct to reduce the compressive reaction load measured through the rigid body of the screw. This is important, as although the FE model was able to simulate the experimental torque versus rotation curve (Figure 8-14), the FE compression versus rotations curve was significantly stiffer, compared to the experimental traces (Figure 8-15). Furthermore, a fully rigid boundary condition was applied to all nodes on the top face of the bone. This was an attempt to simulate the gluing of the bone face to the base-plate; however the bone present in the model would not have been rigidly constrained. In reality, the glued face would have been located much further away from the thread. To better simulate the behaviour of these elements, an elastic constraint would have been a better choice for this face of the bone. This may also account for the concentration of the strain field at the top face of the bone (Figure 8-17).

The augmented Lagrange algorithm was implemented for the contact between the bone and screw. Whilst the penalty method provides the option of adjusting the contact stiffness to achieve a solution, the convergence with augmented Lagrange is more robust. If material nonlinearity is incorporated the penalty method may provide another variable (contact stiffness), that can be utilised to adjust the model to match the experimental simulation.

A further limitation of the current model is the exclusion of a friction coefficient between the bone and screw threads, however during tightening phase the effects of friction between the bone and threads would most likely be negligible. The insertion and tightening of a screw can be broken down into three phases: insertion, tightening and stripping, which are described in detail in section 7.1. The initial phase where the threads cut through the bone is strongly influenced by the friction between the screw material and the bone. The tightening torque, however is primarily a result of the shear strength of the surrounding bone restricting the axial force generated by the screw. For this reason and to reduce complexity of the model, the friction coefficient was omitted. Future models that sought to investigate the effects of including friction, however, could theoretically calculate it from the plateau torque.

The FE model, however, was able to simulate the apparent torque trace up to 20 degrees of rotation past head contact. According to the experimental data this equated to approximately 65% of  $T_{stripping}$ . After this errors associated with element formulation prevented the model from converging. Element formulation errors can occur due to a highly concentrated force, such that the element shape functions are no longer able to characterize the deformed shape of the element under load. In these cases the element formulation errors are often preceded by small or large pivot warnings, as was the case here. In an attempt to eliminate these singularities, elements with a von Mises strain  $> 0.1\%$  were deleted and the analysis resumed, but within 2 degrees similar issues were encountered. It is possible that this was associated with the rigid boundary conditions applied to the top face of the bone, as the highly strained bone elements were limited to this region.

Chapter 5 demonstrated that for on-axis loading nearly ten times the volume of tissue damage accumulation was required before apparent yielding compared to off-axis loading. The shear loads generated by the threads would be more comparable to the off-axis loading condition. Bevill *et al.*, 2009, considered both vertebral and femoral neck specimens under on- and off-axis ( $45^\circ$ ) and reported that femoral neck specimens experienced significantly larger volumes of total tissue failure at apparent yield for on-axis, however off-axis results were similar to vertebral with less than 5% of total tissue failure occurring at yield [124]. Their study, however implemented a higher elastic modulus and very low tissue yield strains (0.81% in compression and 0.33% in tension). Considering a tensile yield strain of 0.33% for this model resulted in a large volume of tensile tissue yielding (Figure 2 13). Others have reported trabecular tissue yields at levels closer to 1% [213, 280, 281, 283, 284]. Applying this level of tissue yielding, a significantly lower volume of tissue had yielded in tension at any equivalent rotation, but the volume undergoing tensile yielding was still almost twice that in compression. Immediately after screw insertion, only the top surface of the thread profile and the crest are in contact with bone [284]. Continued rotation after head contact results in a force applied from the top threads of the screw to the bone-in-contact, whilst the bone on the underside of the thread is released from contact. This is best observed in Figure 8-10, where several gaps appear on the under-side of the thread down the left-hand side of the screw in the “failure” image.

It is important to note the limitations of the study; firstly only one specimen was analysed. A second specimen was tested, however a bug in the software caused errors during the tightening phase and the torque and compression data could not be analysed. In spite of this, the overall goal was a proof of concept and the device and methodology were able to accurately predict  $T_{\text{stripping}}$  and obtain sequential image data at specified time points, with a high degree of accuracy.

A further limitation is the artefact in the image data, which is a result of both the material of the screw (aluminium), but also the debris associated with insertion. Within the images, it is not possible to identify what elements are structurally intact trabeculae and what is debris associated with insertion. Tapping prior to screw insertion may have improved this, however tapping is not clinically performed in osteoporotic bone and so this was not done here. Consequently when segmenting the bone and screw almost the entire surface of the screw appears “coated” in bone. This was the reason for applying the morphological dilation to the screw during the segmentation. As a result, 21,064 out of 80,304 screw elements were in contact with bone, which equates to 26% of the surface. This is not unrealistic, given that the VOI had a BV/TV of 28%. It is possible to reduce the noise associated with the images by reducing the step size and increasing the frame averaging, however this significantly increases the scan time. The ultimate aim of this thesis was to enable step-wise insertion of the screw and allow visualisation of the resultant bone-screw construct at each step. Consequently a second limitation was the need to minimise scan time, which resulted in a higher level of noise in the images.

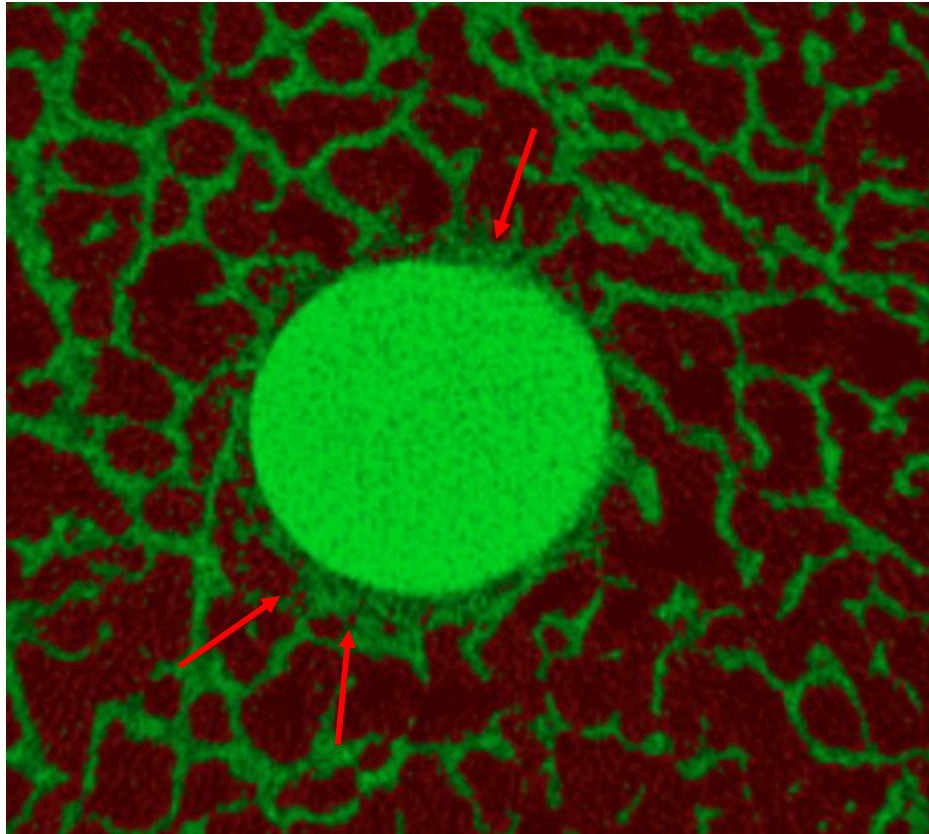


**Figure 8-19: Binarised image of the bone-screw interface. The red arrows indicate regions at the interface where it is not possible to discern fully intact trabeculae from debris.**

In terms of the FE model, the model was restricted to a small VOI due to available computing power. To try to compensate for this, elastic boundary conditions were employed however these were only applied to the sides of the cylinder and should have included the base. A rigid boundary condition was also applied to the top face, which may have been better modelled using an elastic one.

Ideally, the FE model would be generated by segmenting out the screw and the bone in the dataset obtained at head contact. However considerable noise is present at the bone-screw interface. Post-processing analyses are available to minimise the metal-artefact, however there still remains significant debris at the bone-implant interface as a result of the screw insertion. Consequently the screw was virtually placed in the bone however the head contact data was used to obtain the most accurate alignment and position in space, which was then applied to the pre-drill scan by a Boolean subtraction. Using this method does not incorporate any deformation of trabeculae that may have occurred as a result of insertion. Further image analysis and co-registration of the images obtained

prior to drilling with the images obtained at head contact may provide further insight into this.

Finally, the model only incorporated linear material properties. The incorporation of non-linear material properties would be more beneficial if the entire geometry of the femoral head could be analysed. Implementing tissue yielding would require a redistribution of the applied load. Trying to conduct this in a small VOI would result in excessive loading, which would not have occurred experimentally. Any future models should aim to incorporate more bone tissue as well as nonlinear material properties. Models that incorporate material nonlinearity and a larger number of degrees of freedom, however are extremely computationally expensive and can take several weeks to converge.

In conclusion, it has been demonstrated that the micro-test rig device is capable of performing time-elapsd image acquisition during the tightening phase of screw insertion. The algorithm derived in chapter 7 allows accurate prediction of stripping torque and the ability to stop screw insertion at any given time point up to  $T_{\text{stripping}}$ . The sequential image data allows visualisation of the trabecular behaviour during the tightening phase of screw insertion. The post failure images show that the majority of tissue failure occurs within the trabeculae in the immediate vicinity of the thread. The FE model is a simplistic representation of the experimental set up, but demonstrates the ability to quantify the strains generated during screw tightening as well as the volume of tissue damage at specific points. Whilst the model requires further work, the methods outlined here provide a framework for future development. Further testing on a larger number of specimens would allow parameterisation of the FE variables that can be tuned to accurately simulate the torque and compression measured experimentally. Future models would benefit from incorporating as much bone as possible, but this is dependent on computing power available.

# 9 SUMMARY AND FUTURE RECOMMENDATIONS

## 9.1 Summary

Screw stripping during insertion is a common challenge associated with fracture fixation in osteoporotic bone. The overall objective of this dissertation was to develop a method that would allow both qualitative and quantitative assessment of trabecular mechanics during the tightening phase of screw placement in cancellous bone. This was accomplished by a combination of time-elapsing image analysis and image based computational modelling. This has the potential to provide a better understanding of mechanisms that influence over-tightening of screws, as well as identifying specimens that may be at a higher risk of stripping.

### 9.1.1 Micro-FEA vertebral bone

The first section of this dissertation explored the use of the FE method for the analysis of cancellous bone using cadaveric vertebral specimens. It was demonstrated that a smaller volume of interest at least  $6 \text{ mm}^3$  in size was an adequate surrogate of a larger test specimen, provided that the region of interest was selected such that the bone volume fraction was a true representation of the larger specimen.

By analysing vertebral specimens under uniaxial loading conditions in both the SI and AP directions, the validity of an isotropic tissue modulus was demonstrated for micro-FE analysis of cancellous bone. However the micro-mechanics of vertebral trabeculae were found to be distinctly different under the two considered loading conditions. Under SI loading, localised compressive strains dominated, whereas under AP loading, compressive and tensile strains were equivalent.

Results from nonlinear analyses of vertebral specimens emphasised that if rigorous test methods are not available to determine specimen specific tissue modulus, literature derived average tissue modulus values are adequate at enabling simulation of apparent level mechanics. Additionally, the non-linear analysis revealed which micro-level parameters influence the macro-level behaviour; with the tissue level modulus largely influencing the apparent modulus and tissue level yield levels influencing the apparent yield. This information provided a background for trabecular mechanics and tissue properties, which would provide a foundation for the generation of a complex FE model to simulate screw tightening.

### 9.1.2 Understanding screw insertion

Strong linear correlations were found between plateau and stripping torque for the aluminium screw in femoral head bone. This is an important finding, because it confirms the ability to predict  $T_{\text{stripping}}$  based only on the torque required to achieve head contact. Clinically, the final stages of screw tightening after head contact are performed by the surgeon, to what they subjectively perceive to be an adequate tightening torque. In low density bone however, and with screws of different thread profiles and materials, inadvertent stripping of the thread during insertion occurs with relatively high frequencies. The technique of screw insertion described within this dissertation has allowed for the first time the visualisation of trabecular deformation with respect to applied torque. The image data suggests that the largest volume of tissue deformation occurs on average at approximately 86% of stripping torque. Whilst it is known that some amount of tissue loading stimulates bone regrowth; the question remains as to what is a healthy amount and at what level is the bone-screw construct compromised.

The question still remains, however, as to how tight is “tight enough”. Analysis of the torque traces to failure demonstrated that tissue yielding occurred on average at 86% of  $T_{\text{stripping}}$ . This was further evidenced by the analysis of the image data, which showed little bone deformation up to the step at 80 % ( $T_{\text{plateau}} - T_{\text{stripping}}$ ). This suggests that tightening cancellous lag screws past 86% of  $T_{\text{stripping}}$  induces plastic deformation in the peri-implant bone, and may weaken the bone-screw construct. Further investigations would be required to verify the effects on the strength of the bone-screw construct with increasing levels of insertion torque.

Additionally the predictive ability of  $T_{\text{plateau}}$  allowed the development of a method to conduct stepwise screw insertion, where the bone-screw interface can be visualised at specific points along the torque/rotation curve. This is a novel technique that has not been conducted previously.

### 9.1.3 Micro-FE model of the bone-implant interface

The collection of image data at head contact was used to generate a micro-FE model to analyse the behaviour of the peri-implant bone at the micro-structural level during the final tightening phase of screw insertion. Whilst the step-wise image data allows visualisation of the peri-implant bone, the addition of micro-FEA allows

quantification of tissue level strains at specific levels of  $T_{\text{Stripping}}$ . This is the first study to present a methodology to relate the micro-structural biomechanics to macrostructural properties of bone under the unique loading condition of screw insertion.

The FE model demonstrated that the tissue loading is concentrated around the first thread and propagates down the threads with increasing applied torque. Whilst the implementation of only a linear material model means the absolute values of tissue strain measured are not relevant, the pattern of strain concentrations may provide important information for screw design in the future.

## **9.2 Considerations for future work**

### **9.2.1 Micro-FE model**

The micro-FE model presented herein is highly complex comprising nearly one million nodes and over three million elements, as well as incorporating both contact and geometric nonlinearity. Because material nonlinearity was not incorporated accurate simulation of apparent yielding is not possible. Additionally, whilst regions subject to high levels of strain are identifiable, the transmission of loads and subsequent failure mechanisms cannot fully be explored. Future recommendations would be to incorporate nonlinear material properties and potentially incorporate element death to better simulate micro-damage accumulation.

Finally, several model parameters can be modified to allow matching of the FE apparent behaviour to that observed experimentally, such as the yield strains and failure models for nonlinear material incorporation, as well as boundary conditions (elastic versus inelastic), and the incorporation of element death. The next step, would be to analyse the effects of varying these parameters so that the experimental and FE output for simulating compression under the head of the screw can be better matched, and to perform this over further specimens.

### 9.2.2 Validation of the model

Whilst the apparent behaviour of the model can be validated by checking with the experimentally determined torque and compression traces, this does not verify the underlying micro-structural behaviour under these loads. The strength of the step-wise image acquisition is that it is possible to visualise exactly how the trabeculae deform in response to screw tightening. The FE model could be further validated at the micro-structural level by performing digital volume correlation to generate a strain map throughout the trabecular network. Comparison of this with that generated by the FE model at corresponding time points (i.e. degrees of rotation) would verify the ability of the model to accurately simulate the trabecular behaviour during screw insertion. The FE model would also be further validated by the incorporation of a more realistic material model that had been determined from tissue (not apparent) level experimentation.

## 9.3 Applications

The development of such a model has a number of applications; the first is providing a tool to understand the fundamental properties that influence both insertion torque and compression. Compression is a marker of the stability of the bone-screw construct, and insertion torque is the corresponding parameter surgeons have intra-operatively to gauge this. Understanding what factors contribute to each or both of these may help in optimising both insertion techniques and screw designs.

Furthermore the advantage of FE models is that they are able to remove inter-specimen variability. The same specimen can be used to explore the effects of parameters such as insertion torque, screw material, screw thread profile and screw length engagement. Being able to run initial tests of these parameters on FE models would potentially minimise the need for extensive cadaver testing.

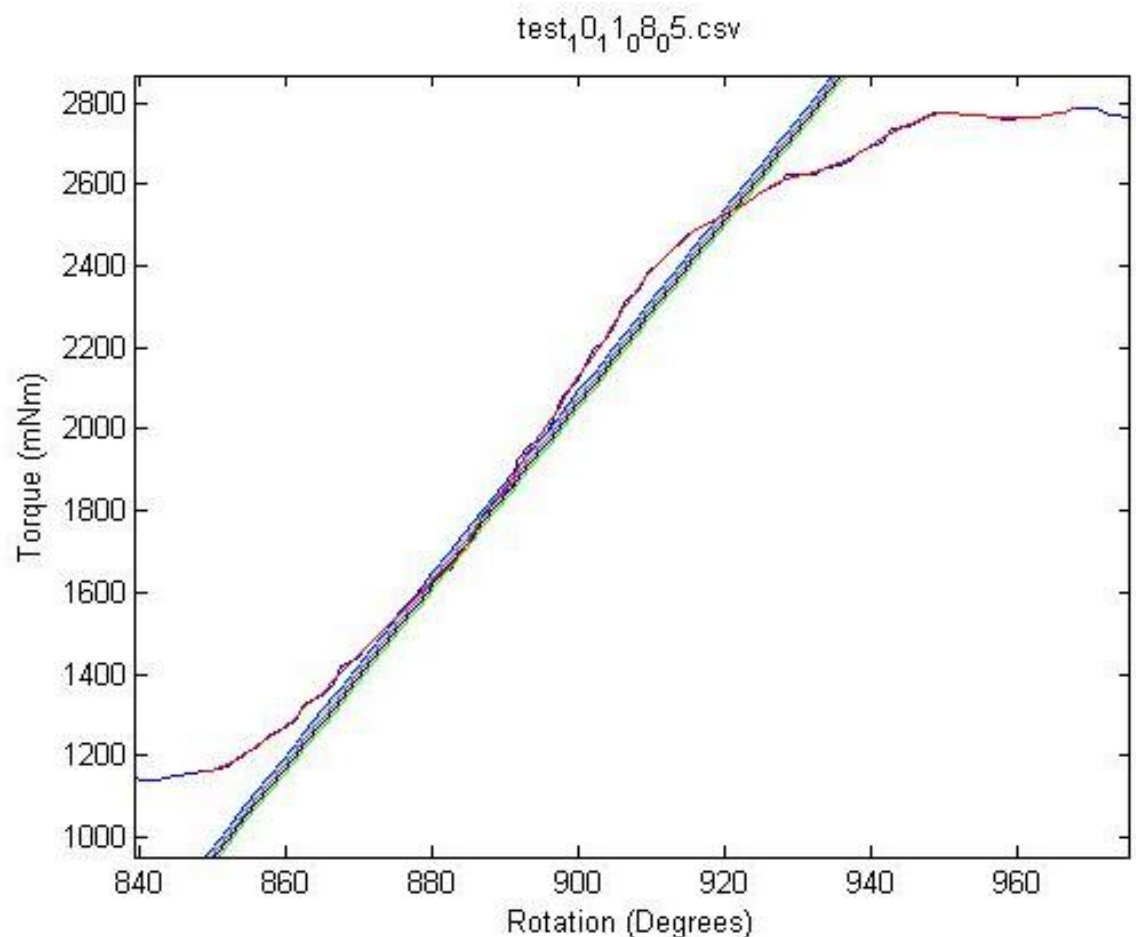
## 9.4 Final Remarks

The micro-test device and the methods described in this thesis have allowed for the first time both qualitative and quantitative assessment of the micro-mechanics of the peri-implant bone during the tightening and stripping phases of screw insertion. With testing of further specimens, this will provide estimates as to the levels of screw tightening that will provide optimal stability of the bone-screw construct (adequate compression) whilst minimising micro-damage to the surrounding bone.

# Appendices

## APPENDIX A: DETERMINATION OF OFFSET FOR ANALYSIS OF THE TORQUE VERSUS ROTATIONS SLOPE.

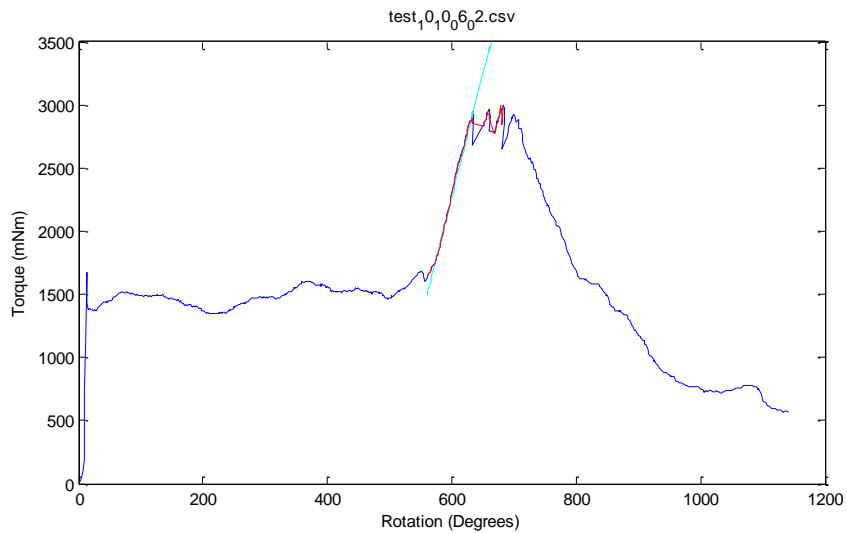
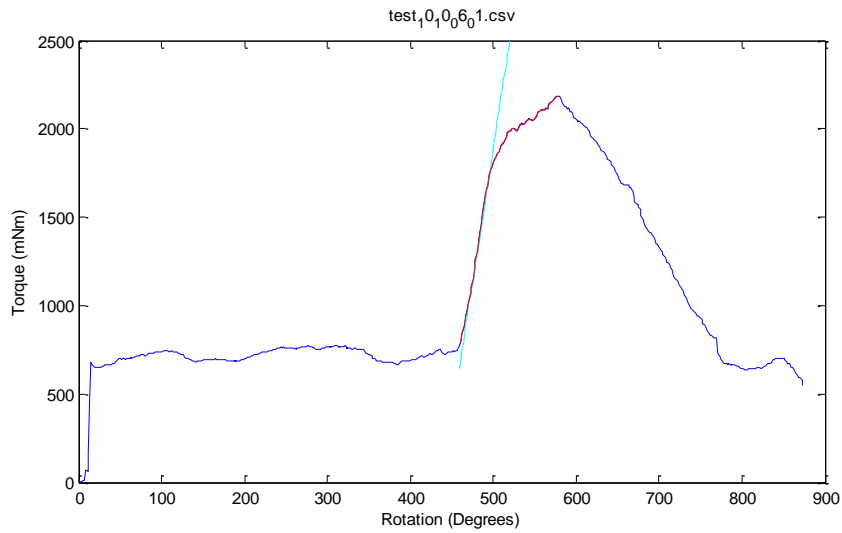
The slope of the torque versus rotation curve was defined over the region of the curve from 0.1 to 0.6 of ( $T_{stripping} - T_{plateau}$ ). An offset line with the same slope was then generated and offset either 0.2 (blue), 0.5 (cyan), 1.0 (magenta), 1.5 (black) or 2 deg (green). By varying the offset the average yield torque varied between 2.04 and 2.13 Nm. The yield torques including average and standard deviation for each offset value are shown below. As can be seen by the plot and table data varying the offset had minimal effect on most specimens. For a few specimens selecting the offset of 2 degrees resulted in the yield close to or after  $T_{stripping}$ . Consequently a 1.0 degree offset was used.

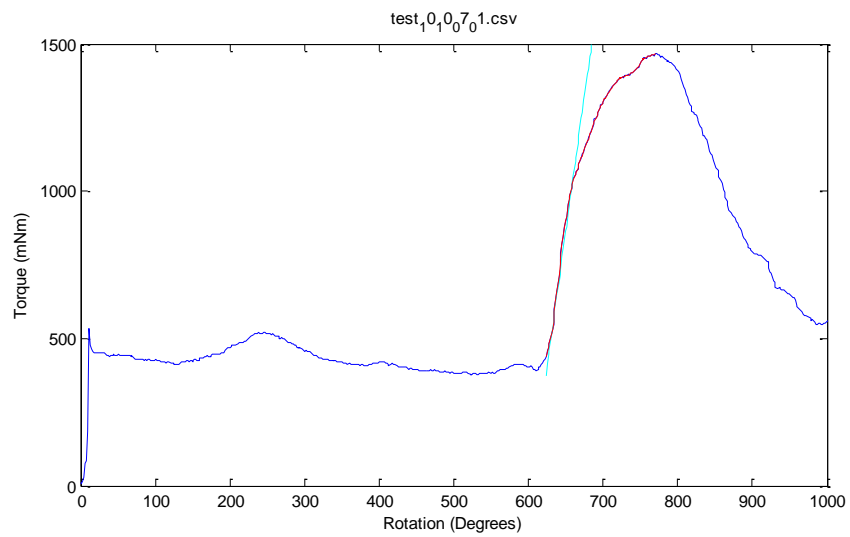
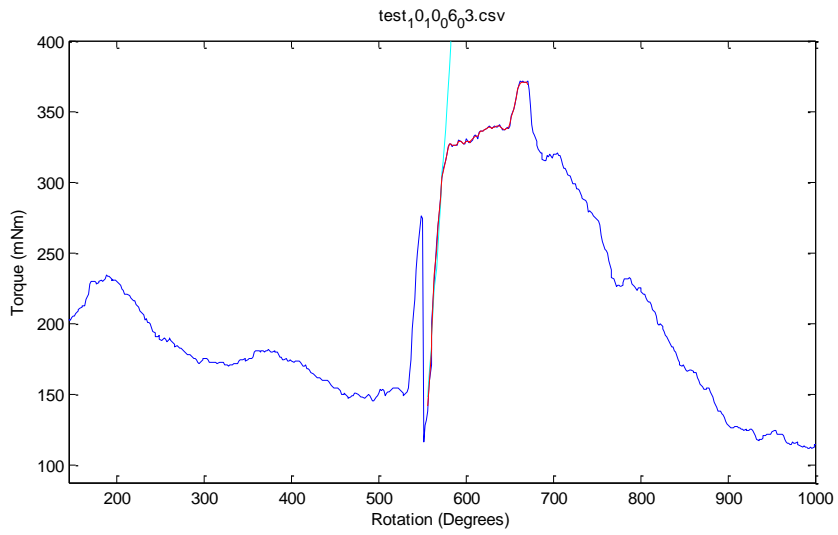


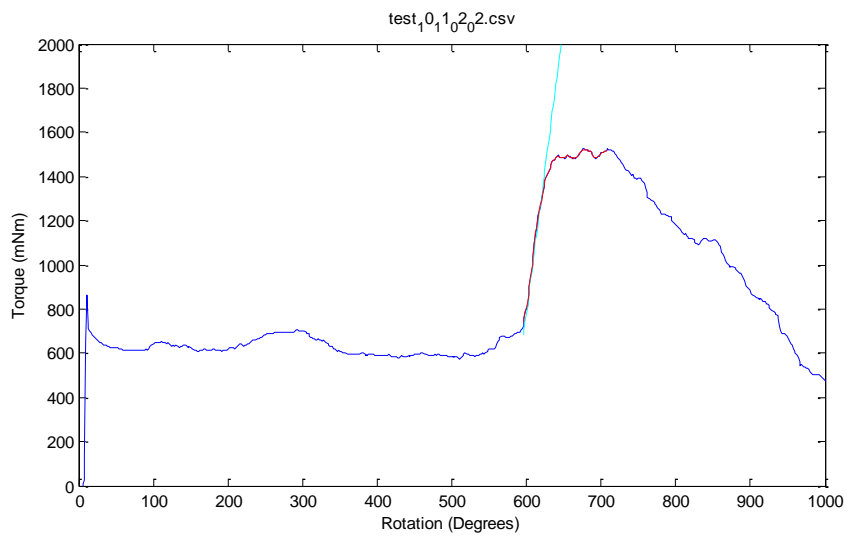
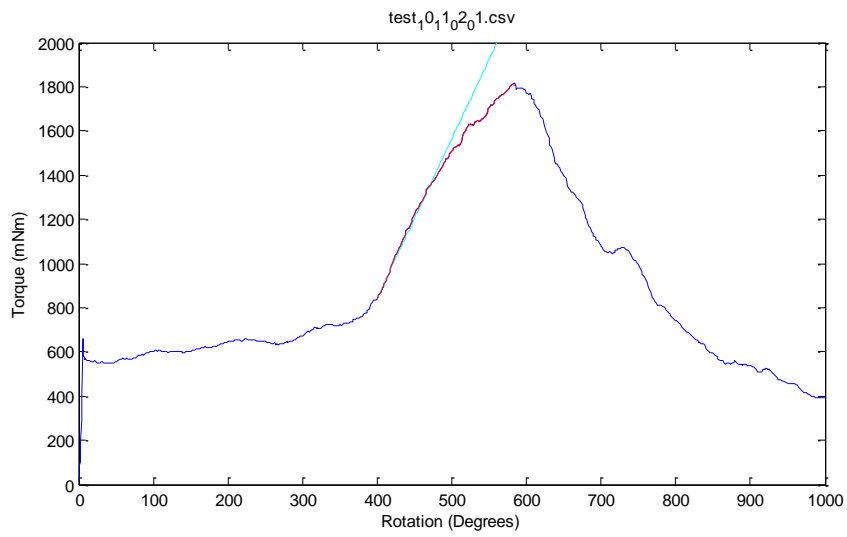
Offset:	0.2 deg	0.5 deg	1.0 deg	1.5 de	2.0 deg
Yield	1.68	1.74	1.78	1.80	1.80
Torques:	2.91	2.91	2.94	2.92	2.92
	3.03	3.03	3.09	3.15	3.20
	1.01	1.02	1.02	1.06	1.07
	1.36	1.36	1.36	1.38	1.38
	1.26	1.30	1.33	1.35	1.35
	3.22	3.31	3.38	3.44	3.48
	2.50	2.50	2.70	2.72	2.77
	1.46	1.53	1.59	1.61	1.63
	3.04	3.04	3.20	3.24	3.28
	1.69	1.69	1.74	1.74	1.76
	1.34	1.40	1.40	1.42	1.47
	2.59	2.59	2.50	2.60	2.61
	3.35	3.35	3.39	3.43	3.47
	2.48	2.50	2.54	2.54	2.55
	1.81	1.81	1.84	1.84	1.85
	3.13	3.21	3.25	3.26	3.26
	1.47	1.47	1.47	1.47	1.47
	1.63	1.63	1.68	1.69	1.72
	2.54	2.55	2.55	2.55	2.57
	1.93	1.93	1.95	1.95	1.95
<b>Mean</b>	2.04	2.05	2.10	2.11	2.13
<b>SD</b>	<b>0.83</b>	<b>0.83</b>	<b>0.86</b>	<b>0.86</b>	<b>0.87</b>

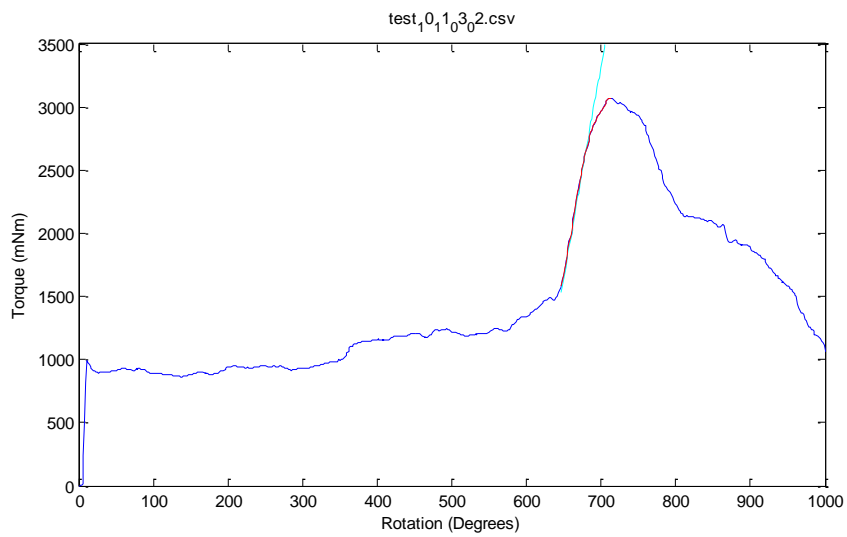
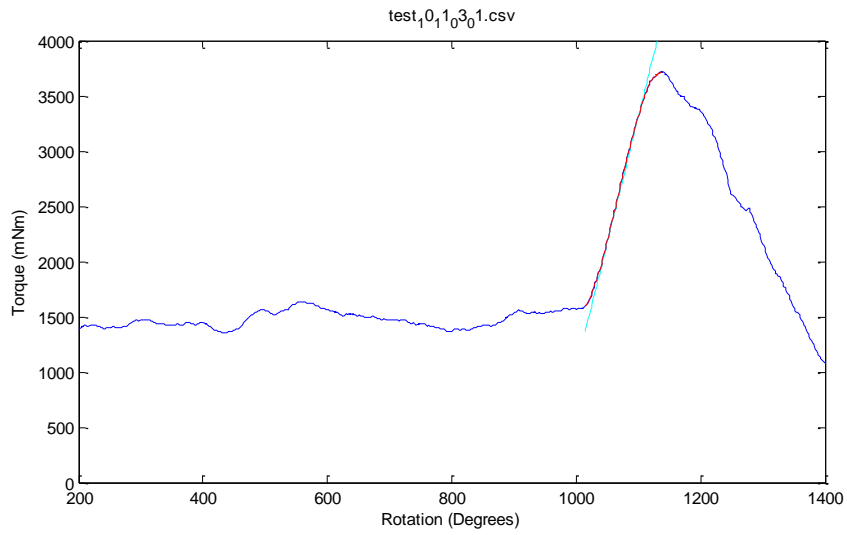
## APPENDIX B: TORQUE VERSUS ROTATION PLOTS

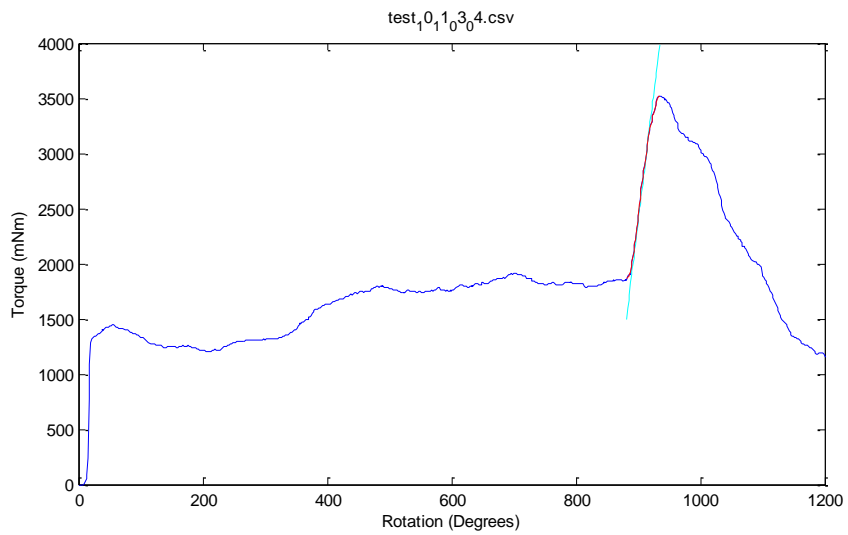
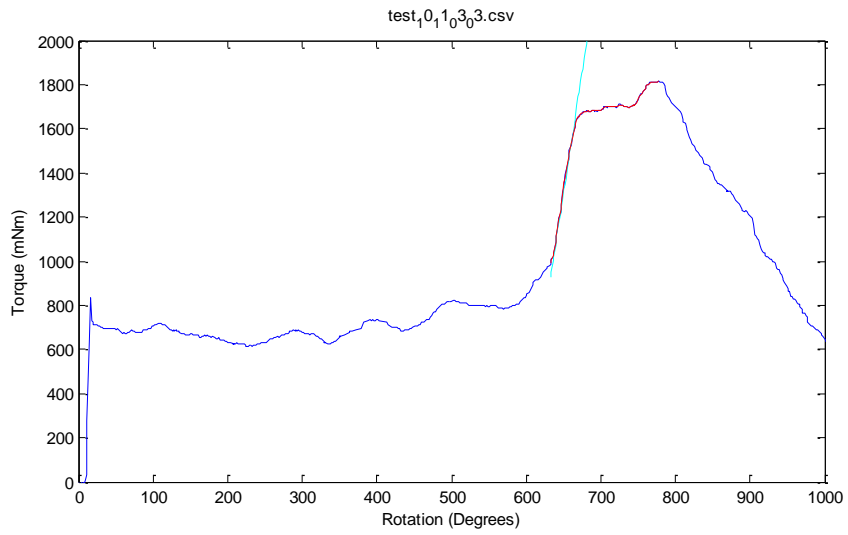
Individual torque versus rotation plots for each specimen. The original trace is displayed in blue, the smoothed trace in red and the 1.0 degree offset in cyan.

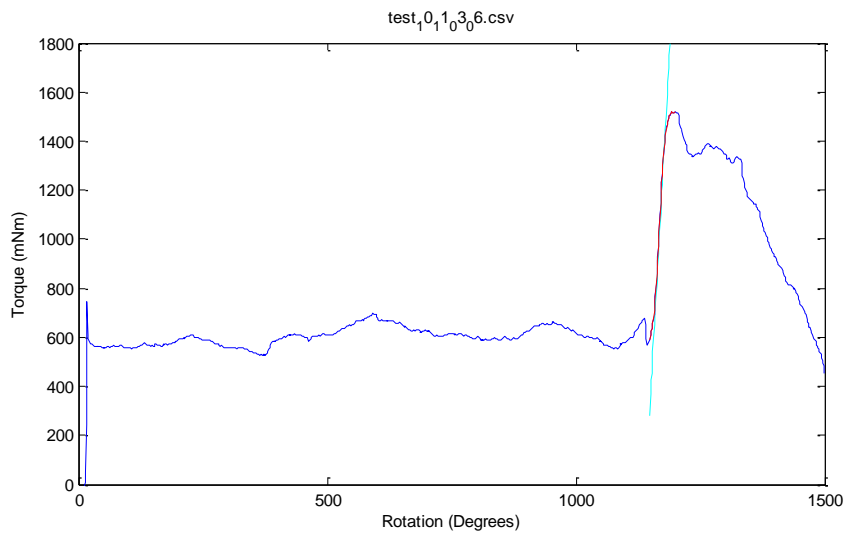
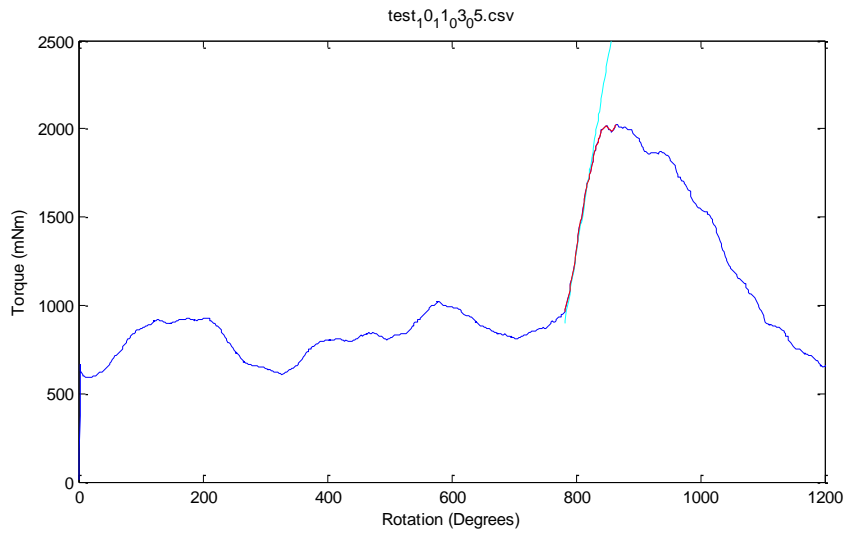


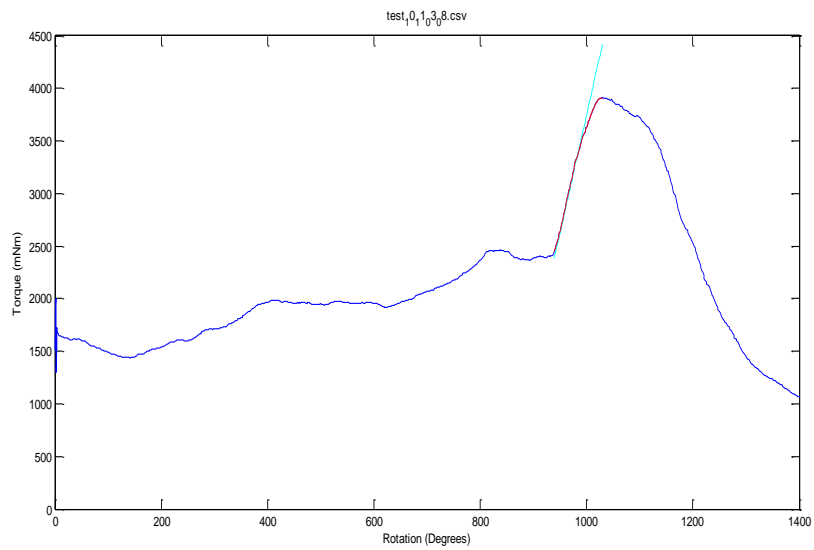
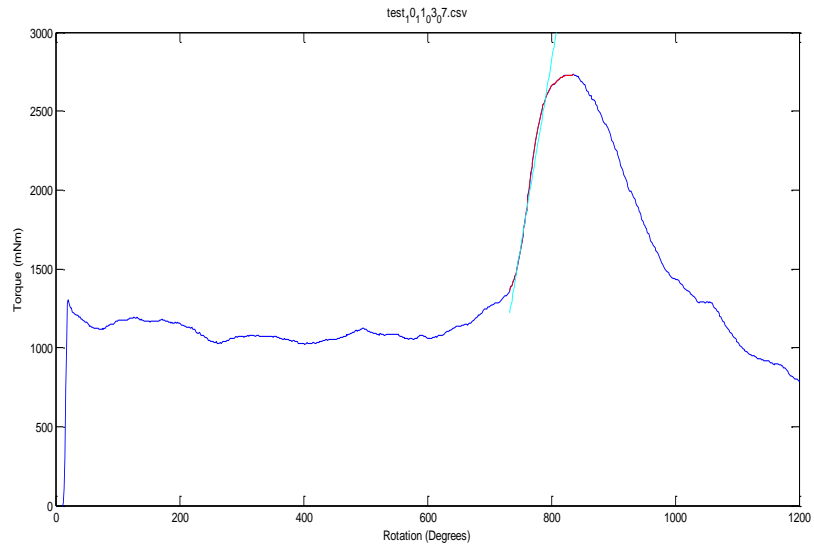


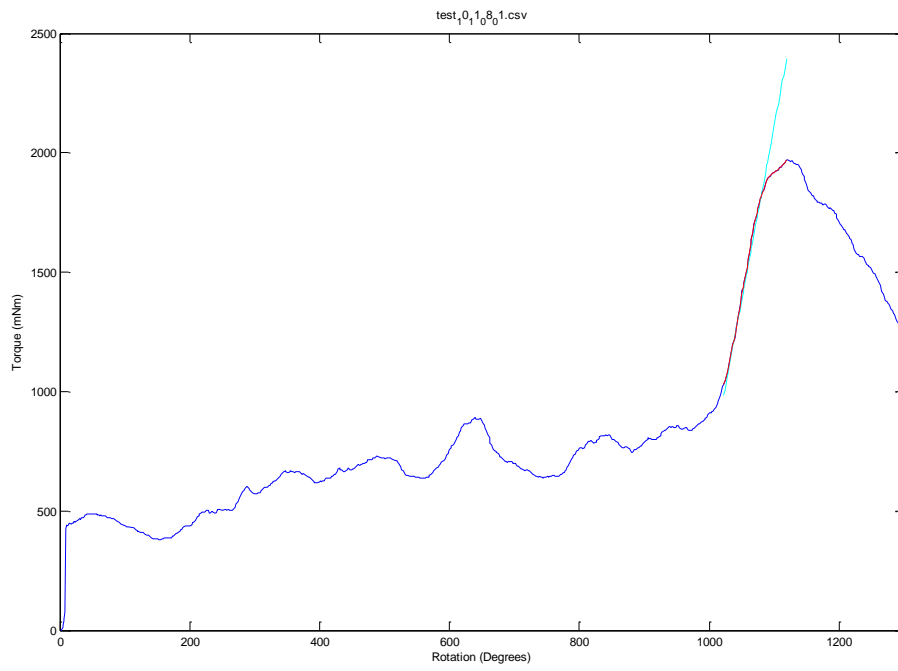
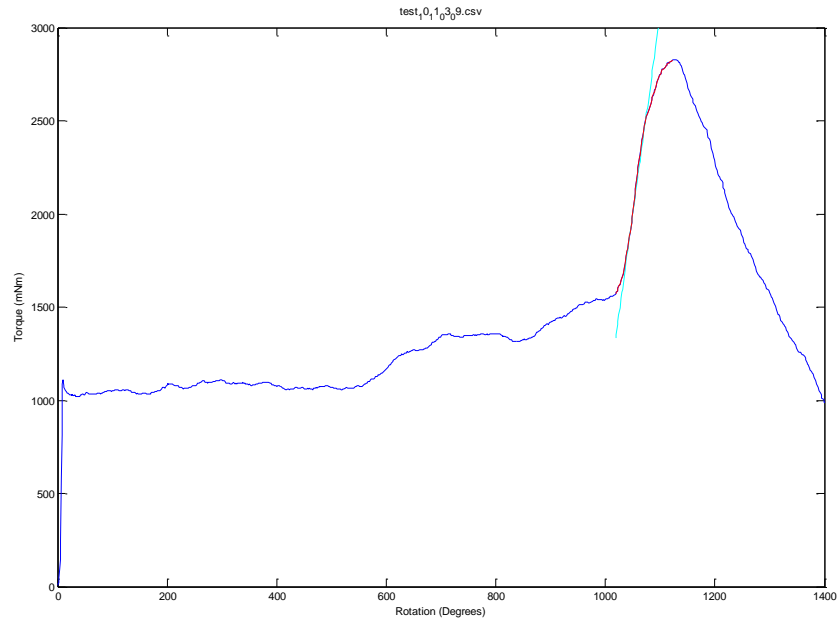


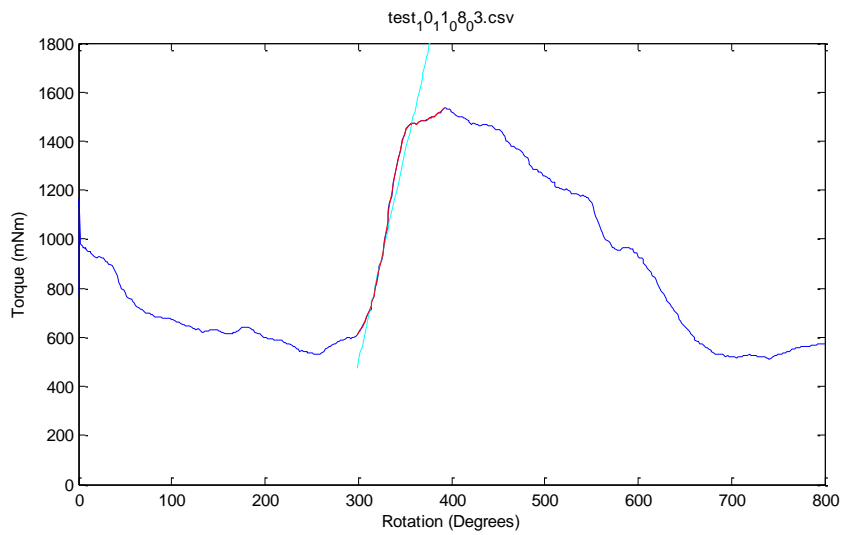
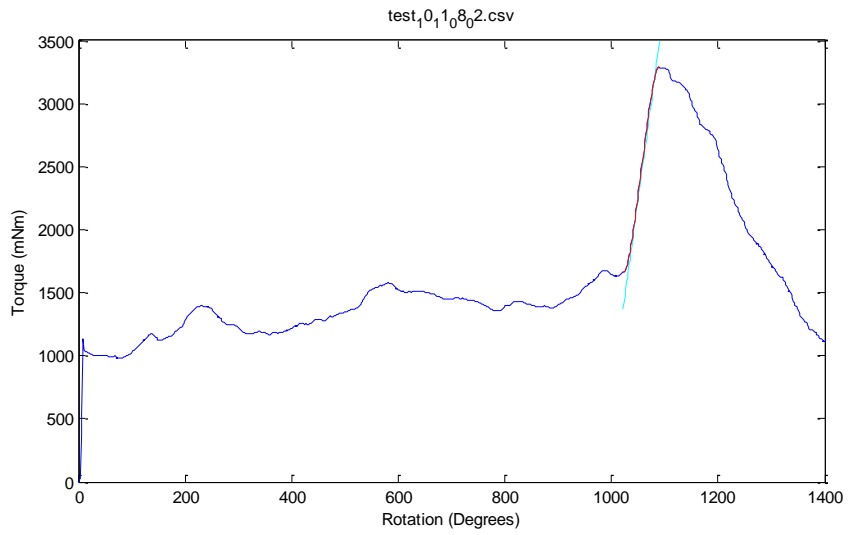


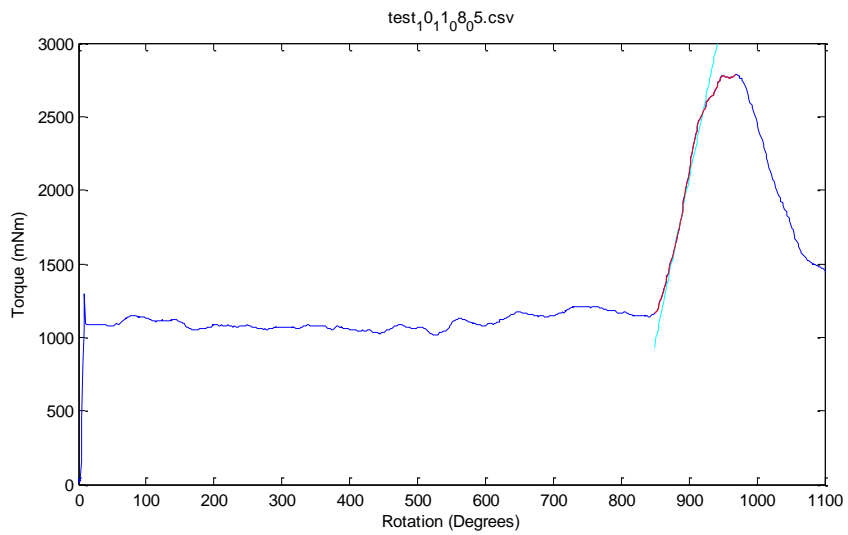
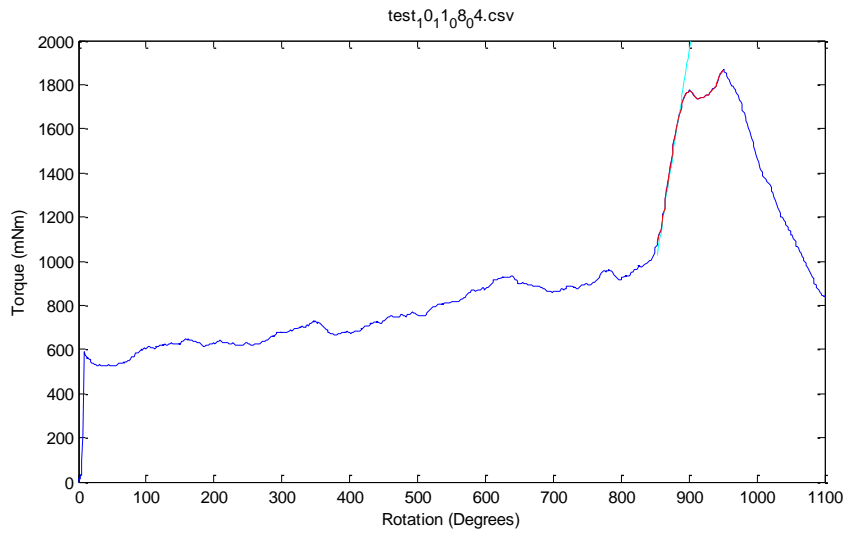


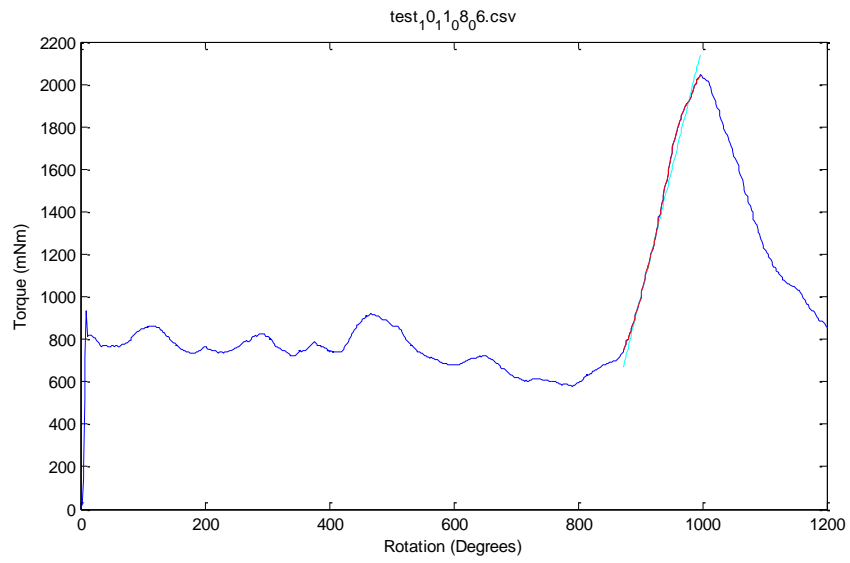






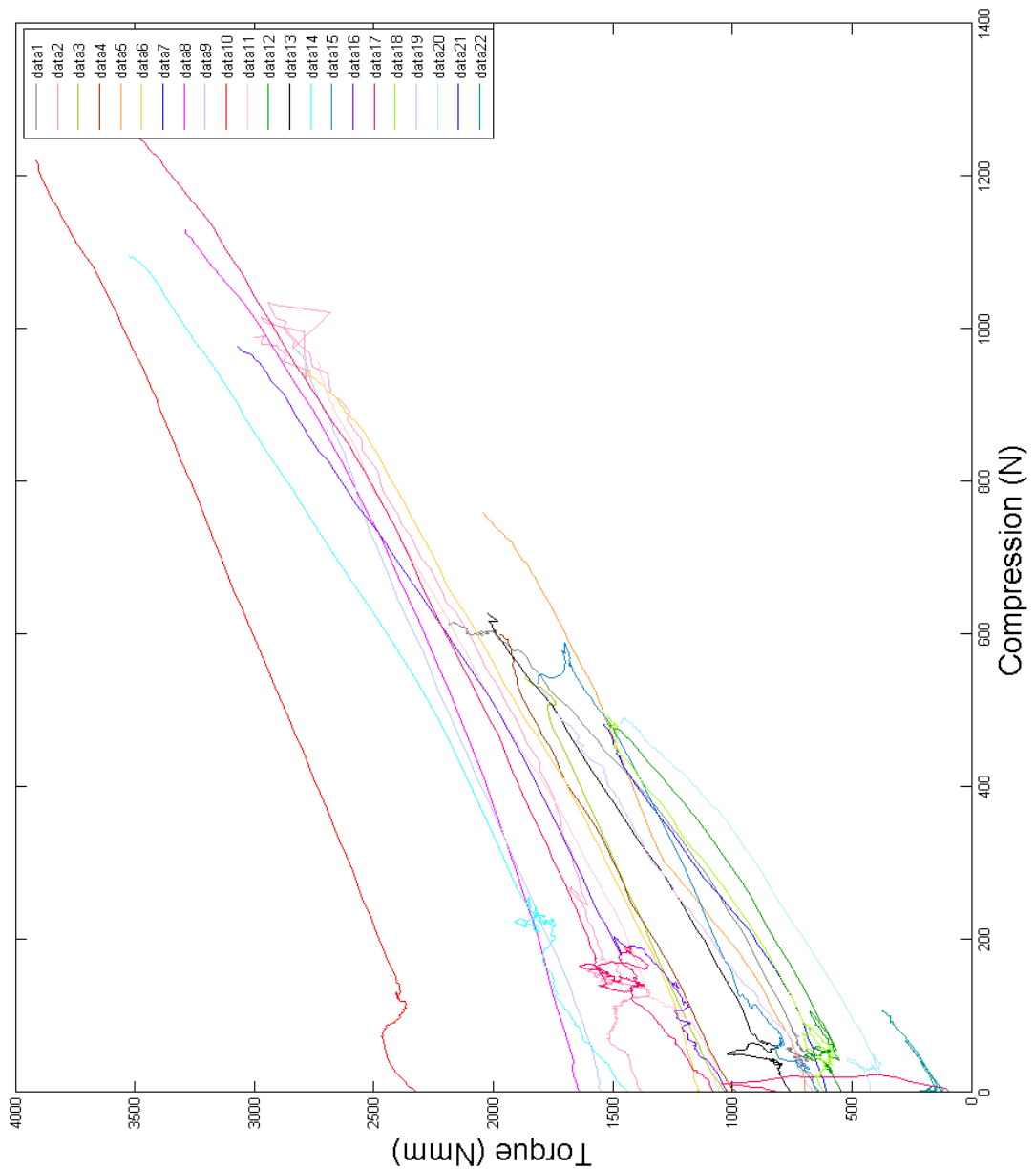






APPENDIX C: TORQUE VERSUS COMPRESSION TRACES

21 aluminium screws were inserted into femoral head specimens. The torque versus compression traces for each test is shown below; each colour represents an individual test. The relationship between compression and torque is determined by the profile of the screw. A linear relationship between compression under the screw head and insertion torque is observed for each screw.



## APPENDIX D: ANOVA of MORPHOLOGY and INSERTION PARAMETERS

## ANOVA

		ANOVA				
		Sum of Squares	df	Mean Square	F	Sig.
BTVV	Between Groups	74.685	2	37.342	1.411	.279
	Within Groups	343.993	13	26.461		
	Total	418.677	15			
TbTh	Between Groups	1421.073	2	710.536	1.285	.310
	Within Groups	7189.485	13	553.037		
	Total	8610.558	15			
TbN	Between Groups	.120	2	.060	1.306	.304
	Within Groups	.597	13	.046		
	Total	.717	15			
TbSp	Between Groups	33038.162	2	16519.081	.741	.496
	Within Groups	289989.185	13	22306.860		
	Total	323027.347	15			
TbPf	Between Groups	9.838	2	4.919	1.958	.181
	Within Groups	32.652	13	2.512		
	Total	42.490	15			
SMI	Between Groups	.632	2	.316	2.359	.134
	Within Groups	1.741	13	.134		
	Total	2.373	15			
DA	Between Groups	.688	2	.344	2.715	.103
	Within Groups	1.648	13	.127		
	Total	2.336	15			
BS	Between Groups	2820084.272	2	1410042.136	1.433	.274
	Within Groups	12789209.996	13	983785.384		
	Total	15609294.268	15			
BSBV	Between Groups	18.677	2	9.338	1.370	.288
	Within Groups	88.587	13	6.814		
	Total	107.264	15			

Post Hoc Tests

Multiple Comparisons

Bonferroni

Dependent Variable	(I) Hole	(J) Hole	Mean Difference (I-J)	Std. Error	Sig.	95% Confidence Interval	
						Lower Bound	Upper Bound
BVTV	1.00	2.00	-.80400	3.11486	1.000	-9.3572	7.7492
		3.00	4.24037	3.11486	.590	-4.3129	12.7936
	2.00	1.00	.80400	3.11486	1.000	-7.7492	9.3572
		3.00	5.04436	3.25337	.435	-3.8892	13.9779
	3.00	1.00	-4.24037	3.11486	.590	-12.7936	4.3129
		2.00	-5.04436	3.25337	.435	-13.9779	3.8892
TbTh	1.00	2.00	17.90149	14.24010	.692	-21.2009	57.0039
		3.00	20.75255	14.24010	.506	-18.3499	59.8550
	2.00	1.00	-17.90149	14.24010	.692	-57.0039	21.2009
		3.00	2.85106	14.87330	1.000	-37.9901	43.6922
	3.00	1.00	-20.75255	14.24010	.506	-59.8550	18.3499
		2.00	-2.85106	14.87330	1.000	-43.6922	37.9901
TbN	1.00	2.00	-.13156	.12974	.987	-.4878	.2247
		3.00	.08567	.12974	1.000	-.2706	.4419
	2.00	1.00	.13156	.12974	.987	-.2247	.4878
		3.00	.21722	.13551	.399	-.1549	.5893
	3.00	1.00	-.08567	.12974	1.000	-.4419	.2706
		2.00	-.21722	.13551	.399	-.5893	.1549
TbSp	1.00	2.00	100.76557	90.43883	.856	-147.5739	349.1051
		3.00	6.36558	90.43883	1.000	-241.9739	254.7051
	2.00	1.00	-100.76557	90.43883	.856	-349.1051	147.5739
		3.00	-94.39999	94.46028	1.000	-353.7821	164.9821
	3.00	1.00	-6.36558	90.43883	1.000	-254.7051	241.9739
		2.00	94.39999	94.46028	1.000	-164.9821	353.7821
TbPf	1.00	2.00	-.30474	.95967	1.000	-2.9399	2.3305
		3.00	-1.80830	.95967	.246	-4.4435	.8269
	2.00	1.00	.30474	.95967	1.000	-2.3305	2.9399
		3.00	-1.50356	1.00234	.472	-4.2559	1.2488
	3.00	1.00	1.80830	.95967	.246	-.8269	4.4435
		2.00	1.50356	1.00234	.472	-1.2488	4.2559
SMI	1.00	2.00	-.08483	.22161	1.000	-.6934	.5237

		3.00		-46066	.22161	.174	-1.0692	.1479
	2.00	1.00		.08483	.22161	1.000	-.5237	.6934
		3.00		-.37582	.23147	.385	-1.0114	.2598
	3.00	1.00		.46066	.22161	.174	-.1479	1.0692
		2.00		.37582	.23147	.385	-.2598	1.0114
DA	1.00	2.00		.23272	.21557	.900	-.3592	.8247
		3.00		.50231	.21557	.110	-.0896	1.0943
	2.00	1.00		-.23272	.21557	.900	-.8247	.3592
		3.00		.26959	.22515	.758	-.3487	.8878
	3.00	1.00		-.50231	.21557	.110	-1.0943	.0896
		2.00		-.26959	.22515	.758	-.8878	.3487
BS	1.00	2.00		-425.33155	600.6007 9	1.000	-2074.5445	1223.8814
		3.00		629.38170	600.6007 9	.941	-1019.8313	2278.5947
	2.00	1.00		425.33155	600.6007 9	1.000	-1223.8814	2074.5445
		3.00		1054.71325	627.3070 6	.350	-667.8335	2777.2600
	3.00	1.00		-629.38170	600.6007 9	.941	-2278.5947	1019.8313
		2.00		-1054.71325	627.3070 6	.350	-2777.2600	667.8335
BSBV	1.00	2.00		-1.59196	1.58070	.997	-5.9325	2.7485
		3.00		-2.57363	1.58070	.382	-6.9141	1.7669
	2.00	1.00		1.59196	1.58070	.997	-2.7485	5.9325
		3.00		-.98167	1.65099	1.000	-5.5152	3.5518
	3.00	1.00		2.57363	1.58070	.382	-1.7669	6.9141
		2.00		.98167	1.65099	1.000	-3.5518	5.5152

# REFERENCES

1. Chestnut, C.I., *Osteoporosis: A world-wide problem* 1990.
2. Eisman, J. *Reducing the burden of osteoporosis*. in *The Bone and Joint Decade Summit*. 2002. Parliament House, Canberra, Australia.
3. Access Economics Pty. Ltd., *The burden of brittle bones: Costing Osteoporosis in Australia*. 2001, Prepared for Osteoporosis Australia: Canberra, ACT.
4. *Assessment of fracture risk and its application to screening for postmenopausal osteoporosis.*, W.S. Group, Editor. 1994, World Health Organisation: Geneva.
5. Kanis, J., et al., *A meta-analysis of previous fracture and subsequent fracture risk*. *Bone*, 2004. **35**(2): p. 375-382.
6. Giannoudis, P.V. and E. Schneider, *Principles of fixation of osteoporotic fractures*. *Journal of Bone and Joint Surgery*, 2006. **88**(10): p. 1272-1278.
7. Schneider, E., J. Goldhahn, and P. Burckhardt, *The challenge: fracture treatment in osteoporotic bone*. *Osteoporos Int*, 2005. **16 Suppl 2**: p. S1-2.
8. Kim, W.Y., et al., *Failure of intertrochanteric fracture fixation with a dynamic hip screw in relation to pre-operative fracture stability and osteoporosis*. *Int Orthop*, 2001. **25**(6): p. 360-2.
9. Chua, D., S. Jaglal, and J. Schatzker, *An orthopedic surgeon survey on the treatment of displaced femoral neck fracture: opposing views*. *Canadian journal of surgery*, 1997. **40**: p. 271-277.
10. Parker, M. and G. Pryor, *Internal fixation or arthroplasty for displaced cervical hip fractures in the elderly: a randomised controlled trial of 208 patients*. *Acta Orthop Scand*, 2000. **71**: p. 440-446.
11. Cordey, J., B. Rahn, and S. Perren, *Human torque control in the use of bone screws*, in *Current concepts of internal fixation of fractures*, H. Uthoff, Editor. 1980, Springer-Verlag: Berlin, Heidelberg, New York. p. 235-243.
12. Tsuji, M., et al., *The biomechanical effect of artificial and human bone density on stopping and stripping torque during screw insertion*. *Journal of the mechanical behavior of biomedical materials*, 2013. **22**: p. 146-156.
13. Messmer, P., S. Perren, and N. Suhm, *Screws*, in *AO principles of fracture management*, T. Ruedi, R. Buckley, and C. Moran, Editors. 2007, AO Foundation publishing: Davos, Switzerland.
14. Stoesz, M., et al., *Surgeon perception of cancellous screw fixation*. *Journal of orthopaedic trauma*, 2014. **28**(1): p. e1-7.
15. Wirth, A., et al., *Implant stability is affected by local bone microstructural quality*. *Bone*, 2011. **49**(3): p. 473-478.
16. Wirth, A., R. Müller, and G. Van Lenthe, *The discrete nature of trabecular bone microarchitecture affects implant stability*. *Journal of biomechanics*, 2012. **45**(6): p. 1060-1067.
17. Tortora, G.J. and S.R. Grabowski, *Principles of Anatomy and Physiology*. 9th ed. 2000, New York: John Wiley & Sons Inc.
18. Morgan, E., G. Barnes, and T. Einhorn, *The bone organ system: form and function*, in *Osteoporosis*, R. Marcus, et al., Editors. 2008, Elsevier Academic Press: Burlington, MA. p. 3-22.
19. Jee, W., *Integrated bone tissue physiology: anatomy and physiology*, in *Bone mechanics hand book*, S. Cowin, Editor. 2001, Informa Healthcare USA Inc: New York. p. 1-68.

20. Bonucci, E., *Basic composition and structure of bone*, in *Mechanical testing of bone and the bone-implant interface*, Y. An and R. Draughn, Editors. 2000, CRC Press LLC: Boca Raton, Florida. p. 3-22.
21. Njeh, C.F., P.H. Nicholson, and J.Y. Rho, *Mechanical Testing*, in *The physical measurement of bone*, C.M. Langton and C.F. Njeh, Editors. 2004, Institute of Physics Publishing: London. p. 125-184.
22. Lucchinetti, E., D. Thomann, and G. Danuser, *Review: Micromechanical testing of bone trabeculae - potentials and limitations*. *Journal of materials science*, 2000. **35**: p. 6057-6064.
23. Nardin, M. and V.H. Frankel, *Basic biomechanics of the musculoskeletal system*. 3rd ed. 2001, New York: Lippincott Williams & Wilkins.
24. *Osteoporosis management: pathophysiology of osteoporosis*. *Pathophysiology of bone loss and fractures 2006* [cited 2010 30 June 2010]; Available from: <http://stg.centrax.com/ama/osteo/part4/module03/02path/index.htm>.
25. Martin, R., D. Burr, and N. Sharkey, *Skeletal tissue mechanics*. 1998, New York: Springer-Verlag New York Inc.
26. Wolff, J., P. Maquet, and R. Furlong, *The law of bone remodelling*, F.R. Translated by Maquet P, Editor. 1986, Springer-Verlag: Berlin, New York.
27. Viguet-Carrin, S., P. Garnero, and P. Delmas, *The role of collagen in bone strength*. *Osteoporosis International*, 2006. **17**: p. 319-336.
28. Jepsen, K. and +others, *Type-I collagen mutation compromises the post-yield behaviour of MOV13 long bone*. *Journal of orthopaedic research*, 1996. **14**(3): p. 493-499.
29. Wang, X. and e. al, *The role of collagen in determining bone mechanical properties*. *Journal of orthopaedic research*, 2001. **19**(6): p. 1021-1026.
30. Nyman, J. and e. al, *The influence of water removal on the strength and toughness of cortical bone*. *Journal of Biomechanics*, 2006. **39**(5): p. 931-938.
31. Jasiuk, I. and M. Ostoja-Starzewski, *Modeling of bone at a single lamella level*. *biomechanics and modeling in mechanobiology*, 2004. **3**: p. 67-74.
32. Ascenzi, A., E. Bonucci, and S. Bocciarelli, *An electron microscope study of osteon calcification*. *Journal of ultrastructure research*, 1965. **12**: p. 287-303.
33. Thurner, P., *Atomic force microscopy and indentation force measurements of bone*. *Wiley interdisciplinary reviews. Nanomedicine and nanobiotechnology*, 2009. **1**(6): p. 624-649.
34. Lips, P., *Vitamin D deficiency and secondary hyperparathyroidism in the elderly*. *Endocrine reviews*, 2001. **22**: p. 477-501.
35. Marieb, E., *Human anatomy & physiology*. 7 ed. 2006, India: Pearson Education India.
36. WHO, *Prevention and management of osteoporosis*, in *WHO technical report series*. 2003, WHO: Geneva.
37. Parfitt, A., *The physiologic and clinical significance of bone histomorphometric data*, in *Bone histomorphometry: techniques and interpretation*, R. Recker, Editor. 1983, CRC Press: Boca Raton, FL. p. 143.
38. Krassas, G. and P. Papadopoulou, *Oestrogen action on bone cells*. *Journal of musculoskeletal and neuronal interactions*, 2001. **2**(2): p. 143-151.
39. Pollack, S., R. Salzstein, and D. Pienkowski, *The electric double layer in bone and its influence on stress generated potentials*. *Calcified tissue international*, 1984. **36**: p. S77-S81.

40. Teitelbaum, S., *Bone resorption by osteoclasts*. Science, 2000. **289**: p. 1504-1508.
41. Rubin, M., *et al.*, *TEM analysis of the nanostructure of normal and osteoporotic human trabecular bone*. Bone, 2003. **33**: p. 269-282.
42. Burger, E. and J. Klein-Nulend, *Mechanotransduction in bone - role of the lacuno-canalicular network*. The Journal of the Federation of American Societies for Experimental Biology, 1999. **13**: p. s101-s112.
43. Müller, R., *et al.*, *Morphometric analysis of human bone biopsies: a quantitative structural comparison of histological section and micro-computed tomography*. Bone, 1998. **23**(1): p. 59-66.
44. Parfitt, A.M., *et al.*, *Bone histomorphometry: standardization of nomenclature, symbols and units*. Journal of bone and mineral research, 1987. **2**(6): p. 595 - 610.
45. Hahn, M., *et al.*, *Trabecular bone pattern factor - a new parameter for simple quantification of bone microarchitecture*. Bone, 1992. **13**: p. 327 - 330.
46. Hildebrand, T. and P. Rüegsegger, *Quantification of bone microarchitecture with the strutre model index*. Computer Methods in biomechanics and biomedical engineering, 1997. **1**(1): p. 15-23.
47. Ulrich, D., *et al.*, *The ability of three-dimensional structural indices to reflect mechanical aspects of trabecular bone*. Bone, 1999. **25**(1): p. 55-60.
48. Ciarelli, T., *et al.*, *Variations in three-dimensional cancellous bone architecture of the proximal femur in female hip fractures and in controls*. Journal of Bone and Mineral Research, 2000. **15**(1): p. 32-40.
49. Harrigan, T., *et al.*, *Limitations of the continuum assumption in cancellous bone*. Journal of biomechanics, 1988. **21**(4): p. 269-275.
50. An, Y., *Mechanical properties of bone*, in *Mechanical testing of bone and the bone-implant interface*, Y. An and R. Draughn, Editors. 2000, CRC Press LLC: Boca Raton. p. 41-63.
51. Keaveny, T., *et al.*, *Differences between the tensile and compressive strengths of bovine tibial trabecular bone depend on modulus*. Journal of biomechanics, 1994. **27**(9): p. 1137-1146.
52. Kopperdahl, D. and T. Keaveny, *Yield strain behavior of trabecular bone*. Journal of Biomechanics, 1998. **31**: p. 601-8.
53. Matsuura, M., *et al.*, *The role of fabric in the quasi-static compressive mechanical properties of human trabecular bone from various anatomical locations*. Biomechanical modelling and mechanobiology, 2008. **7**: p. 27-42.
54. Keaveny, T., *et al.*, *Systematic and random errors in compression testing of trabecular bone*. Journal of orthopaedic research, 1997. **15**(1): p. 101-110.
55. Rho, J., T. Tsui, and G. Pharr, *Elastic properties of human cortical and trabecular lamellar bone measured by nanoindentation*. Biomaterials, 1997. **28**(20): p. 1325-1330.
56. Poumarat, G. and P. Squire, *Comparison of mechanical properties of human, bovine bone and a new processed bone xenograft*. Biomaterials, 1993. **14**: p. 337-.
57. Kang, Q., Y. An, and R. Friedman, *The mechanical properties and bone densities of canine cancellous bones*. Journal of materials science: materials in medicine, 1998. **9**(5): p. 1573-4838.
58. Bourne, B.C. and M.C.H. Van der Meulen, *Finite element models predict cancellous apparent modulus when tissue modulus is scaled from specimen CT-attenuation*. Journal of Biomechanics, 2004. **37**: p. 613-321.

59. Mulder, L., *et al.*, *Intratrabecular distribution of tissue stiffness and mineralisation in developing trabecular bone*. *Bone*, 2007. **41**: p. 256-265
60. Carter, D. and W. Hayes, *The compressive behavior of bone as a two-phase structure*. *Journal of bone and joint surgery (Am)*, 1977. **59**: p. 954 -
61. Choi, K. and S. Goldstein, *A comparison of the fatigue behavior of human trabecular and cortical bone tissue*. *Journal of biomechanics*, 1992. **25**(12): p. 1371-1381.
62. Choi, K., *et al.*, *The elastic moduli of human subchondral, trabecular and cortical bone tissue and the size-dependency of cortical bone modulus*. *Journal of biomechanics*, 1990. **23**(11): p. 1103-1113.
63. Rho, J.Y., R.B. Ashman, and C. Turner, *Young's modulus of trabecular and cortical bone material: ultrasonic and microtensile measurements*. *Journal of biomechanics*, 1993. **26**(2): p. 111-119.
64. Ryan, S. and J. Williams, *Tensile testing of rodlike trabeculae excised from bovine femoral bone*. *Journal of Biomechanics*, 1989. **22**: p. 351-.
65. Turner, C., *et al.*, *The elastic properties of trabecular and cortical bone tissues are similar: results from two microscopic measurement techniques*. *Journal of biomechanics*, 1999. **32**(4): p. 437-431.
66. Busse, B., *et al.*, *Increased calcium content and inhomogeneity of mineralization render bone toughness in osteoporosis: Mineralization, morphology and biomechanics of human single trabeculae*. *Bone*, 2009. **45**(6): p. 1034-1043.
67. Riemer, B., *et al.* *Microstructure and material property variations in compact and trabecular vertebral bone tissue*. in *41st Annual Meeting of Orthopaedic Research Society*. 1995. Anaheim, Ca: ORS.
68. Brennan, O., *et al.*, *Biomechanical properties across trabeculae from the proximal femur of normal and ovariectomised sheep*. *Journal of biomechanics*, 2009. **42**: p. 498-503.
69. Harrison, N., *et al.*, *Heterogeneous linear elastic trabecular bone modelling using micro-CT attenuation data and experimentally measured heterogeneous tissue properties*. *Journal of biomechanics*, 2008. **41**: p. 2589-2596.
70. Zysset, P., *et al.*, *Elastic modulus and hardness of cortical and trabecular bone lamellae measured by nanoindentation in the human femur*. *Journal of biomechanics*, 1999. **32**(10): p. 1005-1012.
71. Bayraktar, H., *et al.*, *Comparison of the elastic and yield properties of human femoral trabecular and cortical bone tissue*. *Journal of biomechanics*, 2004. **37**: p. 27-35.
72. Hou, F., *et al.*, *Human vertebral body apparent and hard tissue stiffness*. *Journal of biomechanics*, 1998. **31**(11): p. 1009-1015.
73. Kabel, J., *et al.*, *The role of effective isotropic tissue modulus in the elastic properties of cancellous bone*. *Journal of biomechanics*, 1999. **32**(7): p. 673-680.
74. Ladd, A. and J. Kinney, *Numerical errors and uncertainties in finite-element modeling of trabecular bone*. *Journal of biomechanics*, 1998. **31**: p. 941-945.
75. Niebur, G., *et al.*, *High Resolution finite element models with tissue strength asymmetry accurately predict failure of trabecular bone*. *Journal of biomechanics*, 2000. **33**: p. 1575-1583.

76. Ulrich, D., *et al.*, *The quality of trabecular bone evaluated with micro-computed tomography, FEA and mechanical testing*. Stud Health Technol Inform, 1997. **40**: p. 97-112.
77. van Rietbergen, B., *et al.*, *A new method to determine trabecular bone elastic properties and loading using micromechanical finite-element models*. Journal of Biomechanics, 1995. **28**(1): p. 69-81.
78. Verhulp, E., *et al.*, *Micro-finite element simulation of trabecular-bone post-yield behaviour - effects of material model, element size and type*. Computer methods in biomechanics and biomedical engineering, 2008. **11**(4): p. 389-395.
79. Guo, X., *Mechanical properties of cortical and cancellous bone tissue*, in *Bone mechanics handbook*, S. Cowin, Editor. 2009, Informa healthcare: New York.
80. Riemer, B., *et al.* *Microstructure and material property variations in compact and trabecular vertebral bone tissue*. in *41st Annual Meeting Orthopaedic Research Society*. 1995. Orlando, USA.
81. Bayraktar, H. *Nonlinear micro finite element analysis of human trabecular bone*. Abaqus technology brief, 2004. **TB-03-HTB-1**, 1-4.
82. Norman, J., *et al.*, *Micromechanical properties of human trabecular bone: A hierarchical investigation using nanoindentation*. Journal of biomedical materials research Part A, 2007. **87A**(1): p. 196-202.
83. Verhulp, E., *et al.*, *Indirect determination of trabecular bone effective tissue failure properties using micro-finite element simulations*. Journal of biomechanics, 2008. **41**: p. 1479-1485.
84. Mente, P., *Micromechanical testing of single trabecular*, in *Mechanical testing of bone and the bone-implant interface*, Y. An and R. Draughn, Editors. 2000, CRC Press LLC: Boca Raton, FL. p. 291-304.
85. Goodship, A. and J. Cunningham, *Pathophysiology of functional adaptation of bone in remodeling and repair in vivo*, in *Bone mechanics hand book*, S. Cowin, Editor. 2001, Informa healthcare USA, Inc: New York, NY.
86. Oliver, W. and G. Pharr, *An improved technique for determining hardness and elastic modulus using load and displacement sensing indentation experiments*. J Mater Res, 1992. **7**: p. 1564-1583.
87. Paschalis, E., F. Betts, and E. DiCarlo, *FTIR microspectroscopic analysis of normal human cortical and trabecular bone*. Calcified Tissue International, 1997. **61**(6): p. 480-486.
88. Gruber, H., *Pathogenesis and histomorphology of osteoporosis*, in *Internal fixation in osteoporotic bone*. 2002, Thieme publishers Inc: New York, USA. p. 3-7.
89. Ebeling, P., *Osteoporosis in men. New insights into aetiology, pathogenesis, prevention, and management*. Drugs and aging, 1998. **13**: p. 421-434.
90. Gennari, C., G. Martini, and R. Nuti, *Secondary osteoporosis*. Aging, 1998. **10**: p. 214-224.
91. Sambrook, P., *et al.*, *Preventing osteoporosis: outcomes of the Australian Fracture Prevention Summit*. Medical Journal of Australia, 2002. **Suppl**: p. S1-16.
92. Parfitt, A., *Osteonal and hemi-osteonal remodeling: the spatial and temporal framework for signal traffic in adult human bone*. Journal of cellular biochemistry, 1994. **55**(3): p. 273-286.
93. Arnett, T. *Bone Research Society*. Available from: [brsoc.org.uk/gallery](http://brsoc.org.uk/gallery).

94. McNamara, L., *et al.*, *Strength of cancellous bone trabecular tissue from normal, ovariectomised and drug-treated rats over the course of ageing*. *Bone*, 2006. **39**: p. 392-400.
95. Zioupos, P., *et al.* *Bone quality issues and matrix properties in OP cancellous bone*. in *Medicine meets Engineering*. 2008. The Netherlands: IOS Press.
96. Rubin, M. and I. Jasiuk, *The TEM characterisation of the lamellar structure of osteoporotic human trabecular bone*. *Micron*, 2005. **36**: p. 2005.
97. Levine, A. and A. Aboulaflia, *Pathologic fractures*, in *Skeletal trauma*. 2008, WB Saunders Company.
98. *Internal fixation for fractures*, in *OrthoInfo*. 2007, American academy of orthopaedic surgeons.
99. Nordin, M. and V. Frankel, *Basic biomechanics of the musculoskeletal system*. 2001, Philadelphia: Lippincott Williams & Wilkins. 390-399.
100. Perren, S., *et al.*, *Technical and biomechanical aspects of screws used for bone surgery*. *International journal of orthopaedic trauma*, 1992. **2**(31): p. 31-48.
101. Cornell, C.N., *Internal fracture fixation in patients with osteoporosis*. *Journal of the American Academy of Orthopaedic Surgeons*, 2003. **11**(2): p. 109 - 119.
102. Hearn, T.C., J. Schatzker, and N. Wolfson, *Extraction strength of cannulated cancellous bone screws*. *Journal of orthopaedic Trauma*, 1993. **7**(2): p. 138 - 141.
103. Perren, S. and J. Cordey, *The concept of interfragmentary strain*, in *Current concepts of internal fixation of fractures*, H. Uthoff, Editor. 1980, Springer-Verlag: Berlin, Heidelberg, New York.
104. Kwok, A.W.L., *et al.*, *Insertional Torque and Pull-out strengths of conical and cylindrical pedicle screws in cadaveric bone*. *Spine*, 1996. **21**(21): p. 2429-2434.
105. Mizuno, K., *et al.*, *Intraoperative insertion torque of lumbar pedicle screw and postoperative radiographic evaluation: short term observation*. *Journal of Orthopaedic Science*, 2005. **10**: p. 137 - 144.
106. Suhm, N., *et al.*, *Mechanical torque measurement predicts load to implant cut-out: a biomechanical study investigating DHS anchorage in femoral heads*. *Archives of Orthopaedic and Trauma Surgery*, 2007. **127**: p. 469-474.
107. Cleek, T., K. Reynolds, and T. Hearn, *Effect of screw torque level on cortical bone pullout strength*. *Journal of orthopaedic Trauma*, 2007. **21**(2): p. 117-123.
108. Lawson, K. and J. Brems, *Effect of insertion torque on bone screw pullout strength*. *Orthopaedics*, 2001. **24**: p. 451-454.
109. Brekelmans, W., H. Poort, and T. Slooff, *A new method to analyse the mechanical behaviour of skeletal parts*. *Acta Orthop Scand*, 1972. **43**(5): p. 301-317.
110. Fung, Y., *A first course in continuum mechanics*. 3rd ed. 1969: Prentice Hall.
111. Homminga, J., *et al.*, *The osteoporotic vertebral structure is well adapted to the loads of daily life, but not to infrequent "error" loads*. *Bone*, 2004. **34**: p. 510-516.
112. Pistoia, W., *et al.*, *Estimation of distal radius failure load with micro-finite element analysis models based on three-dimensional peripheral quantitative computed tomography images*. *Bone*, 2002. **30**(6): p. 842-8.

113. Van Rietbergen, B., *et al.*, *Trabecular bone tissue strains in the healthy and osteoporotic human femur*. J Bone Miner Res, 2003. **18**(10): p. 1781-8.
114. Van Rietbergen, B., *et al.*, *Tissue stresses and strain in trabeculae of a canine proximal femur can be quantified from computer reconstructions*. Journal of Biomechanics, 1999. **32**(2): p. 165-173.
115. Morgan, E. and M. Bouxsein, *Use of finite element analysis to assess bone strength*. BoneKey-Osteovision, 2005. **2**(12): p. 8-19.
116. Pothuaud, L., *et al.*, *Combination of topological parameters and bone volume fraction better predicts the mechanical properties of trabecular bone*. Journal of Biomechanics, 2002. **35**(8): p. 1091-1099.
117. Wehrli, F., S. Hwang, and H. Song, *New architectural parameters derived from micro-MRI for the prediction of trabecular bone strength*. Technology and Health Care, 1998. **6**: p. 307-320.
118. Newitt, D., B. Van Rietbergen, and S. Majumdar, *Processing and analysis of in vivo high-resolution MR images of trabecular bone for longitudinal studies: reproducibility of structural measures and micro-finite element analysis derived mechanical properties*. Osteoporosis International, 2002. **13**: p. 278-287.
119. Majumdar, S., *A review of magnetic resonance (MR) imaging of trabecular bone micro-architecture: contribution to the prediction of biomechanical properties and fracture prevalence*. Technology and Health Care, 1998. **6**: p. 321-7.
120. Majumdar, S., *et al.*, *High-resolution magnetic resonance imaging: three dimensional trabecular bone architecture and biomechanical properties*. Bone, 1998. **22**: p. 445-454.
121. Chung, H., *et al.*, *Three-dimensional nuclear magnetic resonance microimaging of trabecular bone*. Journal of bone and mineral research, 1995. **10**: p. 1452-1461.
122. Arthur Moore, T.L. and L.J. Gibson, *Microdamage accumulation in bovine trabecular bone in uniaxial compression*. Journal of biomechanical engineering, 2002. **124**: p. 63-71.
123. Bayraktar, H. and T. Keaveny, *Mechanisms of uniformity of yield strains for trabecular bone*. Journal of biomechanics, 2004. **37**: p. 1671-1678.
124. Bevill, G., F. Farahmand, and T. Keaveny, *Heterogeneity of yield strain in low-density versus high-density human trabecular bone*. Journal of biomechanics, 2009. **42**: p. 2165-2170.
125. Bevill, G., *Micromechanical modeling of failure in trabecular bone*. 2008, University of California: Berkeley.
126. Chevalier, Y., *et al.*, *Validation of a voxel-based FE method for prediction of the uniaxial apparent modulus of human trabecular bone using macroscopic mechanical tests and nanoindentation*. Journal of biomechanics, 2007. **40**: p. 3333-3340.
127. Nagaraja, S., T.L. Couse, and R.E. Guldborg, *Trabecular bone microdamage and microstructural stresses under uniaxial compression*. J Biomech, 2005. **38**(4): p. 707-16.
128. Nazarian, A. and R. Müller, *Time-lapsed microstructural imaging of bone failure behavior*. J Biomech, 2004. **37**(1): p. 55-65.
129. Niebur, G.L., M.J. Feldstein, and T.M. Keaveny, *Biaxial failure behaviour of bovine tibial trabecular bone*. Journal of Biomechanical Engineering, 2002. **124**: p. 699-705.

130. van Lenthe, G.H. and R. Müller, *Prediction of failure load using micro-finite element analysis models: Toward in vivo strength assessment*. Drug discovery today: Technologies, 2006. **3**(2): p. 221 - 229.
131. van Rietbergen, B., *et al.* *Determination of trabecular bone tissue elastic properties by comparison of experimental and finite element results*. in *Material identification using mixed numerical experimental methods*. 1997. Kerkrade, The Netherlands: Kluwer Academic Publishers.
132. Verhulp, E., B. Van Rietbergen, and R. Huiskes, *Comparison of micro-level and continuum-level voxel models of the proximal femur*. Journal of biomechanics, 2006. **39**: p. 2951-2957.
133. Ding, M., A. Odgaard, and I. Hvid, *Accuracy of cancellous bone volume fraction measured by micro-CT scanning*. Journal of Biomechanics, 1999. **32**(3): p. 323-326.
134. Hara, T., *et al.*, *The influence of microcomputed tomography threshold variations on the assessment of structural and mechanical trabecular bone properties*. Bone, 2002. **31**(1): p. 107-109.
135. Ito, M., *et al.*, *Analysis of trabecular microarchitecture of human iliac bone using microcomputed tomography in patients with hip arthrosis with or without vertebral fracture*. Bone, 1998. **23**: p. 163-169.
136. Rügsegger, P., B. Koller, and R. Müller, *A microtomographic system for the nondestructive evaluation of bone architecture*. Calcified tissue international, 1996. **58**: p. 24-29.
137. Guldberg, R., S. Hollister, and G. Charras, *The accuracy of digital image-based finite element models*. Journal of biomechanical engineering, 1998. **120**(2): p. 289-295.
138. Niebur, G., *et al.*, *Convergence behaviour of high-resolution finite element models of trabecular bone*. Journal of biomechanical engineering, 1999. **121**(6): p. 629-635.
139. McDonnell, P., P. McHugh, and D. O'Mahoney, *Vertebral osteoporosis and trabecular bone quality*. Annals of biomedical engineering, 2007. **35**(2): p. 170-189.
140. Homminga, J., *et al.*, *Cancellous bone mechanical properties from normals and patients with hip fractures differ on the structure level, not on the bone hard tissue level*. Bone, 2002. **30**(5): p. 759-764.
141. Renders, G., *et al.*, *Biomechanical effect of mineral heterogeneity in trabecular bone*. Journal of biomechanics, 2008. **41**: p. 2793-2798.
142. van der Linden, J., *et al.*, *Trabecular bone's mechanical properties are affected by its non-uniform mineral distribution*. journal of biomechanics, 2001. **34**: p. 1573-1580.
143. Stolken, J. and J. Kinney, *On the importance of geometric nonlinearity in finite-element simulations of trabecular bone failure*. Bone, 2003. **33**: p. 494-504.
144. Bevill, G., *et al.*, *Influence of bone volume fraction and architecture on computed large-deformation failure mechanisms in human trabecular bone*. Bone, 2006. **39**: p. 1218-1225.
145. Helgason, B., *et al.*, *Mathematical relationships between bone density and mechanical properties: a literature review*. Clinical biomechanics, 2008. **23**(2): p. 135-146.

146. Keaveny, T., *et al.*, *Theoretical analysis of the experimental artefact in trabecular bone compressive modulus*. *Journal of biomechanics*, 1993. **26**(4/5): p. 599-607.
147. Linde, F. and I. Hvid, *The effect of constraint on the mechanical behaviour of trabecular bone specimens*. *Journal of Biomechanics*, 1989. **22**(5): p. 485-490.
148. Linde, F., I. Hvid, and F. Madsen, *The effect of specimen geometry on the mechanical behaviour of trabecular bone specimens*. *Journal of Biomechanics*, 1992. **25**(4): p. 359-368.
149. Odgaard, A. and F. Linde, *The underestimation of Young's modulus in compressive testing of cancellous bone specimens*. *Journal of biomechanics*, 1991. **24**(8): p. 691-698.
150. Zhu, M., T. Keller, and D. Spengler, *Effects of specimen load-bearing and free surface layers on the compression mechanical properties of cellular materials*. *Journal of Biomechanics*, 1994. **27**(1): p. 57-66.
151. Jacobs, C., *et al.*, *The impact of boundary conditions and mesh size on the accuracy of cancellous bone tissue modulus determination using large-scale finite element modeling*. *Journal of biomechanics*, 1999. **32**: p. 1159-1164.
152. Keaveny, T., *et al.*, *Trabecular bone exhibits fully linear elastic behaviour and yields at low strains*. *Journal of biomechanics*, 1994. **27**(9): p. 1127-1136.
153. Un, K., G. Bevill, and T. Keaveny, *The effects of side-artifacts on the elastic modulus of trabecular bone*. *Journal of biomechanics*, 2006. **39**: p. 2006.
154. Keaveny, T., *et al.*, *Trabecular bone modulus and strength can depend on specimen geometry*. *Journal of biomechanics*, 1993. **26**(8): p. 991-1000.
155. Bevill, G., *et al.*, *The influence of boundary conditions and loading mode on high-resolution finite element-computed trabecular tissue properties*. *Bone*, 2009. **44**: p. 573-578.
156. Wolfram, U., H.-J. Wilke, and P. Zysset, *Valid micro finite element models of vertebral trabecular bone can be obtained using tissue properties measured with nanoindentation under wet conditions*. *Journal of Biomechanics*, 2010. **43**(9): p. 1731-1737.
157. Müller, R., S. Gerber, and W. Hayes, *Micro-compression: a novel technique for the nondestructive assessment of local bone failure*. *Technology and Health Care*, 1998. **6**: p. 433-444.
158. Turner, P., *et al.*, *Time-lapsed investigation of three-dimensional failure and damage accumulation in trabecular bone using synchrotron light*. *Bone*, 2006. **39**: p. 289-299.
159. Chou, H.-Y., J. Jagodnik, and S. Muftu, *Predictions of bone remodeling around dental implant systems*. *Journal of biomechanics*, 2008. **41**: p. 1365-1373.
160. Liao, S.-H., R.-F. Tong, and J.-X. Dong, *Influence of anisotropy on per-implant stress and strain in complete mandible model from CT*. *Computerized medical imaging and graphics*, 2008. **32**: p. 53-60.
161. Cehreli, M., M. Akkocaoglu, and K. Akca, *Numerical simulation of in vivo intraosseous torsional failure of a hollow-screw oral implant*. *Head & Face Medicine*, 2006. **2**(36).
162. Zhang, Q., S. Tan, and S. Chou, *Investigation of fixation screw pull-out strength on human spine*. *Journal of Biomechanics*, 2004. **37**(4): p. 479 - 485.

163. Huang, H., *et al.*, *Comparison of implant body designs and threaded designs of dental implants: A 3-dimensional finite element analysis*. International journal of oral and maxillofacial implants, 2007. **22**(4): p. 551-562.
164. Zhang, Q., S. Tan, and S. Chou, *Effects of bone materialson the screw pull-out strength in human spine*. Medical Engineering & Physics, 2006. **28**: p. 795-801.
165. Jaecques, S.V., *et al.*, *Individualised, micro CT-based finite element modelling as a tool for biomechanical analysis related to tissue engineering of bone*. Biomaterials, 2004. **25**(9): p. 1683-96.
166. Wirth, A., *et al.*, *Mechanical competence of bone-implant systems can accurately be determined by image-based micro-finite element analyses*. Archive of applied mechanics, 2010. **80**: p. 513-525.
167. Guo, X., *Mechanical properties of cortical bone and cancellous bone tissue*, in *Bone mechanics handbook*, S. Cowin, Editor. 2001, Informa healthcare: New York. p. 1-23.
168. Rho, J. and G. Pharr, *Nanonindentation testing of bone*, in *Mechanical testing of bone and the bone-implant interface*, Y. An and R. Draughn, Editors. 2000, CRC Press LLC: Boca Raton, Florida. p. 257-269.
169. Adams, M., *et al.*, *Ultrascaleable implicit finite element analyses in solid mechanics with over a half a billion degrees of freedom*, in *2004 ACM/IEEE conference on supercomputing*. 2004, IEEE Computer Society.
170. Legrand, E., *et al.*, *Trabecular bone microarchitecture, bone mineral density, and vertebral fractures in male osteoporosis*. Journal of bone and mineral research, 2000. **15**(1): p. 13-19.
171. Badiei, A., M. Bottema, and N. Fazzalari, *Influence of orthogonal overload on human vertebral trabecular bone mechanical properties*. Journal of Bone and Mineral Research, 2007. **22**(11): p. 1690-9.
172. Parkinson, I., A. Badiei, and N. Fazzalari, *Variation in segmentation of bone from micro-CT imaging: implications for quantitative morphometric analysis*. Australasian physical and engineering sciences in medicine, 2008. **31**(2): p. 160-164.
173. Badiei, A., *Non-invasive assessment of trabecular bone structural anisotropy - relevance to mechanical anisotropy*, in *Faculty of Health Sciences, Discipline of pathology*. 2008, The university of Adelaide: Adelaide. p. 209.
174. Hibbeler, R., *Mechanical properties of materials*, in *Mechanics of materials*. 2011, Prentice Hall: Singapore. p. 81-118.
175. Cohen, J., *Statistical poer analysis for the behavioural sciences*. 2nd ed. 1988, Hillsdale, NJ: Erlbaum.
176. Borrelli, A., *et al.*, *Bone histomorphometry in Cushing's syndrome*. Journal of endocrinological investigations, 1992. **15**: p. 1992.
177. Meunier, P., *et al.*, *Physiological senile involution and pathological rarefaction of bone*. Journal of clinical endocrinology and metabolism, 1973. **2**: p. 1973.
178. Yeni, Y., *et al.*, *Trabecular shear stresses predict in vivo linear microcrack density but not diffuse damage in human vertebral cancellous bone*. Ann Biomed eng, 2003. **31**: p. 726-732.
179. Yeni, Y., *et al.*, *Trabecular shear stress in human vertebral cancellous bone: Intra- and interindividual variations*. journal of biomechanics, 2001. **34**: p. 1341-1346.

180. Waarsing, J., S. Judd, and H. Weimans, *An improved segmentation method for in vivo micro-CT imaging*. Journal of bone and mineral research, 2004. **19**(10): p. 1640 - 1650.
181. Kim, C., *et al.*, *Effects of thresholding techniques on CT-based finite element models of trabecular bone*. Journal of biomechanical engineering, 2007. **129**: p. 481 - 486.
182. Kuhn, J., *et al.*, *Evaluation of a microcomputed tomography system to study trabecular bone structure*. Journal of orthopaedic research, 1990. **8**: p. 833-842.
183. Yeni, Y., *et al.*, *Effect of microcomputed tomography voxel size on the finite element model accuracy for human cancellous bone*. Journal of biomechanical engineering, 2005. **127**(1): p. 1-8.
184. Yeni, Y. and D. Fyhrie, *Finite element calculated uniaxial apparent stiffness is a consistent predictor of uniaxial apparent strength in human vertebral cancellous bone tested with different boundary conditions*. Journal of Biomechanics, 2001. **34**: p. 1649-1654.
185. Jaasma, M., *et al.*, *Biomechanical effects of intraspecimen variations in tissue modulus for trabecular bone*. Journal of biomechanics, 2002. **35**: p. 237-246.
186. Bevill, G., S. Easley, and T. Keaveny, *Side-artifact errors in yield strength and elastic modulus for human trabecular bone and their dependence on bone volume fraction and anatomic site*. Journal of biomechanics, 2007. **40**: p. 3381-3388.
187. Keaveny, T., *et al.*, *Biomechanics of trabecular bone*. Annual review of biomedical engineering, 2001. **3**: p. 307-333.
188. Fyhrie, D. and D. Vashishth, *Bone stiffness predicts strength similarly for human vertebral cancellous bone in compression and for cortical bone in tension*. Bone, 2000. **26**(2): p. 169-173.
189. Guo, X. and S. Goldstein, *Vertebral trabecular bone microscopic tissue elastic modulus and hardness do not change in ovariectomised rats*. Journal of orthopaedic research, 2000. **18**: p. 333-336.
190. Bala, Y., *et al.*, *Time sequence of secondary mineralization and microhardness in cortical and cancellous bone from ewes*. Bone, 2010. **46**(4): p. 1204-1212.
191. Simmons Jr, E., K. Pritzker, and M. Grynblas, *Age-related changes in human femoral cortex*. Journal of orthopaedic research, 1991. **9**: p. 155-167.
192. Müller, R. and P. Rügsegger, *Three-dimensional finite element modelling of non-invasively assessed trabecular bone structures*. Med Eng Phys, 1995. **17**(2): p. 126-33.
193. Cowin, S., *Bone mechanics*. 1988, Boca Raton, Fl.
194. van Rietbergen, B., *et al.*, *The role of trabecular architecture in the anisotropic mechanical properties of bone*, in *Bone structure and remodeling (Recent Advances in Human Biology)*, A. Odgaard and H. Weinans, Editors. 1995, World Scientific Publishing Company, Inc. p. 137-145.
195. Mosekilde, L., *Age-related changes in vertebral trabecular bone architecture - assessed by a new method*. Bone, 1988. **9**(4): p. 247-250.
196. Kleerekoper, M., *et al.*, *The role of three-dimensional trabecular microstructure in the pathogenesis of vertebral compression fractures*. Calcified tissue international, 1985. **37**: p. 594-597.
197. Ansys, I., *Mechanical APDL command reference*, in *Ansys Help*.

198. Chang, W., *et al.*, *Isotropy of uniaxial yield strains for bovine trabecular bone*. Journal of orthopaedic research, 1999. **17**: p. 582-585.
199. Ford, C. and T. Keaveny, *The dependence of shear failure properties of bovine tibial trabecular bone on apparent density and trabecular orientation*. Journal of Biomechanics, 1996. **29**: p. 1309-1317.
200. Nicholson, P., *et al.*, *Structural and material mechanical properties of human vertebral cancellous bone*. Medical Engineering & Physics, 1997. **19**(8): p. 729-737.
201. Mosekilde, L., L. Mosekilde, and C. Danielsen, *Biomechanical competence of vertebral trabecular bone in relation to ash density and age in normal individuals*. Bone, 1987. **8**(2): p. 79-85.
202. Gong, H., *et al.*, *Regional variations in the apparent and tissue-level mechanical parameters of vertebral trabecular bone with aging using micro-finite element analysis*. Annals of biomedical engineering, 2007. **35**(9): p. 1622-1631.
203. Niebur, G., J. Yuen, and T. Keaveny. *Role of hard tissue quality in trabecular bone failure mechanisms*. in *46th Annual Meeting, Orthopaedic Research Society*. 2000. Orlando Florida.
204. Shi, X., X. Wang, and G. Niebur, *Effects of loading orientation on the morphology of the predicted yielded regions in trabecular bone*. Annals of biomedical engineering, 2009. **37**(2): p. 354-362.
205. Melton, L., *et al.*, *Perspective: How many women have osteoporosis*. J Bone Miner Res, 1992. **7**: p. 1005-1010.
206. Borah, B., *et al.*, *Risedronate preserves trabecular architecture and increases bone strength in vertebra of ovariectomized minipigs as measured by three-dimensional microcomputed tomography*. J Bone Miner Res, 2002. **17**(7): p. 1139-1147.
207. Chung, H., *et al.*, *Relationship between NMR transverse relaxation, trabecular bone architecture and strength*. Proceedings of the National Academy of Sciences of the USA, 1993. **90**(21): p. 10250 - 10254.
208. Niebur, G., *et al.*, *Sensitivity of damage predictions to tissue level yield properties and apparent loading conditions*. Journal of Biomechanics, 2001. **34**(5): p. 699-706.
209. Eswaran, S., *et al.*, *Multi-scale modeling of the human vertebral body: comparison of micro-CT based high resolution and continuum level models*, in *Pacific Symposium on Biomcomputing*. 2009: Big Island, Hawaii.
210. Inc, A., *Ansys Reference Manual 12.0*. 2009.
211. Fyhrie, D.P. and M.B. Schaffler, *Failure mechanisms in human vertebral cancellous bone*. Bone, 1994. **15**(1): p. 105-9.
212. Bayraktar, H., *et al.*, *The role of large deformations in trabecular bone mechanical behavior*, in *Summer Bioengineering Conference*. 2003: Key Biscayne, Florida.
213. Banse, X., T. Sims, and A. Bailey, *Mechanical properties of adult vertebral cancellous bone: correlation with collagen intermolecular cross-links*. Journal of bone and mineral research, 2002. **17**(9): p. 1621-1627.
214. Allard, F. and R. Ashman. *A comparison between cancellous bone compressive moduli determined from surface strain and total specimen deflection*. in *Transactions of the 37th Orthopaedic Research Society* 1991.

215. Ashman, R., J. Rho, and C. Turner, *Anatomical variation of the orthotropic elastic moduli of the proximal human tibia*. Journal of biomechanics, 1989. **22**: p. 895-900.
216. Linde, F. and I. Hvid, *Stiffness behaviour of tabecular bone specimens*. Journal of Biomechanics, 1987. **20**(1): p. 83-89.
217. Odgaard, A., I. Hvid, and F. Linde, *Compressive axial strain distributions in cancellous bone specimens*. Journal of Biomechanics, 1989. **22**(8-9): p. 829-835.
218. Mosekilde, L. and L. Mosekilde, *Sex differences in age-related changes in vertebral body size, density and biomechanical competence in normal individuals*. Bone, 1990. **11**(2): p. 67-73.
219. Koistinen, A., S.K. Santavirta, H, and R. Lappalainen, *Effect of bone mineral density and amorphous diamond coatings on insertion torque of bone screws*. Biomaterials, 2005. **26**: p. 5687-5694.
220. Carmouche, J., et al., *Effects of pilot hole preparation technique on pedicle screw fixation in different regions of the osteoporotic thoracic and lumbar spine*. Journal of neurosurgery: Spine, 2005. **3**(5): p. 364-370.
221. Brown, G., et al., *Mechanical performance of standard and cannulated 4.0mm cancellous bone screws*. Journal of orthopaedic research, 2000. **18**(2): p. 307-12.
222. Shigley, J. and L. Mitchell, *The design of screws fasteners and connections*, in *Mechanical engineering design*. 1983, McGraw-Hill: New York.
223. Egol, K.K., EN, E. Fulkerson, and F.K. Kummer, KJ, *Biomechanics of locked plates and screws*. Journal of orthopaedic Trauma, 2004. **18**(8): p. 488-93.
224. Ricci, W., et al., *A comparison of screw insertion torque and pullout strength*. Journal of orthopaedic trauma, 2010. **24**(6): p. 374-8.
225. Chapman, J.R., *Factors affecting the pullout strength of cancellous bone screws*. Journal of biomechanical engineering, 1996. **118**(3): p. 391 - 398.
226. Thomas, R., K. Bouazza-Marouf, and G. Taylor, *Automated surgical screwdriver: Automated screw placement*. Proceedings of the institution of mechanical engineers, 2008. **22**(5): p. 451-454.
227. McGuire, R., K. St John, and S. Agnew, *Analysis of the torque applied to bone screws by trauma surgeons. Comparisons based on years of experience and material of implant construction*. American journal of orthopaedics, 1995. **24**(3): p. 254-6.
228. Collinge, C., B. Hartigan, and E. Lautenschlager, *Effects of surgical errors on small fragment screw fixation*. Journal of orthopaedic trauma, 2006. **20**(6): p. 410-13.
229. Burstein, A., et al., *Bone strength: the effect of screw holes*. Journal of bone and joint surgery (Am), 1972. **54**: p. 1143-1156.
230. Tencer, A. and K. Johnson, *Biomechanics in orthopaedic trauma*, in *Bone fracture and fixation*. 1994, Martin Dunitz Ltd: London. p. 118-157.
231. Reynolds, K., et al., *Predicting cancellous bone failure during screw insertion*. Journal of biomechanics, 2013. **46**: p. 1207-1210.
232. Suetens, P., *X-ray confirmed tomography*, in *Fundamentals of medical imaging*. 2002, Cambridge University Press: Cambridge, UK. p. 85-87.
233. Buckwalter, K., C. Lin, and J. Ford, *Managing postoperative artifacts on computed tomography and magnetic resonance imaging*. Seminars in musculoskeletal radiology, 2011. **15**(4): p. 309-19.

234. Lee, M.J., *et al.*, *Overcoming artifacts from metallic orthopedic implants at high-field-strength MR imaging and multi-detector CT*. *Radiographics*, 2007. **27**(3): p. 791-803.
235. van der Linden, J. and H. Weinans, *Effects of microarchitecture on bone strength*. *Current osteoporosis reports*, 2007. **5**(2): p. 56-61.
236. Feldkamp, L.A., *et al.*, *The direct examination of three-dimensional bone architecture in vitro by computed tomography*. *Journal of bone and mineral research*, 1989. **4**(1): p. 3 - 11.
237. Otsu, N., *A threshold selection method from gray-level histograms*. *IEEE Transactions on Systems, Man and Cybernetics*, 1979. **9**(1): p. 62-66.
238. Fajardo, R., T. Ryan, and J. Kappelman, *Assessing the accuracy of high-resolution x-ray computed tomography of primate trabecular bone by comparisons with histological sections*. *American journal of physical anthropology*, 2002. **118**(1): p. 1-10.
239. Goulet, R., *et al.*, *The relationship between the structural and orthogonal compressive properties of trabecular bone*. *Journal of biomechanics*, 1994. **27**(4): p. 375-389.
240. Selvan, V., *et al.*, *Optimum configuration of cannulated hip screws for the fixation of intracapsular hip fractures: a biomechanical study*. *Injury*, 2004. **35**(2): p. 136-41.
241. Ross, C.T.F., *Mechanics of solids*. 1999, Albion Horwood Publishers.
242. Barrett, J.F. and N. Keat, *Artifacts in CT: Recognition and Avoidance*. *Radiographics*, 2004. **24**(6): p. 1679-1691.
243. Stoppie, N., *et al.*, *Validation of microfocus computed tomography in the evaluation of bone implant specimens*. *Clinical implant dentistry and related research*, 2005. **7**(2): p. 87-94.
244. Kurtz, S. and J. Devine, *PEEK Biomaterials in Trauma, Orthopedic and Spinal implants*. *Biomaterials*, 2007. **28**(32): p. 4845-4869.
245. Augat, P., *et al.*, *Shear movement at the fracture site delays healing in a diaphyseal fracture model*. *Journal of orthopaedic research*, 2003. **21**(6): p. 1011-1017.
246. Drew, T. and P. Allcock, *A new method of fixation in osteoporotic bone: A preliminary report*. *Injury*, 2002. **33**(8): p. 685-689.
247. Terrier, A., *et al.*, *Tightening force and torque of nonlocking screws in a reverse shoulder prosthesis*. *Clinical biomechanics*, 2010. **25**(6): p. 517-22.
248. Reitman, C.A., L. Nguyen, and G.R. Fogel, *Biomechanical evaluation of relationship of screw pullout strength, insertional torque, and bone mineral density in the cervical spine*. *J Spinal Disord Tech*, 2004. **17**(4): p. 306-11.
249. Ryken, T., *et al.*, *Biomechanical analysis of bone mineral density, insertion technique, screw torque, and holding strength of anterior cervical plate screws*. *Journal of neurosurgery*, 1995. **83**(2): p. 325-9.
250. Nazarian, A., *et al.*, *Functional dependence of cancellous bone shear properties on trabecular microstructure evaluated using time-lapsed micro-computed tomographic imaging and torsion testing*. *Journal of orthopaedic research*, 2009. **27**(12): p. 1667 - 1674.
251. Nazarian, A., *et al.*, *Bone volume fraction explains variation in strength and stiffness of cancellous bone affected by metastatic cancer and osteoporosis*. *Calcified tissue international*, 2008. **83**(6): p. 368-379.

252. Ab-Lazid, R.P., E. M. Ryan, and J.R. Costi, KJ, *Does cancellous screw insertion torque depend on bone mineral density and/or microarchitecture?* Journal of biomechanics, 2014. **47**(2): p. 347-353.
253. Ding, M., *et al.*, *Age-related variations in the microstructure of human tibial cancellous bone.* Journal of orthopaedic research, 2002. **20**(3): p. 615-621.
254. Ikeda, S., *et al.*, *Effect of trabecular bone contour on ultimate strenght of lumbar vertebra after bilateral ovariectomy in rats.* Bone, 2001. **28**(6): p. 625-633.
255. Kang, Q. and Y. An, *The mechanical properties and bone densities of canine cancellous bones.* Journal of materials science and materials in medicine, 1998. **9**(5): p. 263-7.
256. Poodenphant, J., *et al.*, *Bone mass, bone structure and vertebral fractures in osteoporotic patients.* Bone, 1987. **8**(3): p. 127-30.
257. Recker, R., *Architecture and vertebral fracture.* Calcified tissue international, 1993. **Suppl 1**: p. S139-S142.
258. Thomsen, J., E. Ebbesen, and L. Mosekilde, *Relationships between static histomorphometry and bone strength measurements in human iliac crest bone biopsies.* Bone, 1998. **22**(2): p. 153-163.
259. Turner, C. and D. Burr, *Experimental techniques for bone mechanics*, in *Bone Mechanics Handbook*, S. Cowin, Editor. 2001, CRC Press. p. 7/1 - 7/35.
260. Brinley, C., *et al.*, *Pitch and longitudinal fluting effects on the primary stability of miniscrew implants.* The Angle Orthodontist, 2009. **79**(6): p. 1156-1161.
261. Sfeir, C., *et al.*, *Fracture repair*, in *Bone regeneration and repair. Biology and clinical applications*, J. Lieberman and G. Friedlaender, Editors. 2005, Humana press. p. 21-44.
262. Turner, C., *Three rules for bone adaptation to mechanical stimuli.* Bone, 1998. **23**(5): p. 399-407.
263. Bragdon, C., *et al.*, *Differences in stiffness of the interface between a cementless porous implant and cancellous bone in vivo in dogs due to varying amounts of implant motion.* Journal of arthroplasty, 1996. **96**(11): p. 945-951.
264. Jasty, M., *et al.*, *In vivo skeletal responses to porous-surfacedimplants subjected to small induced motions.* Journal of bone and joint surgery (Am), 1997. **79**(5): p. 707-714.
265. Soballe, K., *et al.*, *Tissue ingrowth into titanium and hdroxyapatite-coated implants during stable and unstale mechanical conditions.* Journal of orthopaedic research, 1992. **10**(2): p. 285-99.
266. Rahbek, O., S. Overgaard, and K. Soballe, *Calcium phosphate coatings for implant fixation*, in *Fifteen years of clinical experience with hydorxyapatite coatings in joint arthroplasty*, J.-A. Epinette and M. Manley, Editors. 2004, Springer-Verlag: France. p. 35-52.
267. Carter, D. and N. Giori, *Effect of mechanical stress on tissue differentiation in the bony implant bed.*, in *The bone-biomaterial interface*, J. Davies and T. Albrektsson, Editors. 1991, University of Toronto Press: Buffalo. p. 367-375.
268. Giori, N., L. Ryd, and D. Carter, *Mechanical influences on tissue differentiation at bone-cement interfaces.* Journal of arthroplasty, 1995. **10**: p. 514-22.
269. Mavrogenis, A., *et al.*, *Biology of implant osseointegration.* Journal of musculoskeletal and neuronal interactions, 2009. **9**(2): p. 61-71.

270. Pilliar, R., J. Lee, and C. Maniopoulos, *Observations on the effect of movement on bone ingrowth into porous-surfaced implants*. Clinical orthopaedics and related research, 1986. **208**: p. 108-113.
271. Maurer, S., *et al.*, *Two or three screws for fixation of femoral neck fractures*. American journal of orthopaedics, 2003. **32**(9): p. 438-42.
272. Dinah, A., *et al.*, *Inadvertent screw stripping during ankle fracture fixation in elderly bone*. Geriatric orthopaedic surgery and rehabilitation, 2011. **2**: p. 86-89.
273. Tankard, S., *et al.*, *Does maximum torque mean optimal pullout strength of screws*. Journal of orthopaedic Trauma, 2013. **27**(4): p. 232-235.
274. Silva, M.J. and L.J. Gibson, *Modeling the mechanical behavior of vertebral trabecular bone: Effects of age-related changes in microstructure*. Bone, 1997. **21**(2): p. 191-199.
275. Guo, X.E. and C.H. Kim, *Mechanical consequence of trabecular bone loss and its treatment: a three-dimensional model simulation*. Bone, 2002. **30**(2): p. 404-11.
276. Basler, S., *Towards a biomechanical understanding of implant stability using functional bioimaging and computational modeling*, in *Sciences*. 2012, ETH Zurich: Switzerland.
277. Mueller, T., *et al.*, *Time-lapsed imaging of implant fixation failure in human femoral heads*. Medical Engineering & Physics, 2013. **35**(5): p. 636-43.
278. Marinovic, M., *et al.*, *Histomorphometric analysis of subchondral bone of the femoral head in osteoarthritis and osteoporosis*. journal of the croatian anthropological society, 2011. **35**(Suppl 2): p. 19-23.
279. Stauber, M. and R. Muller, *Age-related changes in trabecular bone microstructures: global and local morphometry*. Osteoporosis International, 2006. **17**(4): p. 616-626.
280. Jungmann, R., *et al.*, *Local strain and damage mapping in single trabeculae during three-point bending tests*. Journal of the mechanical behavior of biomedical materials, 2011. **4**: p. 523-534.
281. Szabo, M., *et al.*, *Similar damage initiation but different failure behaviour in trabecular and cortical bone tissue*. Journal of the mechanical behaviour of biomedical materials, 2011. **4**: p. 1787-1796.
282. Basler, S., *et al.*, *Peri-implant bone microstructure determines dynamic implant cut-out*. Medical Engineering & Physics, 2013. **35**(10): p. 1442-9.
283. Kopperdahl, D. and T. Keaveny, *Yield strain behaviour of trabecular bone*. Journal of Biomechanics, 1998. **31**(7): p. 601-608.
284. Uhthoff, H., *Mechanical factors influencing the holding power of screws in compact bone*. The journal of bone and joint surgery, 1973. **55B**(3): p. 633-639.